



Cape Peninsula
University of Technology

**Performance optimisation of horizontal axis wind turbine rotors
retrofitted with an aerodynamic device**

by

Daniel Barnard

**Thesis submitted in fulfilment of the requirements for the degree,
Doctor of Engineering in Mechanical Engineering**

**Faculty of Engineering and the Built Environment at the Cape Peninsula University of
Technology**

**Supervisor: Prof. G. Oliver
Co-supervisor: Dr. H. Fawkes**

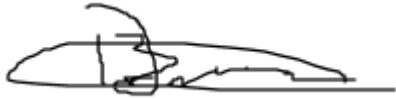
**Bellville
February 2025**

CPUT copyright information

The dissertation/thesis may not be published either in part (in scholarly, scientific or technical journals), or as a whole (as a monograph), unless permission has been obtained from the University.

Declaration

I, Daniel Barnard declare that the contents of this dissertation/thesis represent my own unaided work, and that the dissertation/thesis has not previously been submitted for academic examination towards any qualification. Furthermore, it represents my own opinions and not necessarily those of the Cape Peninsula University of Technology.



13 February 2025

Signed

Date

Abstract

Horizontal axis wind turbines (HAWTs) worldwide have a fixed operational performance profile determined by the initial design of the rotor. Over the years, design methods for HAWT rotors have advanced, allowing for customisation based on specific environmental conditions at the installation site. Typically, wind turbines have an average lifespan of 20 years before rotor replacement or decommissioning. Some post-installation methods can enhance a turbine's performance profile during its operational life. This research focused on improving rotor performance by placing an aerodynamic device (a ring vane) near the hub region and upstream of the rotor plane for post installation improvement.

The ring vane consists of a ring with aerofoil profile supported by three streamlined struts spaced at 120 degrees and attached to the hub. Various ring vanes with different diameters relative to the rotor diameter were tested. The percentage of ring vane diameter to rotor outer diameter was used to describe the different ring vane sizes. Ring vanes ranged from 15% to 20% of the rotor diameter, with 1% increments.

The performance of six retrofitted ring vane rotors was compared to a standard rotor without a ring vane, which served as the baseline. Performance data were obtained through computational fluid dynamics (CFD) simulations and physical testing using a vertical-travel test apparatus that drove the rotors at a constant relative velocity of 0.5 m/s into a body of stationary water. The rotors had a diameter of 280 mm for both physical testing and simulations and used water as the working fluid. Additionally, a case study using simulations was conducted to evaluate the performance of the best-performing ring vane and the standard rotor at a higher relative free stream velocity of 1 m/s.

Simulation results at a relative velocity of 0.5 m/s indicated that the 18% ring vane rotor had the best performance improvement, with a peak increase of 2.3% compared to the baseline rotor at 5.3 tip speed ratio. The 18% ring vane rotor outperformed the standard with 4.04% and 3.2% at off design tip speed ratios of 4.7 and 5.9 respectively. Post-simulation processing revealed that the 18% ring vane rotor exhibited enhanced axial and angular induction factors across the blade, indicating aerodynamic benefits.

Physical testing at the same relative velocity confirmed that the 18% ring vane rotor had the best performance profile, improving across a range of tip speed ratios from 4.4 to 5, with a peak increase of 4.35% at respective peak tip speed ratio. The 18% ring vane rotor outperformed the standard with 0.24% and 25% at off design tip seed ratios of 4.4 and 5 respectively.

The case study at a higher relative velocity of 1 m/s, beyond the capabilities of physical testing, showed that the 18% ring vane rotor continued to improve performance across the entire operational speed range, although with a lower peak increase of 0.8%. The 18% ring vane rotor outperformed the standard with 1.34% and 1.74% at off design tip speed ratios of 4.4 and 6 respectively.

The axial and angular induction improvements at this higher velocity confirmed the ring vane's positive aerodynamic impact.

Overall, this research demonstrates that retrofitting HAWTs with a ring vane can significantly enhance their operational performance, providing a viable method for improving the efficiency of existing wind turbines.

Acknowledgements

I wish to thank Prof. G. Oliver for his supervision and Dr. H. Fawkes for his dedication to this field of study and his mentorship. Also, thanks to, K. Snyders and Dr. O. Nemraoui for your support.

List of publications

Here is a list of publications related to this research, including those already published and those currently under review.

1. Published conference paper on a preliminary CFD study for rotor retrofitted with guide rings.
D. R. Barnard and Dr F. Ismail (2022) “CFD Simulation of Horizontal Axis Wind Turbine Rotor with fitted guide ring”. 3rd Energy & Human Habitat Conference 2022 (EHH2022), Zenodo. doi: 10.5281/zenodo.7366044.
2. Published journal Article for the physical testing results of this research.
Barnard DR, Fawkes HT, Oliver GJ. Performance enhancement of horizontal axis wind turbine with guide ring. Wind Engineering. 2024;0(0). doi:10.1177/0309524X241292362
3. Submitted journal article under review.
Title: Simulation of performance enhancement of horizontal axis wind turbine with guide ring
Journal: Wind Engineering

Contents

Declaration	ii
Abstract	iii
Acknowledgements	v
List of publications	vi
List of Figures	ix
List of Tables.....	xi
Glossary	xi
List of Symbols.....	xiii
CHAPTER ONE: Introduction.....	2
1.1 Motivation for this work	2
1.2 Assumptions.....	2
1.3 Research objectives.....	3
1.3.1 Cad modelling.....	4
1.3.2 Ansys fluent simulation	4
2.3.3 Manufacturing of the rotors	4
2.3.4 Physical testing of the rotors.....	5
1.4 Case study	5
1.5 Outputs.....	5
1.6 Scope of work	6
CHAPTER TWO: Literature review	7
2.1 Aerodynamics of HAWT rotor	7
2.1.1 Induction factors	12
2.2 Blade element momentum method	14
2.3 Efficiency of a HAWT.....	20
2.4 Typical power curves of HAWTs	21
2.5 Key factors reducing rotor efficiency	22
2.6 Current efficiency improvements	23
2.6.1 Pre-installation optimisation	23
2.6.2 Post-installation optimisation	27
2.7 CFD Simulation	28
2.8 Physical testing	29
CHAPTER THREE: Research methodology	33
3.1 Modelling of rotors	34
3.1.1 Ring vanes.....	36
3.1.2 Model set for CFD simulation	37
3.1.3 Model set for 3D printing	39
3.2 CFD methodology.....	40
3.2.1 Solver model setup for simulation	42
3.2.2 Boundary layer.....	44
3.2.3 Mesh independence study	45
3.3 Testing methodology	49
3.3.1 Test equipment.....	50
3.3.2 Testing Operation	54
3.3.3 Data Handling	54
3.4 Case study methodology	56
3.5 Results accuracy	57

CHAPTER FOUR: Discussion of results	61
4.1 CFD simulation for all rotors	61
4.2 Physical test results for all rotors	69
4.3 CFD case study simulation	70
4.4 CFD simulation versus physical test	76
CHAPTER FIVE: Conclusion and future work.....	77
5.1 Conclusion	77
5.2 Future work.....	78
Appendix A: Blade aerofoil spline x, y, and z coordinates sample	79
Appendix B: Domain and part names of simulation virtual models	81
Appendix C: Solver settings for all rotors at 0.5 m/s free stream velocity	84
Appendix D: Mesh independence study for rotors.....	87
Appendix E: Handheld measuring device specifications	91
Appendix F: Experimental decay curves and standard deviation	97
Appendix G: Statistical summary of the decay curves for all experimental data on all rotors	99
Appendix H: Axial, radial and tangential flow visualisation for the standard and 18% ring vane rotors for 0.5 m/s free stream velocity	101
Appendix I: Axial and angular induction factor for standard and 18% ring vane rotor at off-peak performance at 4.7 and 5.9 tip speed ratios	113
Appendix J: Axial, radial and tangential flow visualisation for the standard and 18% ring vane rotors for 1 m/s free stream velocity	115
Appendix K: Axial and angular induction factor for standard and 18% ring vane rotor at off-peak performance at 4.4 and 6 TSR for 1 m/s free stream velocity	121
REFERENCES	124

List of Figures

Figure 1.1: Tangential flow (left) and Radial flow (right) (Wind Turbine Components - Windmills Tech, no date).....	3
Figure 1.2: Graphical representation of rotor fitted with 15% ring vane	4
Figure 2.1: Circular cross-section of stream tube boundary (Burton et al., 2011).....	7
Figure 2.2: Streamline of air with axial velocity and static pressure up and downstream of the rotor (Adapted from Hansen, 2008)	8
Figure 2.3: Velocity at various stages expressed in terms of axial induction (Adapted from McGowan J, et al 2009).....	8
Figure 2.4: Stream tube with rotating wake (McGowan J, et al 2009).....	9
Figure 2.5: Blade root and tip vertices with effect on wake (Fawkes, 2023)	9
Figure 2.6: Lift and drag on stationary aerofoil (Adapted from Johnson, 2006)	10
Figure 2.7: Lift and drag on stationary aerofoil (Johnson, 2006)	10
Figure 2.8: Aerofoil definitions (Johnson, 2006)	11
Figure 2.9: Aerofoil profiles with different pitches to create twist in blade (Kaya et al., 2018)....	11
Figure 2.10: Tangential and radial flow on the rotor blade (Herráez, et al 2014)	12
Figure 2.11: Turbine rotor states for various axial induction (Rajan and Ponta, 2019)	13
Figure 2.12: Axial and angular induction factor across a rotor blade (Manwell et al., 2010).....	14
Figure 2.13: Rotor plane used for momentum theory (Hansen, 2008)	14
Figure 2.14: Illustration of blade profile element and blade lift, drag and velocity profile at rotor plane (Hansen, 2008)	15
Figure 2.15: Momentum theory with Glauert empirical correction (Ning and Lu, 2019).....	19
Figure 2.16: Betz and GGS theoretical limits (Adapted from Hansen, 2008).....	20
Figure 2.17: Typical power coefficient versus tip speed ratio (λ) curves (Wilson, 1980).....	22
Figure 2.18: Sample of blade profile optimisation (Airfoil profiles TikZ example, n.d.)	24
Figure 2.19: Flow through rotor with a diffuser (Wilson, 1980).....	24
Figure 2.20: Automated pitch control (Adapted from Zhou & Liu, 2018)	25
Figure 2.21: Blade optimisation using fences (Arumugam et al., 2016)	25
Figure 2.22: Active twist of blade (Barlas and van Kuik, 2010).....	26
Figure 2.23: Blowing air into the boundary layer (Vos, 2018)	26
Figure 2.24: Sucking of air out of boundary layer (Vos, 2018)	26
Figure 2.25: Closed and open circuit wind tunnels (National Aeronautics and Space Administration, no date).....	30
Figure 2.26: Example of vehicle-top test rig (Dawoud et al., 2007)	30
Figure 2.27: Water tunnel testing sample (Álvarez-Álvarez et al., 2020).....	31
Figure 2.28: Vertical-travel test apparatus for water testing (Adapted from Fawkes, 2023)	32
Figure 3.1: Overall methodology flow diagram.....	34
Figure 3.2: Spline aerofoil profiles for blade	35
Figure 3.3: Airship nose cone profile of hub {Adapted from (Fawkes, 2023)}	35
Figure 3.4: NACA 0024 aerofoil profile. (NACA 0024 (<i>naca0024-il</i>), no date)	36
Figure 3.5: NACA 0024 Cl, Cd and Alpha graphs (Adapted from NACA 0024 (<i>naca0024-il</i>), no date)	37
Figure 3.6: Sample of ring vane and struts added to hub.....	37
Figure 3.7: Blade and hub of standard rotor within rotating domain disc.....	38
Figure 3.8: Sample of complete 120° pie-slice CFD model with standard rotor within rotating domain inside fluid domain	38
Figure 3.9: Three dissected parts used for 3D resin printing and assembly of complete rotors for physical testing	39
Figure 3.10: 3D resin printed parts: rotor with 15% ring vane (left) and all ring vanes (right) ..	40
Figure 3.11: Flow diagram for CFD Simulation	41
Figure 3.12: Lift versus axial induction for GEKO and SST turbulence models. (Semantic Scholar, no date).....	43

Figure 3.13: Velocity profiles in turbulent wall flow Source: www.learncax.com .	44
Figure 3.14: Rotor boundary layer and sub-layers with mesh height calculation	45
Figure 3.15: Mesh independence study of standard rotor with torque versus cell count.	46
Figure 3.16: A plane through fluid domain showing rotating domain containing hub, blade and ring.	47
Figure 3.17: Rotating domain with hub, blade and ring highlighted.	48
Figure 3.18: Close-up view of hub with blade and ring vane attached.	48
Figure 3.19: Leading edge of blade root.	49
Figure 3.20: Flow diagram for physical testing	50
Figure 3.21: Water tank with drop frame.	51
Figure 3.22: Free rotating shaft with rotor attached (left), Slider with free rotating shaft attached (right).	51
Figure 3.23: Slider with generator and instrumentation.	52
Figure 3.24: Generator calibration for all resistive loads with DC volt output versus angular velocity.	53
Figure 3.25: Exponential decay curve and asymptote for rotation speed of 17% ring vane rotor.	55
Figure 3.26: Rotor boundary layer and sub-layers with mesh height calculation for case study.	56
Figure 4.1: Simulation results for all rotors at 0.5 m/s free stream velocity	62
Figure 4.2: Simulation results for standard and 18% ring vane rotors at 0.5 m/s free stream velocity	63
Figure 4.3: Axial velocity contours on standard rotor (left) and 18% ring vane rotor (right) at 5.3 TSR for 0.5 m/s free stream velocity at plane 2mm in front of rotor	63
Figure 4.4: Close up view of axial velocity contours on standard rotor (left) and 18% ring vane rotor (right) at 5.3 TSR for 0.5 m/s free stream velocity at plane 2mm in front of rotor	64
Figure 4.5: Close up view of tangential velocity contours on standard rotor (left) and 18% ring vane rotor (right) at 5.3 TSR for 0.5 m/s free stream velocity at plane 2mm in front of rotor	65
Figure 4.6: Close up view of radial velocity contours on standard rotor (left) and 18% ring vane rotor (right) at 5.3 TSR for 0.5 m/s free stream velocity at plane 2mm in front of rotor	65
Figure 4.7: Closeup view of axial velocity and near wake for standard (left) and 18% ring vane rotor (right) at 5.3 TSR for 0.5 m/s free stream velocity on cross section plane	66
Figure 4.8: Axial induction factor for standard and 18% ring vane rotor at 180 rpm for 0.5 m/s free stream velocity	66
Figure 4.9: Axial velocity profile for standard and 18% ring vane rotor at 5.3 TSR for 0.5 m/s free stream velocity at plane 2mm in front of rotor	67
Figure 4.10: Angular induction factor for standard and 18% ring vane rotor at 180 rpm for 0.5 m/s free stream velocity	68
Figure 4.11: Axial velocity and wake for standard (left) and 18% ring vane rotor (right) at 5.3 TSR for 0.5 m/s free stream velocity on cross section plane.	68
Figure 4.12: Power versus rotational speed for all rotors at 0.5 m/s free stream velocity (physical testing)	69
Figure 4.13: Power versus rotational speed for standard and 18% ring vane rotor at 0.5 m/s free stream velocity (physical testing)	70
Figure 4.14: Power versus rotational speed for standard and 18% ring vane rotor at 1 m/s free stream velocity	71
Figure 4.15: Close up view of axial velocity contours on standard rotor (left) and 18% ring vane rotor (right) at 4.4 TSR for 1 m/s free stream velocity at plane 2mm in front of rotor	71
Figure 4.16: Close up view of tangential velocity contours on standard rotor (left) and 18% ring vane rotor (right) at 4.4 TSR for 1 m/s free stream velocity at plane 2mm in front of rotor	72
Figure 4.17: Close up view of radial velocity contours on standard rotor (left) and 18% ring vane rotor (right) at 4.4 TSR for 1 m/s free stream velocity at plane 2mm in front of rotor	72
Figure 4.18: Closeup view of axial velocity and near wake for standard (left) and 18% ring vane rotor (right) at 5.1 TSR for 1 m/s free stream velocity on cross section plane	73

Figure 4.19: Axial induction factor for standard and 18% ring vane rotor at 5.1 TSR for 1 m/s free stream velocity	74
Figure 4.20: Axial velocity profile for standard and 18% ring vane rotor at 5.1 TSR for 1 m/s free stream velocity at plane 2mm in front of rotor	74
Figure 4.21: Angular induction factor for standard and 18% ring vane rotor at 5.1 TSR for 1 m/s free stream velocity	75
Figure 4.22: Axial velocity and wake for standard (left) and 18% ring vane rotor (right) at 5.1 TSR for 1 m/s free stream velocity on cross section plane.....	75
Figure 4.23: Simulation and physical test results for the standard and 18% ring vane rotor at 0.5 m/s.....	76

List of Tables

Table 2.1 Summary of HAWT efficiency improvement	23
Table 3.1: Rotor and ring vane parameters.....	36
Table 3.2: Percentage change of torque for mesh independence study of standard rotor	46
Table 3.3: Percentage change of torque for mesh independence study for all rotors	57
Table 3.4: Standard deviation for all rotor RPM measured during physical testing	59

Glossary

AC	alternating current
BEMM	blade element momentum method
BEM	blade element momentum
CFD	computational fluid dynamics
DC	direct current
GEKO	generalised k-omega
GRBL	g-code reference block library
HAWT	horizontal axis wind turbine
LCD	liquid crystal display
RANS	Rynolds average Navier-Stokes
3D	three-dimensional
2D	two-dimensional
aerofoil	curved profile shape of blade on 2D plane
angle of attack	angle between the chord line and the direction of relative wind velocity
angular induction	a ratio of the rotation speed imparted to the wake and the rotation speed of the rotor
axial induction	the fractional decrease in fluid velocity between the free stream and the rotor plane
axial velocity	velocity parallel to axis of rotor rotation
blade	wing-shaped component of rotor that converts wind energy to rotational energy
blockage ratio	ratio between the frontal area of the rotor and the cross-sectional area of the wind tunnel test section
boundary layer	slower-moving layer of fluid close to the surface of a solid body in a fluid stream
chord line	straight line connecting the leading and trailing edges of an aerofoil
drag	the component (parallel to the free stream) of the force exerted by a flowing fluid on an object
hub	component that connects the blades to the drive shaft of a

	wind turbine
leading edge	the front edge of the blade (facing the oncoming fluid)
lift	the component (perpendicular to the free stream) of the force exerted by a flowing fluid on an object
near-hub region	the area surrounding the space occupied by the hub – usually referring to a region of flow through the rotor or the location on the rotor blades
power coefficient	the ratio of power absorbed by the rotor divided by power available in the wind
rotor	combination of blades and hub as one unit.
solidity	the solid blade area compared to the rotor area in a plane
thrust	the force, perpendicular to the rotor plane, that is exerted by the wind on the rotor
tip speed ratio	ratio between the tangential speed of tip of blade and the actual wind speed
trailing edge	the rearmost edge of a rotor blade where the airflow leaves the blade
twist of blade	the change in pitch angle along the blade from root to tip
vortex	a rotating region of fluid
wake	region of fluid that has interacted with the rotor, characterised by vortices and turbulence downstream of the rotor

List of Symbols

<i>Symbol</i>	Chapter 2 – section 2.1	Units
dr	control volume thickness	-
F_l	parallel lift force	N
F_d	perpendicular drag force	N
U_1	free stream velocity	m/s
U_2	free stream velocity at rotor plane	m/s
w	wake angular velocity	m/s
a	axial induction factor	-
β	pitch angle	°
r	rotor radius	m
γ	angle of attack	°
Ω	rotor angular velocity	m/s
	Chapter 2 - section 2.2	
r/R	non-dimensional blade radius	-
a'	angular induction factor	-
	Chapter 2 - section 2.3	
B	number of blades	-
c	chord length of airfoil	M
C_l	lift coefficient	-
C_d	drag coefficient	-
C_{norm}, C_n	normal load coefficient	-
$c(r)$	chord radial position of the control volume	-
C_{tan}, C_t	tangential load coefficient	-
D	drag	N
dr	control volume thickness (height)	m
dT	thrust on annular element	N
F	prandtl's tip loss factor	-
f	frequency	-
L	lift	N
P_n	load normal to rotor plane	N
P_t	load tangential to rotor plane	N
R	total rotor radius	m
r	radius of blade	m
V_{rel}	relative velocity	m/s
V_o	wind speed	m/s

a	axial induction	-
α	local angle of attack	°
ω	angular velocity of rotor	m/s
θ	pitch angle	°
ϕ	flow angle	°
ρ	density	kg/m ³
σ	solidity fraction	-
$\sigma(r)$	solidity fraction at radial position r	-
	Chaperter 2 - section 2.4	
A_r	rotor-swept area	m ²
C_p	power coefficient	-
P_r	power extracted by the rotor	W
w	wake angular velocity	m/s
a	axial induction factor	-
a'	angular induction factor	-
Ω	rotor angular velocity	m/s
ρ	water density	kg/m ³
	Chaperter 2 - section 2.5	
C_p	power coefficient	-
λ	tip speed ratio	-
	Chaperter 3 - section 3.3.1	
P	rotor power	W
T	rotor torque	N.m
ω	rotor rotational speed	Rad/s
	Chaperter 3 - section 3.3.3	
U_t	friction velocity	m/s
y^+	dimensionless distnace from first grid cell to wall surface	-
y	first cell height	m
μ	kinematic viscosity	N s/m ²
	Chaperter 3 - section 3.5.1	
Ω	resistive load	ohm
	Chaperter 3 - section 3.5.2	
Ω	resistive load	ohm
	Chaperter 3 - section 3.5.3	
A	curve amplitude	-
A_r	rotor-swept area	m ²

k	constant decay rate	-
P_r	rotor power	W
P_w	power available from water	W
R	resistive load	ohm
s	standard deviation	-
t	time	s
v	DC voltage	v
v_i	relative water velocity	m/s
Y	rpm curve value at any time t	rpm
Y_0	asymptote value	-
δ^2	squared deviation	-
Ω	resistive load	ohm
ρ	water density	kg/m ³
	Chaperter 3 - section 3.6	
y^+	dimensionless distance from first grid cell to wall surface	-

CHAPTER ONE

INTRODUCTION

1.1 Motivation for this work

The design of horizontal axis wind turbines (HAWTs) deployed globally is a meticulous process, considering various factors to optimize rotor performance tailored to the specific local conditions of installation. Historically, enhancements and optimizations to HAWT rotor performance were typically conducted prior to installation, resulting in a fixed performance profile once the turbine was deployed. Modern day large scale HAWTs have automated pitch control which allows the rotor to operate at maximum performance for different wind speeds. It is important to note that, even with these advancements, the rotor performance remains fixed as per the initial design specifications (Hertel et al., 2004).

This study extends the work of Fawkes (2023) by introducing a stationary annular ring near the hub region of a HAWT rotor hub. While Fawkes (2023) focused on an adaptive blade element momentum method to address spillage and radial pumping for large hub ratio HAWT's, this research advances the understanding by adding an annular ring near the hub region that may reduce radial flow and enhance performance.

A preliminary study utilizing computational fluid dynamics (CFD) simulations, conducted at the Department of Mechanical Engineering at Cape Peninsula University of Technology (CPUT), has revealed promising prospects for improving HAWT rotor power performance with an annular ring near the hub region (Barnard and Ismail, 2022). This investigation focused on the implementation of a retrofitted concentric ring vane—annular ring—upstream of the HAWT rotor, unlike shrouded rotors commonly used for small scale HAWTs, the focus was on placing the ring vane near the hub region of the rotor at a percentage of the rotor diameter, positioned in front of the rotor plane, with the explicit goal of increasing power performance. This approach suggests the possibility of retrofitting already installed HAWTs with a ring vane, even before the end of their life cycle, as an effective means of enhancing performance, and presents a cost-effective alternative to the complete replacement of the rotor as a means to improve performance levels.

1.2 Assumptions

In the aerodynamics of wind turbine rotors, a portion of the incoming air, initially directed axially as the wind speed, transforms into radial and tangential flows as it traverses the plane of rotation of the rotor. This transformation is integral to the energy conversion process and contributes to the power generation mechanism. Specifically, the axial wind flow is redirected along the rotor blade, constituting radial flow, and across the blade, manifesting as tangential flow, as shown in Figure 1.1 with tangential flow on the left and radial flow on the right.



Figure 1.1: Tangential flow (left) and Radial flow (right) (Wind Turbine Components - Windmills Tech, no date)

A fundamental assumption in this study is centred on installing a ring vane positioned in front of the plane of rotation, near the hub region of the rotor. The ring vane's objective is to block a portion of the axial wind flow from undergoing conversion to radial and tangential flows. This strategic placement is assumed to retain more axial velocity for the rotor, thus increasing power performance. The underlying premise is that by obstructing upstream transformation to radial flow, the ring vane optimises the availability of axial velocity to the rotor, thereby enhancing its overall power output.

1.3 Research objectives

The objective of this research was to compare the power generated, axial, tangential and radial velocity profiles of a HAWT rotor in its original configuration, referred to as standard rotor for this study and retrofitted with ring vanes at various positions near the hub region. The expectation was that installing a ring vane at a specific location near the hub would yield the maximum increase in power performance. Ring vanes were systematically positioned to pinpoint the optimal placement for performance enhancement. Ring vanes were placed at a percentage ratio of the rotor diameter. The ring vane ratio was determined from the rotor diameter to the centre line of the ring vane diameter. Ring vanes were positioned at intervals from 15% to 20% of the rotor diameter, with placements at each 1% increment. This resulted in the study of a total of six ring vanes. The effect of ring vanes was studied with a 280 mm diameter HAWT model. Upon confirmation, through numerical simulations and experimental tests, that the incorporation of a ring vane indeed resulted in improved performance, a subsequent CFD simulated case study was conducted using the same HAWT model at a higher free stream velocity. This case study specifically focused on the placement of the ring vane which demonstrated the most significant increase in performance. Figure 1.2 shows a rotor retrofitted with a ring vane positioned at 15%.

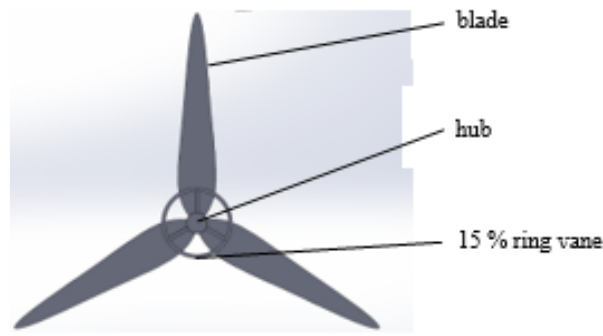


Figure 1.2: Graphical representation of rotor fitted with 15% ring vane

1.3.1 CAD modelling

This study utilised the three-dimensional (3D) blade and hub geometry of rotors obtained from previous research. To ensure compatibility with the rotors used in this study, the retrofitted ring vanes were modelled accordingly. The solid modelling software employed in this process needed to be compatible with the CFD simulation software used.

1.3.2 ANSYS Fluent simulation

The ANSYS Fluent software package served as the computational tool for simulating the rotor configurations, both in their original state without any ring vane and in a retrofitted state with ring vanes positioned at specific locations near the hub region. The primary objective of employing ANSYS CFD simulation was to scrutinise the potential enhancements in power performance resulting from various placements of ring vanes. Since physical testing involved a vertical-travel test apparatus driving the rotor into stationary water, the simulation also used water as the working fluid, ensuring a comparison between the virtual and physical experimental conditions.

The simulation focused on a comprehensive comparison, encompassing the evaluation of power generated by the rotors, examination of velocities at the rotor plane, and the comparative analysis of axial and angular induction factors. This approach enabled a thorough investigation into the impact of ring vane placement on key performance metrics, providing valuable insights into the effectiveness of this retrofitting technique for enhancing HAWT rotor performance.

1.3.3 Manufacturing of the rotors

The manufacturing process employed 3D printing technology to produce both the rotor and ring vanes. A critical consideration during the manufacturing phase was facilitating the straightforward assembly of the rotor and ring vanes onto the test equipment.

The test equipment design and specifications were seen as falling outside of the scope of this thesis. The primary focus was ensuring the seamless integration and compatibility of the manufactured components with the test equipment. This approach ensured that the constructed rotor and ring vanes could be readily incorporated into the test equipment for subsequent experimentation and evaluation.

1.3.4 Physical testing of the rotors

The physical testing phase required the evaluation of the manufactured rotors on the vertical-travel test equipment. This critical stage involved the placement of instruments to facilitate accurate measurements. The primary objective of the physical testing was to verify the anticipated performance benefits obtained from the ANSYS simulations. In assessing options for physical testing, considerations were made regarding availability, cost, testing duration and accuracy. The vertical-travel test apparatus housed within the Department of Mechanical Engineering at CPUT satisfied all the above criteria and was used for the physical testing in this research.

1.4 Case Study

A case study was undertaken, utilising an identical HAWT and the ring vane with the best performance increase from the study, and subjecting them to a higher fluid velocity than could be achieved by the vertical-travel test apparatus utilised in previous physical tests. The primary objective of the case study was to investigate whether the performance of the rotor could exhibit further improvements under increased, off design “wind speed” and rotation speeds of the rotor.

This approach gave insight into the adaptability and effectiveness of the retrofitted ring vane operating within a broad range of ‘wind speed’ and rotation speeds.

1.5 Outputs

The research outputs related to the positioning of retrofitted ring vanes in front of the plane of rotation for HAWT rotors to enhance performance efficiency were:

- *Investigation of aerodynamic effects:*
Comprehensive examination of the aerodynamic effects by employing CFD simulations on a rotor. Quantified improvements in power efficiency. Insights into airflow characteristics.
- *Assessment of power generation enhancement:*
Analysis of power output, explaining the direct impact of ring vanes on HAWTs' overall power generation efficiency.
- *Validation through experimental testing:*
Experimental testing of a rotor to validate the findings derived from CFD simulations.
Comparison of performance characteristics and efficiency gains observed during testing with the standard rotor as a baseline.
- *Simulated case study:*
A simulated case study on an identical HAWT, implementing a ring vane at the optimal position identified in the earlier research finding.
Evaluation of the resulting power performance increase in the case study at increased free stream velocity and rotor rotation speeds.

The accomplishment of these research objectives provided a comprehensive understanding of the benefits and limitations of placing a ring vane in front of the plane of rotation of HAWT rotors. The outcomes of this research project not only contribute to the current understanding of ring vane applications but also lay the groundwork for further exploration in this domain. The research outcomes will contribute to the optimisation of wind turbine design, improved energy production, increased efficiency of already installed HAWTs and the advancement of sustainable wind energy technology.

1.6 Scope of work

This research aimed to compare the performance between a standard rotor and the same rotor retrofitted with various ring vanes positioned near the hub region. The investigation included CFD simulations and physical testing of the rotors, explicitly aiming to determine the performance enhancement effects of ring vanes. The research did not account for the influence of tower, tail, near-ground effects, and generator losses. All simulations and physical testing were conducted using water as the working fluid. This research excluded structural analysis of wind turbine rotors and any designed structure to be used during physical testing. The study excluded the design and commissioning of the vertical-travel test apparatus.

CHAPTER TWO

LITERATURE REVIEW

This literature review covers theory related to HAWT rotor aerodynamics and efficiency and focusses on three major themes:

- Aerodynamics of HAWT rotors, key factors affecting aerodynamic performance and design of HAWT rotors using the Blade Element Momentum method.
- Efficiency of rotors, theory and key factors that affect efficiency.
- Performance validation methods for HAWT rotors, covering computational fluid dynamics and physical testing.

2.1 Aerodynamics of HAWT rotor

The important aerodynamic variables for this research, the axial and angular induction factors quantified how well the rotor absorbed power from the wind. As wind turbines harness kinetic energy from the wind, the velocity of the wind is reduced due to the extraction of kinetic energy. This alteration solely affects the mass of the wind that traverses through the rotor. By assuming that the impacted air mass is distinct from the air mass bypassing the rotor, a circular cross-sectional stream tube boundary can be illustrated both upstream and downstream of the rotor. Figure 2.1 illustrates the outlined boundary of the affected air stream tube. No air crosses this boundary, and there is no compression of the air. Consequently, the cross-sectional area downstream of the rotor expands due to the decreased velocity (Burton et al., 2011).

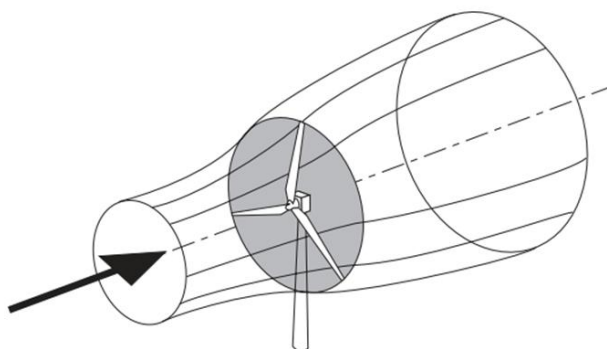


Figure 2.1: Circular cross-section of stream tube boundary (Burton et al., 2011)

The presence of the rotor leads to a deceleration of the free stream air upstream of the rotor, causing the stream tube to expand despite no work being performed. This deceleration increases static pressure to absorb the decrease in kinetic energy. Upon passing through the rotor, the air experiences a drop in static pressure due to the work being done, reaching levels below atmospheric pressure. Downstream of the rotor, both the velocity and static pressure of the air continue to decrease, defining the region known as the wake of the rotor. Further downstream, the static pressure gradually returns to equilibrium at the expense of kinetic energy. Consequently, while the static pressure far upstream and far downstream of the rotor remains equal, there is a reduction in kinetic energy. Figure 2.2 illustrates

the expansion of the air stream tube alongside the reduction in axial velocity, accompanied by the static pressure profile (Wilson, 1980).

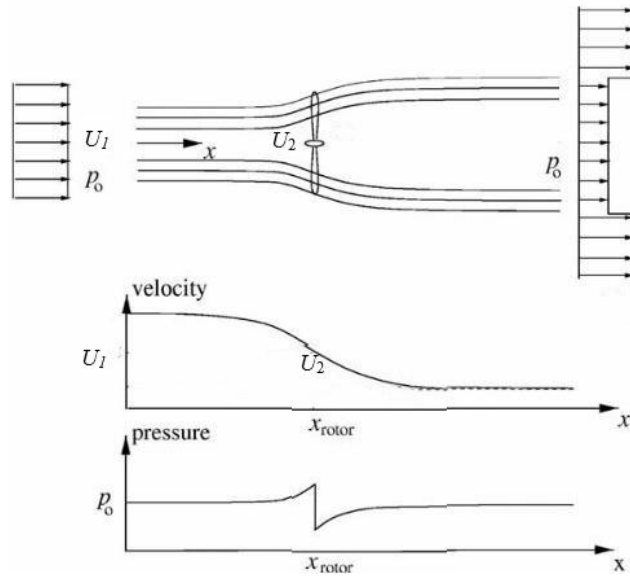


Figure 2.2: Streamline of air with axial velocity and static pressure up and downstream of the rotor (Adapted from Hansen, 2008)

The fractional decrease in axial wind velocity between the free stream, U_1 and at the rotor plane, U_2 is called the axial induction factor and is expressed as:

$$\alpha = \frac{U_1 - U_2}{U_1} \quad (2.1)$$

The velocities at various stages within the stream tube can be expressed in terms of free stream velocity, U_1 and axial induction, α in Figure 2.3 with subscript denoting the position within the stream tube.

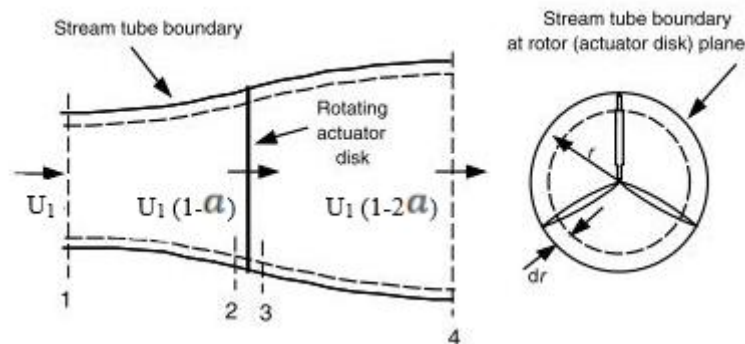


Figure 2.3: Velocity at various stages expressed in terms of axial induction (Adapted from McGowan J, et al 2009)

Because of the rotor's rotation, the wake rotates in the opposite direction to the rotor as a response to the flow activated by the rotor. This rotational wake reduces the rotor's capacity to extract kinetic energy from the air. Figure 2.4 depicts an air streamline both upstream and downstream of the rotor. It

is presumed that the rotational speed of the wake is considerably smaller than the rotation speed of the rotor.

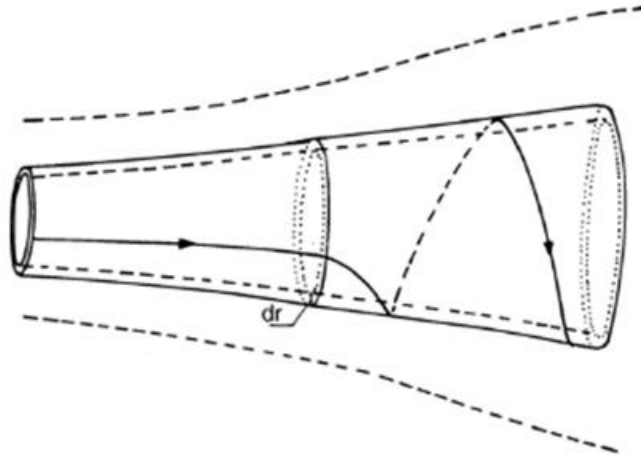


Figure 2.4: Stream tube with rotating wake (McGowan J, et al 2009)

When contemplating a control volume with a thickness of dr within the stream tube, a relationship between the rotor angular velocity, Ω , and the wake angular velocity, w , which are dependent on the rotor radius r can be deduced from the energy equation under the assumption that the static pressure far upstream and downstream is identical. This ratio between the rotor and wake angular velocities is termed the angular induction factor and is denoted as (Manwell et al., 2010):

$$a' = w/2\Omega \quad (2.2)$$

The blade root and tip vortices induce additional losses within the wake because of rotor rotation. Figure 2.5 shows the root and tip vortices along with their impact on the rotating wake.

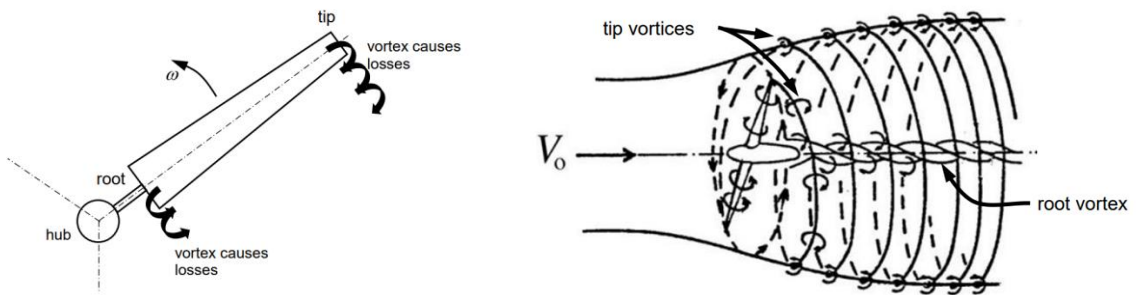


Figure 2.5: Blade root and tip vortices with effect on wake (Fawkes, 2023)

In HAWT rotor designs, aerofoils are also used on the blade profile to convert wind kinetic energy into useful energy. When air moves over a stationary aerofoil, it generates lift force perpendicular to the direction of flow and drag force aligned with the airflow, as shown in Figure 2.6.

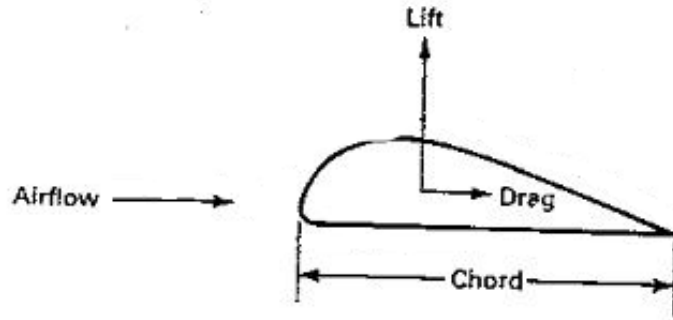


Figure 2.6: Lift and drag on stationary aerofoil (Adapted from Johnson, 2006)

Considering that the aerofoil moves in the direction of lift, the interaction between the aerofoil motion and the airflow yields a relative wind direction. Figure 2.7 illustrates the re-orientation of the aerofoil to maintain the lift and drag ratio.

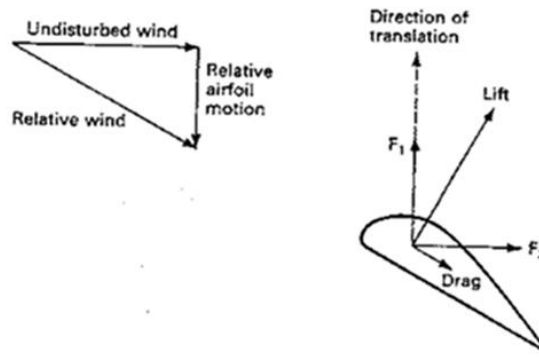


Figure 2.7: Lift and drag on stationary aerofoil (Johnson, 2006)

The lift force now acts perpendicular to the relative wind, while the drag force aligns with the relative wind. The lift and drag forces can be divided into components parallel and perpendicular to the undisturbed wind, denoted as F_1 and F_2 , respectively. The F_1 force generates torque on the rotor, while force F_2 represents the drag force that the rotor must endure. The performance of the rotor hinges on the design and orientation of the aerofoil. Other critical parameters of the blade aerofoils include the *pitch angle*, β , which is the angle between the *chord line* of the aerofoil and the *plane of rotation*. The *chord line* is the straight line from the *trailing* to the *leading edge* of the aerofoil, while the *plane of rotation* is the plane in which the blade tips lie as they rotate. Figure 2.8 illustrates the various aerofoil terminologies and positions. It is essential to emphasise that the pitch angle is a static parameter.

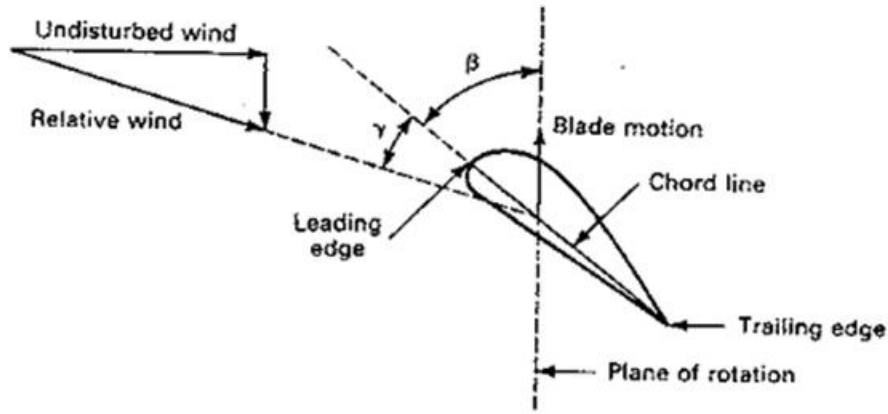


Figure 2.8: Aerofoil definitions (Johnson, 2006)

In contrast to the *pitch angle*, the *angle of attack*, γ , which is the angle between the aerofoil *chord line* and the relative wind, is a dynamic angle dependent on the rotation speed of the blade and the wind speed. Since lift and drag attain optimal values for the *angle of attack*, blades have a variation in the *angle of attack* across the blade at radius r from the hub, known as the *twist* of the blade. The *blade twist* compensates for the variation in relative wind speed across the blade at radius r from the hub. Figure 2.9 illustrates the twist of a blade at various radii (Kaya et al., 2018).

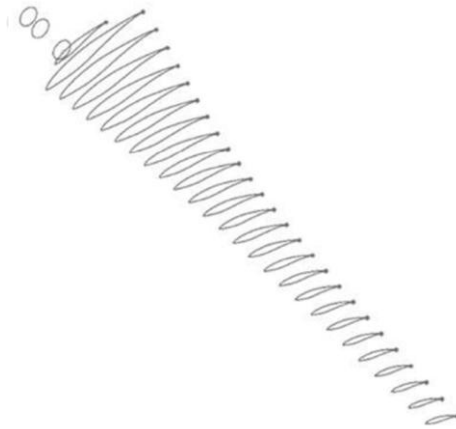


Figure 2.9: Aerofoil profiles with different pitches to create twist in blade (Kaya et al., 2018)

As the incoming air encounters the rotor's plane of rotation, a fraction of it, initially directed axially with the wind speed, undergoes a transformation into radial and tangential components. More precisely, the axial wind flow is diverted along the rotor blade, resulting in radial flow, while some of the airflow is redirected across the blade, creating tangential flow. Figure 2.10 provides a closer examination of the tangential and radial flow on the rotor blade (Herráez et al., 2014).

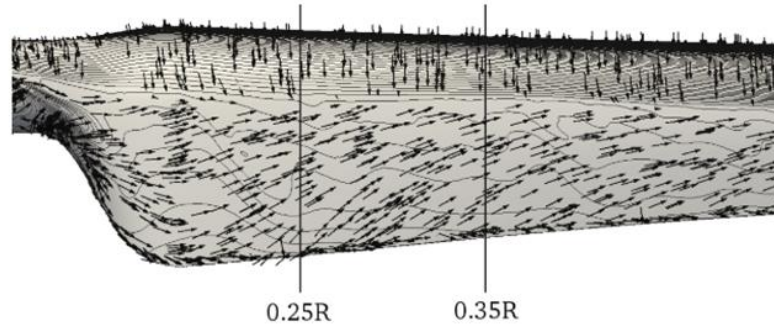


Figure 2.10: Tangential and radial flow on the rotor blade (Herráez, et al 2014)

2.1.1 Induction factors

In this section, the axial and angular induction factors were discussed. The axial induction factor, denoted as α , represents the ratio between the free stream velocity and the fractional decrease of axial velocity at the plane of rotation of the rotor.

The axial induction factor is a key indicator of rotor performance, indicating the state in which the rotor operates. Figure 2.11 illustrates the relationship between the thrust coefficient, CT , which describe the force exerted by the rotor in axial direction and the axial induction factor for rotors operating in the turbulent wake state. Based on varying levels of blade-wake interaction, a rotor has four working states: propeller, windmill, turbulence, and vortex ring.

- *Propeller state:* This state initiates when flow reversal occurs throughout the rotor, and the wind turbine releases energy into the flow like a propeller.
- *Windmill state:* In this state, the rotor harnesses energy from the flow to rotate, and the streamlines extend and orderly expand in the wake.
- *Turbulence state:* Here, the rotor still extracts energy from the flow, but the streamlines become turbulent in the wake.
- *Vortex ring state:* This state arises when rotor vortices accumulate in the wake, forming a loop around the rotor.

The turbine rotor's working states correspond to the axial induction factor α , as depicted. The windmill and turbulent working states are the most relevant states for wind turbines installed (Dong et al., 2022).

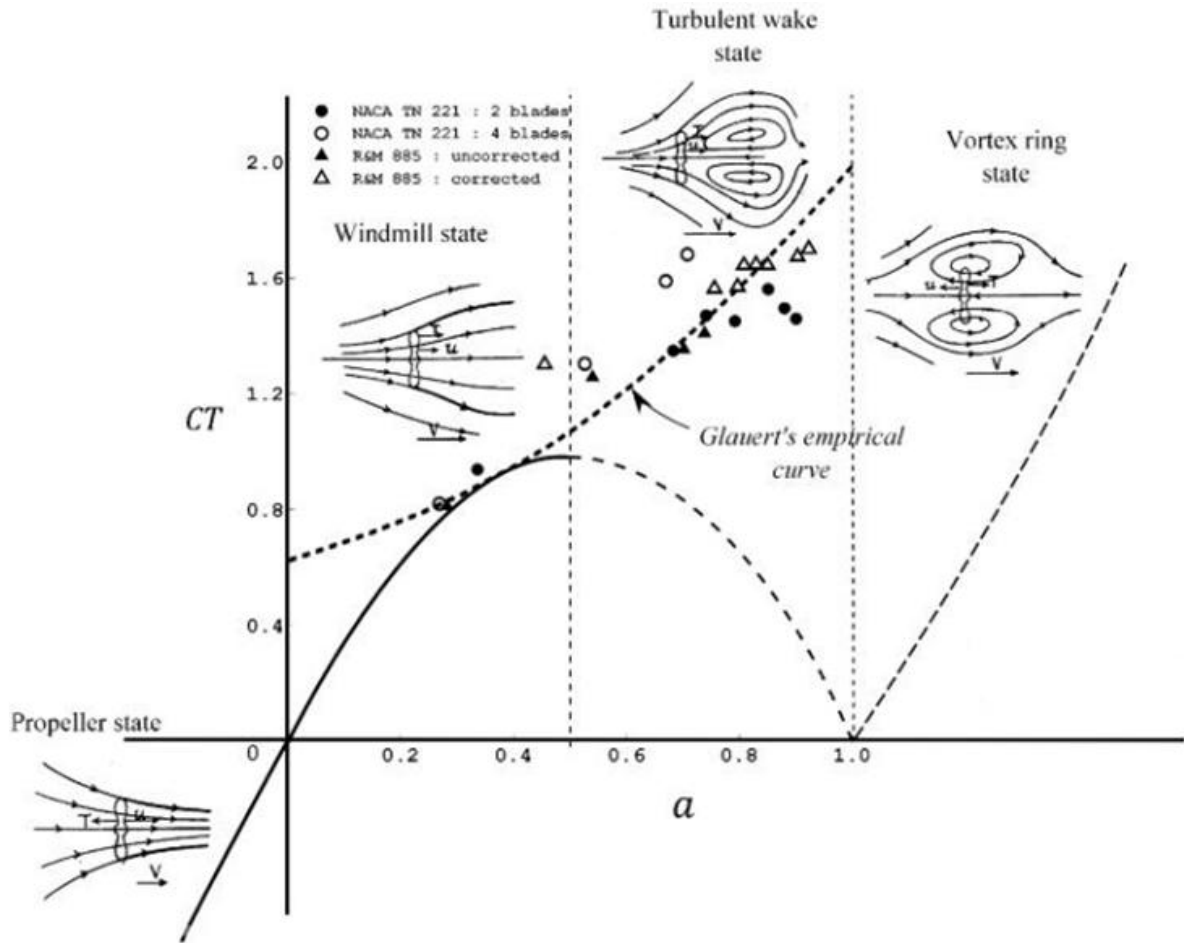


Figure 2.11: Turbine rotor states for various axial induction (Rajan and Ponta, 2019)

The angular induction factor, which is the ratio of the rotor and wake angular velocity represented as:

$$\alpha' = w/2\Omega \quad (2.3)$$

The wake's rotation diminishes the rotor's ability to extract kinetic energy from the wind. Thus, a high angular induction factor signifies poor performance, whereas a low value suggests improved performance.

In Figure 2.12, the axial and angular induction factors across a blade are depicted for an ideal rotor design at a non-dimensional blade radius, r/R . In the hub region, the angular induction factor is high, indicating poor kinetic energy extraction of the blade. Conversely, towards the tip of the blade, a lower angular induction factor suggests increased kinetic energy extraction. The slight increase in the axial induction factor from the hub region towards the tip of the blade indicates that less axial velocity is available from the wind for the blade aerofoil to perform towards the tip when applying the axial induction equation 2.1 (Manwell et al., 2010).

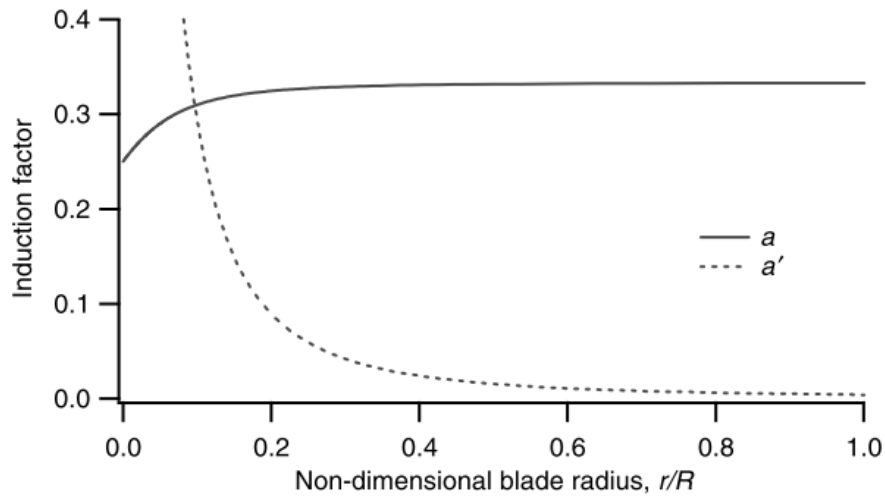


Figure 2.12: Axial and angular induction factor across a rotor blade (Manwell et al., 2010)

When designing a rotor, all aerodynamic factors must be considered. Additionally, other aspects related to the rotor's design should incorporate parameters of the installation location, such as local average wind speeds, topology of the area, and elevation above sea level, among others. The basic Blade Element Momentum (BEM) theory or rotor design will be discussed in the next section.

2.2 Blade element momentum method

The current or conventional method for designing blades for wind turbines is the BEM method. The theoretical foundation for this method combines two principles: momentum theory and blade-element theory.

Momentum theory involves analysing the forces acting on the blade within a control volume based on the conservation of linear and angular momentum. It assumes that the loss of pressure or momentum is due to the work done (Moriarty and Hansen, 2005). Figure 2.13 illustrates the rotor plane utilised in momentum theory. Momentum theory is applicable to local events occurring on the actual blades. It introduces stream tubes with a height dr and a number of tubes across the rotor, as depicted in Figure 2.13.

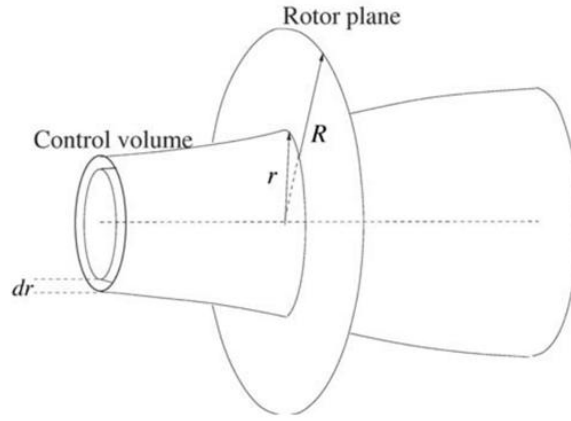


Figure 2.13: Rotor plane used for momentum theory (Hansen, 2008)

Using the momentum theory, *thrust* is computed by applying the integral momentum equation over the control volume encompassing the rotor's cross-sectional area. Similarly, *torque* is determined by evaluating the integral moment of momentum over the control volume. Equations derived from the integral momentum and integral moment of momentum serve as the foundation for the equations employed in the blade element momentum method (BEMM) (Hansen, 2008).

Blade element theory involves examining the forces acting on 2D sections of the blade according to its geometry. It establishes a connection between the blade profile's capability to harness power from the wind (McGowan et al., 2009). Figure 2.14 shows an illustration of a single element's 2D blade lift, drag, and velocity profile.

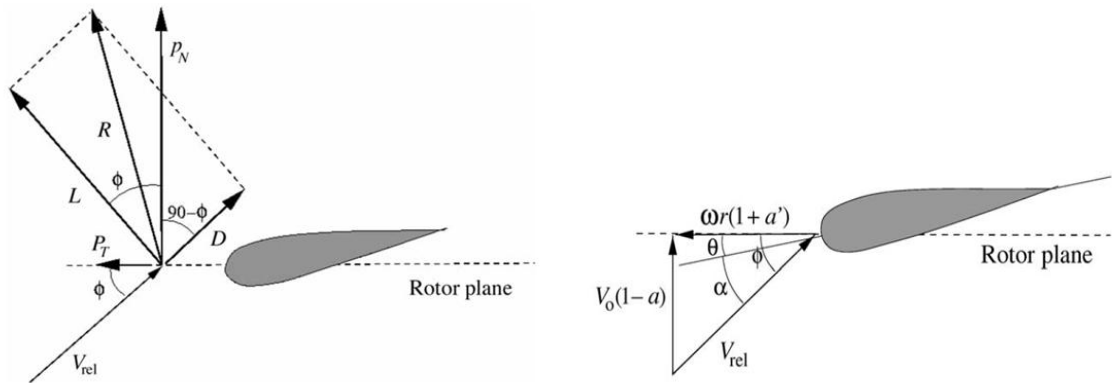


Figure 2.14: Illustration of blade profile element and blade lift, drag and velocity profile at rotor plane (Hansen, 2008)

In the velocity vector diagram, the local angle of attack is calculated as:

$$\alpha = \phi - \theta \quad (2.4)$$

α – local angle of attack

ϕ – flow angle

θ – pitch angle

The flow angle represents the angle between the relative velocity V_{rel} and the plane of rotation, also known as the rotor plane:

$$\tan \phi = \frac{(1-a) V_0}{(1-a') \omega r} \quad (2.5)$$

ϕ – flow angle

r – radius

V_0 – wind speed

a – axial induction factor

ω - angular velocity of rotor

a' - angular induction factor

Equations (2.4) and (2.5) are directly utilised within the BEMM, whereas the *thrust* and *torque* equations derived from the momentum theory serve as the basis for deriving equations employed by the BEMM (Hansen, 2008). In the forces vector diagram illustrated in Figure 2.14, the following equations are derived and are utilised in the BEMM:

$$C_{norm} = P_n / 1/2 \rho V_{rel}^2 c \quad (2.6)$$

$$C_{tan} = P_t / 1/2 \rho V_{rel}^2 c \quad (2.7)$$

C_{norm} – normal load coefficient

C_{tan} – tangential load coefficient

P_n – load normal to rotor plane

P_t – load tangential to rotor plane

c –chord length of airfoil

V_{rel} –relative velocity to airfoil

ρ –density

The normal and tangential loads P_n and P_t are calculated by determining the lift and drag with:

$$L = 1/2 \rho V_{rel}^2 c C_l \quad (2.8)$$

$$D = 1/2 \rho V_{rel}^2 c C_d \quad (2.9)$$

L – lift

D – drag

V_{rel} –relative velocity to airfoil

c –chord length of airfoil

C_l – lift coefficient

C_d – drag coefficient

The lift and drag forces are projected into the normal and tangential planes, as depicted in the force vector diagram:

$$P_n = L \cos \phi + D \sin \phi \quad (2.10)$$

$$P_t = L \sin \phi - D \cos \phi \quad (2.11)$$

P_n – load normal to rotor plane

P_t – load tangential to rotor plane

L – lift

D – drag

ϕ – flow angle

Two additional equations are derived by combining momentum and element equations to express the variation of axial and tangential forces on the blade through the axial induction and angular induction factors:

$$a = \frac{1}{\frac{4 \sin^2 \phi}{\sigma C_n} + 1} \quad (2.12)$$

$$a' = \frac{1}{\frac{4 \sin \phi \cos \phi}{\sigma C_t} - 1} \quad (2.13)$$

a – axial induction factor

a' - angular induction factor

C_n – normal load coefficient

C_t – tangential load coefficient

ϕ – flow angle

σ – solidity fraction

The *solidity* fraction σ represents the blade area compared to the rotor area on the planar or annular area in the control area and is expressed by (Hansen, 2008):

$$\sigma(r) = c(r)B / 2\pi r \quad (2.14)$$

$\sigma(r)$ – solidity fraction at radial position r

$c(r)$ – chord radial position of the control volume

B – number of blades

r - radius

The BEMM model enables the calculation of *thrust*, *torque*, and *power* for various values of *wind speed*, *pitch angle*, and *rotational speed*. This model relies on two assumptions:

1. *No dependencies*: This assumption suggests that events at one location within the rotor do not affect other locations. In other words, each element of the rotor operates independently.

2. *Uniform forces*: The forces exerted by the blade are considered constant across the flow within each annular element. This assumption is made under the premise of a rotor with an infinite number of blades.

The BEMM model makes use of an iterative method with the following steps.

- Step 1. Assume initial α and α' . Normally close to zero.
- Step 2. Determine the flow angle ϕ using equation (2.5).
- Step 3. Determine local angle of attack α using Equation (2.4).
- Step 4. Use $C_l(\alpha)$ and $C_d(\alpha)$ from aerofoil information table.
- Step 5. Determine C_n and C_t with equations (2.6) and (2.7).
- Step 6. Determine α and α' using equations (2.12) and (2.13).
- Step 7. If α and α' change significantly, repeat from step 2; otherwise, finish.
- Step 8. Calculate local loads on blades.

Below is a summary of equations used in the iteration method.

$$\tan \phi = \frac{(1-\alpha) V_0}{(1-\alpha') \omega r} \quad (2.15)$$

$$\alpha = \phi - \Theta \quad (2.16)$$

$$C_n = C_l \cos \phi + C_d \sin \phi \quad (2.17)$$

$$C_t = C_l \sin \phi - C_d \cos \phi \quad (2.18)$$

$$\alpha = \frac{1}{\frac{4 \sin^2 \phi}{\sigma C_n} + 1} \quad (2.19)$$

$$\alpha' = \frac{1}{\frac{4 \sin \phi \cos \phi}{\sigma C_t} - 1} \quad (2.20)$$

Step 1 to step 8 was the basic BEMM. However, two corrections to the algorithm need to be applied. The Prandtl's tip loss factor, denoted as F , is employed to rectify the design and performance prediction for a rotor with a finite number of blades. F is determined by:

$$F = \frac{2}{\pi} \cos^{-1}(e^{-f}) \quad (2.21)$$

Where:

$$f = \frac{B}{2} \frac{R-r}{r \sin \phi} \quad (2.22)$$

B – number of blades

f – frequency

R – total rotor radius

r – local radius

ϕ – flow angle

Introducing the Prandtl's tip loss factor to equations (2.15) and (2.16), they become:

$$a = \frac{1}{\frac{4F \sin^2 \phi}{\sigma C_n} + 1} \quad (2.23)$$

$$a' = \frac{1}{\frac{4F \sin \phi \cos \phi}{\sigma C_t} - 1} \quad (2.24)$$

Equations (2.23) and (2.24) must be used in the BEMM iteration step 6 instead of (2.15) and (2.16), and Prandtl's tip loss factor F must be determined after step 2 (Hansen, 2008).

The second correction is the Glauert correction, which is an empirical relation used for axial induction factors greater than 0.4, where the validity of the one-dimensional momentum theory is compromised. This empirical relation between thrust and axial induction factor is expressed as:

$$C_t = 4(\alpha_c^2 + (1 - 2\alpha_c)\alpha)F \quad (2.25)$$

where α_c is approximately 0.2.

From local aerodynamics, the thrust dT on an annular element is:

$$C_t = \frac{(1-a)^2 \sigma C_n}{\sin^2 \phi} \quad (2.26)$$

Equating equation (2.25) and (2.26) for axial induction factor $\alpha > \alpha_c$ is given as:

$$\alpha = \frac{1}{2} [2 + K(1 - 2\alpha_c) - \sqrt{(K(1 - 2\alpha_c) + 2)^2 + 4(K\alpha_c^2 - 1)}] \quad (2.27)$$

$$\text{where } K = \frac{4F \sin^2 \phi}{\sigma C_n} \quad (2.28)$$

In Figure 2.15 both the momentum theory and the Glauert empirical correction are depicted, with the dotted line indicating that the momentum theory becomes invalid for axial induction factors higher than 0.4.

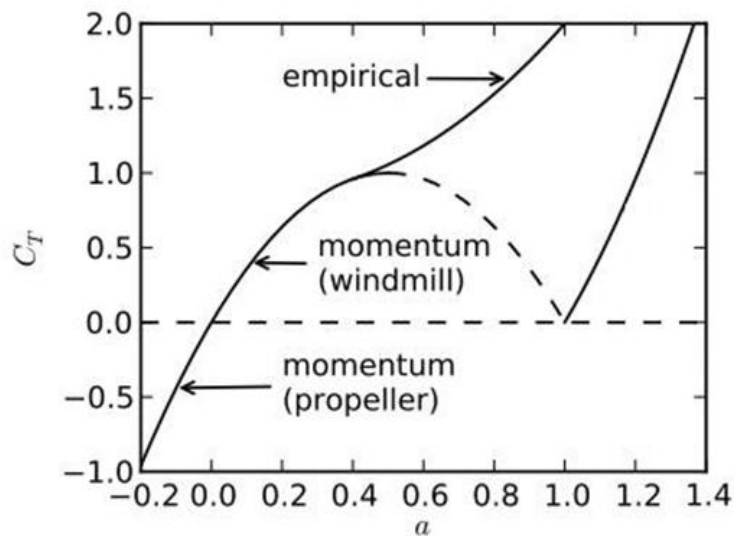


Figure 2.15: Momentum theory with Glauert empirical correction (Ning and Lu, 2019)

The BEMM is used in blade design software created for the wind turbine industry. Below is a list of established software packages.

- Smart Blade (Smart Blade.n.d. <https://www.smart-blade.com> [2019])
- QBlade (Marten, 2012)
- Bladed (Det Norske Veritas, n.d. <http://www.dnvgl.com> [2019])
- AeroDyn (Jonkman et al., 2015)

The BEMM relies on the following simplified assumptions (Zhao et al., 2019):

- *No radial and circumferential dependencies:* Events at one location within the rotor do not influence other locations.
- *Uniform forces on the blade within each annular element:* This assumption is made under the premise of a rotor with an infinite number of blades.
- *Steady state with incompressible flow and inviscid:* The flow is considered steady, incompressible, and inviscid.

2.3 Efficiency of a HAWT

The theoretical efficiency limit of HAWTs was established by Betz in the 1920s. The Betz limit capped the efficiency at 59.3%. In terms of power coefficient (C_p), this corresponds to a value of 0.593 at a theoretically optimum axial induction, α equal to 0.33. Betz's theory was grounded in one-dimensional rate of momentum change principles, assuming incompressible flow and constant velocity across any section within the airstream. Additionally, pressure was assumed to have a uniform distribution across the rotor. Betz's theory, utilising the rate of momentum change and Bernoulli relations, tended to overestimate the forces and torque on the rotor. Later studies by Gorban, Gorlov, and Silantyev, referred to as the GGS model, introduced factors such as non-uniform pressure, curvilinear flow, and the degenerated flow of the wake. This model predicted a peak efficiency of 30.1% or C_p equal to 0.301 with higher axial induction factors (Gorban et al., 2001). Figure 2.16 illustrates the theoretical limits proposed by both the Betz and GGS models.

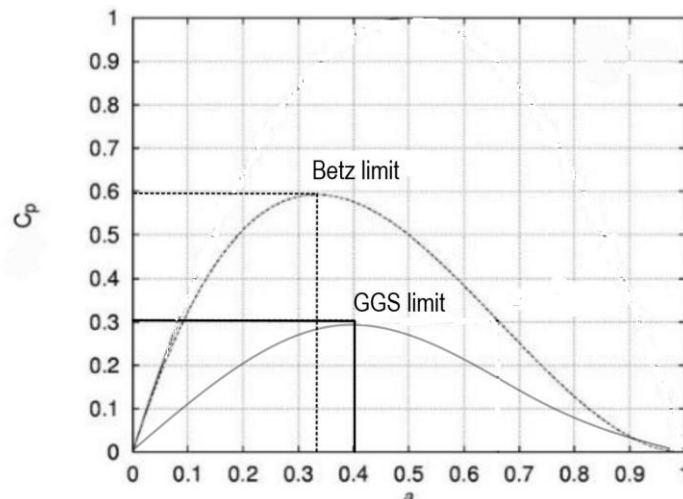


Figure 2.16: Betz and GGS theoretical limits (Adapted from Hansen, 2008)

Since the 2000s, computational fluid dynamics (CFD) simulation has gained popularity, incorporating boundary layer computation. CFD simulations have typically produced efficiencies falling between the theoretical limits proposed by the GGS model and Betz's theory (Hartwanger and Horvat, 2008).

The efficiency of HAWT rotors can be expressed in various ways. Fundamentally, efficiency represents the ratio of the power generated by the rotor to the power available from the wind. One common way to express efficiency is through the power coefficient, which is a dimensionless quantity that relates the power extracted by the rotor to the power available in the wind. It is commonly defined as:

$$C_p = \frac{P_r}{0.5 \rho A_r v_i^3} \quad (2.29)$$

Where P_r is the power extracted by the rotor, ρ is the water density, and A_r is the rotor-swept area. The power coefficient can also be expressed in terms of the axial induction factor, α as:

$$C_p = 4\alpha (1 - \alpha)^2 \quad (2.30)$$

This expression directly relates the power coefficient to the axial induction factor, offering insights into how the rotor's aerodynamic efficiency depends on the extent of air diverted from the rotor (Burton et al., 2011).

Overall, these expressions contribute to characterising the efficiency and performance of HAWT rotors in extracting power from the wind, with the axial induction factor playing a crucial role in understanding the rotor's aerodynamic behaviour. Another aspect of rotor efficiency pertains to the formation of the near wake, which comprises angular and axial flow components. The wake angular flow rotates in the opposite direction to the rotor, representing a loss as it cannot be utilised for torque extraction. The efficiency of the rotor concerning angular flow can be quantified using the angular induction factor.

The angular induction factor, denoted as α' , signifies the ratio of the rotor's angular velocity to the angular velocity imparted to the wake (Burton et al., 2011). As mentioned earlier, a lower axial induction enhances the rotor's efficiency, while a higher angular induction signifies poorer extraction of kinetic energy from the wind. Both axial and angular induction indicate the rotor's aerodynamic performance. Improving the aerodynamics of rotors involves consideration of the induction factors as well as lift, drag, flow angle and angle of attack – all of which influence rotor performance.

2.4 Typical power curves of HAWTs

A typical power curve for a HAWT rotor has a parabolic shape with power or power coefficient (C_p) on the y-axis and rotation speed (rpm) or tip speed ratio (λ) on the x-axis. Figure 2.17 shows power curves for two HAWT rotor designs. Design 1 has a high peak performance but climbs and drop off rapidly before and after the peak. Design 2 has a lower peak performance but has higher performance

for a wider range of tip speed ratios. The type of design chosen depends on the wind speed and how stable the optimal wind speed is. For example, a very stable wind speed, design 1 would be desirable to gain maximum performance and unstable wind speed conditions favours design 2. It can be said that design 1 is sensitive to rotational speed and design 2 is less sensitive (Wilson, 1980).

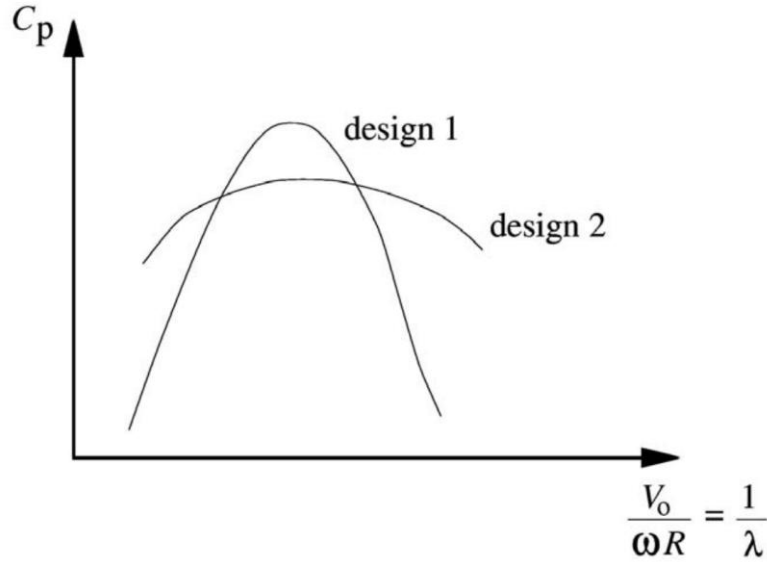


Figure 2.17: Typical power coefficient versus tip speed ratio (λ) curves (Wilson, 1980)

2.5 Key factors reducing rotor efficiency

Wind turbine performance is influenced by various aerodynamic, structural, and environmental factors that lead to efficiency losses. Key performance-reducing elements include, flow separation, stall, surface degradation, installation issues, and interference effects. Understanding these phenomena is essential for explaining the behaviour of the performance curve and the impact of wind conditions on turbine operation. Furthermore, it establishes the rationale for implementing design modifications and retrofits to enhance performance.

Flow separation occurs when the boundary layer of air traveling over the turbine blade loses adherence to the blade surface, leading to turbulence and energy dissipation. This phenomenon typically arises due to excessive angle of attack, where the airflow can no longer smoothly follow the blade contour. Flow separation contributes to aerodynamic stall, significantly reducing lift and increasing drag forces. Under steady-state conditions, stall can result in a sharp drop in power output. (Hansen, 2015).

HAWT's are particularly susceptible to rotor stall when operating under high wind speeds or at excessive angles of attack. Rotor stall occurs when airflow over the turbine blades becomes separated due to adverse pressure gradients, leading to a significant drop in lift and an increase in drag. This aerodynamic phenomenon severely impacts the efficiency of the turbine, causing fluctuations in power output (Burton et al., 2011).

Blade surface degradation due to erosion, dirt accumulation, or icing also negatively impacts turbine performance. Leading-edge erosion, for instance, alters the blade's aerodynamic profile, increasing surface roughness and promoting early flow separation. Icing can exacerbate this effect by increasing weight and distorting airflow patterns, further contributing to power losses (Sareen et al., 2014).

Proper turbine siting and installation are crucial for minimizing performance losses. Factors such as wake interference from upstream turbines, terrain-induced turbulence, and suboptimal tower height can degrade performance. Wake effects cause velocity deficits and increased turbulence intensity, reducing the energy available to downstream turbines (Vermeer et al., 2003).

2.6 Current efficiency improvements

The design of HAWTs and the optimisation of rotor performance are customised to suit the wind conditions of the installation site. Historically improvements and optimisations to HAWT rotor performance were carried out before installation, leading to a fixed performance profile once the turbine was deployed. However, optimisation methods are implemented post-installation in modern large-scale HAWTs, including operational control and maintenance strategies. Table 2.1 summarises HAWT efficiency improvements for pre- and post-installation requirements.

Table 2.1 Summary of HAWT efficiency improvement

Pre-Installation Optimization	Reference
Aerofoil Optimization	(Ram et al., 2019)
Shrouded Rotor Design	(Katooli and Noorollahi, 2022)
Pitch Control Systems	(Civelek et al., 2015)
Boundary Layer Fences	(Zhao et al., 2022)
Twisted or Variable Geometry Blades	(Barlas and van Kuik, 2010)
Boundary Layer Control	(Vos, 2018)
Post-Installation Optimization	Reference
Operational Optimization	(Rodríguez-López et al., 2020)
Maintenance and Inspection	(Park and Kim, 2016)
Blade Retrofitting	(Jiang et al., 2022)
Surface Coatings	(Parthasarathi et al., 2024)
Wake Steering and Farm Layout Optimization	(Howland et al., 2019)
Dynamic Stall Control	(Guoqiang et al., 2019)
Rotor Dynamic Control Strategies	(Elkodama et al., 2023)

2.6.1 Pre-installation optimisation

Pre-installation optimisation involves improving a rotor's performance during the design stage. Blade aerofoil optimisation has been extensively studied by numerous researchers, who aim to select the optimal aerofoil profiles for rotor blades under specific operational conditions and design inputs. Factors such as free stream wind velocity, tip speed ratio, axial induction, and angular induction all

influence the design of an optimal aerofoil profile. Figure 2.18 displays samples of various aerofoil profiles. The selection of aerofoil profiles is aimed at enhancing rotor performance, and is highly specific for each rotor size, position along the blade and design conditions, aiming to enhance rotor performance (Ram et al., 2019).

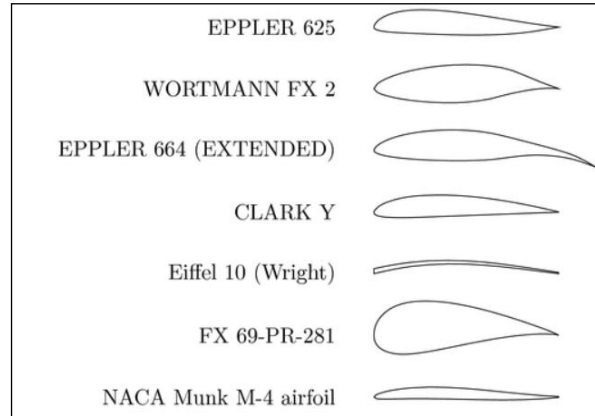


Figure 2.18: Sample of blade profile optimisation (Airfoil profiles | TikZ example, n.d.)

Shrouded rotors for small-scale HAWTs enhance rotor performance by enclosing the rotor within a diffuser, as shown in Figure 2.19. When the cross-section of the diffuser is shaped like an aerofoil, the flow passing through the diffuser generates lift force, which induces an increase in velocity in the mass flow through the rotor. This velocity increase directly impacts the axial induction, thereby improving the performance of the rotor (Katooli and Noorollahi, 2022). The disadvantage of shrouded rotors is the extra weight which makes it impractical to use on medium to large scale HAWT's.

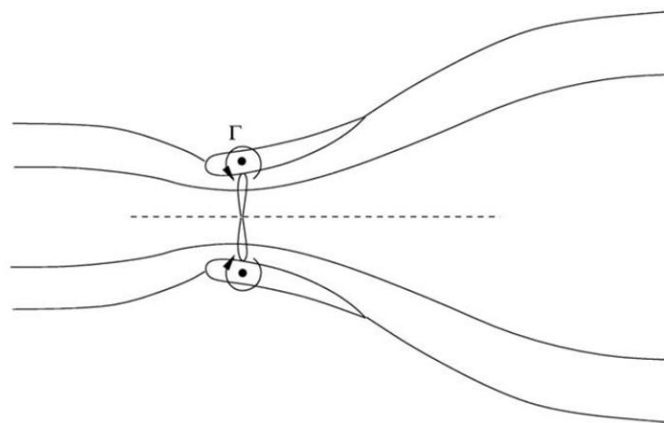


Figure 2.19: Flow through rotor with a diffuser (Wilson, 1980)

Pitch control for rotors isn't directly associated with improving rotor aerodynamics but is a mechanism that enables a working rotor to adjust the pitch angle of the blades. This adjustment allows the rotor to operate at design specifications for various free stream velocities, thereby increasing the rotor's performance across a broader operational range. Figure 2.20 shows the concept of pitch control (Civelek et al., 2015).



Figure 2.20: Automated pitch control (Adapted from Zhou & Liu, 2018)

Boundary layer fences are small protrusions or barriers added to the surface of rotor blades shown in Figure 2.21. They are strategically placed to manipulate the airflow and minimise flow separation, especially at high angles of attack by reducing radial flow along the blade. By effectively managing the boundary layer, these fences help maintain attached flow over the blade surface, thereby improving aerodynamic performance and reducing aerodynamic losses. The addition of boundary layer fences can enhance the lift-to-drag ratio of the blades, leading to improved efficiency and overall performance of the rotor. Zhao et al (2022) work demonstrates the effectiveness of this technique in optimising rotor blade design and maximising energy extraction from the wind. The disadvantage of fences is that it can thicken the boundary layer that may cause early separation when the fences are incorrectly placed, excessive fence height and poor designed fences for high Reynolds numbers.

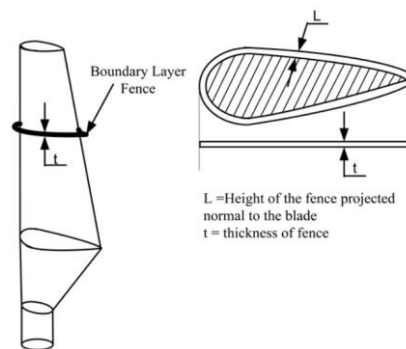


Figure 2.21: Blade optimisation using fences (Arumugam et al., 2016)

Research conducted by Barlas and van Kuik in 2010 focused on twisted or variable geometry blade designs, which aimed to enhance the performance of rotors. They introduced an active blade twist design, which enabled the blade to adjust its twist angle during operation, as shown in Figure 2.22. This design optimised the rotor's aerodynamic performance for different wind conditions. By dynamically changing the twist angle, the rotor could adapt to varying wind speeds and directions, maximising energy capture efficiency. The study demonstrated the potential of an active blade twist design to improve the overall performance and versatility of a wind turbine.

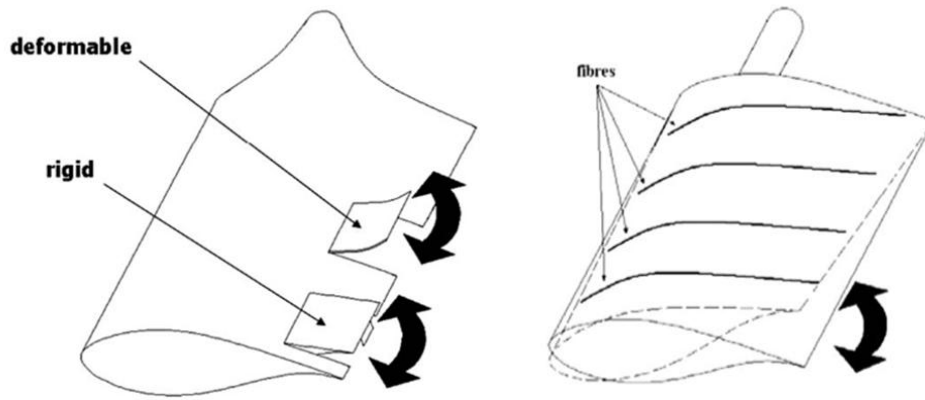


Figure 2.22: Active twist of blade (Barlas and van Kuik, 2010)

Active boundary layer control employs either injection or extraction of small amounts of energy into or out of the blade's aerodynamic system. The primary objective of boundary layer control is to mitigate flow separation over the surface of the blade.

In the injection method, energy is injected into the flow over the aerofoil profile, particularly where the flow has low energy. This is achieved by adding air from a slit parallel to the blade, as depicted in Figure 2.23. By injecting additional kinetic energy into the boundary layer, separation is avoided, and the blade aerodynamic performance is enhanced (Vos, 2018).



Figure 2.23: Blowing air into the boundary layer (Vos, 2018)

The second method avoids separation by removing the air elements that are low in energy by suction, as shown in Figure 2.24.

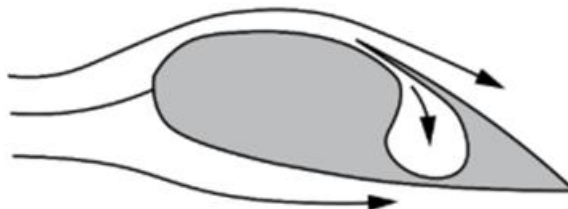


Figure 2.24: Sucking of air out of boundary layer (Vos, 2018)

All pre-installation optimisation methods must be considered during the rotor design stage. Once the rotor is installed, no further design optimisation is feasible without removing and replacing it. This implies that the rotor's performance profile for pre-installation optimisation remains fixed throughout its lifespan.

2.6.2 Post-installation optimisation

Post-installation optimisation methods listed in Table 2.1 aim to uphold the original engineering manufacturer's performance profile while enhancing operational control. These measures, including complete rotor replacement can be implemented post-installation. Operational optimization involves the modelling of HAWT power curves for existing wind farms integrating the environmental parameters by using artificial neural networks and fuzzy logic rules. This allows for better operation of existing wind farms by monitoring power curves more effectively (Rodríguez-López et al., 2020).

Maintenance and inspection of HAWTs are to maintain the wind turbine's performance according to its original engineering specifications (Park and Kim, 2016). Blade retrofitting refers to the replacement of the HAWT rotor with an improved design and is very costly (Jiang et al., 2022).

New and improved surface coatings on blades and their leading edges can mitigate rain and solid particle erosion, enabling HAWTs to operate longer within the original engineering manufacturer's energy profile (Parthasarathi et al., 2024).

Wake steering for wind farms enhances overall power output by managing the wakes of HAWTs, which affect downstream turbines. This is achieved by deliberately misaligning the yaw of individual or multiple HAWTs to optimize wake flow through the wind farm (Howland et al., 2019).

Dynamic stall control utilizes plasma flow control actuators on the blade to reduce flow separation, thereby improving the lift coefficient of the blade aerofoil. These actuators are monitored using dynamic pressure synchronous measurements, and are triggered by an external electronic particle acquisition system (Guoqiang et al., 2019).

Rotor dynamic control strategies involve employing suitable monitoring methods for various outputs of the wind turbine, such as yaw, torque, and pitch. These strategies encompass classical control using proportional-integral-derivative (PID) control and modern control techniques, which refer to soft computing or artificial intelligence. Each strategy algorithm can result in different power outputs for the wind turbine, and the appropriate or adapted strategy can be implemented post-installation to optimize performance (Elkodama et al., 2023).

As research advances in the field of rotor performance, alternative pre- and post-installation strategies can be added to the list. A potential strategy (and the focus of this research) that could improve rotor efficiency post-installation is the retrofitting of a ring vane near the hub region of the rotor. The ring vane could modify the flow pattern near the hub, potentially improving rotor aerodynamic efficiency. The concept of the ring vane, positioned near the hub region and in front of the plane of rotation, draws inspiration from both shrouded rotors and boundary layer fences. Previous studies have shown that shrouded rotors can enhance axial velocity and improve aerodynamic efficiency by reducing wake

losses and increasing mass flow through the rotor plane (Aranake & Duraisamy, 2017). Similarly, boundary layer fences have been employed to mitigate radial flow development and improve aerodynamic performance in rotor systems.

By applying these principles, the ring vane is expected to influence axial velocity in a comparable manner, with the advantage of being more feasible for larger HAWT's due to its lower weight and structural simplicity compared to full shrouds. Furthermore, the ring vane serves to reduce the conversion of axial flow into radial flow, a function similar to boundary fences. However, unlike fences, which must be attached to the blade and consequently introduce additional skin friction (Gad-El-Hak, 2000), the ring vane operates independently of the blade, thereby minimizing drag while still contributing to aerodynamic efficiency.

2.7 CFD Simulation

Computational Fluid Dynamic (CFD) simulation rose in popularity from the 2000s onwards due to the inclusion of viscous computation (Hartwanger & Horvat, 2008). Some BEMM software packages like Smart Blade and QBlade include limited CFD analysis capabilities, however, the research community widely uses standalone CFD simulation packages like ANSYS Fluent and SIMULIA. These standalone CFD packages offer more input options for flow regimes, ranging from laminar to complex turbulent models. Additionally, they provide powerful post-processing capabilities, allowing for in-depth analysis of various parameters within the simulated model (Koç et al, 2016).

With CFD simulation, the model can be exposed to various conditions, including off-design parameters, enabling the investigation of a full range of scenarios. Unlike the BEMM, which assumes no radial and circumferential dependencies, CFD simulation allows for full 3D flow with flow dependencies (when events at one location can influence another), and it includes viscous computations on the boundary layer, providing a more comprehensive analysis of aerodynamic performance. This makes CFD simulation a valuable tool for predicting rotor performance (Resolved Analytics, no date). ANSYS Fluent was utilized in this research to simulate rotor performance at constant free stream velocity across various rotor rotational speeds. Power curves were generated, and post-processing of the simulation data was employed to visualize the flow at the rotor plane. This facilitated comparison and enabled the determination of axial and angular induction factors.

While CFD has revolutionized wind turbine analysis, it is not a replacement for experimental testing. Instead, the two approaches are complementary—CFD provides detailed insights into flow physics and design optimization, while experiments offer real-world validation and help refine numerical models. CFD has well defined boundary conditions, turbulence models and aeroelastic interaction prediction yet real-world conditions are highly variable and difficult to model accurately. Experiments allow for the direct observation of these effects. (Chamorro & Porté-Agel, 2010) The cost of running full-scale wind turbine simulations remains a major limitation due to computer resources required

(Spalart, 2009). A balanced approach, combining CFD simulations with experiments, remains the most robust strategy for advancing wind turbine aerodynamics (Sørensen, 2011).

2.8 Physical testing

Physical testing of rotors to analyse performance or validate CFD simulation results can be conducted in various ways, with the choice of testing method often driven by factors such as availability, cost, and the size of the rotor. For large-scale HAWTs, scaling is typically necessary for testing purposes. Below are some testing options for HAWT rotors:

- Wind tunnel testing.
- Vehicle mounted testing.
- Stationary testing.
- Testing in water.

Wind tunnel testing often demonstrates a strong correlation between CFD simulation predictions and physical results due to the controlled environment it provides. However, research by Refan and Hangan (2012) highlighted the limitations of wind tunnel testing, particularly regarding size availability, cost efficiency, and the need for blockage correction when testing larger HAWT rotors. The selection of a wind tunnel for testing primarily depends on the rotor size and whether scaling the rotor is permissible for the specific research objectives.

Figure 2.25 illustrates the operation of closed-circuit and open-circuit wind tunnels, which are commonly used in aerodynamic testing. Closed-circuit wind tunnels recirculate air within a closed loop, while open-circuit wind tunnels draw air from the surrounding environment.

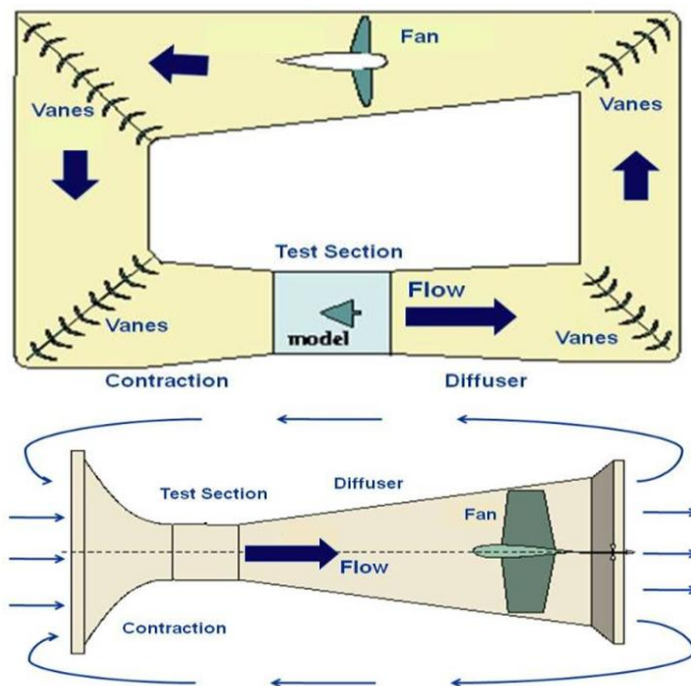


Figure 2.25: Closed and open circuit wind tunnels (National Aeronautics and Space Administration, no date)

Vehicle-mounted testing involves mounting the wind turbine on the back of a moving vehicle, where the relative velocity of the vehicle simulates the wind tunnel environment. This testing method is often more cost-effective than wind tunnel testing and is well-suited for shorter-duration tests. However, it also has limitations, particularly regarding rotor size.

Studies by Dawoud et al. (2007) compared vehicle-top testing of a small HAWT to BEMM predictions. A vehicle-top test rig, as shown in Figure 2.26, allows for easy rotor changes and instrumentation placement compared to wind tunnel testing (Song, 2012). This method provides a practical alternative for rotor testing, especially when wind tunnel testing is not feasible due to cost or size constraints. Downsides of vehicle-top testing may include duration and reproducibility of the test, ground effects and vehicle aerodynamic interference (Berg et al., 2009).



Figure 2.26: Example of vehicle-top test rig (Dawoud et al., 2007)

The stationary testing method involves testing a wind turbine rotor mounted on a tower at a suitable location with expected wind speeds, as used in the BEMM and CFD simulation. This method of field testing typically requires several months to gather enough data for performance evaluation at the correct wind speed.

During stationary testing, the wind turbine operates under real-world conditions, allowing for direct observation of its performance in the intended environment. This method requires careful planning and monitoring to ensure accurate data collection and analysis. Additionally, factors such as weather variations and site-specific characteristics can influence the results of stationary testing, making it essential to conduct tests over an extended period to capture a range of operating conditions (Song, 2012).

Testing rotors in water as the working fluid offers the advantage of easier matching of Reynolds numbers for scaled models to the prototype. This is particularly beneficial for accurately simulating the flow characteristics of the full-scale rotor. However, there are disadvantages to water testing, such

that the model may damage or break if not manufactured with correct material to withstand velocities higher than design velocity.

Water tunnels and water flumes operate on the principle where the test subject remains stationary while water flows at the desired velocity. This setup allows for precise measurements within a controlled environment, although the initial setup and test infrastructure can be expensive. Figure 2.27 illustrates a sample of a water tunnel.

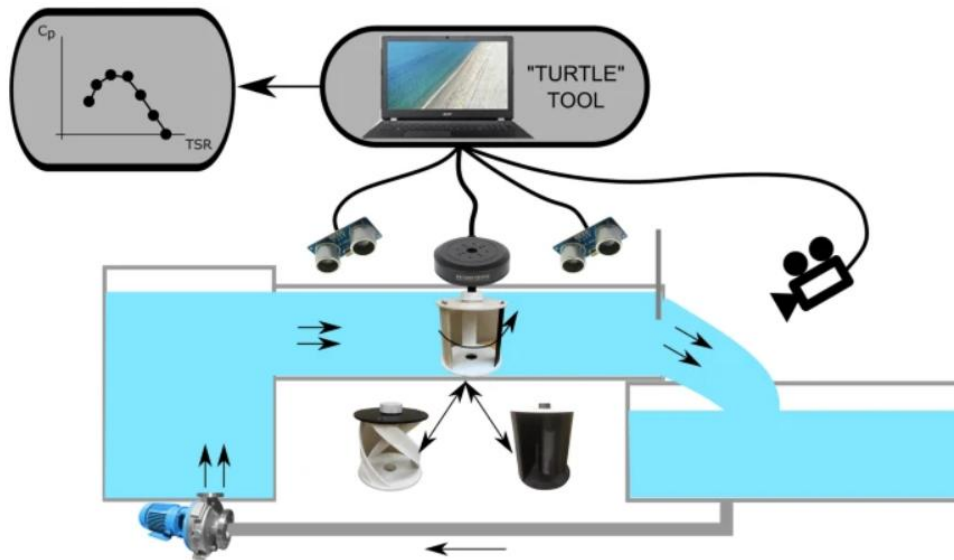


Figure 2.27: Water tunnel testing sample (Álvarez-Álvarez et al., 2020)

Another water testing method is where the water is kept stationary while driving the rotor through the fluid at the desired relative velocity. This setup allows for controlled experimentation and accurate measurement of rotor performance.

Research by Fawkes (2023) utilised a vertical-travel test apparatus for water testing and reported a good relationship between performance predictions and physical test results. Figure 2.28 illustrates the apparatus used in this study, the equipment was reported to have adequate precision and produced reliable results.

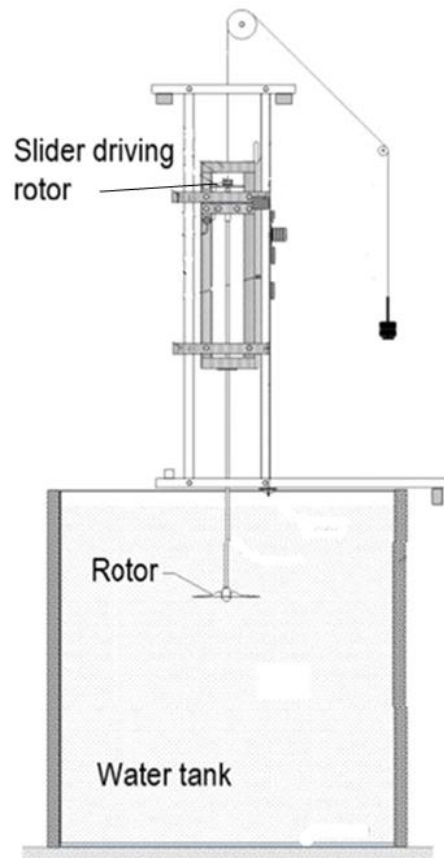


Figure 2.28: Vertical-travel test apparatus for water testing (Adapted from Fawkes, 2023)

When selecting the testing option for this research, advantages and limitations, including cost, data collection time, and ease of model interchangeability were considered. Wind tunnel testing would provide controlled conditions and precise data collection, but a much larger model (compared to water-testing) would have been required and unavailability and cost for use of an adequately sized wind tunnel was a barrier. Vehicle-mounted testing would be more cost-effective, allow for testing of a larger model, avoids test-section ‘blockage’ concerns, and allows for quick model interchangeability, though it may not offer an environment as controlled as wind tunnel testing. Considering the specific research outcomes and requirements such as the desired level of precision and available resources, the chosen testing method for this research was the vertical-travel test apparatus, similar to that used by Fawkes (2023).

CHAPTER THREE

RESEARCH METHODOLOGY

The methodology for this study involved a comparative analysis between a standard rotor and the same rotor retrofitted with six different sized ring vanes. Utilizing a 280 mm ideal rotor design, as detailed in the research conducted by Fawkes (2023), this study included three distinct investigations.

- SolidWorks was used to model seven 280 mm rotors: one standard rotor and six rotors equipped with ring vanes. Computational Fluid Dynamics (CFD) simulations of these 3D virtual rotor models were conducted using ANSYS Fluent to generate power versus rotation speed curves for comparison, using water as the working fluid.
- Physical testing of these rotors was performed using a vertical-travel test apparatus with water as working fluid. The SolidWorks models were used to manufacture 3D resin printed models used during testing. All parameters used during physical testing were also applied for CFD simulations.
- A case study comparing the standard rotor and the best-performing retrofitted rotor (as determined by the CFD simulations and physical testing.) This analysis involved using CFD simulations to evaluate the rotors at a higher fluid velocity, beyond the capabilities of the vertical-travel test apparatus. The purpose of this case study was to verify that the enhanced output of the best-performing rotor remained consistent under different flow conditions.

The flow diagram illustrating the overall methodological approach for this study is depicted in Figure 3.1. Detailed flow diagrams for the three specific investigations are provided within their respective sections. SolidWorks was employed to model various ring vanes, ensuring seamless integration with the existing 280 mm rotor. The CFD simulation setup ensured mesh independence for each simulation. Simulations were conducted at various rotational speeds, with a free stream velocity of 0.5 m/s, using water as the working fluid for each rotor. From the simulation results, power versus rotational speed curves were generated for comparative analysis.

Physical testing for each rotor was conducted using the vertical-travel test apparatus at 0.5 m/s free stream velocity using water as working fluid. Physical test results were used to generate power versus rotational speed curves enabling a comparative analysis of the rotors.

CFD simulation and physical test results were used to determine the best performing retrofitted rotor. A subsequent CFD simulation case study was conducted with both the standard rotor and the best-performing retrofitted rotor at a higher free stream velocity of 1 m/s.

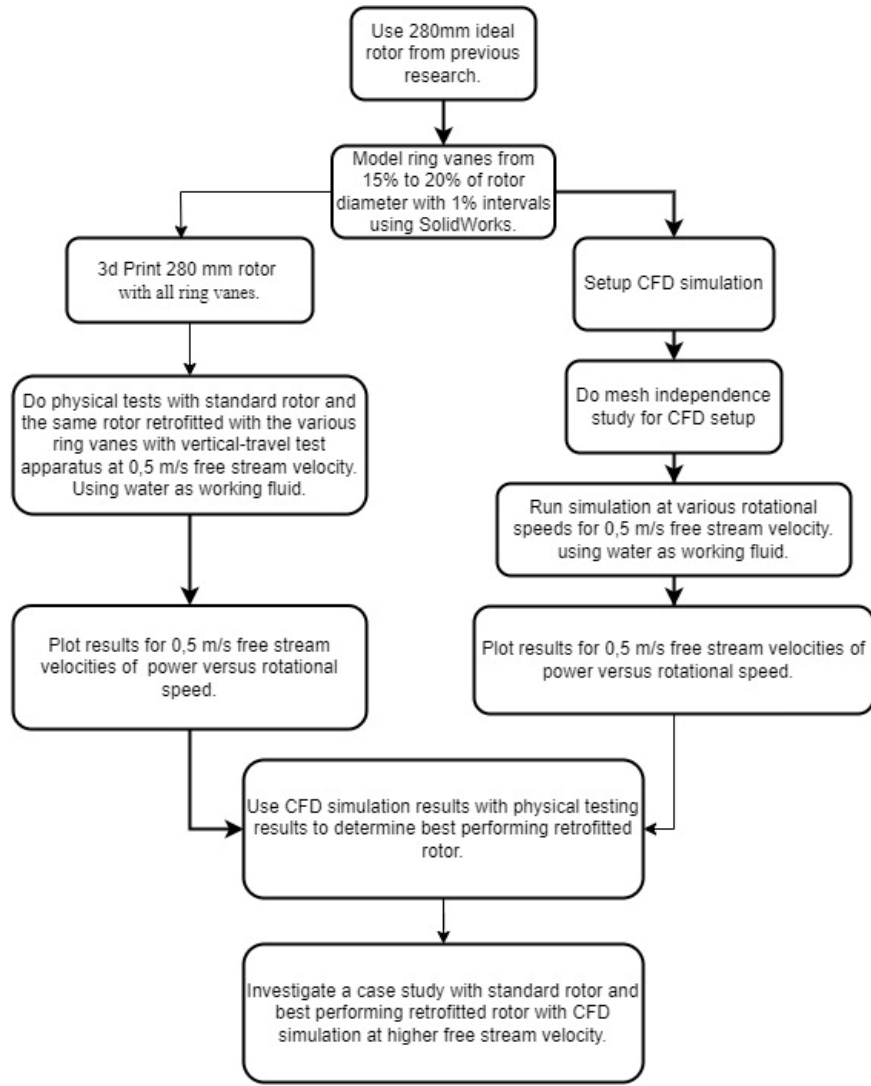


Figure 3.1: Overall methodology flow diagram

3.1 Modelling of rotors

The 280 mm ideal rotor used in this research was modelled from geometry data obtained from research by Fawkes (2023) where the BEMM was used to generate the blade design data. This data was integrated into SolidWorks to model the 280 mm rotors. Two distinct sets of rotor models were created: the first set for CFD simulation, and the second set for 3D resin printing for physical testing. Both sets were geometrically the same, but the second set was an assembled design for manufacturing purpose.

The blade aerofoil and hub profiles were provided as x , y , and z spline coordinates, which were imported into SolidWorks. Each blade comprised 40 spline elements representing aerofoil profiles from root to tip, while the hub section featured an airship nose cone spline profile. These imported splines in SolidWorks were used to loft solid bodies for both the blade and hub components. Figure 3.2 and Figure 3.3 illustrate the blade aerofoil and hub airship nose cone profiles for the rotor. A sample of x , y , and z spline coordinates for blade aerofoil profiles is provided in Appendix A.

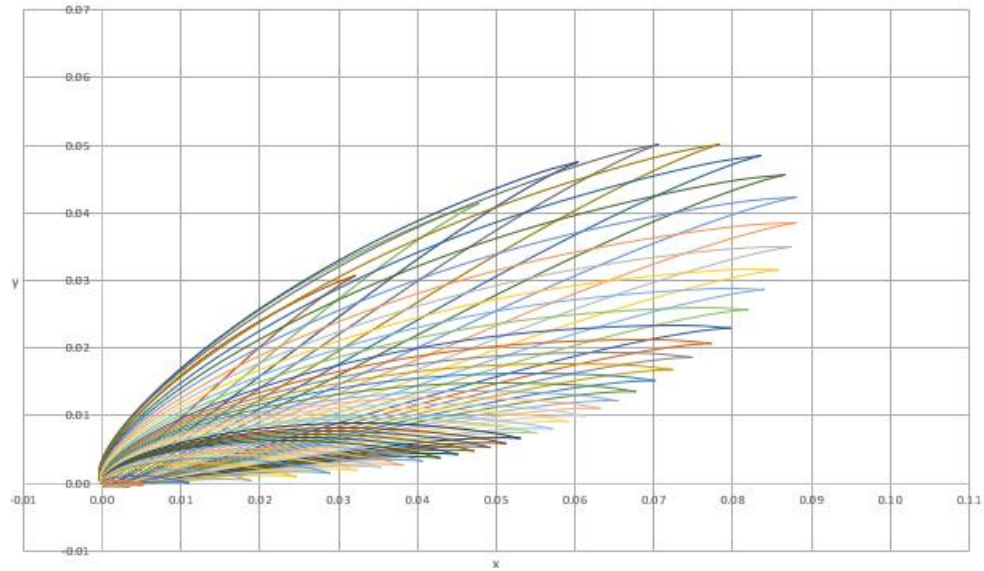


Figure 3.2: Spline aerofoil profiles for blade

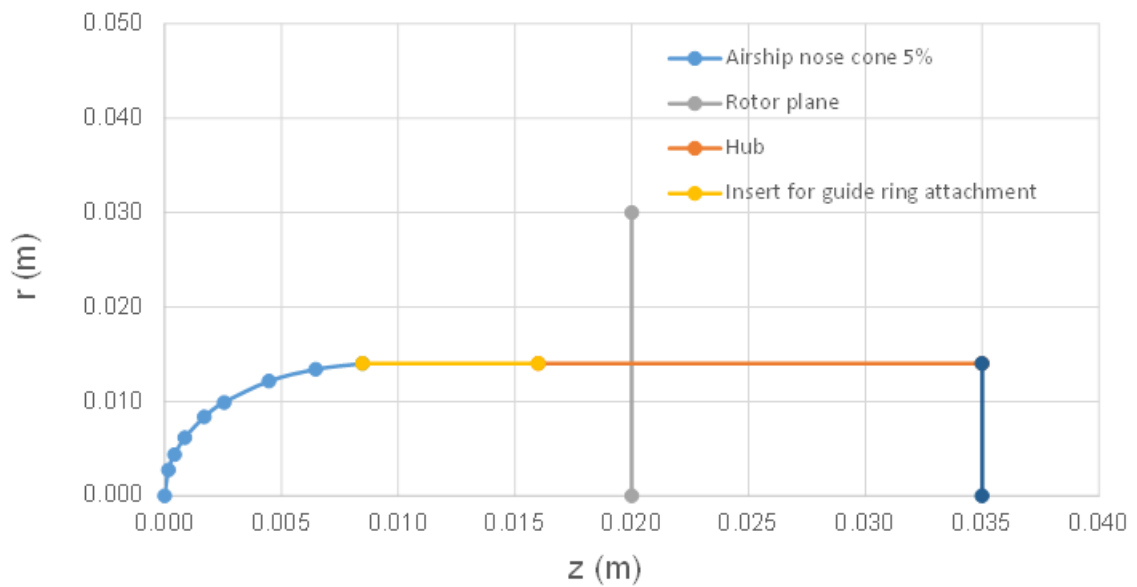


Figure 3.3: Airship nose cone profile of hub {Adapted from (Fawkes, 2023)}

The rotor featured three blades evenly spaced at 120 degrees, with a hub-to-rotor diameter ratio of 5%. To accommodate retrofitted rotors with ring vanes, a 33 mm insert was added to the hub in front of the rotor plane. This insert was also incorporated into the standard rotor hub to maintain consistent basic geometry across all configurations.

Six different sized ring vanes were modelled for the retrofitted rotors. The sizes of these ring vanes were determined using a percentage ratio of the rotor diameter to the diameter of the ring vane. Specifically, ring vanes were modelled at 15%, 16%, 17%, 18%, 19%, and 20% of the rotor diameter as shown in Table 3.1. Throughout this document, the term "16% ring vane rotor," for instance, denotes the rotor retrofitted with the 16% ring vane.

Table 3.1: Rotor and ring vane parameters

Description	Value
Rotor diameter (m)	0.28
Design tip speed ratio	4.8
Number of blades	3
Hub ratio	0.5
Hub diameter (m)	0.0140
15 % ring vane diameter (m)	0.0420
16 % ring vane diameter (m)	0.0448
17 % ring vane diameter (m)	0.0476
18 % ring vane diameter (m)	0.0504
19 % ring vane diameter (m)	0.0532
20 % ring vane diameter (m)	0.0560

3.1.1 Ring vanes

The ring vanes were constructed from an aerofoil ring secured by three struts spaced at 120 degrees. Both the ring and struts featured symmetrical NACA 0024 aerofoil profiles as shown in Figure 3.4 set at zero angle of attack.

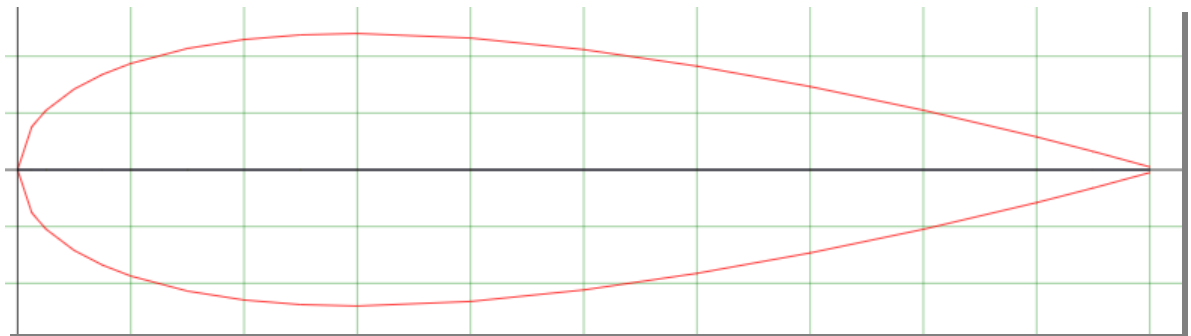


Figure 3.4: NACA 0024 aerofoil profile. (NACA 0024 (*naca0024-il*), no date)

These profiles were imported into SolidWorks and transformed into solid surfaces using lofting techniques. The choice of the NACA 0024 aerofoil profile was based on its suitability for low Reynolds numbers - aiming to minimize drag while maintaining zero lift characteristics. Figure 3.5 displays the lift and drag coefficients for the NACA 0024 aerofoil, where the black line denotes zero lift and zero angle of attack, with a drag coefficient below 0.02 (NACA 0024 (*naca0024-il*), no date). Figure 3.6 shows a sample of the ring vane with struts attached to the hub.

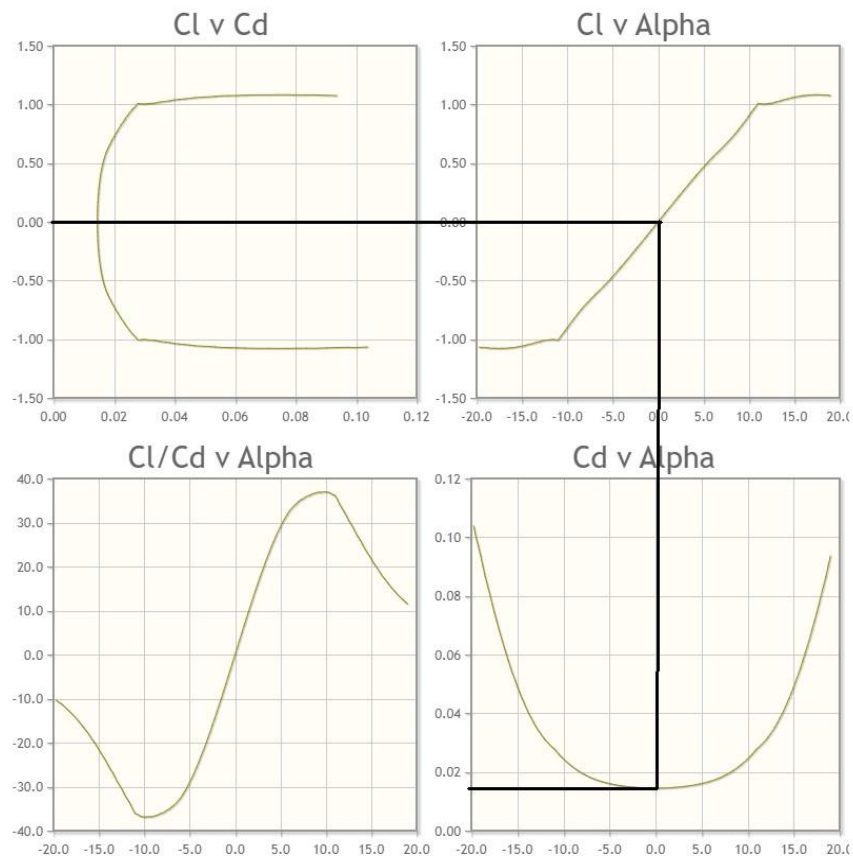


Figure 3.5: NACA 0024 C_l , C_d and α graphs (Adapted from NACA 0024 (*naca0024-il*), no date)

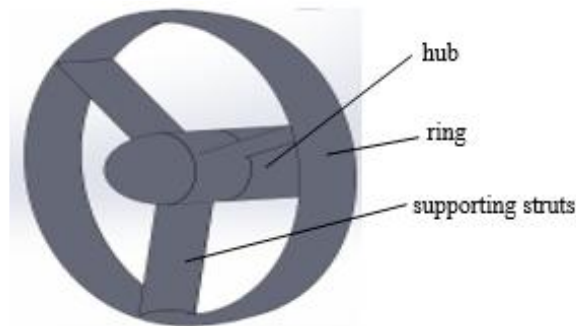


Figure 3.6: Sample of ring vane and struts added to hub

3.1.2 Model set for CFD simulation

The first set of rotors modelled for CFD simulation were contained within a rotating domain disc with a diameter of 400 mm and a length of 60 mm. This rotating domain was placed inside the fluid domain, representing the water tank of the vertical-travel test apparatus. The fluid domain matched the dimensions of the physical test water tank, with a diameter of 1400 mm and a depth of 1700 mm. Each rotor, along with its rotating domain, was positioned 560 mm from the inlet side of the fluid domain. Rotational periodicity was used in the simulation, and a 120° angle extrusion cut was applied across the entire CFD model for this purpose. This technique allowed for accurate representation of the rotating flow conditions with a far lower computing requirement than if a full rotor had been used. The

first set of rotor models for CFD simulation comprised seven variations - the standard rotor and six rotors retrofitted with ring vanes. Figure 3.7 shows a sample of the standard rotor within the rotating domain disc and Figure 3.8 the complete CFD model after the 120° extrusion cut.

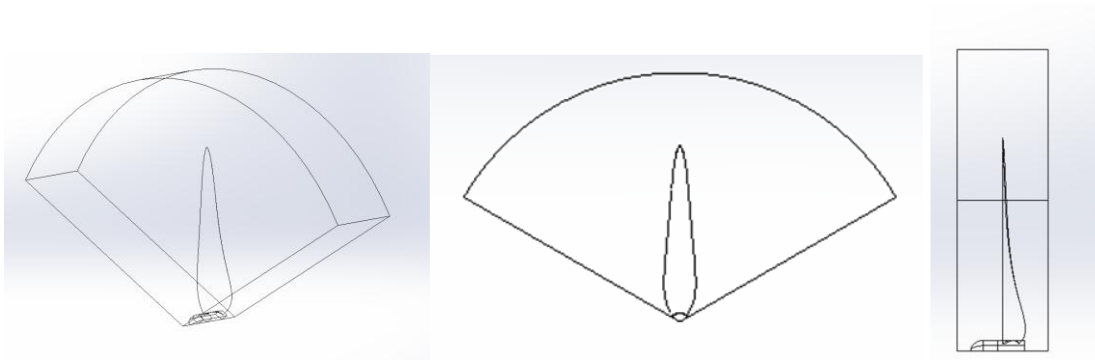


Figure 3.7: Blade and hub of standard rotor within rotating domain disc

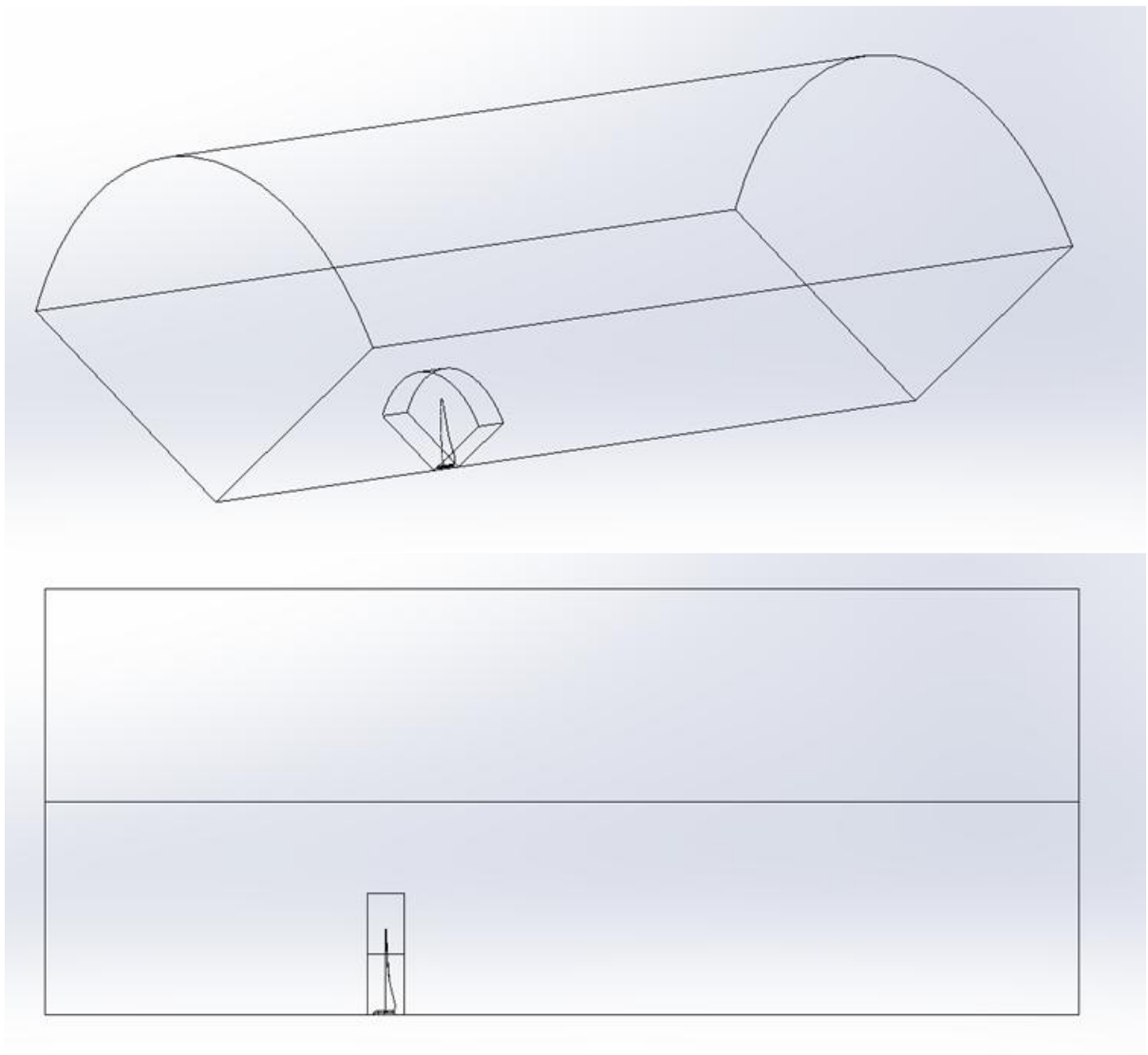


Figure 3.8: Sample of complete 120° pie-slice CFD model with standard rotor within rotating domain inside fluid domain

3.1.3 Model set for 3D printing

The second set of rotors was designed specifically for 3D resin printing. Each completed rotor model was divided into three parts to facilitate the printing process and subsequent assembly for physical testing. Figure 3.9 shows the three separate parts of a retrofitted rotor that were 3D resin printed. In this configuration, only one hub with three blades was 3D printed.

The various 3D-printed ring vanes were designed to be interchangeable on the standard rotor, to allow for comparative evaluation during physical testing.

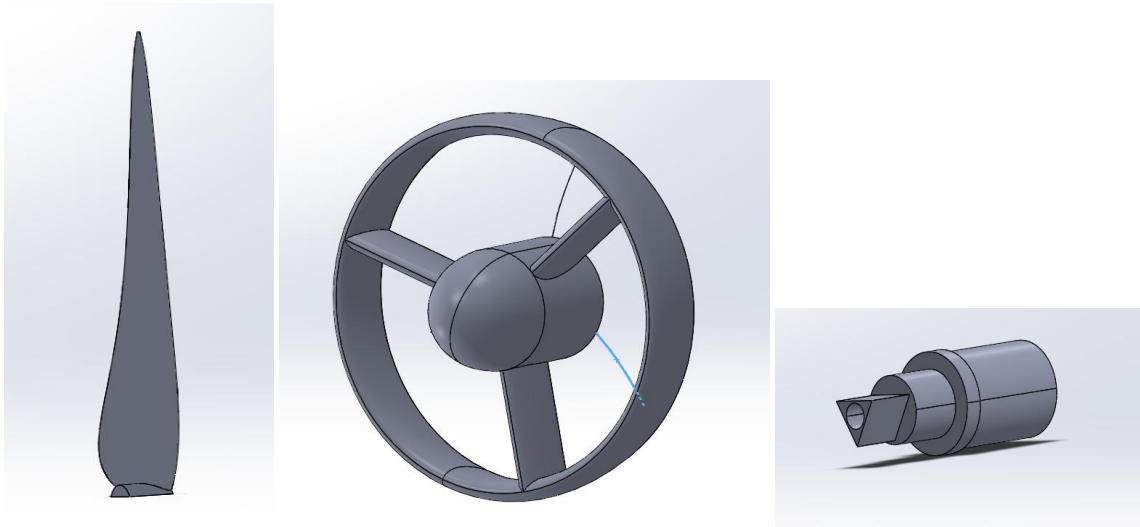


Figure 3.9: Three dissected parts used for 3D resin printing and assembly of complete rotors for physical testing

A Creality Halot 3D resin printer was used for printing all parts with a 50-micron layer height setting. All printed parts were cured with an ultraviolet light. Figure 3.10 shows the standard rotor retrofitted with the 15% ring vane on the left and the all the ring vanes ranging from 15% to 20% on the right.



Figure 3.10: 3D resin printed parts: rotor with 15% ring vane (left) and all ring vanes (right)

3.2 CFD methodology

For the CFD simulations, ANSYS Fluent 2022 R2 version was utilized on a Lenovo system equipped with an 11th generation i5 core processor running at 2.4 GHz, paired with 8 GB of RAM and a solid-state drive. Seven virtual models were created for this study, including a standard rotor and six rotors fitted with different sizes of ring vanes, as specified in section 3.1. The setup for each model followed a consistent process, ensuring that all solver settings and input parameters were identical across simulations. This approach aimed to generate comparative results that could be directly analysed to assess the performance changes due to different ring vane sizes. Figure 3.11 illustrates the methodological flow followed for generating these results. The diagram outlines the steps involved in setting up each CFD simulation.

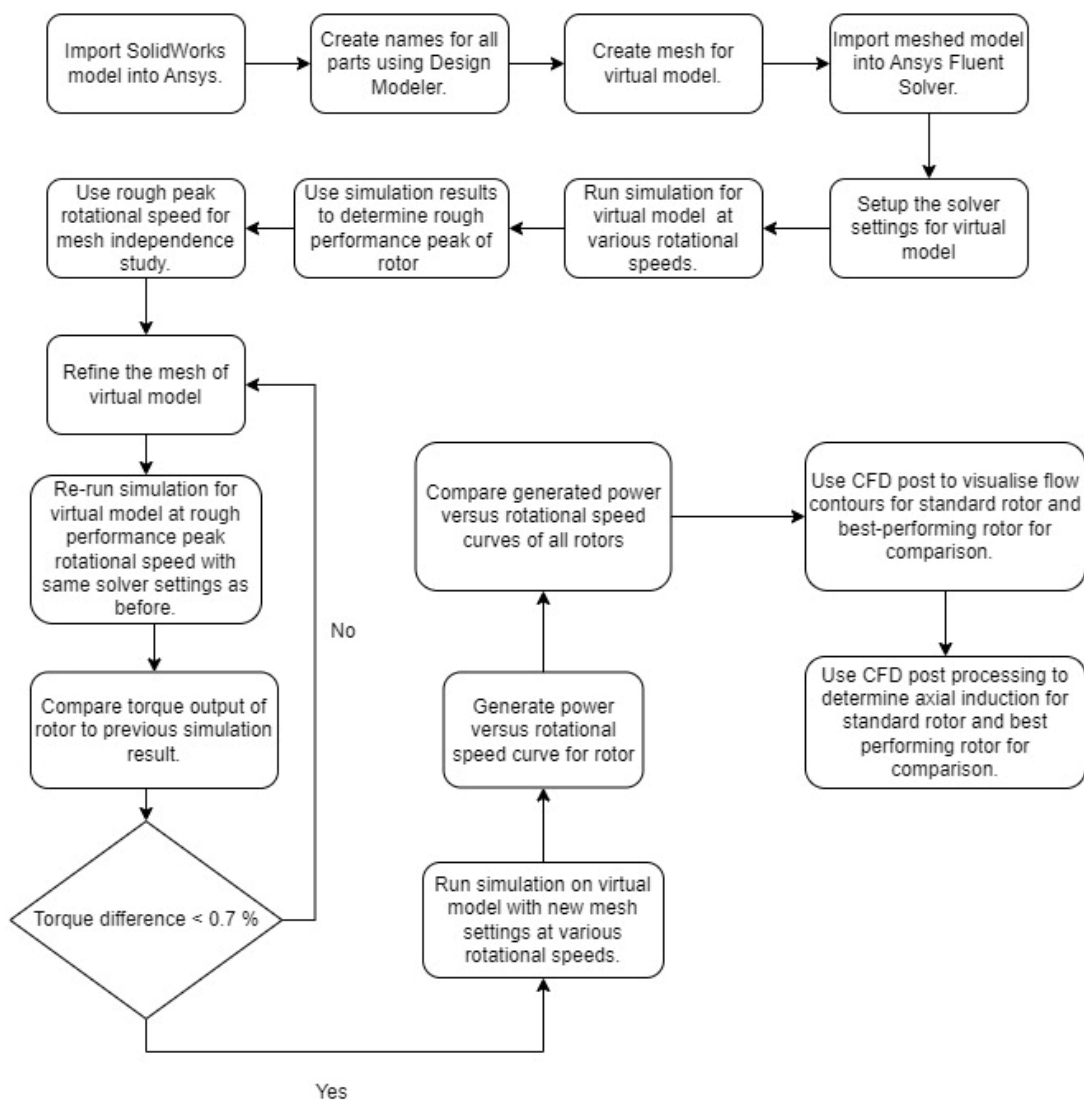


Figure 3.11: Flow diagram for CFD Simulation

Solid models created in SolidWorks were imported into ANSYS, and all parts and domains were named using the built-in platform Design Modeller. The virtual models were structured with a fluid domain encompassing a rotating domain that contained the rotor. Part names included blade, ring

vane, hub, inlet, outlet, rotational periodicity 1, rotational periodicity 2 and outer wall, as shown in Appendix B.

The named virtual models were imported into ANSYS Fluent for meshing. The watertight geometry workflow in Fluent meshing had the following main settings.

Surface mesh		
	Min. size	0.0016 (m)
	Max. size	0.0425 (m)
	Growth rate	1.2
	Size function	Curvature & Proximity
	Curvature normal angle	
	Cells per gap	1
	Scope proximity to	Edges
Rotational periodic boundaries	Periodicity angle 120°	
Boundary layer settings		
	Offset method type	Aspect ratio
	Number of layers	4
	First aspect ratio	5
	Growth rate	1.2
Volume settings		
	Fill with	poly-hexcore
	Buffer layers	1
	Peel layer	1

Once the virtual models were meshed in ANSYS Fluent, they were imported into the ANSYS Fluent solver for further setup and execution of the CFD simulations. This step involved configuring solver settings, specifying boundary conditions, and defining operating parameters necessary to conduct the simulations accurately.

3.2.1 Solver model setup for simulation

ANSYS Fluent employs the Reynolds-averaged Navier-Stokes (RANS) equations for solving fluid flow problems, incorporating transport equations to address the chosen turbulent viscosity model. The available turbulent viscosity model options in ANSYS Fluent include:

- the one-equation model (Spalart-Allmaras)
- the two-equation models (k - ϵ Standard, k - ϵ RNG, k - ϵ Realisable, k - ω Standard, k - ω BSL, k - ω GEKO and SST k - ω)
- Reynolds Stress models
- Transition Models (k - kl -, Intermittency Models and Transition SST)

The k - ω turbulence model is widely recognized for its effectiveness in handling flows with low Reynolds numbers by resolving the viscous sublayer. It utilizes turbulent kinetic energy and a specific turbulent dissipation rate, making it particularly suitable for near-wall treatments. In contrast, the k - ϵ turbulence model employs empirical damping functions in the viscous sublayer, which can lead to reduced accuracy in pressure gradient boundary layer flows (SimScale, no date).

For this research, the two-equation *Generalized k- ω* (GEKO) turbulence model was selected. This model builds upon the k - ω formulation but offers enhanced flexibility to adjust parameters across a

broad range of flow scenarios. It retains the fundamental benefits of the $k-\omega$ model while allowing adjustments to tailor its performance to specific application types without compromising its foundational calibration (Ansys, no date). The free parameters for this model that can be adjusted included the following coefficients.

- CSEP — customises the flow separation from smooth walls.
- CNW — customises the heat transfer for near-wall flows.
- CMIX — customises free shear flow mixing.
- CJET — customises free jet spreading rates.
- CCORNER — customises corner flow separation.
- CCURV — customises vortex flows.

In Figure 3.12 various settings of the Generalized $k-\omega$ (GEKO) turbulence model are compared to the $k-\omega$ Shear Stress Transport (SST) model for the lift coefficient versus axial induction of the DU-96-W-180 aerofoil. The SST model and GEKO (1.75 / 2.00 / 2.50) is shown to over-predict lift at higher axial induction. At lower axial induction the GEKO (2.00 / 2.50) tends to under predict lift.

For simulating the 280 mm rotors in this research, the default coefficient settings of the $k-\omega$ GEKO (1.75) model were utilized. These settings were chosen to provide a balanced approach in turbulence modelling, aiming to accurately capture the flow dynamics around the rotors without biasing towards over or under predicted lift as the GEKO (2.00 / 2.50) and SST does.

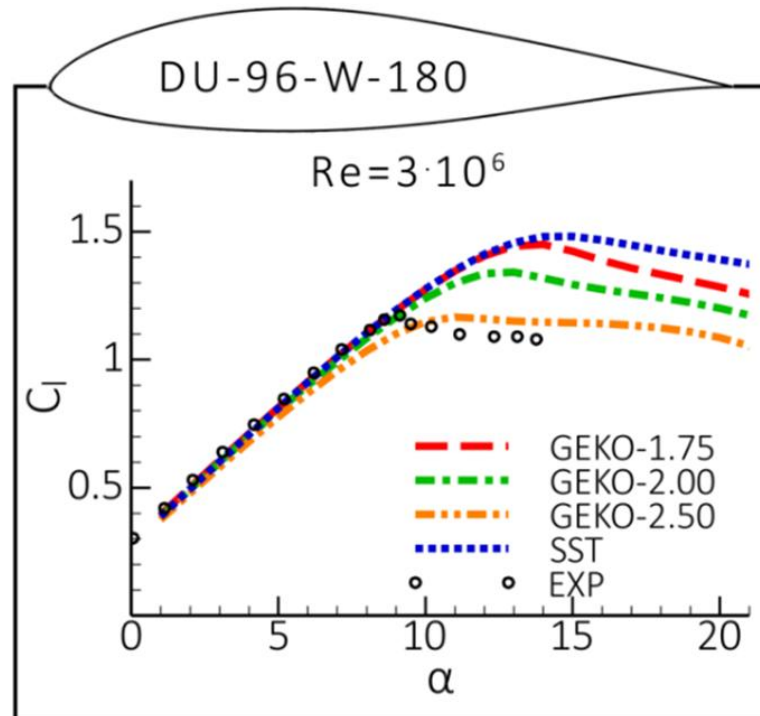


Figure 3.12: Lift versus axial induction for GEKO and SST turbulence models. (Semantic Scholar, no date)

Identical solver settings were used to simulate all models. A complete report of all solver setup setting is provided in Appendix C. A steady-state, pressure-based solver was employed with the $k-\omega$

Generalized (GEKO) turbulence model, using water as the working fluid. A fluid inlet velocity of 0.5 m/s was set, and the rotating domain containing each rotor was varied in rotational speed from 140 rpm to 220 rpm to approximate peak performance with initial mesh settings. Power output was calculated using

$$(P = T \cdot \omega), \quad (3.1)$$

where T represented the torque acting on the blades and hub, and ω was derived from torque reports and rotating domain settings during solution iterations. The solution method involved a coupled pressure and velocity approach with a pseudo-transient solver allowing user-specified time steps. Convergence criteria were met when scaled residuals of x, y, and z fluid velocities reached approximately 10^{-6} , and continuity approached 10^{-6} , ensuring output torque converged to an oscillating 5th significant digit. Following determination of rough peak performance, a mesh independence study with refined mesh settings around the identified peak rotational speeds for each virtual rotor model to enhance result accuracy and reliability was done.

3.2.2 Boundary layer

To accurately capture the boundary layer dynamics in the simulations of the 280 mm rotor models, additional inflation mesh layers were incorporated into the virtual models. These layers were essential for correctly capturing the boundary layer. The maximum expected Reynolds number (approximately 2.5×10^4) was considered to capture the boundary layer correctly for the 280 mm rotor models at mid-span of the blade. However, there is disagreement about the critical Reynolds number when the flow regime changes within the boundary layer from laminar to the transition layer and to fully turbulent. Carmichael (1982) approximated the critical Reynolds number at 5×10^4 for an incompressible, undisturbed environment. This was also supported by Huang and Lin (1995) and later on, by Derksen et al (2008). Nava et al (2016) found that boundary layer transition for a similar aerofoil initiated at 2×10^4 with a slow or sudden transition completion at Reynolds number of 2×10^5 . The expected Reynolds number at the midspan of the blade fell within the transitional boundary layer. The ring vane was anticipated to increase the Reynolds number over the blade, promoting an earlier transition to turbulent flow. This effect could occur through multiple mechanisms, acting as a trip device to trigger turbulence, energizing the boundary layer to reduce flow separation, or accelerating the local airflow increasing Reynolds number over the blade.

The boundary layer at the mid-span of the blade at $y+=1$ and $y+=5$ was used to determine the inflation layers of the mesh required to capture the boundary layer correctly with the $k-\omega$ GEKO turbulence model. Figure 3.13 shows the velocity profile relationship of turbulent wall flow and $y+$ value.

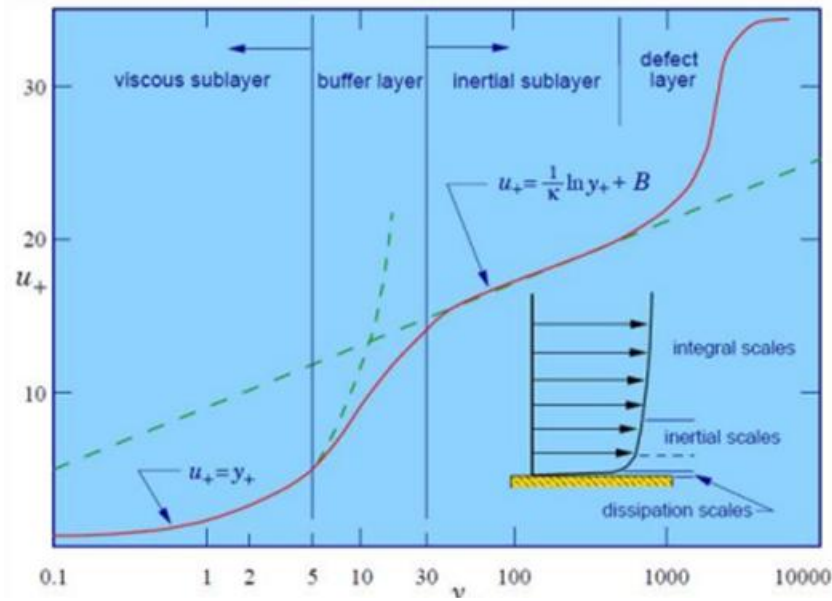


Figure 3.13: Velocity profiles in turbulent wall flow Source: www.learncax.com.

The y_+ value is a dimensionless parameter that represents the distance from the first grid cell to the surface wall and is expressed as:

$$Y_+ = \frac{U_t y}{\mu} \quad (3.2)$$

Where U_t is the friction velocity, y is the first cell height and μ the kinematic viscosity. The boundary layer at mid-span of the blade was determined for $y_+=1$ and $y_+=5$, and the first inflation layer height y was within that range ensuring that the viscous laminar region was adequately captured during the simulation process. The inflation layer settings for all virtual models included an aspect ratio of 10 and a growth rate of 1.2, with a total of 4 inflation layers between model walls and volume mesh. Figure 3.14 shows the placement of inflation layers compared to the $y_+=1$ and $y_+=5$ boundaries for the 280 mm rotor.

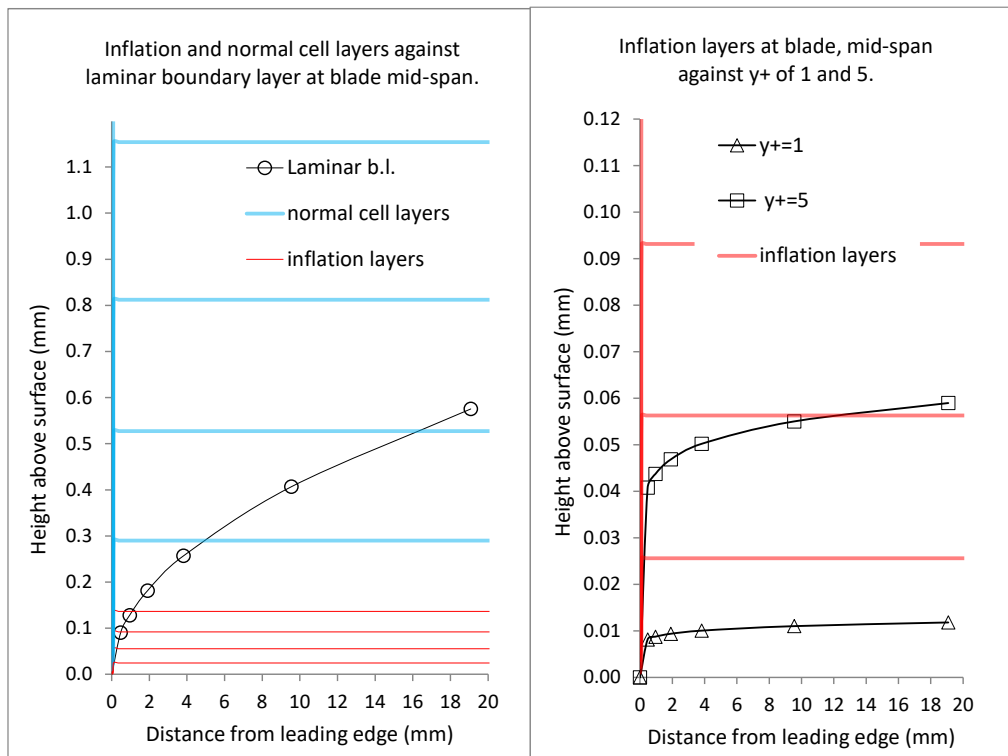


Figure 3.14: Rotor boundary layer and sub-layers with mesh height calculation

3.2.3 Mesh independence study

After identifying the rough peak performance for each rotor using initial mesh settings, a mesh independence study was conducted using these parameters. The purpose of this study was to ensure that the solution was not overly dependent on the mesh size and that the near-wall boundary layer was accurately captured.

The torque generated on the blade and hub served as the indicator for mesh independence. As the mesh size was systematically decreased, the torque output varied. New torque values resulting from smaller mesh sizes were compared to previous values to assess convergence. The reduction in mesh size led to an increase in the number of cells within the virtual model.

Figure 3.14 depicts the results of the mesh independence study conducted on the standard rotor, illustrating the change in torque as the cell count of the virtual model increased with decreasing mesh size. This iterative process continued until the change in torque output fell within an acceptable range, of below 1% indicating convergence and ensuring that further reductions in mesh size did not significantly alter the simulation results versus the computational time and resources required (Celik et al., 2008).

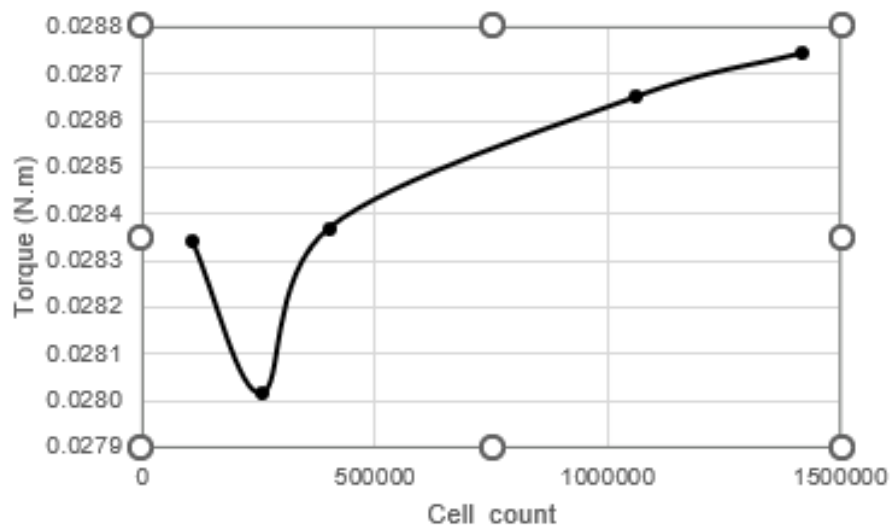


Figure 3.15: Mesh independence study of standard rotor with torque versus cell count.

Table 3.2 presents the percentage change in torque as the mesh refinement progressed for the standard rotor. Detailed mesh independence studies for all virtual models, including their respective percentage changes in torque, are provided in Appendix D. This mesh independence verified how the torque output changed with the refinement of mesh size, ensuring the accuracy and reliability of the simulation results across different rotor configurations.

Table 3.2: Percentage change of torque for mesh independence study of standard rotor

Standard rotor at 180 rpm

Cell count	Torque hub (N.m)	Torque blade (N.m)	Torque total (N.m)	Percentage change in torque
106858	4.40E-06	0.028340	0.028344	-
254994	4.40E-06	0.028014	0.028018	-1.15%
403129	4.40E-06	0.028370	0.028374	1.27%
1062314	4.30E-06	0.028650	0.028654	0.99%
1419545	4.47E-06	0.028744	0.028748	0.33%

The final mesh settings used for all rotor types with an acceptable percentage torque change of below 0.7 % were as follows.

Surface mesh

Min. size	0.00001 (m)
Max. size	0.000256 (m)
Growth rate	1.2
Size function	Curvature & Proximity
Curvature normal angle	18
Cells per gap	1
Scope proximity to	Edges

Rotational periodic boundaries Periodicity angle 120°

Boundary layer settings

Offset method type	Aspect ratio
Number of layers	4
First aspect ratio	10
Growth rate	1.2

Volume settings

Fill with	poly-hexcore
Buffer layers	1
Peel layer	1

Figure 3.15 to 3.18 Shows the final meshed virtual model for the 15% ring vane rotor of the virtual model demonstrating the overall mesh structure.

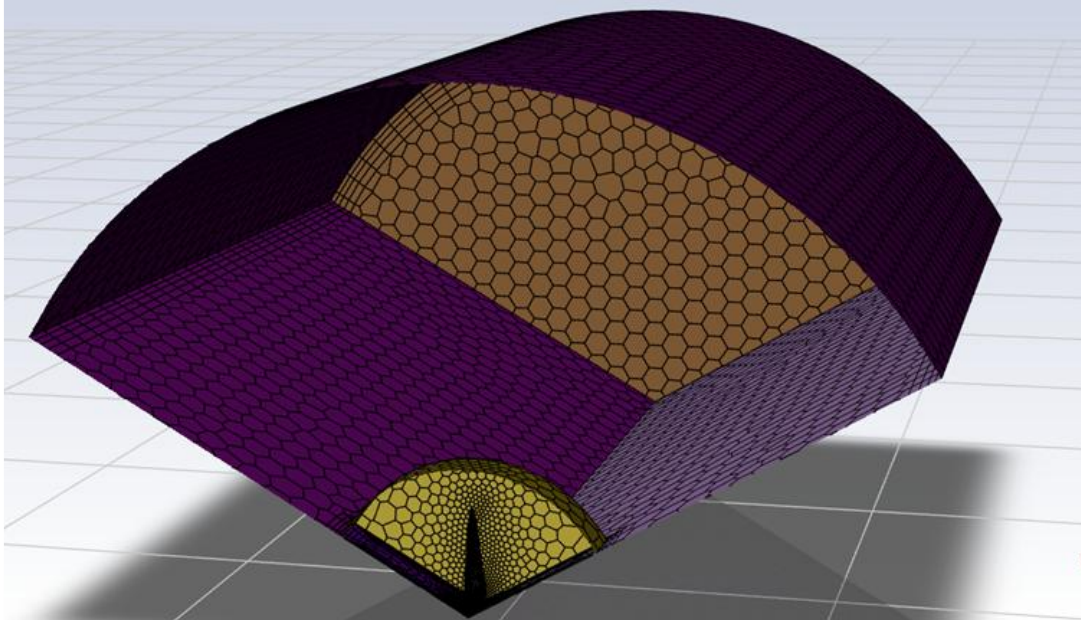


Figure 3.16: A plane through fluid domain showing rotating domain containing hub, blade and ring

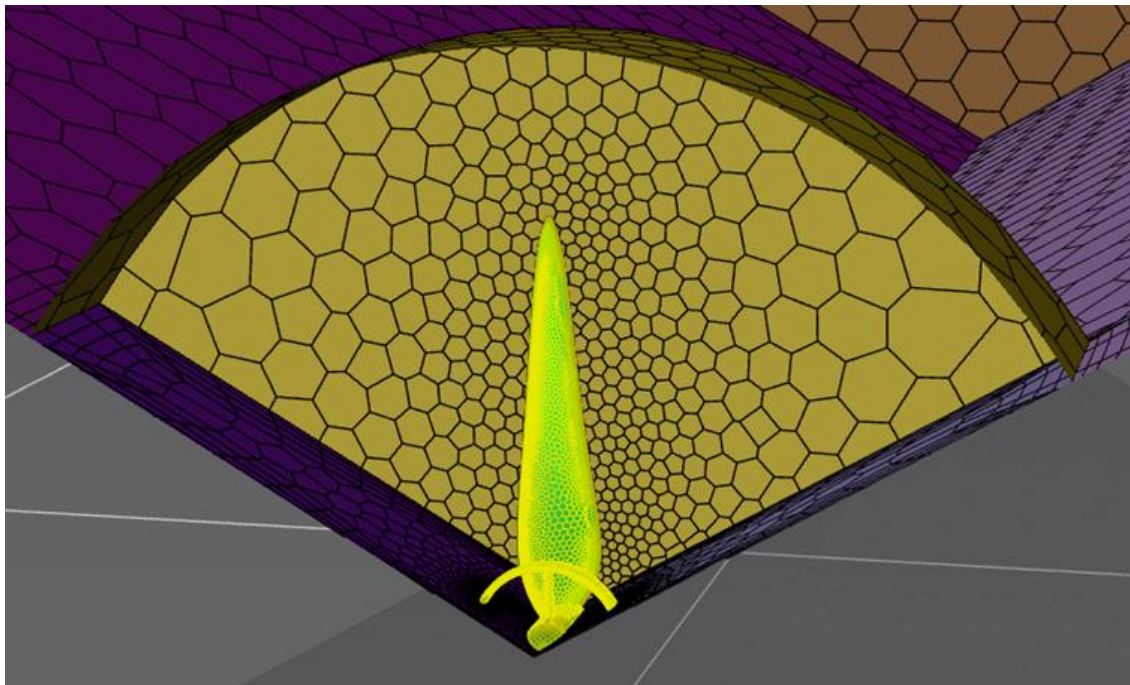


Figure 3.17: Rotating domain with hub, blade and ring highlighted.

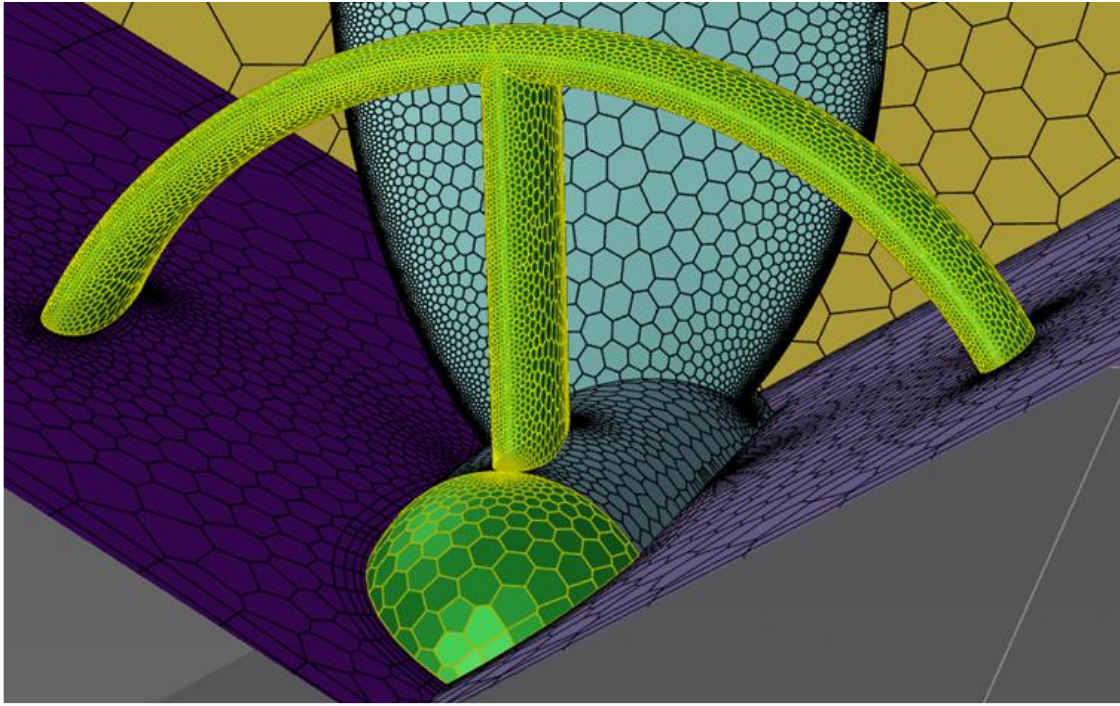


Figure 3.18: Close-up view of hub with blade and ring vane attached.

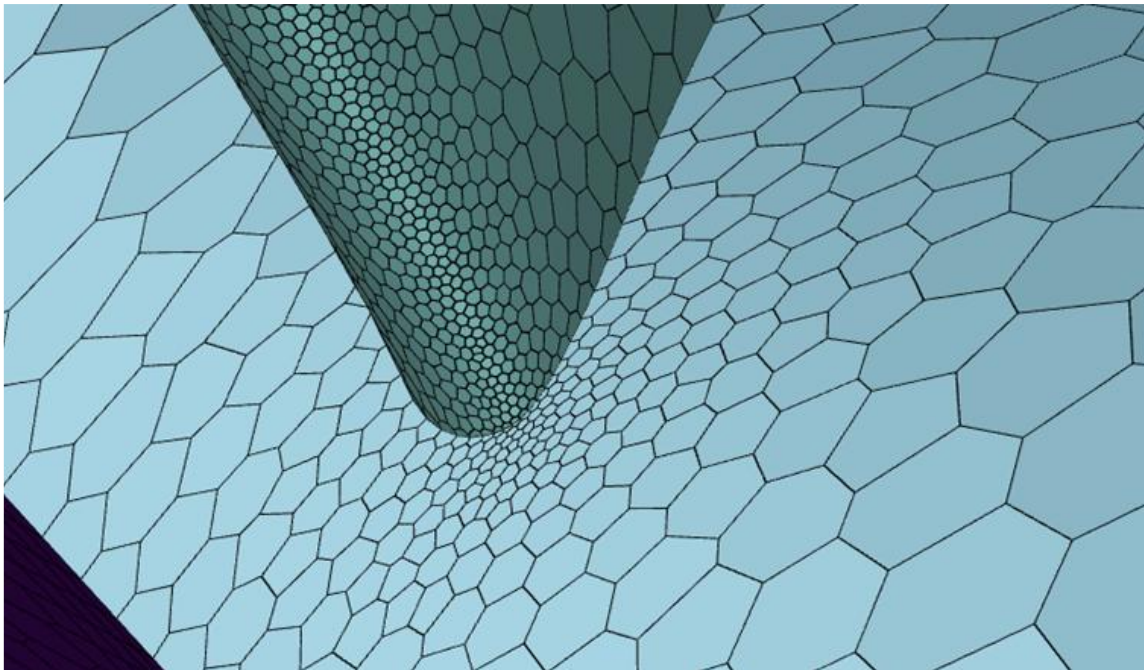


Figure 3.19: Leading edge of blade root.

Results from CFD simulation are presented in the results chapter where the power output for each type of rotor was calculated across a range of rotational speeds. The power was derived from the product of the rotor's net torque output and the rotational speed in radians per second. Specifically, the net torque output was calculated as the torque generated on the blade minus the torque experienced by the hub. Each data point in the results corresponds to an individually solved simulation, for the specific

combination of rotor type and rotational speed tested. The power output of each rotor type was solved for a range of rotational speeds.

CFD flow visualisation was obtained from ANSYS CFD post processing, to visualise the axial, radial and tangential velocity at a plane located 2 mm upstream of the rotor plane. Velocity visualisations were done for the standard rotor and the best performing retrofitted rotor at peak performance, (at rotational speed of 180 rpm) and at 160 rpm and 200 rpm, which were off-peak rotational speeds.

ANSYS CFD post processing was also used to determine the axial and angular induction factors along the blade in annular segments of width 10 mm. There were a total of 15 segments from blade root to tip, and the axial and angular induction factors were calculated for each segment. The axial induction factor was obtained at a plane 2 mm in front of the rotor plane, and the angular induction factor was obtained from a plane 20 mm behind the rotor plane, within the near wake of the rotor. Axial and angular induction factors were calculated for peak rotational speeds of 180 rpm, and at 160 rpm and 200 rpm which were off-peak for both the standard rotor and the 18% ring vane rotor.

3.3 Testing methodology

Experimental testing of the rotors, including those retrofitted with various ring vanes, was conducted using a vertical-travel test apparatus similar to the setup described by Fawkes (2023). Each rotor underwent standardized testing procedures to evaluate its performance characteristics under controlled conditions. Figure 3.19 shows the specific method used for physical testing of each rotor. This methodology ensured consistency in how each rotor was assessed, providing a reliable basis for comparing their performance metrics.

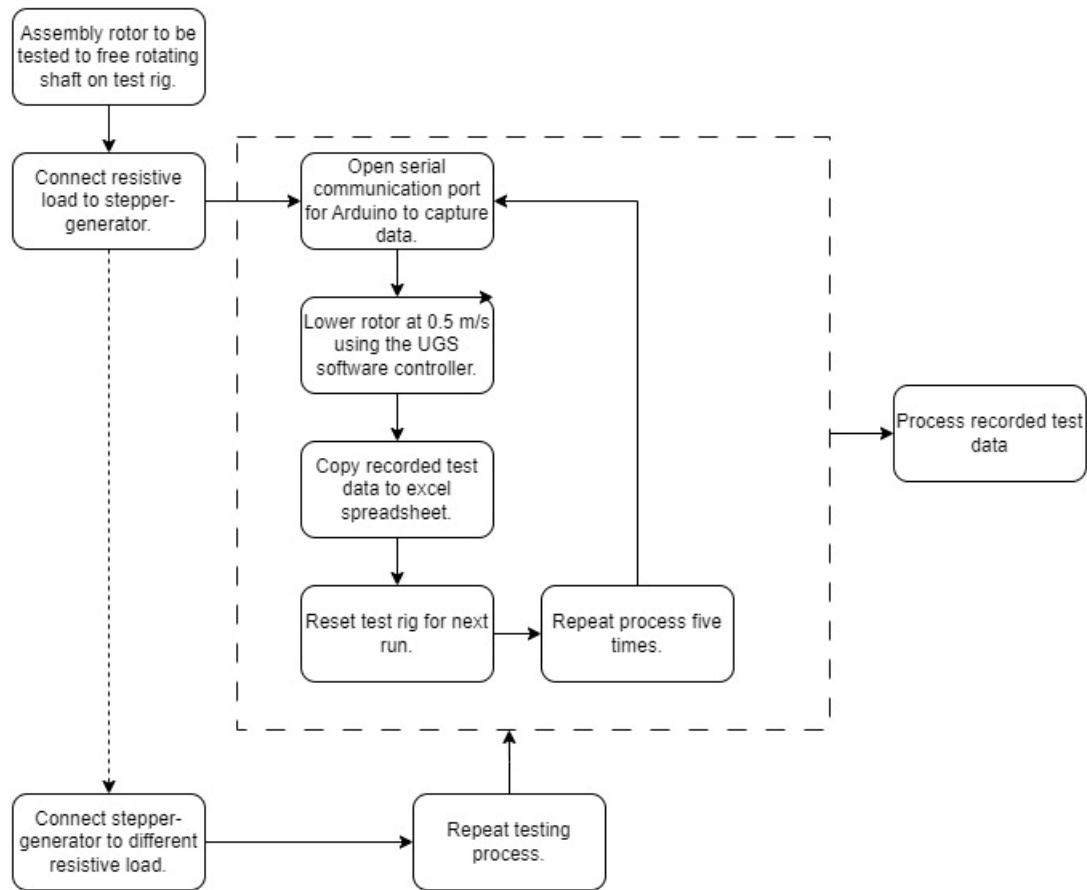


Figure 3.20: Flow diagram for physical testing

3.3.1 Test equipment.

The vertical-travel test apparatus comprised a drop frame positioned above a water tank measuring 1.4 m in diameter and 1.5 m in height. Within the frame, a slider driven by a stepper motor moved along two parallel 22 mm shafts, supported by four linear bearings. This slider propelled the rotor, attached to a freely rotating shaft into the water at a pre-determined, constant velocity. The main rotating shaft, housing the rotor, was linked to the slider via two self-aligning angular bearings. Detailed illustrations and comprehensive descriptions of all apparatus components can be found in Figure 3.20 to 3.22.

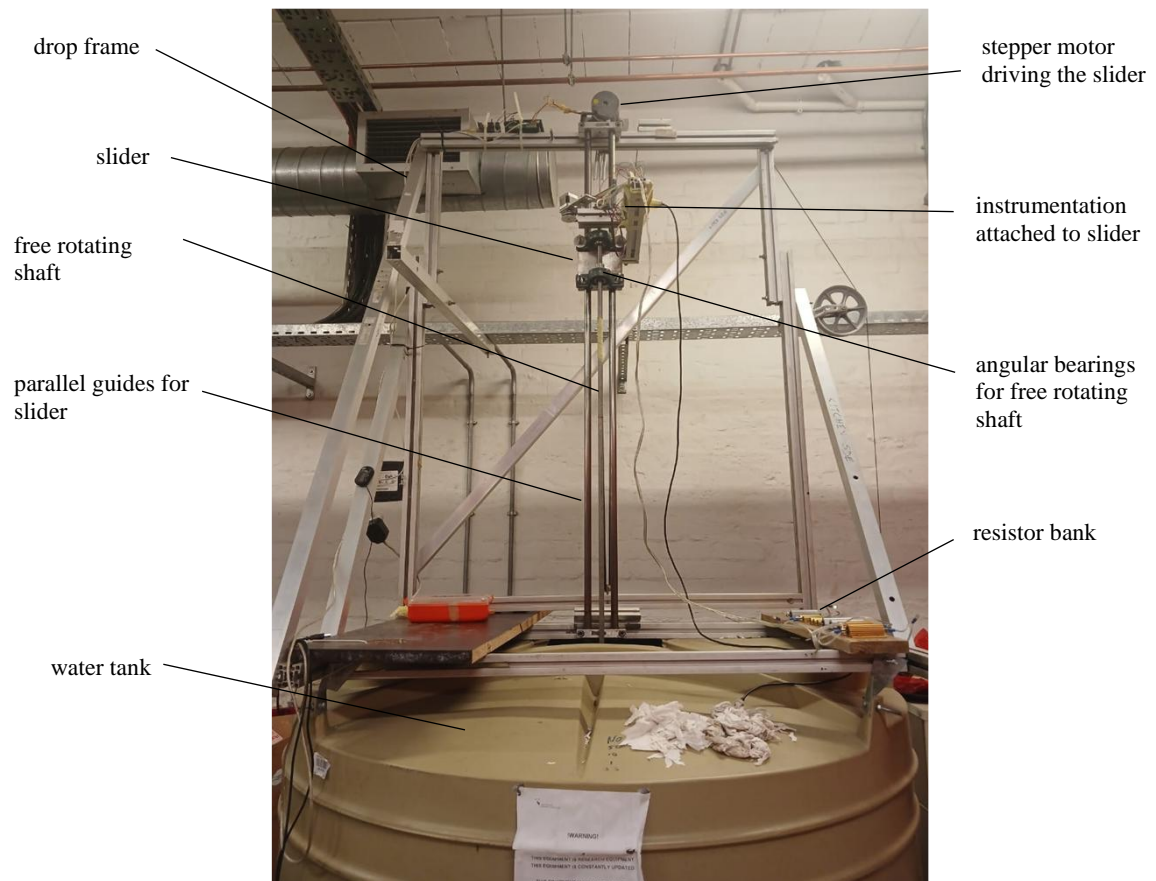


Figure 3.21: Water tank with drop frame

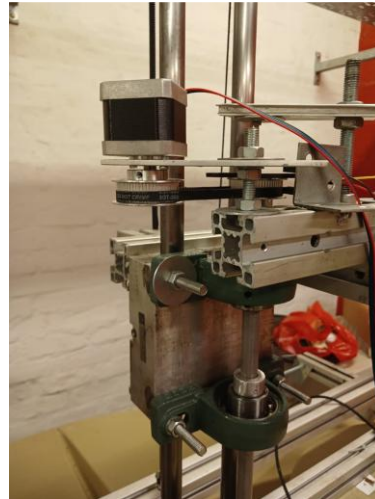
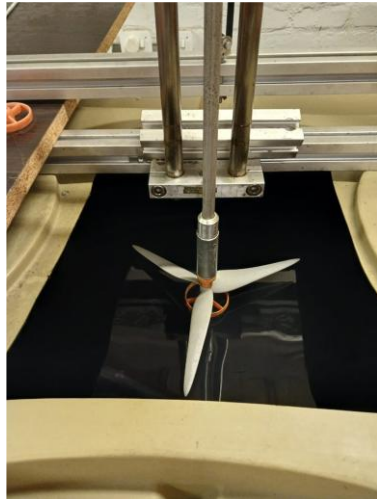


Figure 3.22: Free rotating shaft with rotor attached (left), Slider with free rotating shaft attached (right).

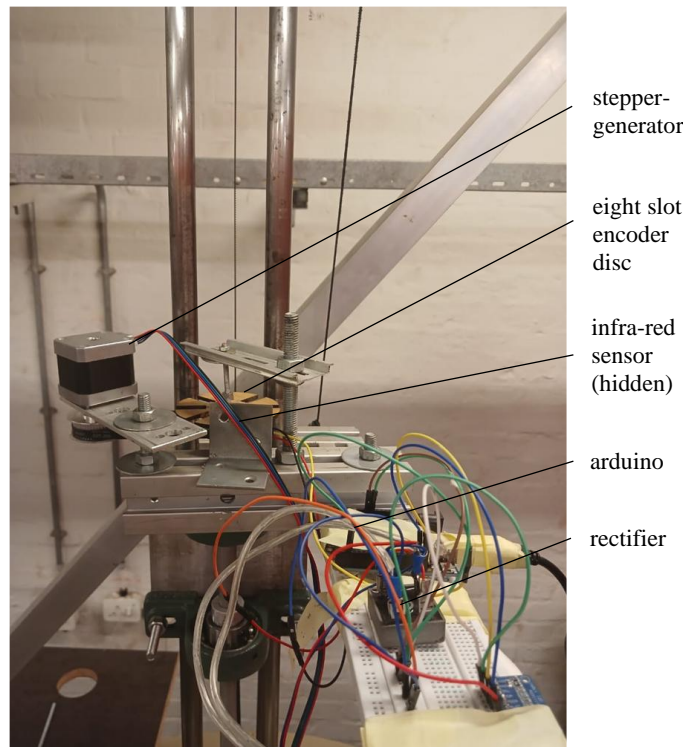


Figure 3.23: Slider with generator and instrumentation.

The slider of the apparatus is powered by a stepper motor controlled via an Arduino using the GRBL (G-code reference block library) computer numerical control (CNC) software. This stepper motor, a 3.8 Nm 1.8° unipolar type, drives the slider through a GT2 timing belt connected to a 60-toothed pulley mounted on the motor shaft.

A second stepper motor, originally a 0.28 Nm 1.8° unit, acted as a generator within the slider mechanism. It provided torque resistance and was driven by the main free rotating shaft via a GT2 9 mm belt. Both the shaft and the stepper-generator featured 60-toothed pulleys, maintaining a 1:1 rotation ratio. The AC output from the stepper-generator was converted to DC using a single-phase rectifier and then directed to a resistor bank with adjustable resistance. This configuration allowed the stepper-generator to operate effectively under variable loads and rotational speeds. During testing, loads were applied using power resistors with resistances of 50 Ω , 20 Ω , 10 Ω , 5 Ω , and 2 Ω .

An eight-slot encoder disc was mounted at the top of the primary shaft to monitor rotation speed using an infrared optical sensor, which interfaced with an Arduino controller board. Data transmission from the Arduino controller was achieved via serial communication with a laptop computer. Additionally, water temperature readings were obtained using a digital LCD thermometer and recorded before each test run.

Prior to testing, the stepper-generator underwent calibration to correlate rotation speed with DC voltage output across the various resistive loads used in testing. This calibration was performed on a workbench where the stepper-generator was driven by a DC motor via a GT2-toothed belt to maintain consistent rotation speed. Rotation speed was monitored using a handheld tachometer (Major Tech MT950), while voltage output was measured with a Brymen multi-meter (Brymen TBM811).

Specifications for both instruments are detailed in Appendix E. Figure 3.23 illustrates the calibration graph for the "stepper-generator" across all resistive loads used during testing.

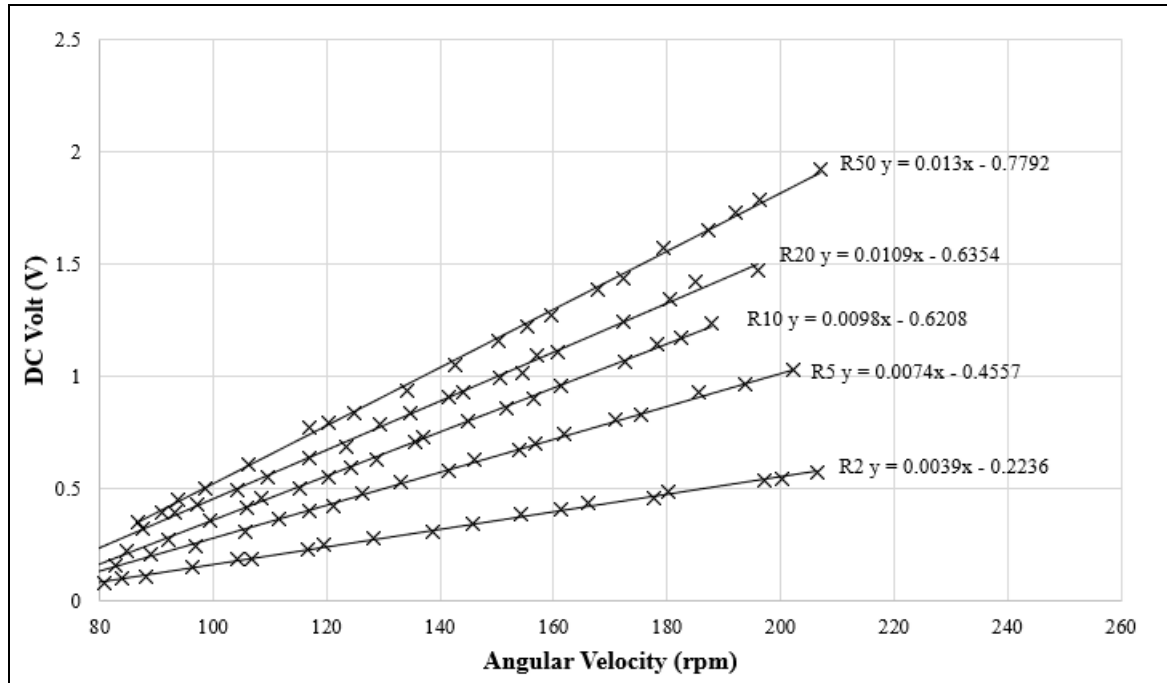


Figure 3.24: Generator calibration for all resistive loads with DC volt output versus angular velocity

A large-diameter water tank was utilized to minimize blockage effects during testing, resulting in a blockage ratio of 4%—the ratio between the frontal areas of the test area (tank) and the swept area of the rotor. Research by Chen and Liou (2011) demonstrated that blockage ratios below 10% in wind tunnel testing led to blockage errors of less than 5%. Previous studies by Fawkes (2023), using the same rotor as in this research, indicated that with a blockage ratio of 4%, the blockage error remained below 1%, which is considered acceptable for research purposes.

Additionally, careful consideration was given to the travel distance of the rotor within the water tank. It was crucial to ensure that the near wake fully developed during testing and that the rotor's stopping position was sufficiently elevated above the tank floor to avoid flow interference. Therefore, a travel distance of 1140 mm, equivalent to over four rotor diameters, was implemented, with the rotor stopping position set at 560 mm above the tank floor. These parameters for travel length and stopping position were selected to promote the complete development of the near wake provided by Bastankhah and Porté-Agel (2017) and prevent any unwanted flow disturbances originating from proximity to the tank floor discussed by Fawkes (2023).

To summarize, the vertical-travel test apparatus lowered the rotor at a constant velocity of 0.5 m/s across a distance of 1140 mm, exceeding four rotor diameters. An infrared optical sensor, connected to an Arduino controller board, monitored the rotor rotation. The "stepper-generator" was connected to different resistive loads to provide brake torque during the tests.

3.3.2 Testing Operation

Seven distinct rotors underwent testing: one standard rotor served as the baseline for comparison, and six rotors were retrofitted with ring vanes. Ring vane sizes varied from 15% to 20%, with increments of 1%, determined by the ratio of the rotor diameter to the diameter of the ring vane. All ring vanes shared identical aerofoil shapes and strut configurations, differing only in their diameter.

Each rotor underwent five test runs per resistive load, with rotation speed and elapsed time monitored via serial communication from the Arduino board. Resistive loads applied to each rotor to determine power output included 50 Ω , 20 Ω , 10 Ω , 5 Ω , and 2 Ω . The rotor under test was attached to the freely rotating shaft and connected to the chosen resistive load. It was lowered into the water at a constant velocity of 0.5 m/s using the GRBL software interface, covering a distance of 1140 mm. The Arduino communication was established prior to each test run, and water temperature data was logged during testing. Upon completion of each test run, raw data including *elapsed time*, *water temperature*, and *rotor rpm* was recorded. This procedure was repeated for each rotor across 5 test runs per resistive load, resulting in a total of 175 test runs for the entire set of rotors evaluated.

3.3.3 Data Handling

The raw test data comprised measurements of water temperature, rotor rotation speed, and elapsed time, all recorded under a relative fluid velocity of 0.5 m/s. The average rotor rotation speed in rpm was plotted against elapsed time for each of the five runs per resistive load to analyse the dataset. Subsequently, an exponential decay function (3.3) was applied to the data using Excel Solver for further analysis.

$$Y = Y_0 + Ae^{-kt} \quad (3.3)$$

Where Y is the rpm curve value at any time t , and Y_0 is the asymptote value. The amplitude of the curve is described by constant A , and the decay rate constant is k . Excel solver optimizes Y_0 , A and k by minimizing the sum of squared deviation, δ^2 values of the raw data. The asymptote of the exponential decay function provided the final rotation speed of the rotor.

Throughout the test runs, the rotor rotation speed accelerated to maximum and then gradually decelerated as the near wake formed. A notable indication that the near wake fully developed within the 4-diameter travel distance was observed in the exponential decay curves of the test runs, which closely approached the asymptote towards the end of the elapsed time. As an example, a decay function plot of the 17% ring vane rotor with a 5 Ω resistive load is shown in Figure 3.24.

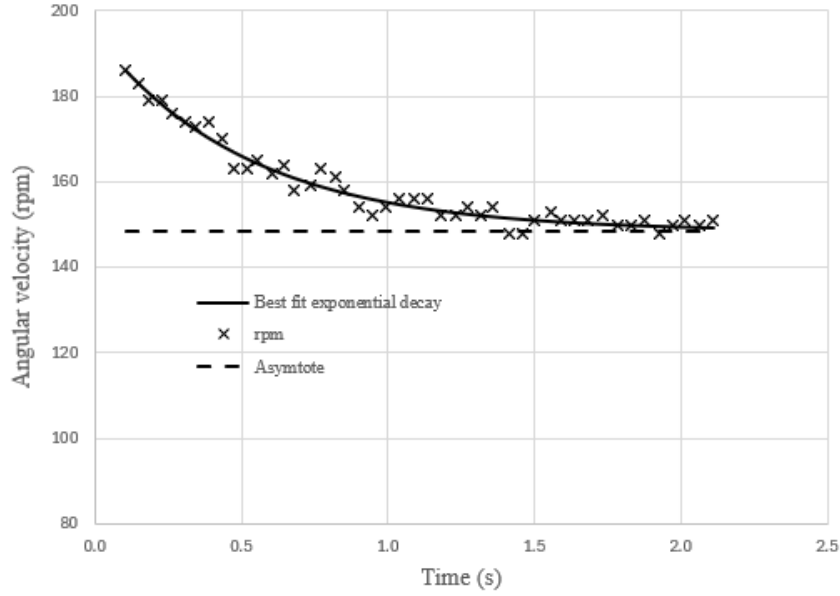


Figure 3.25: Exponential decay curve and asymptote for rotation speed of 17% ring vane rotor.

Decay curves for all rotors tested are provided in Appendix F and a summary of the statistics of the decay curves provided in Appendix G. The statistical summary includes the squared deviation, \mathcal{S}^2 and standard deviation, s , of experimental rpm data versus the rpm of the best fit decay curve.

Power was calculated using the final rotation speed obtained from the previously determined asymptote and the "stepper-generator" calibration curve to derive the corresponding DC voltage. The power calculation was performed using

$$P_r = \frac{v^2}{R} \quad (3.4)$$

where v represents the DC voltage and R denotes the resistive load.

Power versus rotation speed curves were generated for each rotor by determining the asymptotes of the rotation speed for each test run. The rotation speed was then used to ascertain the "stepper-generator" DC output voltage and calculated power. This procedure was repeated for each set of resistive loads, including 50 Ω , 20 Ω , 10 Ω , 5 Ω , and 2 Ω .

Temperature data from the test runs were recorded to assess its impact on water density, influencing the performance of the rotors. This approach ensured that the results were compared fairly, accounting for variations in power available from the water. Available power from the water is:

$$P_w = 0.5 \rho A_r v_i^3 \quad (3.5)$$

Where ρ is the water density influenced by water temperature, A_r is the rotor swept area and v_i is the relative water velocity. Temperature recorded during test runs had a range between 24°C and 25.7°C. The impact on density for the range of temperature had a 0.043% effect on power available from the

water. Therefore, no correction to power for the tests was deemed necessary and was thus excluded from consideration.

3.4 Case study methodology

A case study employing ANSYS CFD simulation was conducted for both the standard rotor and the best performing retrofitted rotor identified through prior testing and simulation. The objective of the case study was to determine whether the retrofitted rotor retained its performance advantage at a free stream velocity of 1 m/s, exceeding the design velocity of the rotor and surpassing the operational range of the vertical-travel test apparatus. The simulation methodology for the case study utilized identical settings, mesh sizes, and turbulence model as those employed in simulations at 0.5 m/s. Boundary layer mesh sizes were validated for the case study using the same approach as applied to the full set of rotors, determining the boundary layer height at the mid-span of the blade for $y^+=1$ and $y^+=5$ for the $k-\omega$ GEKO turbulence model. The expected Reynolds number at the blade's midspan was 5.2×10^4 , placing the flow regime within the turbulent state. Figure 3.25 shows that the first boundary layer falls between $y^+=1$ and $y^+=5$ for the rotors in the case study at free stream velocity of 1 m/s.

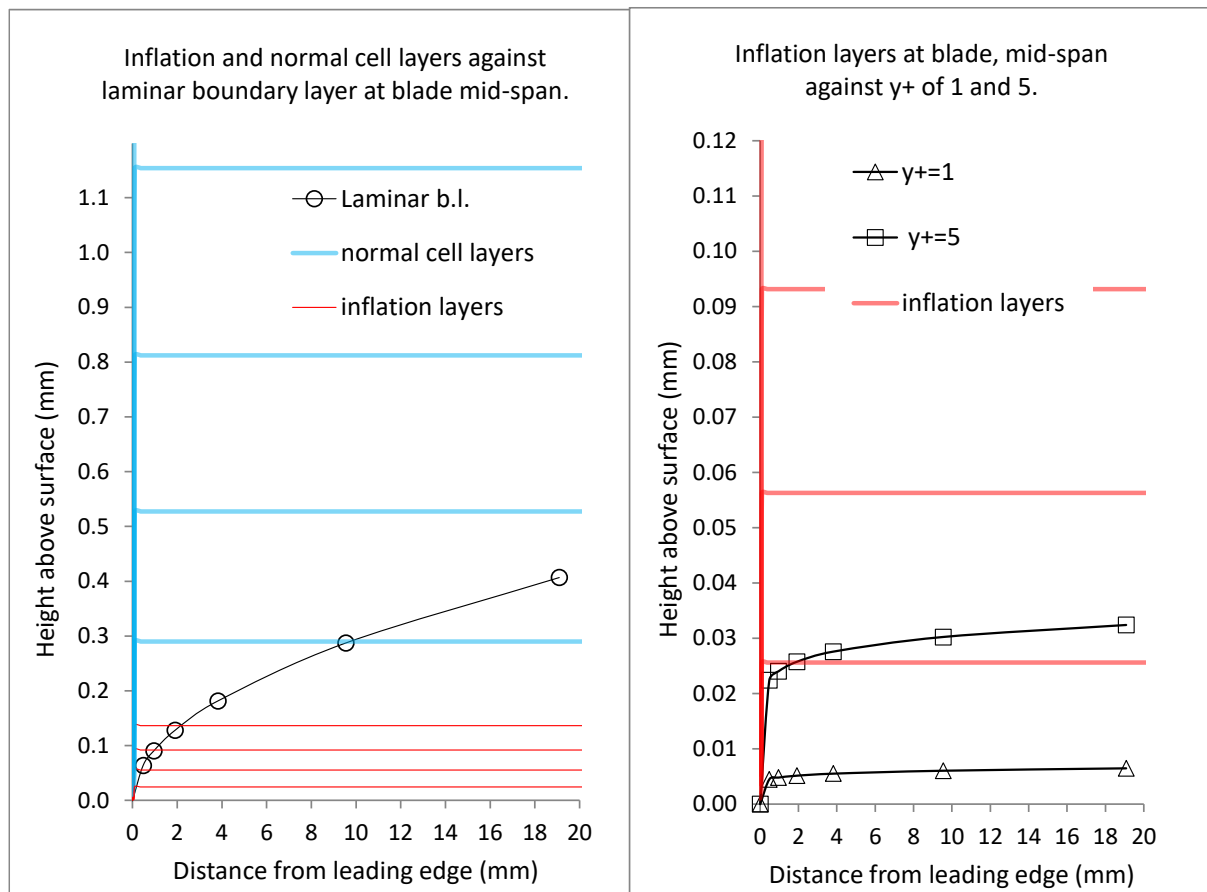


Figure 3.26: Rotor boundary layer and sub-layers with mesh height calculation for case study.

Power versus rotational speed curves for both the standard rotor and the best performing retrofitted rotor were generated by conducting simulations across a range of rotational speeds. The rotor net torque was utilized to calculate the power output for each rotational speed. Similar to the previous

simulation set in Section 3.2.3, each data point on the curves represented results obtained from individually solved simulations.

Flow visualisation, and axial and angular induction were obtained using ANSYS CFD post processing with the same methodology method as per the CFD simulations in Section 3.2.3. The flow visualisation and induction factors for the standard and best performing retrofitted rotor are presented at peak rotational speed of 350 rpm, and at off-peak rotational speeds of 300 rpm and 400 rpm.

3.5 Results accuracy

The CFD simulation results accuracy depended on the mesh independence studies that were done on all individual virtual models at free stream velocity of 0.5 m/s. Torque generated on the blade was used as the mesh independence study independent factor. The main mesh size settings were reduced until the percentage change of torque generated was in an acceptable range without compromising computing power. The mesh independence studies investigated a range of cell count from 250 000 to 3 200 000, and results showed percentage torque changes of below 0.7%. The final mesh settings for the virtual models at 0.5 m/s free stream velocity were also used for the simulations at free stream velocity of 1 m/s. Mesh independence curves with cell count versus torque can be found in Appendix D. Table 3.3 shows cell count, torque of hub and blade with percentage change of torque as mesh was refined. Convergence criteria for all simulations were met when scaled residuals of x , y , and z fluid velocities reached approximately 10^{-6} , and continuity approached 10^{-6} , ensuring output torque converged to an oscillating 5th significant digit.

Table 3.3: Percentage change of torque for mesh independence study for all rotors

Standard rotor at 180 rpm

Cell count	Torque hub (N.m)	Torque blade (N.m)	Torque total (N.m)	Percentage change in torque
106858	4.40E-06	0.028340	0.028344	-
254994	4.40E-06	0.028014	0.028018	-1.15%
403129	4.40E-06	0.028370	0.028374	1.27%
1062314	4.30E-06	0.028650	0.028654	0.99%
1419545	4.47E-06	0.028744	0.028748	0.33%

15% ring vane rotor at 180 rpm

Cell count	Torque hub (N.m)	Torque blade (N.m)	Torque total	Percentage change in torque
153694	0.00E+00	0.027805	0.027805	-
337701	3.80E-06	0.028145	0.028149	1.24%
520829	3.80E-06	0.028455	0.028459	1.10%
1402699	3.80E-06	0.028757	0.028761	1.06%
2058634	3.90E-06	0.028624	0.028628	-0.46%

16% ring vane rotor at 180 rpm

Cell count	Torque hub (N.m)	Torque blade (N.m)	Torque total	Percentage change in torque
183771	3.90E-06	0.028281	0.028285	-
463523	3.80E-06	0.027720	0.027724	-1.98%
732324	3.80E-06	0.028257	0.028261	1.94%
2124246	3.90E-06	0.028790	0.028794	1.89%
3156602	3.10E-06	0.028905	0.028908	0.40%

17% ring vane rotor at 180 rpm

Cell count	Torque hub (N.m)	Torque blade (N.m)	Torque total	Percentage change in torque
183771	3.80E-06	0.028281	0.028285	-
463523	3.80E-06	0.027900	0.027904	-1.35%
732324	3.80E-06	0.028196	0.028200	1.06%
2124246	3.90E-06	0.028627	0.028631	1.53%
3156602	3.90E-06	0.028645	0.028649	0.06%

18% ring vane rotor at 180 rpm

Cell count	Torque hub (N.m)	Torque blade (N.m)	Torque total	Percentage change in torque
142738	3.80E-06	0.028402	0.028406	-
352457	3.90E-06	0.028102	0.028106	-1.06%
544733	3.90E-06	0.028530	0.028534	1.52%
1428777	3.90E-06	0.029310	0.029314	2.73%
2120265	3.80E-06	0.029411	0.029415	0.35%

19% ring vane rotor at 180 rpm

Cell count	Torque hub (N.m)	Torque blade (N.m)	Torque total	Percentage change in torque
144921	3.80E-06	0.028370	0.028374	-
357021	3.80E-06	0.028001	0.028005	-1.30%
550817	3.80E-06	0.028420	0.028424	1.50%
1470353	3.80E-06	0.028760	0.028764	1.20%
2208979	3.80E-06	0.028877	0.028880	0.41%

20% ring vane rotor at 180 rpm

Cell count	Torque hub (N.m)	Torque blade (N.m)	Torque total	Percentage change in torque
147060	3.90E-06	0.028470	0.028474	-
361627	3.80E-06	0.028160	0.028164	-1.09%
550616	3.80E-06	0.028540	0.028544	1.35%
1488141	3.90E-06	0.028900	0.028904	1.26%
2225662	3.80E-06	0.029094	0.029098	0.67%

Rotor rotational speed measured with an eight-slot encoder disc during physical testing generated a cyclical error. This error was mitigated by applying an exponential decay function to the raw rotational speed data to determine the asymptote towards which rotational speed decreased when the near wake formed. The best fit exponential decay curves for each test run are shown in Appendix F, with the standard deviation of the raw rotational speed data for each run for the different resistive loads provided in Table 3.4.

Table 3.4: Standard deviation for all rotor RPM measured during physical testing

Std rotor		
Resistive load	Total deviation = $\Sigma(\delta^2)$	Standard Deviation (s)
R50	451.81	2.92
R20	419.65	2.90
R10	333.98	2.67
R5	230.16	2.29
R2	249.60	2.38

15% ring vane rotor		
Resistive load	Total deviation = $\Sigma(\delta^2)$	Standard Deviation (s)
R50	416.72	2.80
R20	345.85	2.60
R10	304.26	2.52
R5	206.65	2.14
R2	165.99	1.94

16% ring vane rotor		
Resistive load	Total deviation = $\Sigma(\delta^2)$	Standard Deviation (s)
R50	272.29	2.31
R20	523.02	3.27
R10	181.24	1.92
R5	177.26	2.03
R2	250.76	2.41

17% ring vane rotor		
Resistive load	Total deviation = $\Sigma(\delta^2)$	Standard Deviation (s)
R50	341.17	2.54
R20	615.70	3.47
R10	351.47	2.73
R5	168.16	1.91
R2	184.97	2.05

18% ring vane rotor

Resistive load	Total deviation = $\Sigma(\delta^2)$	Standard Deviation (s)
R50	307.08	2.48
R20	320.98	2.73
R10	164.85	1.87
R5	142.11	1.80
R2	165.85	1.96

19% ring vane rotor

Resistive load	Total deviation = $\Sigma(\delta^2)$	Standard Deviation (s)
R50	333.66	2.51
R20	316.46	2.52
R10	151.51	1.81
R5	161.72	1.87
R2	329.83	2.87

20% ring vane rotor

Resistive load	Total deviation = $\Sigma(\delta^2)$	Standard Deviation (s)
R50	247.46	2.16
R20	450.26	3.06
R10	278.31	2.43
R5	213.02	2.15
R2	228.19	2.28

The 0.28 Nm, 1.8° stepper motor used as a generator, was calibrated for each resistive load used prior to testing. Resistive loads were checked with a multi-meter (Brymen TBM811) during calibration. Calibration curves of fixed rotational speed versus DC voltage output (Figure 3.23 in Section 3.3.1) were used to determine power generated correlated to the final rotational speed for each test run, as determined from exponential decay function asymptotes. Resistive loads used for testing had an electric resistive range of 0.027% based on resistor specification of 100ppm/°C for ambient temperature range of 26°C to 28.7°C. Water temperature recorded during test runs had a range between 24°C and 25.7°C. The impact on density for the range of temperature had a 0.043% effect on power available from the water.

CHAPTER FOUR

DISCUSSION OF RESULTS

This chapter presents three sets of results. The first set is CFD simulation results for all rotors at a relative free stream velocity of 0.5 m/s. This set includes power coefficient (C_p) versus tip speed ratio curves with flow visualisation of the axial, radial and tangential velocities at a plane 2 mm in front of the rotor plane. It also includes axial and angular induction factors. Flow visualisation and induction factors were presented at peak and at off-peak rotational speeds.

The second set of results were the physical test results, obtained from the vertical-travel test apparatus, for all rotors at relative free stream velocity of 0.5 m/s. Results were presented as power coefficient (C_p) versus tip speed ratio curves for all rotors.

The CFD simulation case study provided the third set of results. These results were for the standard and 18% ring vane rotor (best performing retrofitted rotor) only. Results were presented in the same way as the first set of CFD results, with power coefficient (C_p) versus tip speed ratio curves, flow visualisation, and induction factors.

4.1 CFD simulation for all rotors

The first set of results is the CFD simulation of the standard rotor and the six rotors, retrofitted with ring vanes in a range from 15% to 20% with 1% interval of the rotor diameter, at free stream velocity of 0.5 m/s. Simulation results of power coefficient versus tip speed ratio consistently showed improved performance for the retrofitted rotors compared to the standard rotor. Figure 4.1 shows results for all rotors at a free stream velocity of 0.5 m/s. The power coefficient curves show that the 18% ring vane rotor exhibited the best performance, achieving the highest peak power and maintaining superior performance across nearly the entire range of tip speed ratios.

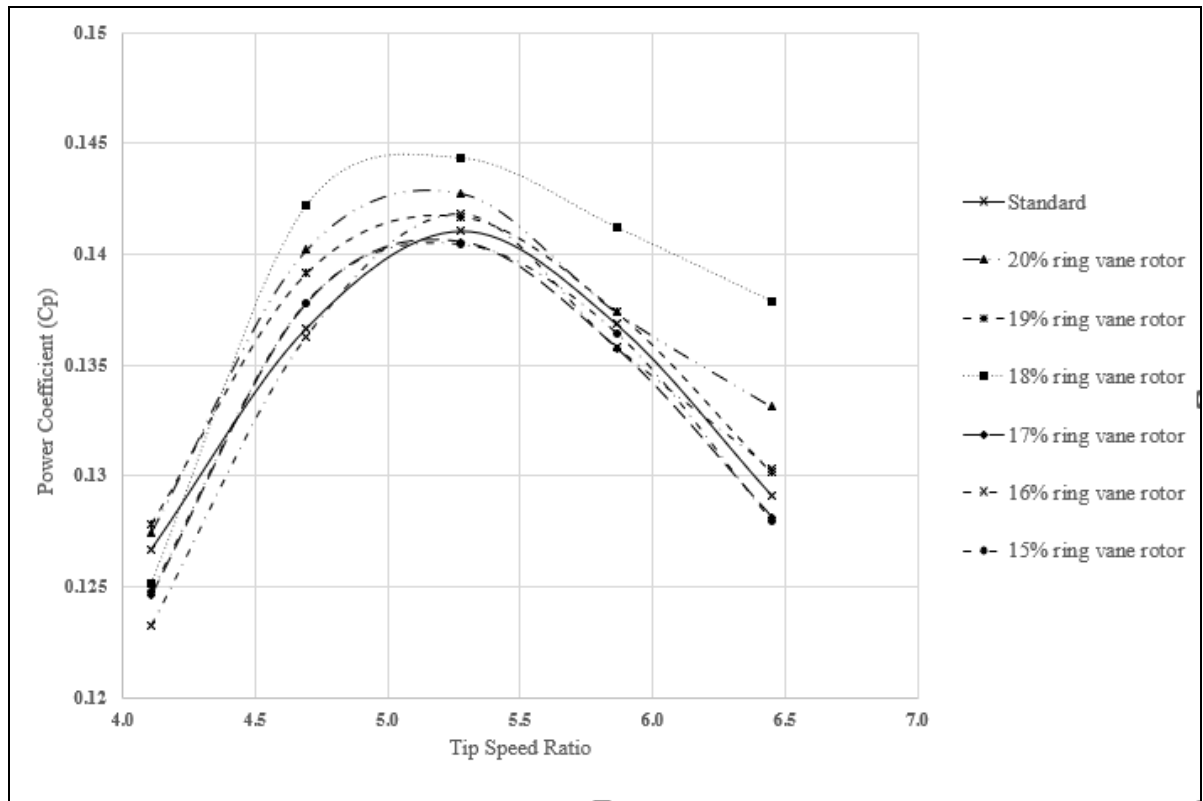


Figure 4.1: Simulation results for all rotors at 0.5 m/s free stream velocity

Figure 4.2 shows the comparison between the standard rotor and the rotor retrofitted with an 18% ring vane only for better clarification. Here it can be seen that the standard rotor only performs better at very low tip speed ratios. The peak performance improvement for the 18% ring vane rotor is 2.3% at tip speed ratio 5.3, with enhancements in operational performance observed across tip speed ratios starting from 4.2. The 18% ring vane rotor outperformed the standard with 4.04% and 3.2% at off design tip speed ratios of 4.7 and 5.9 respectively.

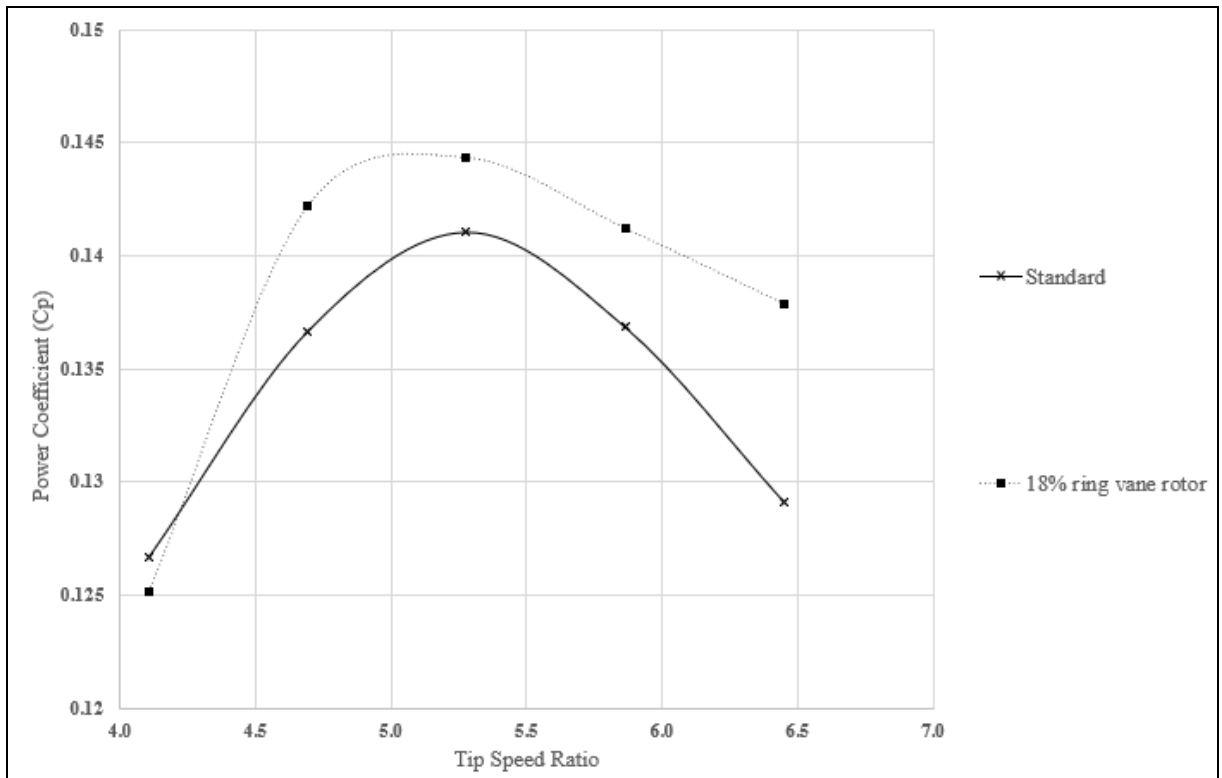


Figure 4.2: Simulation results for standard and 18% ring vane rotors at 0.5 m/s free stream velocity

Comparison of flow contours for axial, tangential, and radial velocities at a plane located 2 mm in front of the rotor during peak performance, of the standard rotor and the 18% ring vane rotor, is shown in Figure 4.3 to 4.6. In the axial velocity contours observed in Figure 4.3, minimal variation is noticeable along the blade beyond the ring vane region for both the standard rotor and the 18% ring vane rotor.

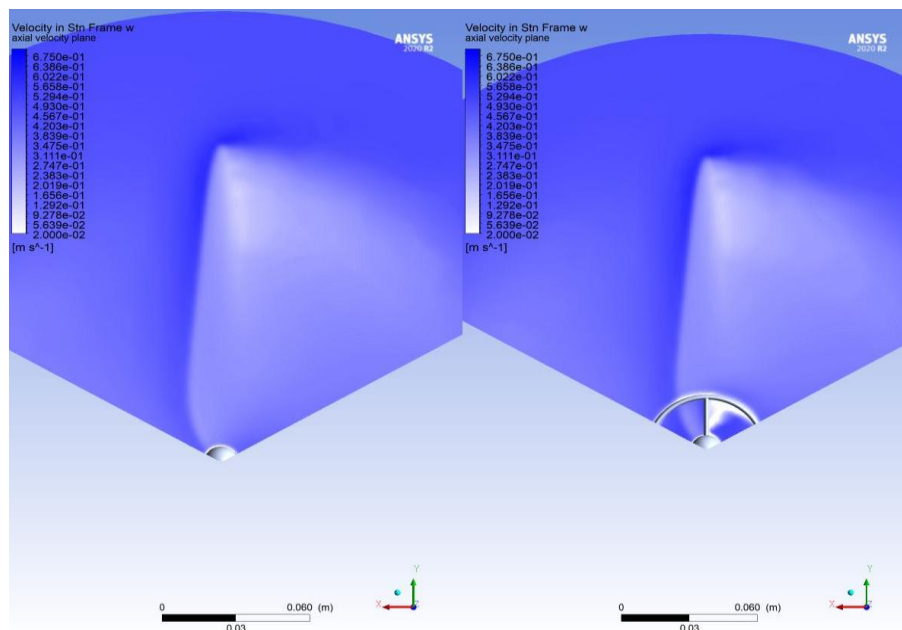


Figure 4.3: Axial velocity contours on standard rotor (left) and 18% ring vane rotor (right) at 5.3 TSR for 0.5 m/s free stream velocity at plane 2mm in front of rotor

A closer view in Figure 4.4 at the hub region of the rotor shows how the presence of the ring vane alters the flow dynamics near the rotor hub. There is higher axial velocity within the ring vane area (shown as darker blue zone) and in the circle area.

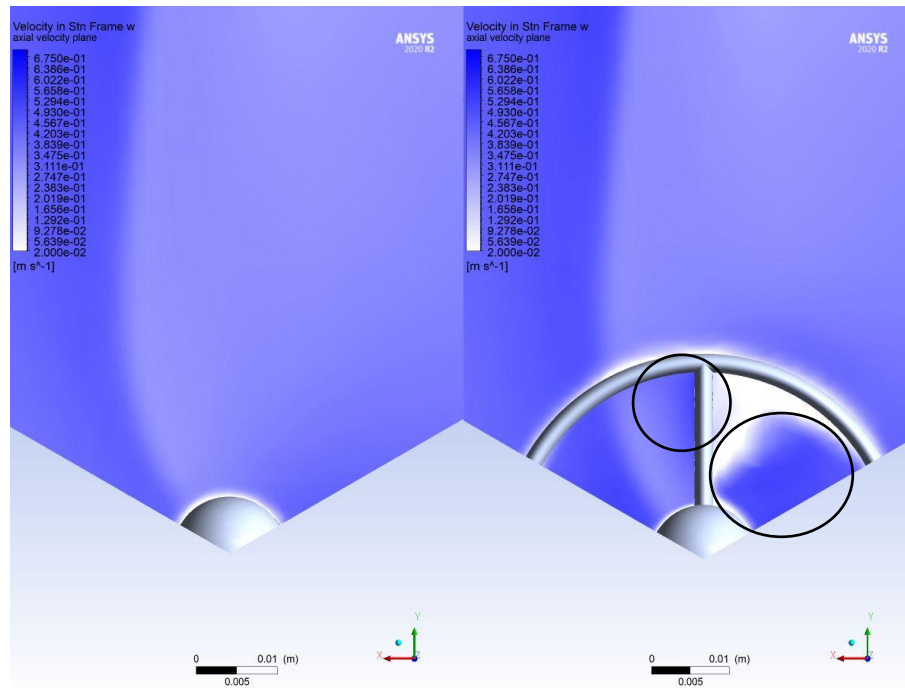


Figure 4.4: Close up view of axial velocity contours on standard rotor (left) and 18% ring vane rotor (right) at 5.3 TSR for 0.5 m/s free stream velocity at plane 2mm in front of rotor

Close up views of the tangential and radial velocity contours for the standard and 18% ring vane rotor show a concentration of flow (indicating blockage of flow) within the ring vane in Figure 4.5 and Figure 4.6 as indicated by the circles.

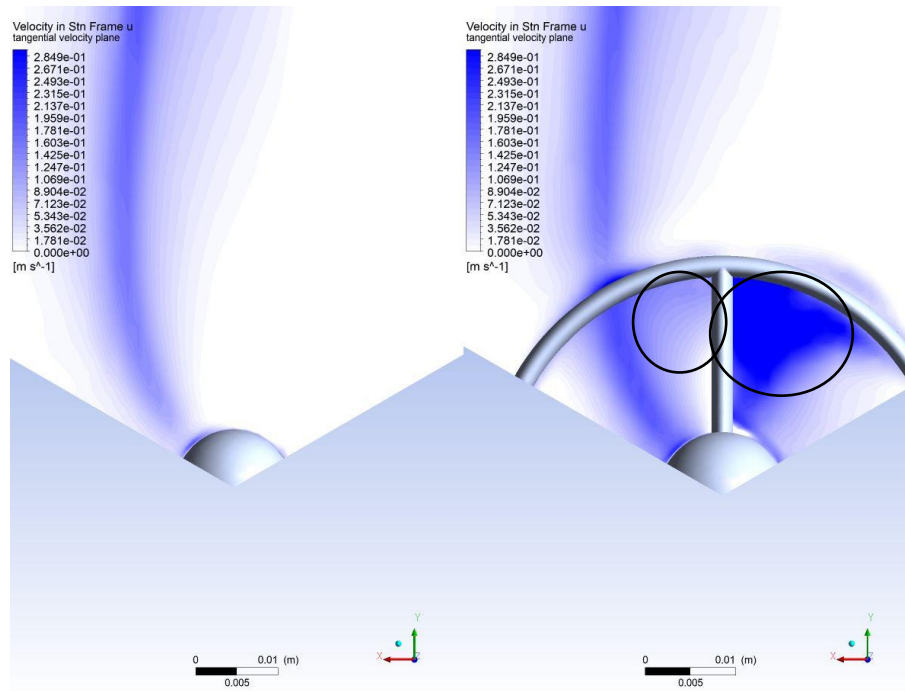


Figure 4.5: Close up view of tangential velocity contours on standard rotor (left) and 18% ring vane rotor (right) at 5.3 TSR for 0.5 m/s free stream velocity at plane 2mm in front of rotor

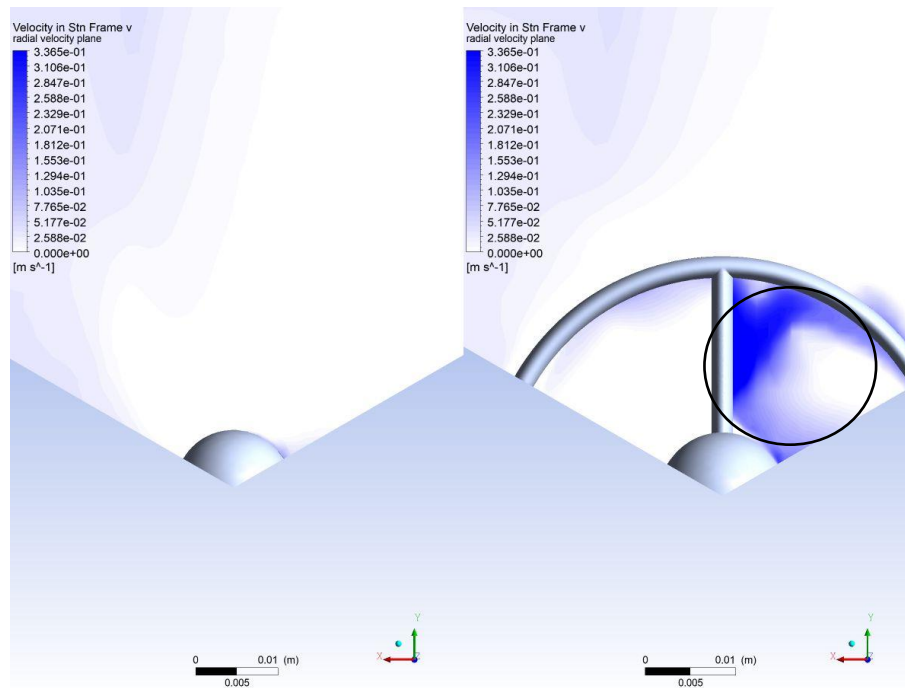


Figure 4.6: Close up view of radial velocity contours on standard rotor (left) and 18% ring vane rotor (right) at 5.3 TSR for 0.5 m/s free stream velocity at plane 2mm in front of rotor

Close up views in Figure 4.4 to 4.6 revealed that the ring vane partially prevented the conversion of initial axial velocity into radial and tangential components. This partial prevention ensured that more axial velocity was retained and available for interaction with the rotor blades. Axial, radial, and tangential velocity contours, for the standard and 18% ring vane rotors at off-peak tip speed ratios of 4.7 and 5.9 at 0.5 m/s free stream velocity, are provided in Appendix H.

The axial and angular induction factors along the blade are presented in Figure 4.8 and Figure 4.10 for both the standard and 18% ring vane rotors. The axial induction factor was calculated at a plane 2 mm in front of the rotor plane. The axial induction factor for the 18% ring vane rotor was lower than the standard rotor along the blade with a spike starting at the inside of the ring vane diameter, and which peaked at the outside of the ring vane diameter. This was caused by the wake that the ring vane generated and indicated poor aerodynamics for the blade at that section as can be seen in Figure 4.7. A lower axial induction factor indicates more axial velocity available to the blade. The lower axial induction within and outside of the ring vane, up to the mid-span of the blade, indicated that the ring vane improved the aerodynamics for those areas of the blade, by delaying the axial velocity conversion to tangential and radial velocities. Figure 4.9 presents the axial velocity profile of both the standard rotor and the 18% ring vane rotor. The profile indicates that at the point where the axial induction spikes, the axial velocity of the 18% ring vane rotor is lower than that of the standard rotor. However, beyond the ring vane's diameter, the axial velocity of the 18% ring vane rotor is slightly higher than the standard rotor, contributing to its improved performance.

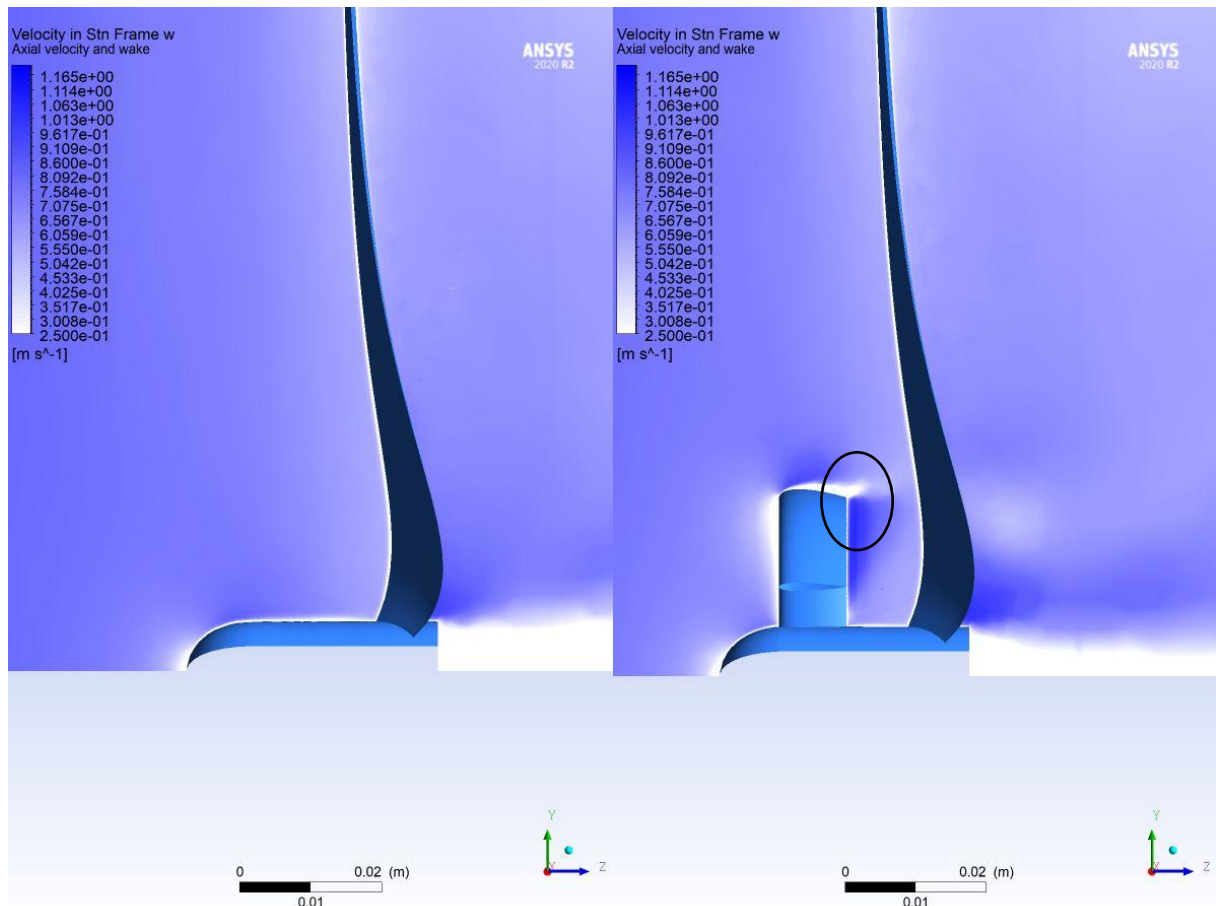


Figure 4.7: Closeup view of axial velocity and near wake for standard (left) and 18% ring vane rotor (right) at 5.3 TSR for 0.5 m/s free stream velocity on cross section plane

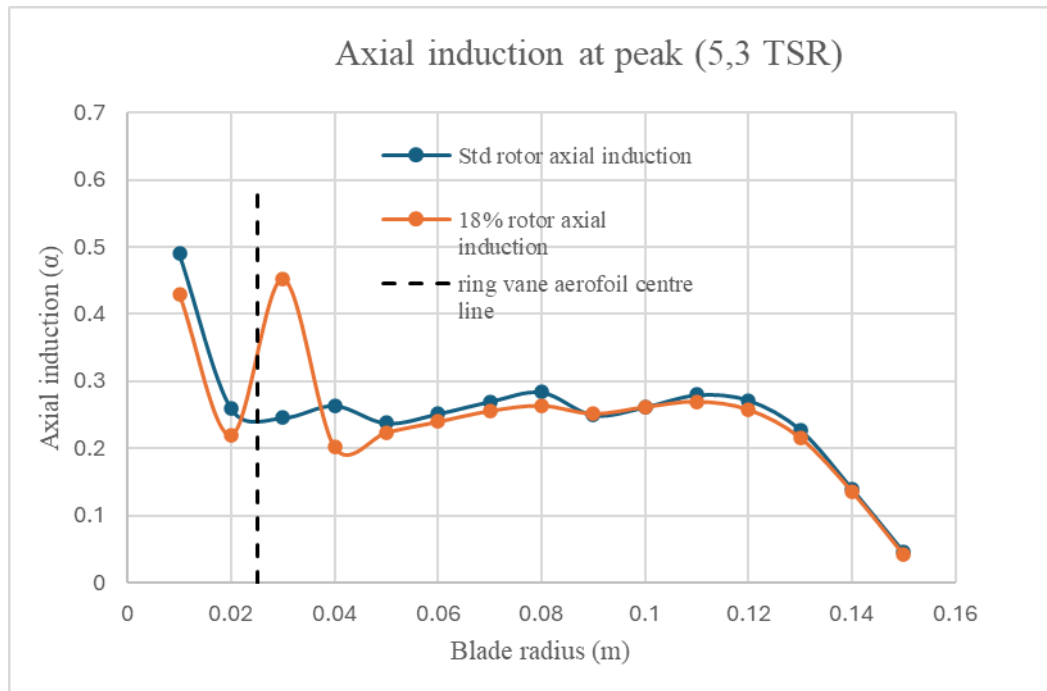


Figure 4.8: Axial induction factor for standard and 18% ring vane rotor at 180 rpm for 0.5 m/s free stream velocity

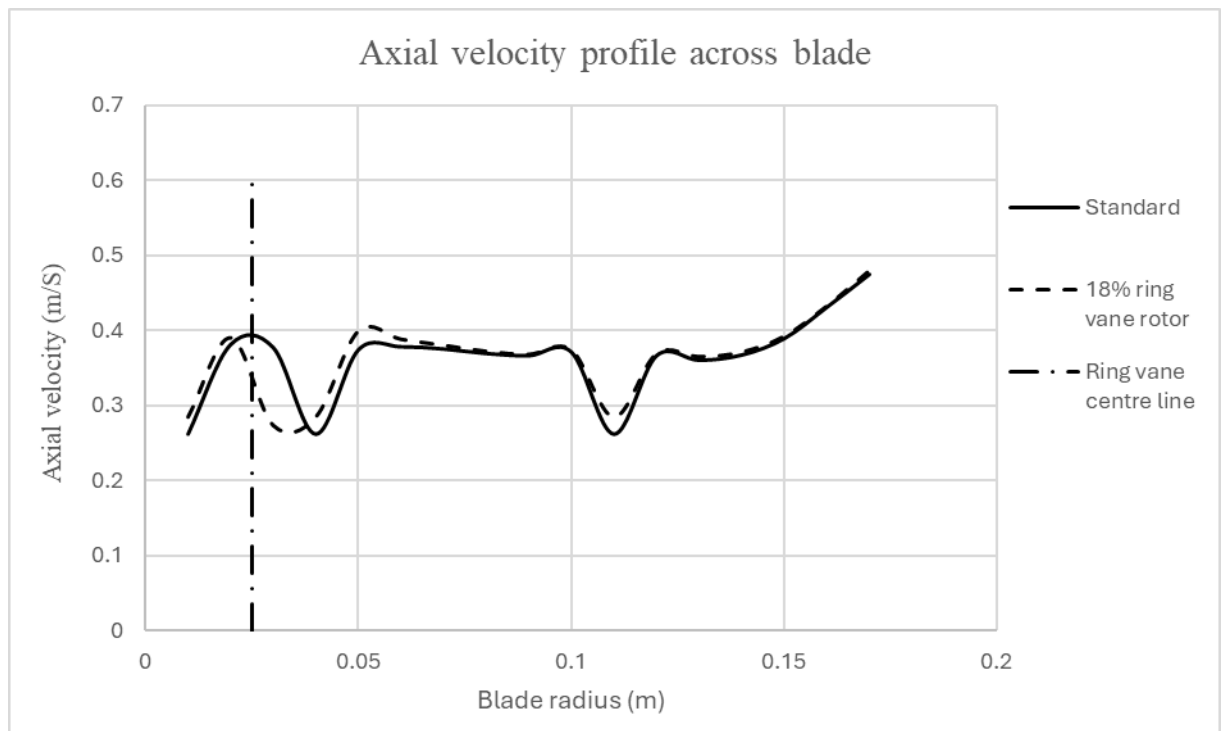


Figure 4.9: Axial velocity profile for standard and 18% ring vane rotor at 5.3 TSR for 0.5 m/s free stream velocity at plane 2mm in front of rotor

In Figure 4.10 the 18% ring vane rotor produced a lower angular induction from the blade root up to the outside of the ring vane. The angular induction factor was calculated at a plane 20 mm behind the rotor plane within the near wake of the rotor. The lower angular induction within the area of the ring vane, indicates that rotor rotation speed increased relative to near wake rotation speed. The lower angular induction was possibly caused by the presence of ring vane struts and the increased axial

velocity within the ring vane area as there was no change in angular induction further along the blade. In Figure 4.11 it can be seen that there is higher axial velocity present in the near wake.

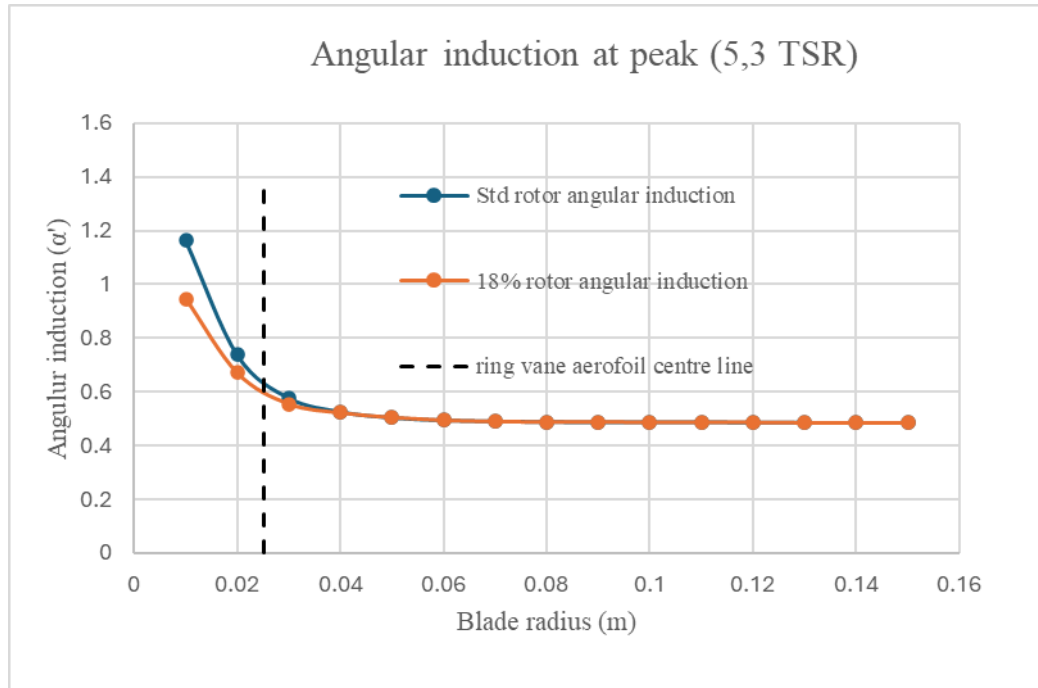


Figure 4.10: Angular induction factor for standard and 18% ring vane rotor at 5.3 TSR for 0.5 m/s free stream velocity

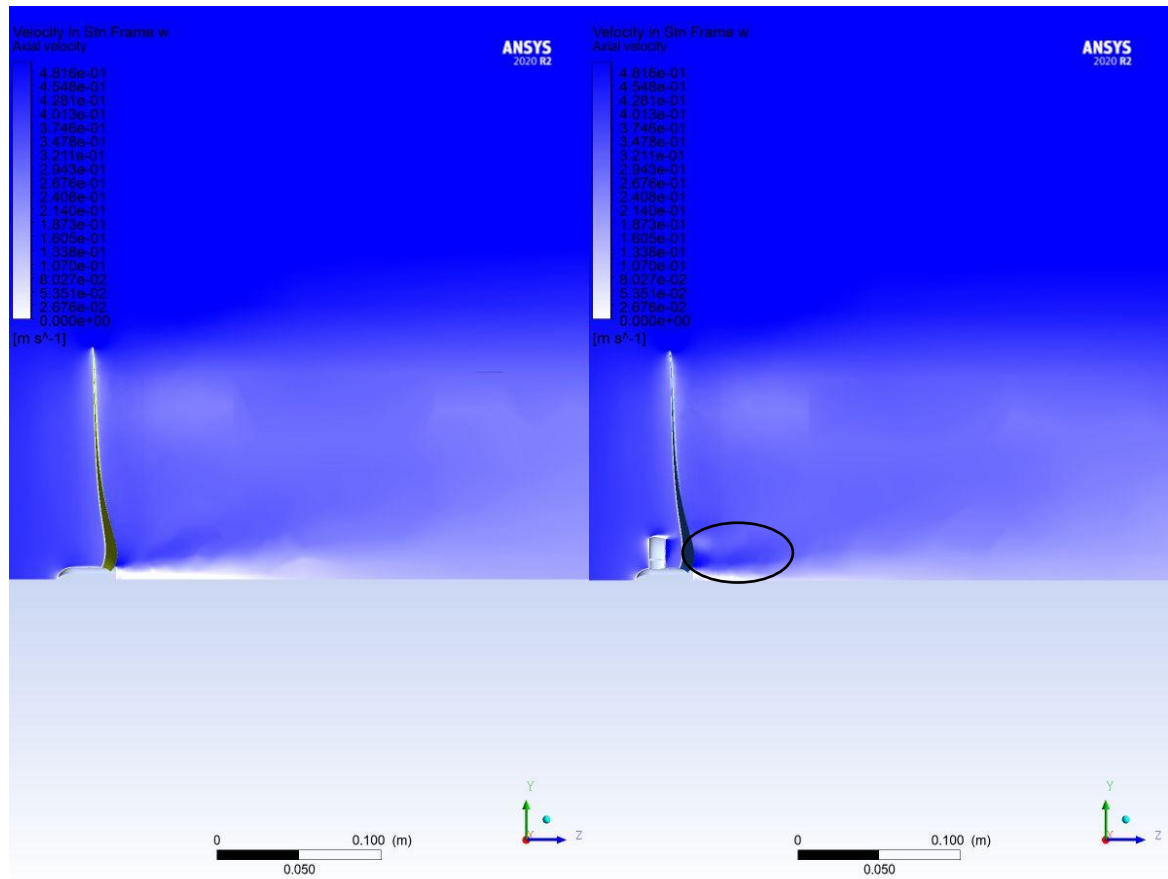


Figure 4.11: Axial velocity and wake for standard (left) and 18% ring vane rotor (right) at 5.3 TSR for 0.5 m/s free stream velocity on cross section plane

Graphs of rotor axial and angular induction at off-peak performance, for tip speed ratios of 4.7 and 5.9 is provided in Appendix I.

4.2 Physical test results for all rotors

Physical testing of all rotors with the vertical-travel test apparatus was conducted at a constant free stream velocity of 0.5 m/s. Power coefficient versus tip speed ratio for all rotors is shown in Figure 4.12. Physical testing results showed that all rotors retrofitted with a ring vane outperformed the standard rotor peak performance. In all cases the standard rotor outperformed the retrofitted rotors at very low and very high tip speed ratios. The 18% ring vane rotor emerged as the best performing option, showing significant improvements across the operational range of rotational speeds, although with a peak performance slightly lower than that of the 20% ring vane rotor.

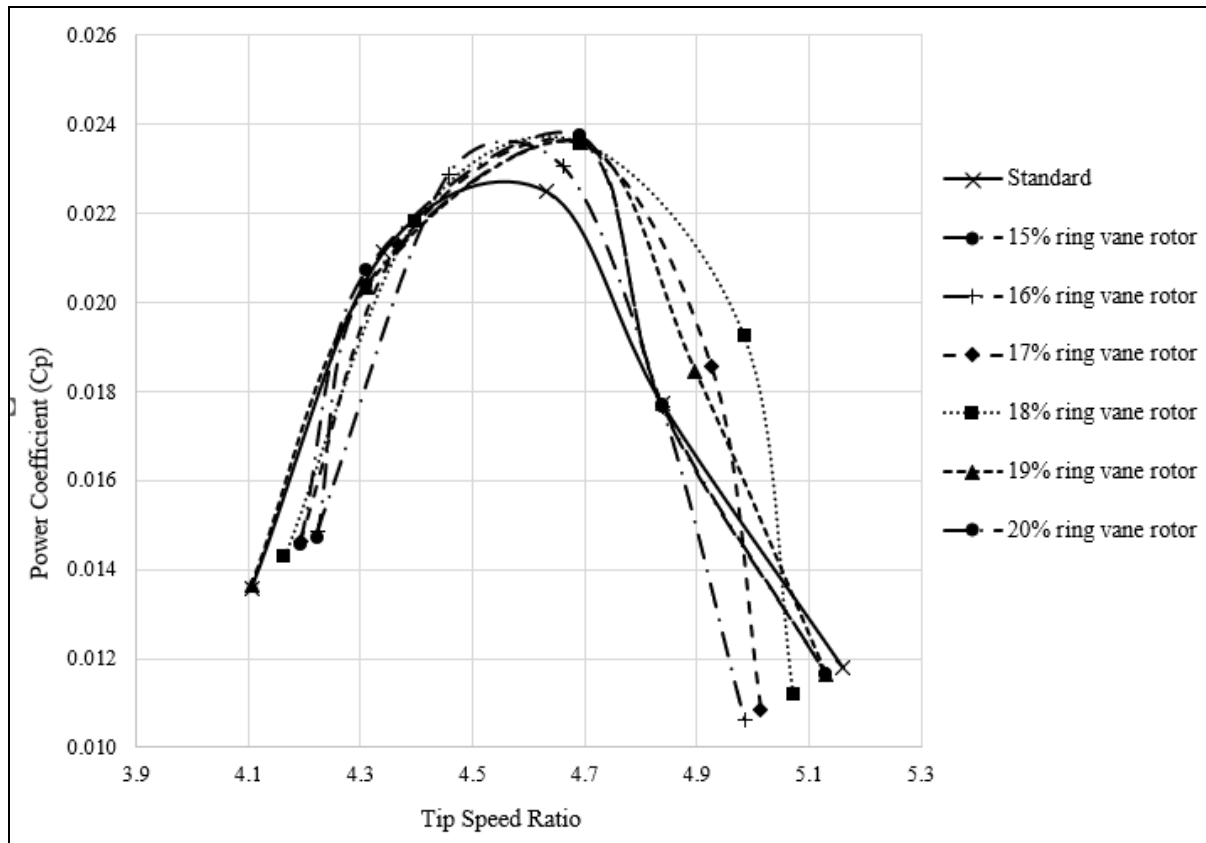


Figure 4.12: Power versus rotational speed for all rotors at 0.5 m/s free stream velocity (physical testing)

For clarity Figure 4.13 presents the comparison between the standard rotor and the 18% ring vane rotor only. The 18% ring vane rotor outperformed the standard rotor by 4.35% at peak performance, at tip speed ratio of 4.55 for the standard rotor and at 4.6 for the 18% ring vane rotor. The 18% ring vane rotor outperformed the standard with 0.24% and 25% at off design tip speed ratios of 4.4 and 5 respectively. Performance increase was observable across the operational range from 4.4 to 5 tip speed ratios.

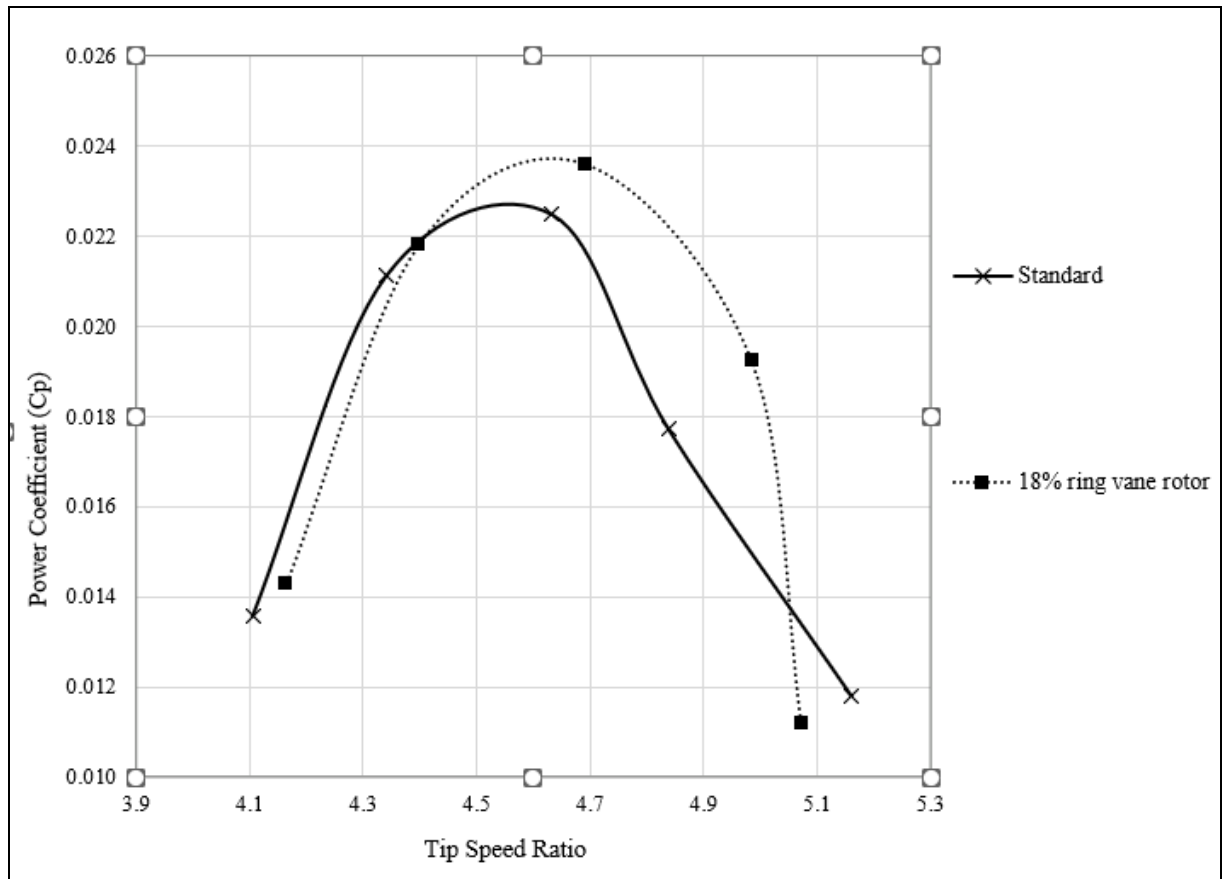


Figure 4.13: Power versus rotational speed for standard and 18% ring vane rotor at 0.5 m/s free stream velocity (physical testing)

At higher rotational speed the retrofitted rotor had a steeper curve drop off compared to the standard rotor. This was possible due to the increased near wake hub region losses. The point of increased near wake losses causing the curve drop off were possible caused by the various guide rings sizes relative to rotor diameter. At lower rotational speed the standard rotor had less radial flow along the blade and the guide rings added no benefit to the blade design possible due to the losses associated with the guide rings.

4.3 CFD case study simulation

In the simulated case study results, the comparison was made between the standard rotor and the 18% ring vane rotor (identified as the best performer) at off design higher free stream velocity of 1 m/s - which exceeded the capability of the vertical-travel test apparatus.

Figure 4.14 illustrates the power coefficient versus tip speed ratio curves for both rotors at this increased free stream velocity. The 18% ring vane rotor showed increased performance compared to the standard rotor, achieving a 0.8% improvement at peak performance, and with enhanced performance across the entire operational range. The 18% ring vane rotor outperformed the standard with 1.34% and 1.74% at off design tip speed ratios of 4.4 and 6 respectively.

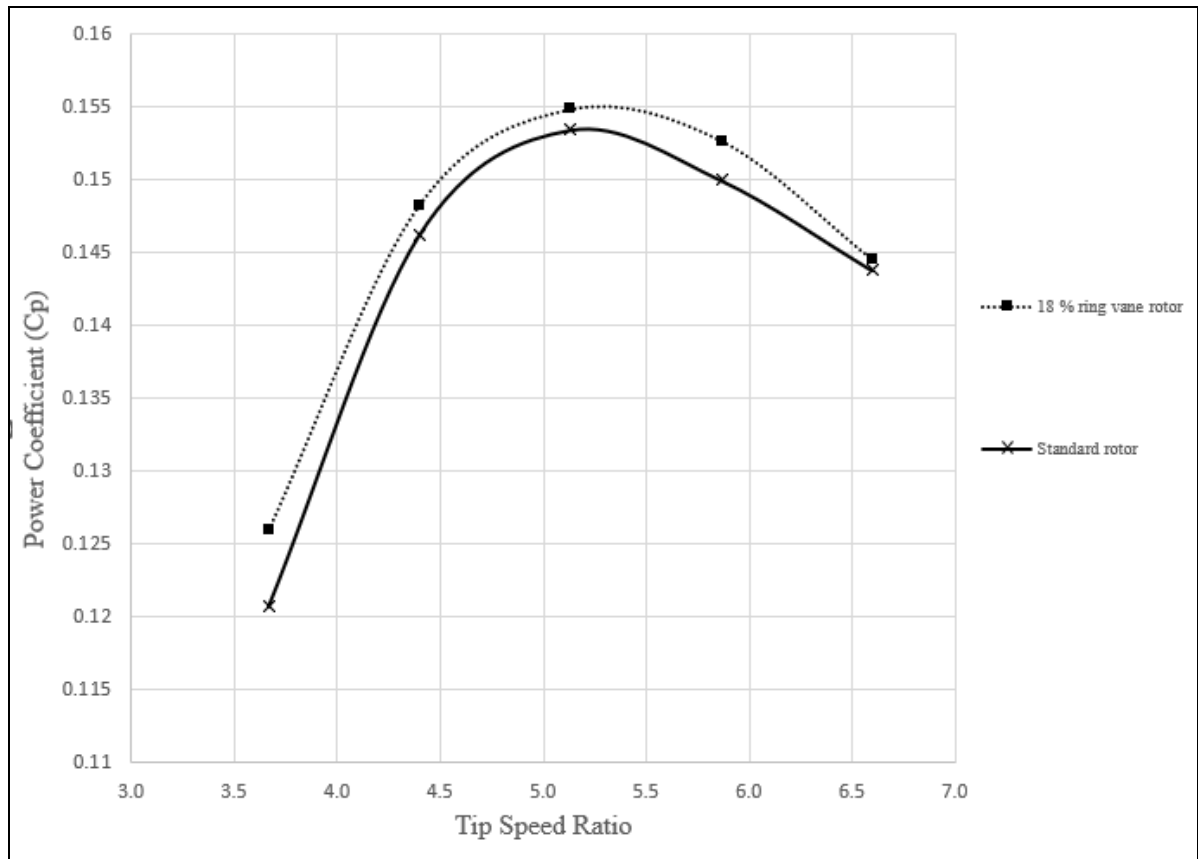


Figure 4.14: Power versus rotational speed for standard and 18% ring vane rotor at 1 m/s free stream velocity

Flow visualisation of the axial, tangential and radial velocities, on a plane 2 mm in front of the rotor, revealed similarities to the previous simulations. A higher axial velocity was visible (shown as darker blue zone) within the ring vane area as shown in Figure 4.15.

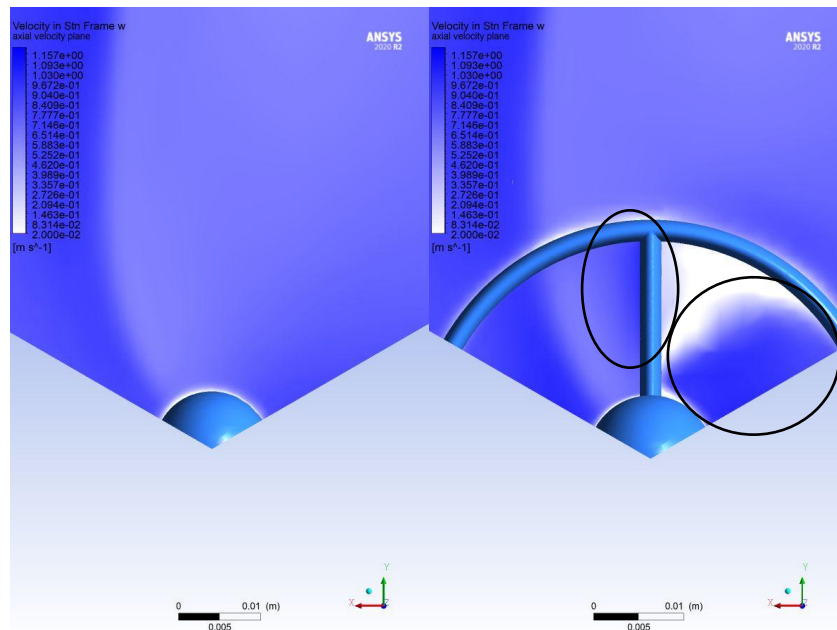


Figure 4.15: Close up view of axial velocity contours on standard rotor (left) and 18% ring vane rotor (right) at 5.1 TSR for 1 m/s free stream velocity at plane 2mm in front of rotor

Tangential velocity in Figure 4.16 and radial velocity in Figure 4.17 shows the concentration of flow within the ring vane area. This was again an indication that axial velocity conversion to tangential and radial flow was delayed by the presence of the ring vane.

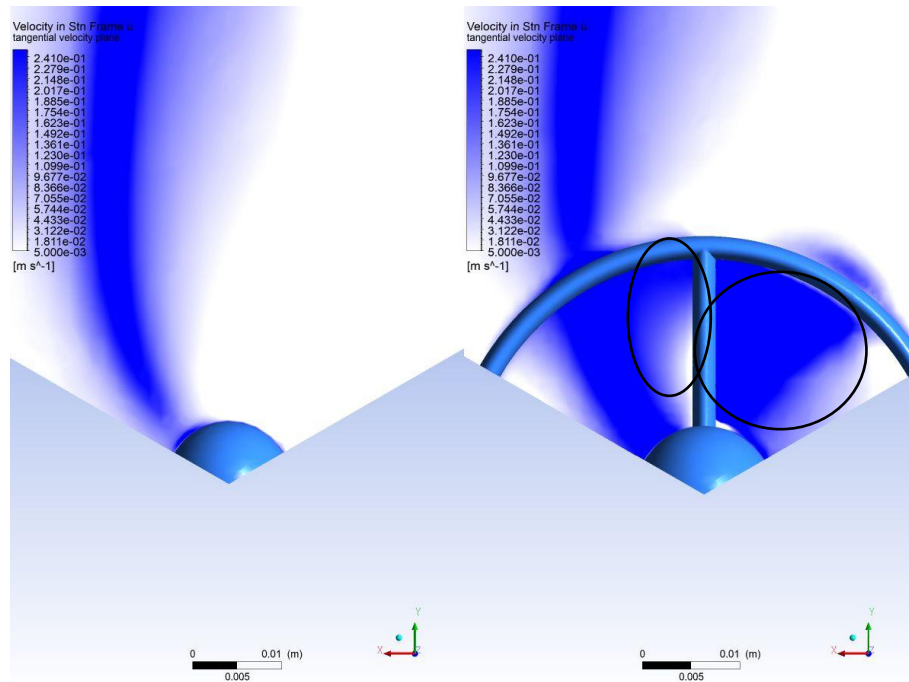


Figure 4.16: Close up view of tangential velocity contours on standard rotor (left) and 18% ring vane rotor (right) at 5.1 TSR for 1 m/s free stream velocity at plane 2mm in front of rotor

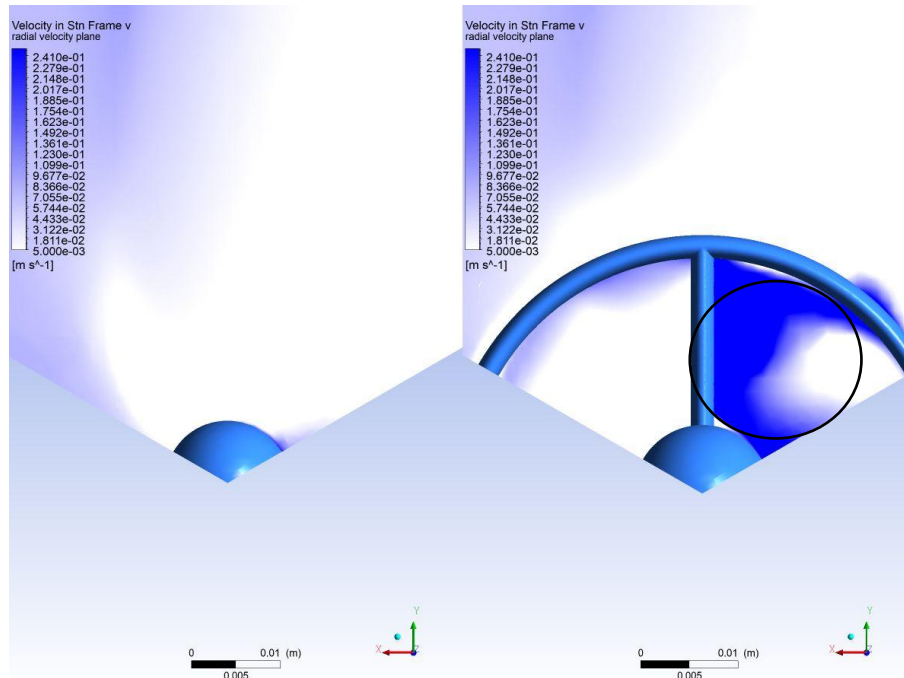


Figure 4.17: Close up view of radial velocity contours on standard rotor (left) and 18% ring vane rotor (right) at 5.1 TSR for 1 m/s free stream velocity at plane 2mm in front of rotor

Appendix J contains the axial, radial, and tangential velocity contours for both the standard rotor and the 18% ring vane rotor at off-peak tip speed ratios of 4.4 and 6, at a free stream velocity of 1 m/s.

The axial induction, calculated at a plane 2 mm in front of the rotor plane for the 18% ring vane rotor, followed a similar pattern (spike) as the same rotor at 0.5 m/s free stream velocity, as seen in Figure 4.19. The difference between the axial induction factors of the standard and 18% ring vane rotors at 1 m/s were greater than the difference at 0.5 m/s. This meant that at higher free stream velocity, the axial induction factor was reduced by a larger amount when a ring vane was present. The lower induction factor value in Figure 4.19 indicates a higher axial velocity availability in the rotor plane. Figure 4.20 presents the axial velocity profile of both the standard rotor and the 18% ring vane rotor. The profile indicates that at the point where the axial induction spikes, the axial velocity of the 18% ring vane rotor is lower than that of the standard rotor.

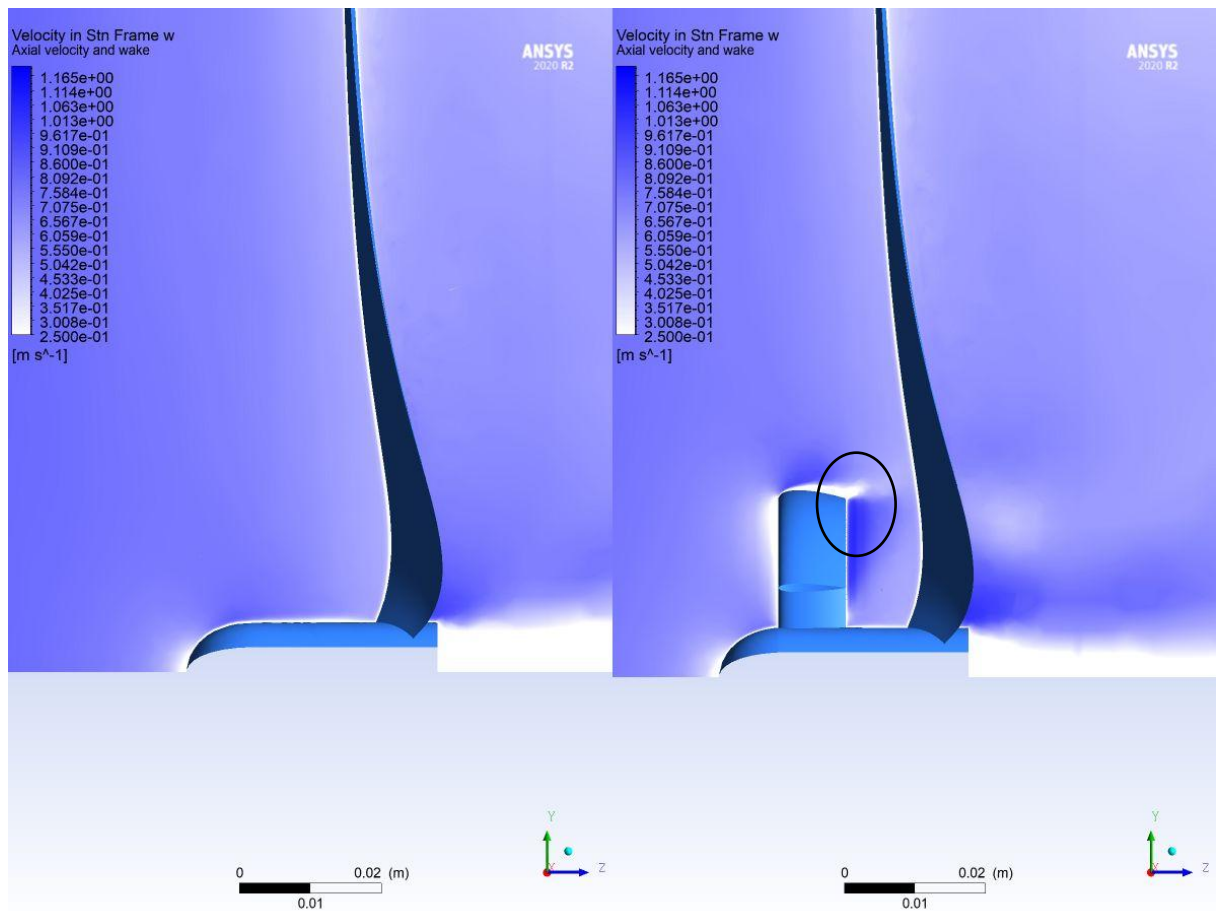


Figure 4.18: Closeup view of axial velocity and near wake for standard (left) and 18% ring vane rotor (right) at 5.1 TSR for 1 m/s free stream velocity on cross section plane

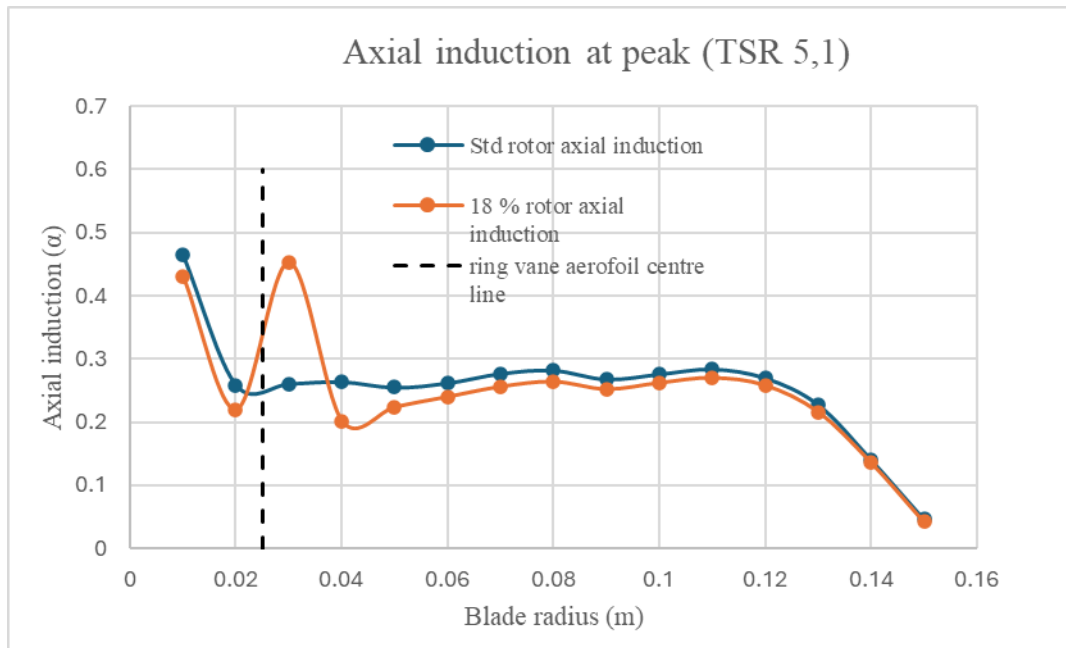


Figure 4.19: Axial induction factor for standard and 18% ring vane rotor at 5.1 TSR for 1 m/s free stream velocity

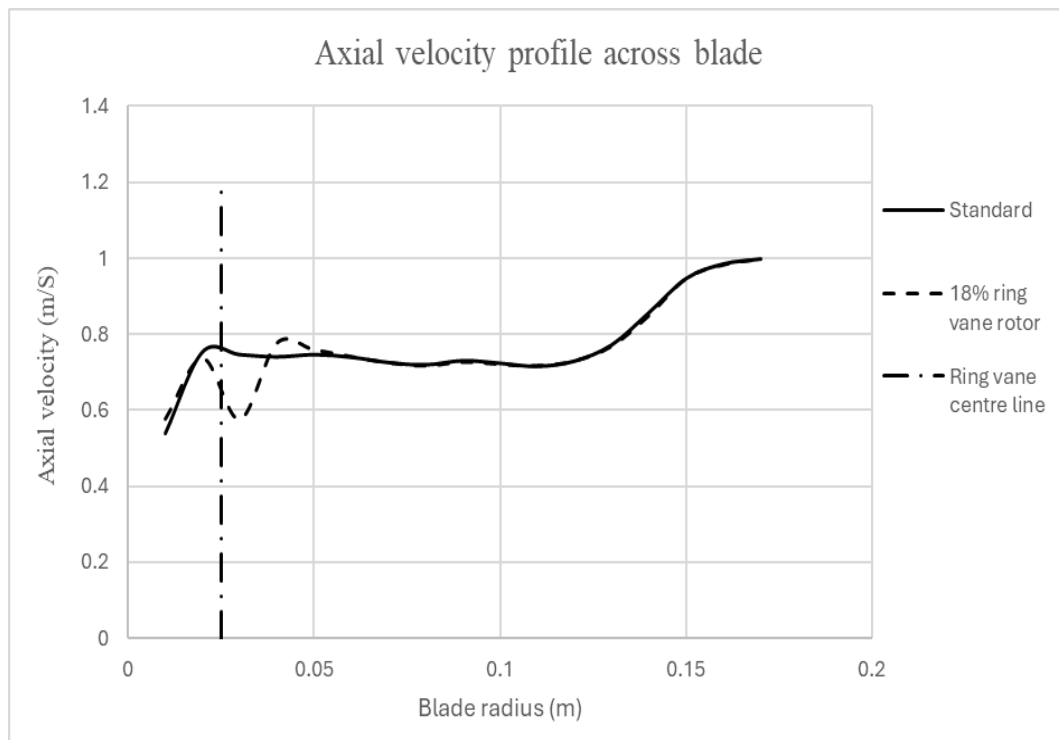


Figure 4.20: Axial velocity profile for standard and 18% ring vane rotor at 5.1 TSR for 1 m/s free stream velocity at plane 2mm in front of rotor

Figure 4.21 shows that there was little difference in the angular induction factor calculated at a plane 20 mm behind the rotor plane within the near wake for the standard and 18% ring vane rotors at 1 m/s free stream velocity. This possibly indicates that at higher free stream velocity, the ring vane struts do not influence the near wake rotation as much as at lower free stream velocities, but that the increase of axial velocity within the ring vane area may have the higher impact.

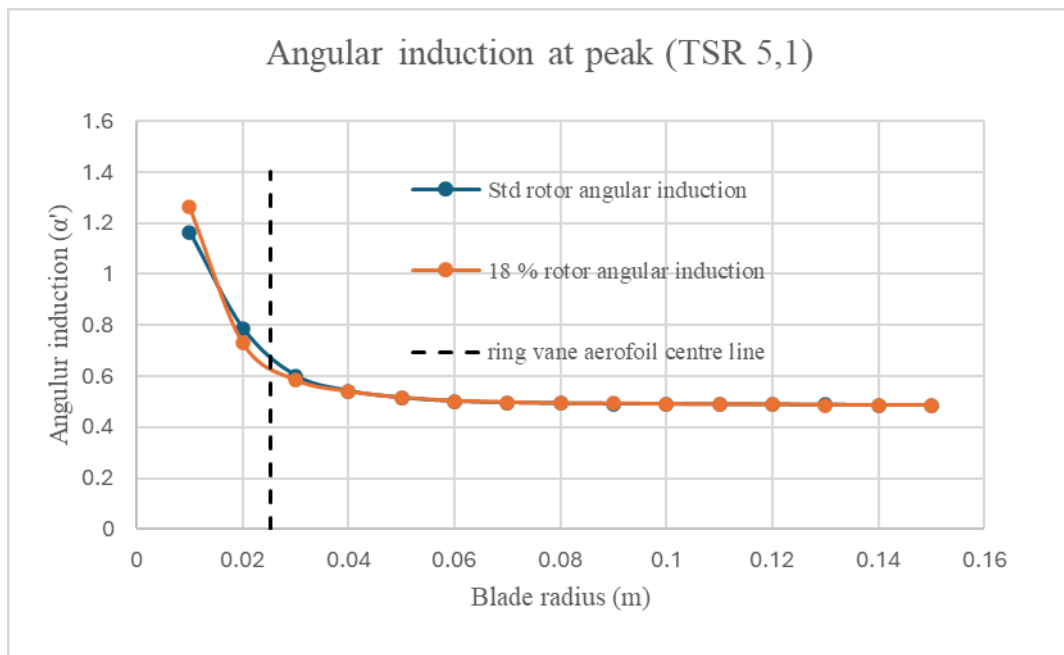


Figure 4.21: Angular induction factor for standard and 18% ring vane rotor at 5.1 TSR for 1 m/s free stream velocity

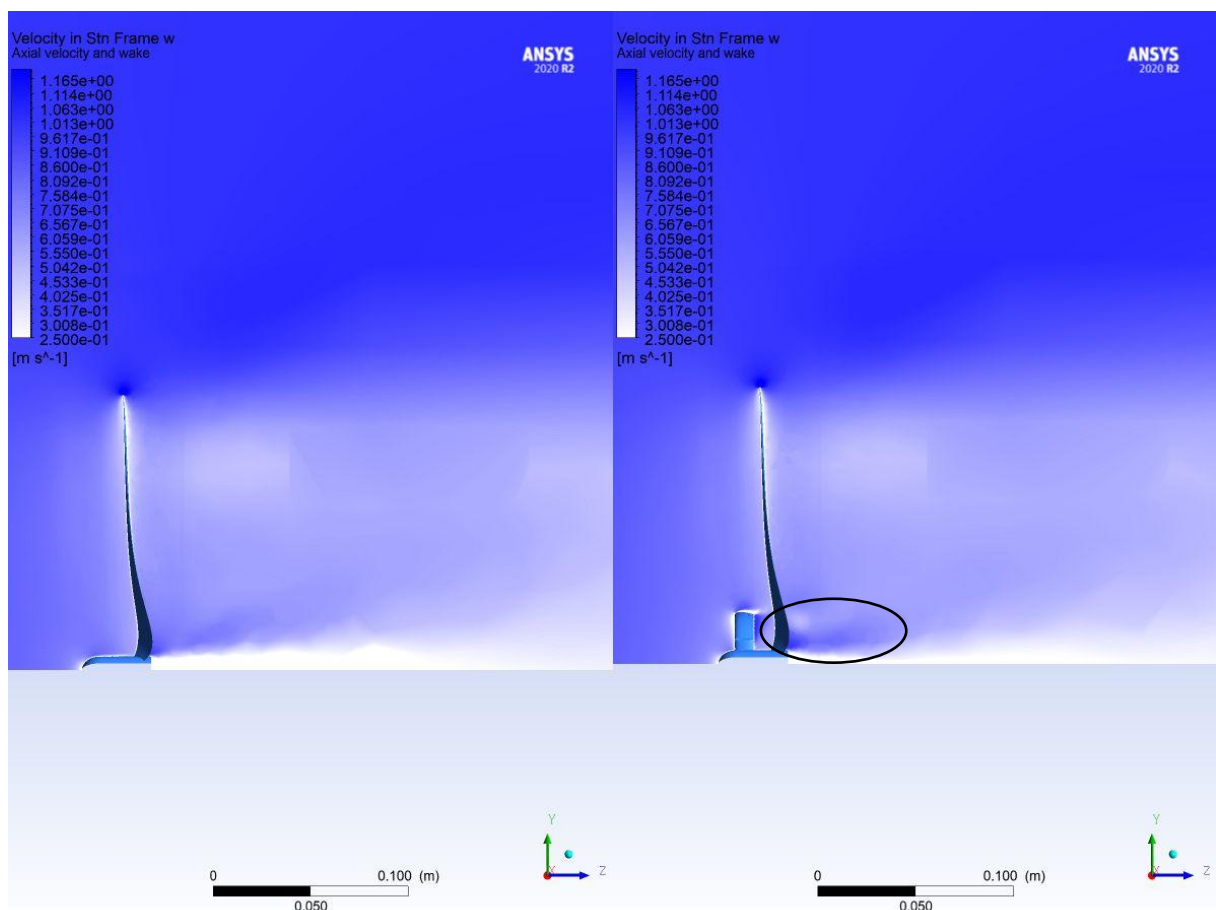


Figure 4.22: Axial velocity and wake for standard (left) and 18% ring vane rotor (right) at 5.1 TSR for 1 m/s free stream velocity on cross section plane

In Figure 4.22 it can be seen that there is higher axial velocity present in the near wake. Axial and angular induction factor graphs for the standard and 18% ring vane rotors for off-peak tip speed ratios of 4.4 and 6 at 1 m/s free stream velocity are provided in Appendix K.

4.4 CFD simulation versus physical test

A comparison of the standard and 18% ring vane rotors is presented using both simulation and experimental results, analysing power coefficient against tip speed ratio. Figure 4.23 illustrates the results at a free stream velocity of 0.5 m/s. The experimental peak performance occurred at lower tip speed ratios compared to the simulation, with the performance curve shifting to the left. Additionally, the steeper gradient of the experimental results indicates greater sensitivity to rotational speed, whereas the simulation exhibited a broader operational range due to lower sensitivity. This discrepancy highlights the inherent differences between simulations and real-world conditions, which are often more variable and challenging to model accurately. In this comparative study, the physical results did not fully validate the simulation model. However, both sets of results agreed that the 18% ring vane rotor exhibited the highest performance increase at peak tip speed ratios and demonstrated an improved operational performance range.

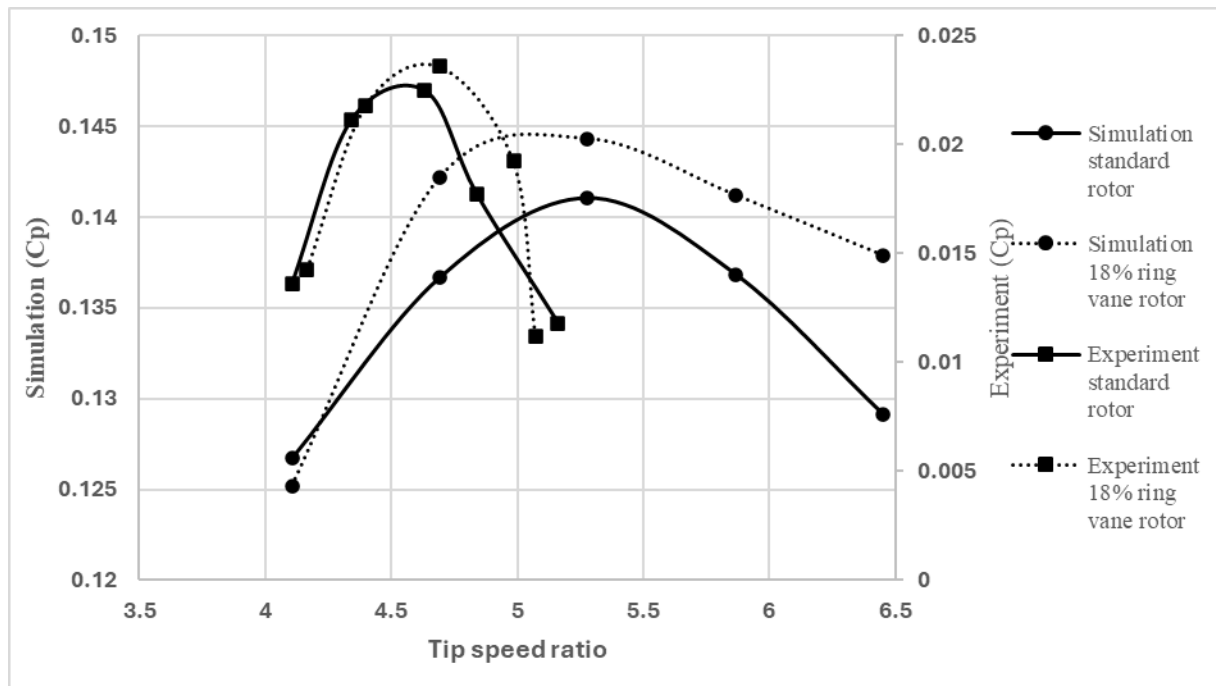


Figure 4.23: Simulation and physical test results for the standard and 18% ring vane rotor at 0.5 m/s

CHAPTER FIVE

CONCLUSION AND FUTURE WORK

5.1 Conclusion

This research study set out to answer the following questions concerning ring vanes:

- *Will the peak performance of a HAWT improve with a retrofitted ring vane near the hub region?* Simulation and physical testing of the 280 mm rotor and same rotor retrofitted with ring vanes indicated that there is an improvement of peak performance for free stream velocity of 0.5 m/s. The 18% ring vane rotor shown to have the best peak performance increase compared to the standard rotor with a 2.3% increase from simulation results and a 4.35% increase from physical testing.
- *Will the performance of the HAWT improve over a range of operational rotation speeds?* Both simulation and physical testing using free stream velocity of 0.5 m/s revealed that the 280 mm rotor retrofitted with a ring vane improved performance over a range of rotational speeds. The best performing, the 18% ring vane rotor simulation showed improved operation performance starting from 4.2 tip speed ratio and physical tests showed an improvement of performance from tip speed ratios 4.4 to 5.
- *At what position near the hub region in a range from 15% to 20% of the rotor diameter will produce the best performance increase with retrofitted ring vane?* Simulation predicted that the 18% ring vane rotor performed best at peak and had improved performance over a range of rotational speed for free stream velocity of 0.5 m/s. Physical testing confirmed that the 18% ring vane rotor was the best performing rotor.
- *Will the retrofitted ring vane produce performance increase at higher free stream velocity?* The case study simulation of the standard and 18% ring vane rotor at a higher free stream velocity of 1 m/s revealed that the peak power performance increase was 0.8% and an improved performance across the complete operational range was observed.

In the pursuit of these answers ring vanes were placed within the hub region of a rotor at 15% to 20% of the rotor diameter in 1% increments. A 280 mm diameter rotor from previous research was chosen as a suitable rotor for comparison and physical testing.

The CFD simulation of the rotor without a ring vane and same rotor retrofitted with ring vanes was necessary to determine the ring vane diameter that produced the best performance increase of peak and operational rotation speeds. Simulation revealed that a ring vane placed at 18% of the rotor diameter had the best performance increase for peak and operational rotation speeds. Simulation of the standard rotor and the 18% (best performing) ring vane rotor was simulated at a higher free stream velocity to

validate that the performance increase was valid at an off-design scenario. Simulation benefitted from perfect control over input variables and zero rotor flex.

Physical testing in water with the vertical-travel test apparatus for all 280 mm rotors at 0.5 m/s free stream velocity produced measurable power output for all rotational speeds. The testing method was accurate and repeatable for achieving flow through the rotors. Blockage effect during testing was mitigated through use of a 1.4 metre diameter tank (test section). Complete development of rotor near wake was indicated by rotor rotational speed reaching the asymptotes for the raw test data, as determined by a best-fit decay function. Physical test results confirmed, as simulation predicted, that the 18% ring vane produced the best peak performance increase, as well as increased performance across a range of operational rotation speeds. The vertical-travel testing method can be recommended for future use in small model testing.

5.2 Future work

This research focused on enhancing the performance of a HAWT rotor by positioning a ring vane near the hub region, in front of the plane of rotation. The concept of the ring vane in this study was inspired by a combination of shrouded rotors and boundary layer fences. This work serves as a foundation for future research aimed at optimizing the geometry and design of the ring vane to further improve HAWT rotor performance.

Ring vane improvement

The ring vanes (including supporting struts) used a symmetrical aerofoil profile aligned parallel to the axial direction. The performance increase may be further improved by investigation into:

- Optimisation of the ring vane aerofoil by reconfiguring the ring to have positive or negative angle of attack relative to the rotor plane.
- Optimisation of the struts holding the ring vane in place, to influence angular induction of the rotor by adjusting the strut aerofoil profile to a negative or positive angle of attack.
- The use of multiple ring vanes on the same rotor to improve aerodynamics for specific regions.
- The exploration of free rotating ring vanes and their effect.

Blade design improvement

This research showed that there was an improvement in axial and angular induction across the blade for rotors retrofitted with ring vanes. Performance increase may further benefit from:

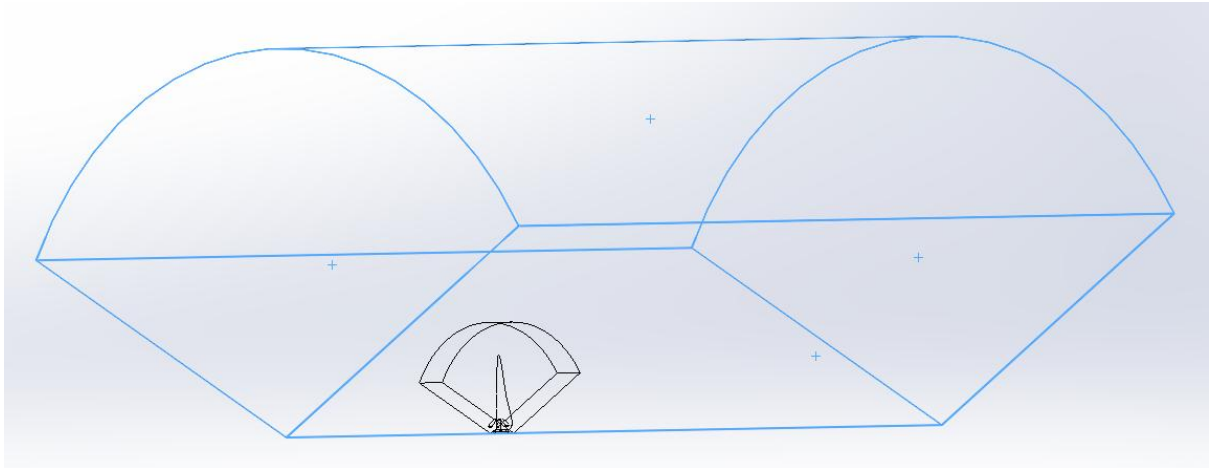
- Re-design of the blade aerofoil profiles and angle of attack to benefit from improved axial and angular induction when deployed with a ring vane.
- Re-design of only part of the blade, where there was a significant improvement in axial induction within the ring vane region in order to benefit from the higher axial velocities.

Appendix A: Blade aerofoil spline x, y, and z coordinates sample

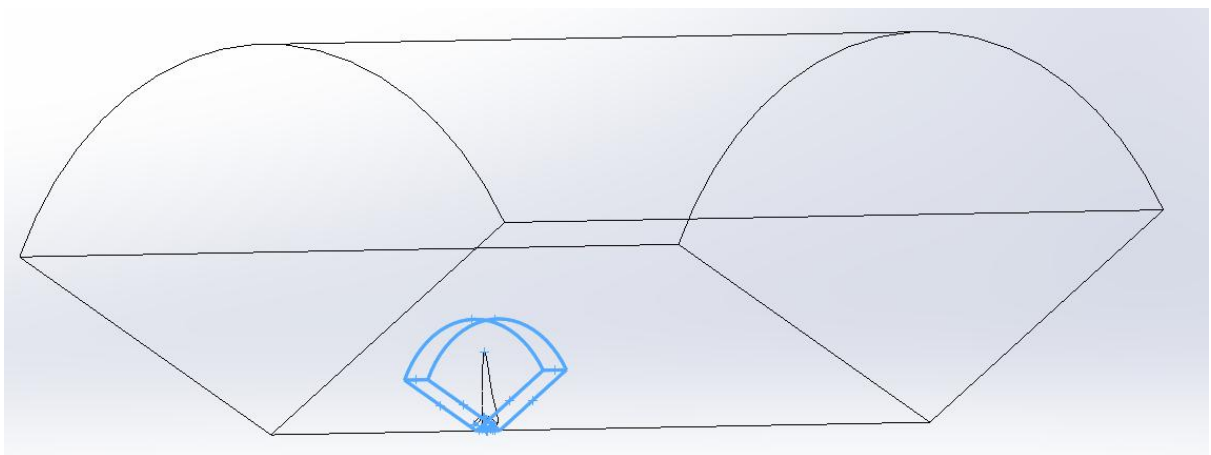
Element 40			39			38		
x	y	z	x	y	z	x	y	z
0.005079	0.000335	0.464097	0.009037	0.000934	0.452285	0.011817	0.001476	0.440467
0.005080	0.000356	0.464097	0.009038	0.000963	0.452285	0.011818	0.001512	0.440466
0.005078	0.000377	0.464097	0.009031	0.000991	0.452285	0.011806	0.001546	0.440467
0.005071	0.000397	0.464097	0.009016	0.001016	0.452285	0.011783	0.001574	0.440467
0.005060	0.000415	0.464097	0.008995	0.001036	0.452286	0.011751	0.001592	0.440468
0.005045	0.000430	0.464098	0.008969	0.001049	0.452286	0.011701	0.001606	0.440470
0.005028	0.000442	0.464098	0.008838	0.001087	0.452289	0.011309	0.001723	0.440480
0.005008	0.000450	0.464098	0.008489	0.001185	0.452295	0.010855	0.001844	0.440491
0.004893	0.000481	0.464099	0.008092	0.001288	0.452303	0.010339	0.001970	0.440504
0.004639	0.000550	0.464102	0.007652	0.001395	0.452310	0.009768	0.002100	0.440517
0.004361	0.000622	0.464105	0.007172	0.001505	0.452318	0.009144	0.002234	0.440530
0.004063	0.000695	0.464107	0.006655	0.001617	0.452326	0.008474	0.002369	0.440544
0.003746	0.000769	0.464110	0.006107	0.001728	0.452334	0.007762	0.002503	0.440557
0.003413	0.000842	0.464112	0.005531	0.001838	0.452341	0.007014	0.002635	0.440569
0.003066	0.000914	0.464115	0.004931	0.001944	0.452348	0.006235	0.002761	0.440581
0.002708	0.000982	0.464117	0.004311	0.002043	0.452354	0.005431	0.002878	0.440592
0.002340	0.001044	0.464119	0.003675	0.002132	0.452360	0.004606	0.002981	0.440601
0.001962	0.001100	0.464121	0.003023	0.002210	0.452365	0.003760	0.003070	0.440609
0.001577	0.001149	0.464122	0.002359	0.002275	0.452369	0.002900	0.003142	0.440615
0.001187	0.001190	0.464123	0.001687	0.002327	0.452372	0.002028	0.003197	0.440620
0.000793	0.001224	0.464124	0.001008	0.002365	0.452374	0.001148	0.003234	0.440624
0.000398	0.001249	0.464125	0.000326	0.002390	0.452375	0.000266	0.003254	0.440625
0.000002	0.001266	0.464125	-0.000354	0.002400	0.452375	-0.000616	0.003255	0.440625
-0.000391	0.001275	0.464125	-0.001030	0.002397	0.452374	-0.001491	0.003238	0.440622
-0.000779	0.001276	0.464124	-0.001699	0.002379	0.452372	-0.002356	0.003202	0.440619
-0.001162	0.001268	0.464124	-0.002356	0.002347	0.452369	-0.003206	0.003149	0.440613
-0.001536	0.001252	0.464122	-0.002999	0.002301	0.452365	-0.004037	0.003078	0.440607
-0.001900	0.001229	0.464121	-0.003623	0.002242	0.452360	-0.004845	0.002990	0.440598
-0.002252	0.001197	0.464120	-0.004227	0.002171	0.452355	-0.005625	0.002887	0.440589
-0.002590	0.001159	0.464118	-0.004806	0.002088	0.452349	-0.006374	0.002769	0.440579
-0.002912	0.001113	0.464116	-0.005358	0.001994	0.452343	-0.007086	0.002637	0.440568
-0.003217	0.001061	0.464114	-0.005879	0.001890	0.452337	-0.007759	0.002493	0.440557
-0.003502	0.001003	0.464112	-0.006367	0.001777	0.452330	-0.008388	0.002337	0.440545
-0.003767	0.000940	0.464110	-0.006819	0.001655	0.452324	-0.008972	0.002171	0.440534
-0.004010	0.000872	0.464108	-0.007234	0.001526	0.452317	-0.009506	0.001997	0.440522
-0.004230	0.000800	0.464106	-0.007608	0.001391	0.452311	-0.009988	0.001815	0.440512
-0.004426	0.000724	0.464104	-0.007941	0.001252	0.452305	-0.010416	0.001629	0.440502

Element 40			39			38		
x	y	z	x	y	z	x	y	z
-0.004596	0.000646	0.464102	-0.008230	0.001108	0.452300	-0.010788	0.001438	0.440493
-0.004741	0.000565	0.464101	-0.008475	0.000962	0.452296	-0.011103	0.001244	0.440485
-0.004860	0.000483	0.464100	-0.008676	0.000817	0.452292	-0.011360	0.001052	0.440479
-0.004953	0.000402	0.464099	-0.008832	0.000672	0.452289	-0.011559	0.000861	0.440473
-0.005021	0.000321	0.464098	-0.008945	0.000530	0.452287	-0.011703	0.000675	0.440470
-0.005063	0.000245	0.464097	-0.009013	0.000396	0.452285	-0.011789	0.000502	0.440467
-0.005080	0.000173	0.464097	-0.009038	0.000273	0.452285	-0.011819	0.000342	0.440466
-0.005074	0.000112	0.464097	-0.009025	0.000167	0.452285	-0.011800	0.000204	0.440467
-0.005037	0.000068	0.464098	-0.008960	0.000094	0.452286	-0.011714	0.000111	0.440469
-0.004962	0.000039	0.464098	-0.008829	0.000048	0.452289	-0.011544	0.000054	0.440474
-0.004851	0.000017	0.464100	-0.008637	0.000015	0.452293	-0.011295	0.000015	0.440480
-0.004705	0.000004	0.464101	-0.008386	0.000000	0.452297	-0.010970	0.000000	0.440488
-0.004524	0.000000	0.464103	-0.008075	0.000002	0.452303	-0.010567	0.000008	0.440498
-0.004308	0.000003	0.464105	-0.007703	0.000018	0.452309	-0.010086	0.000036	0.440510
-0.004057	0.000012	0.464107	-0.007272	0.000046	0.452317	-0.009529	0.000080	0.440522
-0.003774	0.000026	0.464110	-0.006786	0.000083	0.452324	-0.008900	0.000137	0.440535
-0.003460	0.000043	0.464112	-0.006247	0.000127	0.452332	-0.008203	0.000204	0.440549
-0.003118	0.000062	0.464115	-0.005660	0.000177	0.452340	-0.007444	0.000279	0.440562
-0.002751	0.000083	0.464117	-0.005030	0.000231	0.452347	-0.006629	0.000360	0.440575
-0.002360	0.000105	0.464119	-0.004359	0.000288	0.452354	-0.005762	0.000446	0.440587
-0.001950	0.000127	0.464121	-0.003655	0.000346	0.452360	-0.004851	0.000535	0.440598
-0.001522	0.000150	0.464123	-0.002921	0.000406	0.452366	-0.003902	0.000626	0.440608
-0.001081	0.000172	0.464124	-0.002164	0.000467	0.452370	-0.002923	0.000718	0.440615
-0.000629	0.000195	0.464125	-0.001388	0.000527	0.452373	-0.001919	0.000810	0.440621
-0.000170	0.000217	0.464125	-0.000599	0.000588	0.452375	-0.000899	0.000903	0.440624
0.000294	0.000240	0.464125	0.000198	0.000650	0.452375	0.000132	0.000998	0.440625
0.000762	0.000262	0.464124	0.001001	0.000711	0.452374	0.001170	0.001093	0.440623
0.001231	0.000284	0.464123	0.001806	0.000771	0.452371	0.002212	0.001185	0.440619
0.001698	0.000301	0.464122	0.002609	0.000824	0.452367	0.003249	0.001268	0.440613
0.002159	0.000314	0.464120	0.003400	0.000868	0.452362	0.004272	0.001340	0.440604
0.002608	0.000322	0.464118	0.004172	0.000903	0.452356	0.005272	0.001400	0.440593
0.003043	0.000324	0.464115	0.004920	0.000929	0.452348	0.006240	0.001447	0.440581
0.003460	0.000322	0.464112	0.005637	0.000945	0.452340	0.007168	0.001480	0.440567
0.003856	0.000314	0.464109	0.006317	0.000951	0.452331	0.008048	0.001500	0.440551
0.004226	0.000301	0.464106	0.006954	0.000947	0.452322	0.008872	0.001507	0.440536
0.004567	0.000283	0.464103	0.007542	0.000933	0.452312	0.009634	0.001500	0.440520
0.004877	0.000262	0.464099	0.008075	0.000912	0.452303	0.010324	0.001482	0.440504
0.004972	0.000254	0.464098	0.008548	0.000884	0.452294	0.010937	0.001455	0.440489
0.004996	0.000255	0.464098	0.008957	0.000851	0.452286	0.011467	0.001419	0.440476
0.005020	0.000261	0.464098	0.008960	0.000856	0.452286	0.011710	0.001397	0.440469
0.005041	0.000274	0.464098	0.008987	0.000866	0.452286	0.011746	0.001400	0.440468
0.005058	0.000291	0.464097	0.009010	0.000883	0.452285	0.011779	0.001416	0.440468
0.005071	0.000312	0.464097	0.009027	0.000907	0.452285	0.011804	0.001443	0.440467
0.005079	0.000335	0.464097	0.009037	0.000934	0.452285	0.011817	0.001476	0.440467

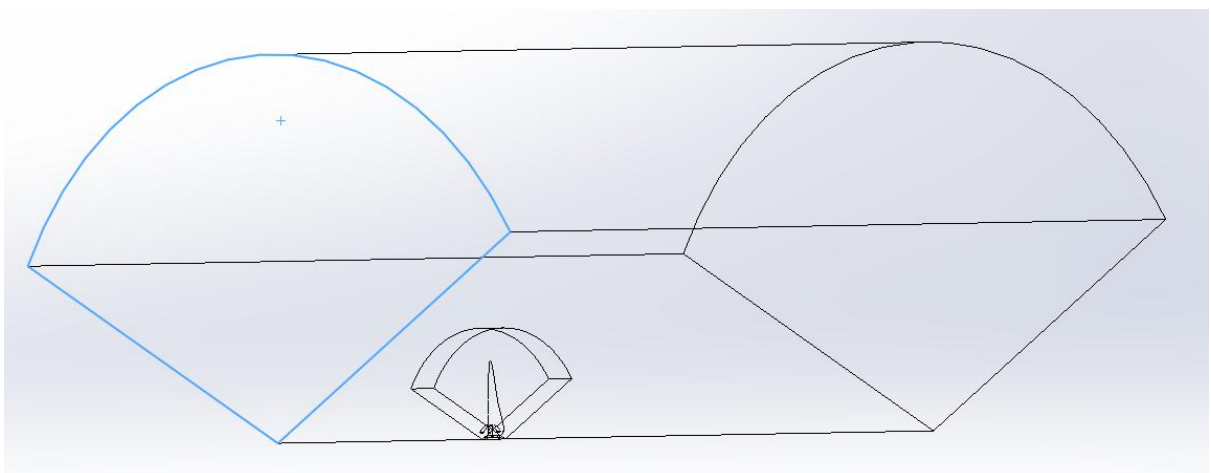
Appendix B: Domain and part names of simulation virtual models



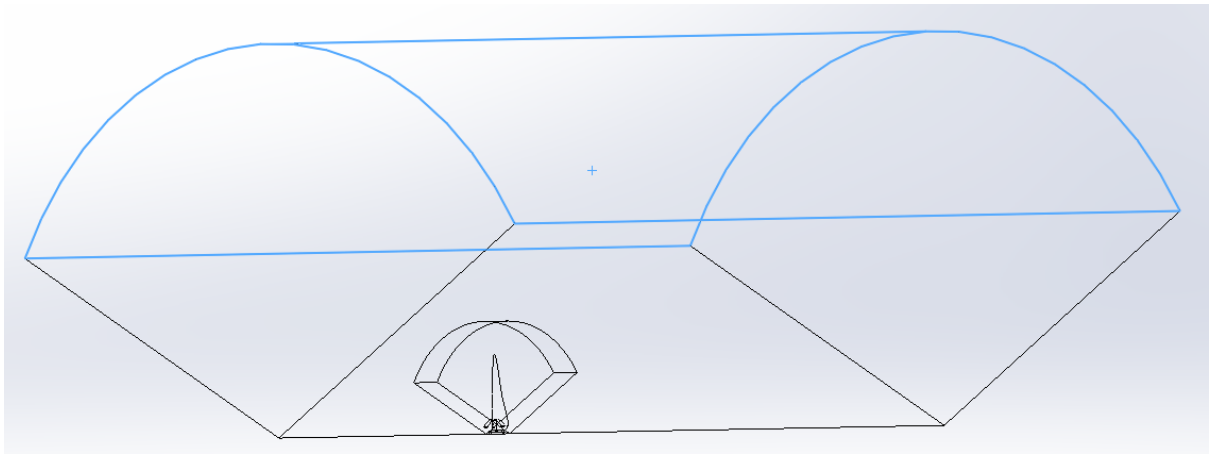
The fluid domain is highlighted in blue



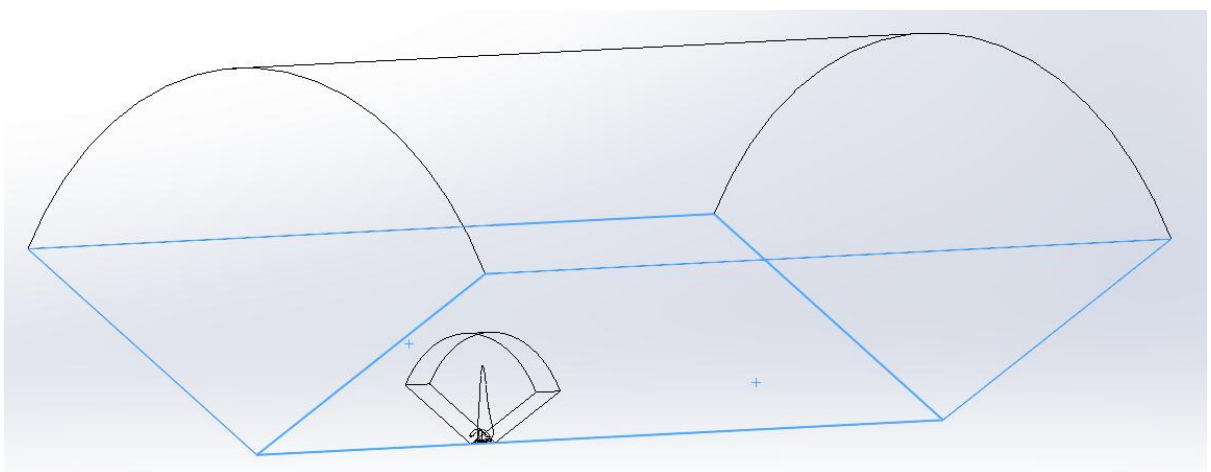
The rotating domain is highlighted in blue



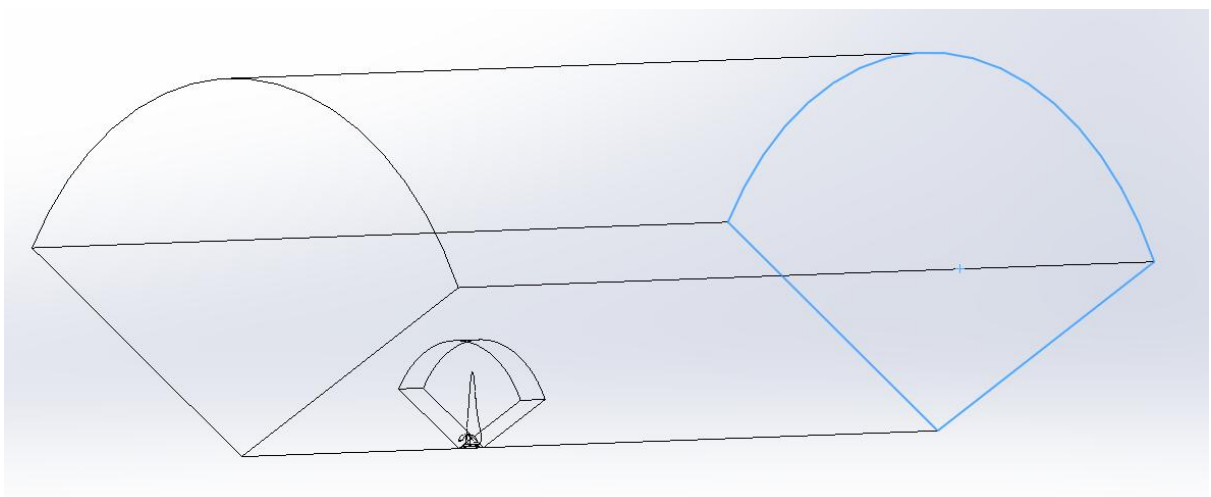
The inlet is highlighted in blue



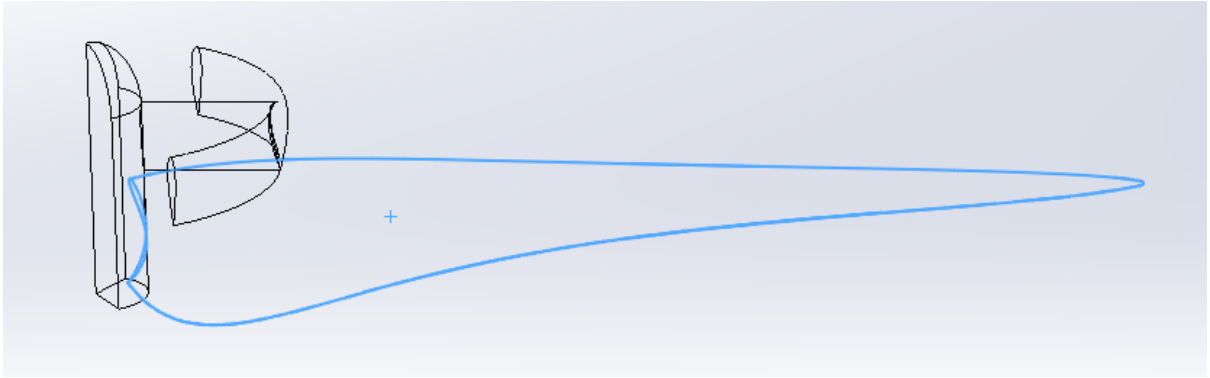
The outer fluid wall is highlighted in blue



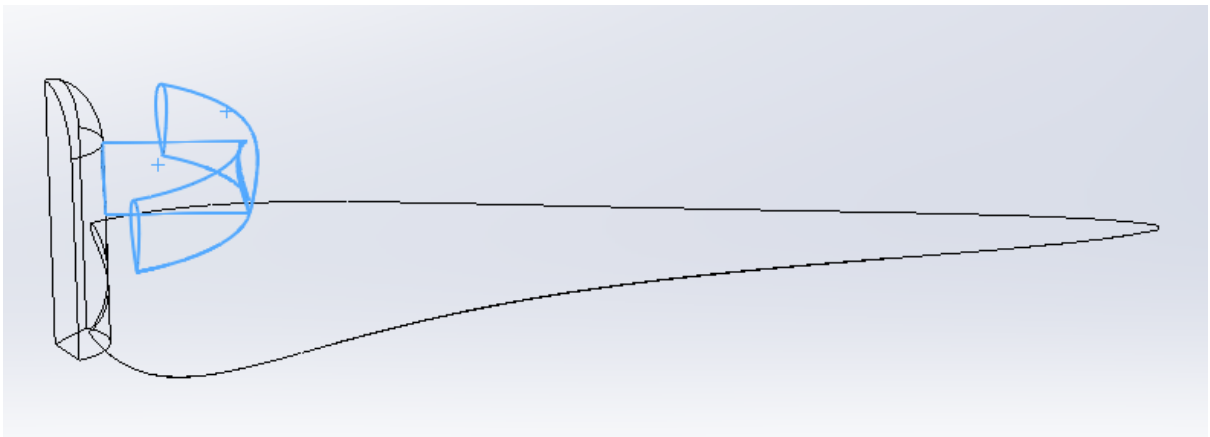
The rotational periodicity wall is highlighted in blue



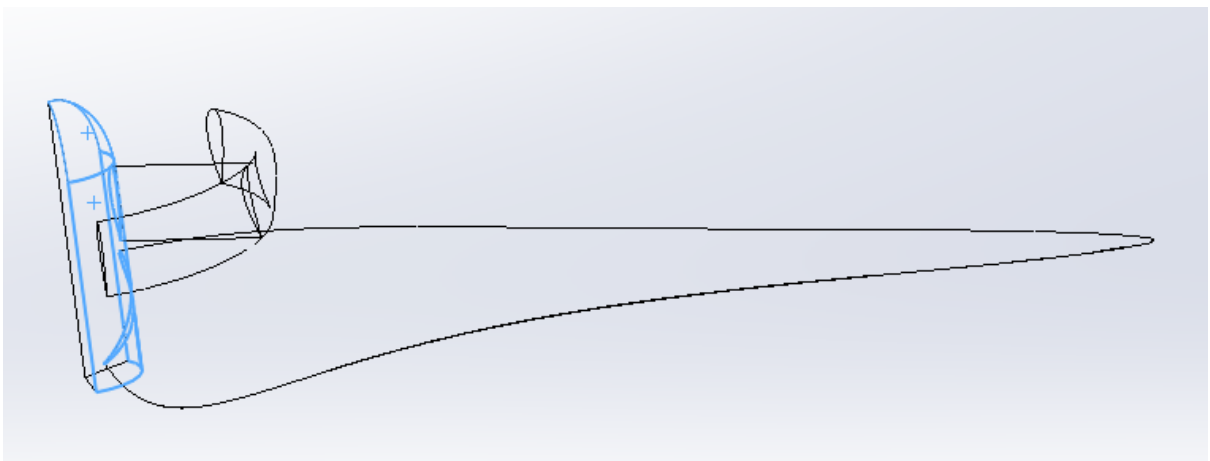
The outlet is highlighted in blue



The blade is highlighted in blue



The ring vane is highlighted in blue



The hub is highlighted in blue

Appendix C: Solver settings for all rotors at 0.5 m/s free stream velocity

Fluent

Version: 3d, pbns, geko (3d, pressure-based, Generalized k-omega)

Release: 20.2.0

Title:

Models

Model	Settings
Space	3D
Time	Steady
Viscous	GEKO k-omega turbulence model
Heat Transfer	Disabled
Solidification and Melting	Disabled
Species	Disabled
Coupled Dispersed Phase	Disabled
NOx Pollutants	Disabled
SOx Pollutants	Disabled
Soot	Disabled
Mercury Pollutants	Disabled
Structure	Disabled
Acoustics	Disabled
Eulerian Wall Film	Disabled
Potential/Li-ion Battery	Disabled
Multiphase	Disabled

Material Properties

Material: water-liquid (fluid)

Property	Units	Method	Value(s)
Density	kg/m3	constant	998.2
Cp (Specific Heat)	j/kg-k	constant	4182
Thermal Conductivity	w/m-k	constant	0.6
Viscosity	kg/m-s	constant	0.001003
Molecular Weight	kg/kmol	constant	18.0152
Thermal Expansion Coefficient	1/k	constant	0
Speed of Sound	m/s	none	#f

Cell Zone Conditions

Zones

name	id	type
fluiddomain	10737	fluid
rotatingdomain	10732	fluid

Setup Conditions

fluiddomain

Condition Value

Frame Motion? no

rotatingdomain

Condition Value

Frame Motion? yes

Reference Frame Rotation Speed (rpm) -180

Reference Frame Z-Origin of Rotation-Axis (m) 1

Boundary Conditions

Zones

name	id	type
inlet	68	velocity-inlet
outlet	69	pressure-outlet
hub	75	wall
ring	74	wall
blade	76	wall
outerwall	73	wall

Setup Conditions

inlet

Condition	Value
-----------	-------

Velocity Specification Method Magnitude and Direction

Velocity Magnitude (m/s) 0.5

X-Component of Flow Direction 0

Z-Component of Flow Direction 1

outlet

Condition	Value
-----------	-------

hub

Condition	Value
-----------	-------

Wall Motion	Moving Wall
Shear Boundary Condition	No Slip
Define wall motion relative to adjacent cell zone?	yes
Apply a rotational velocity to this wall?	yes

ring

Condition	Value
-----------	-------

Wall Motion Stationary Wall

Shear Boundary Condition No Slip

blade

Condition	Value
-----------	-------

Wall Motion	Moving Wall
Shear Boundary Condition	No Slip
Define wall motion relative to adjacent cell zone?	yes
Apply a rotational velocity to this wall?	yes

outerwall

Condition	Value
-----------	-------

Wall Motion	Stationary Wall
Shear Boundary Condition	No Slip

pie1-fluiddomain

Condition	Value
-----------	-------

Rotationally Periodic? yes

pie1-rotatingdomain

Condition	Value
-----------	-------

Rotationally Periodic? yes

Solver Settings

Equations

Equation	Solved
----------	--------

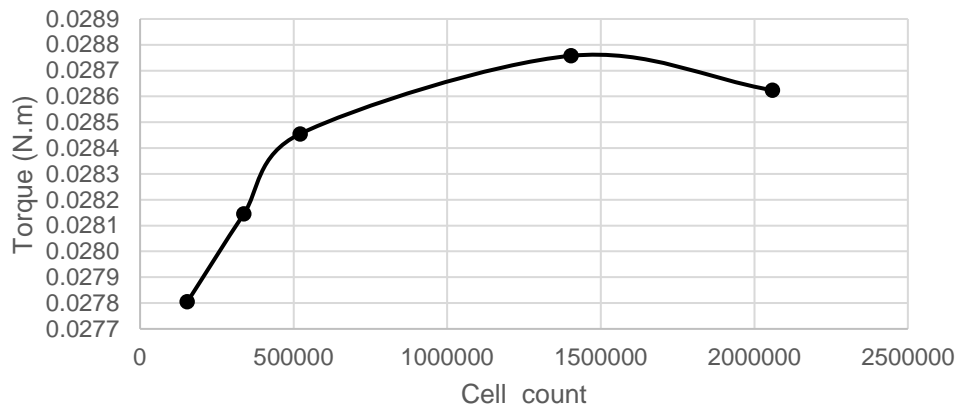
```

-----
Flow      yes
Turbulence yes
Numerics
Numeric      Enabled
-----
Absolute Velocity Formulation  yes
Relaxation
Variable      Relaxation Factor
-----
Density      1
Body Forces  1
Turbulent Kinetic Energy  0.75
Specific Dissipation Rate  0.75
Turbulent Viscosity      1
Linear Solver
Variable      Solver Type  Termination Criterion  Residual Reduction Tolerance
-----
Flow      F-Cycle  0.1
Turbulent Kinetic Energy  F-Cycle  0.1
Specific Dissipation Rate  F-Cycle  0.1
Pressure-Velocity Coupling
Parameter      Value
-----
Type      Coupled
Pseudo Transient      yes
Explicit momentum under-relaxation  0.5
Explicit pressure under-relaxation  0.5
Discretization Scheme
Variable      Scheme
-----
Pressure      Second Order
Momentum      Second Order Upwind
Turbulent Kinetic Energy  First Order Upwind
Specific Dissipation Rate  First Order Upwind
Solution Limits
Quantity      Limit
-----
Minimum Absolute Pressure  1
Maximum Absolute Pressure  5e+10
Minimum Temperature      1
Maximum Temperature      5000
Minimum Turb. Kinetic Energy  1e-14
Minimum Spec. Dissipation Rate  1e-20
Maximum Turb. Viscosity Ratio  100000

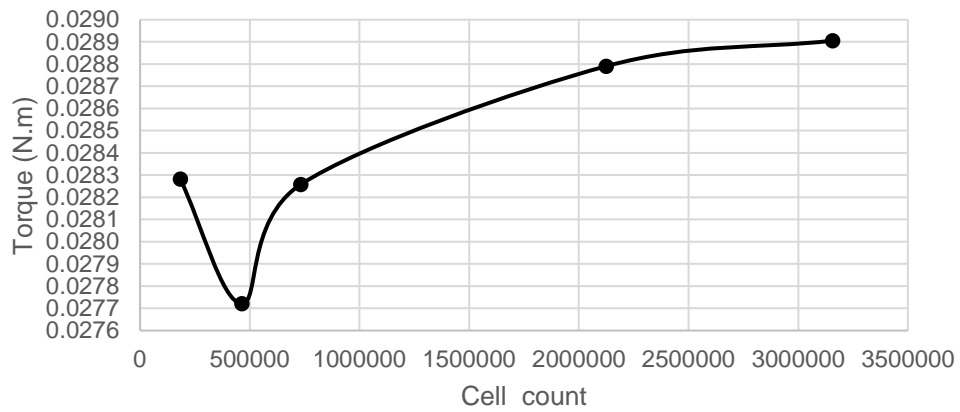
```

Appendix D: Mesh independence study for rotors

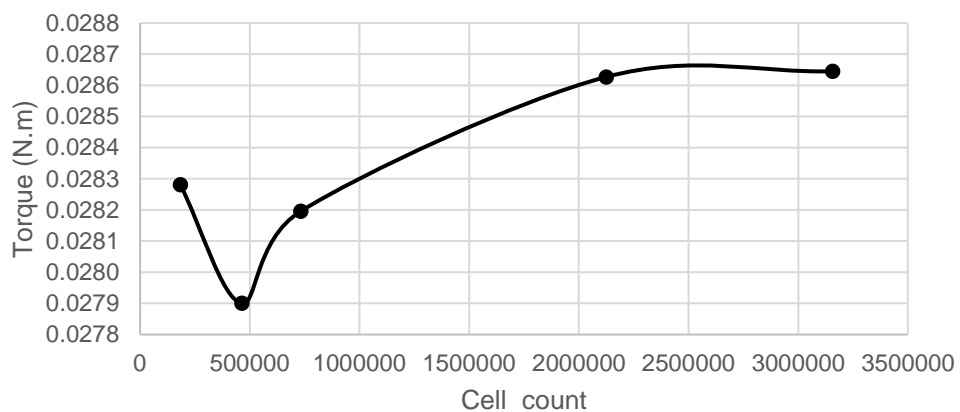
Mesh independence - 15% guide ring rotor

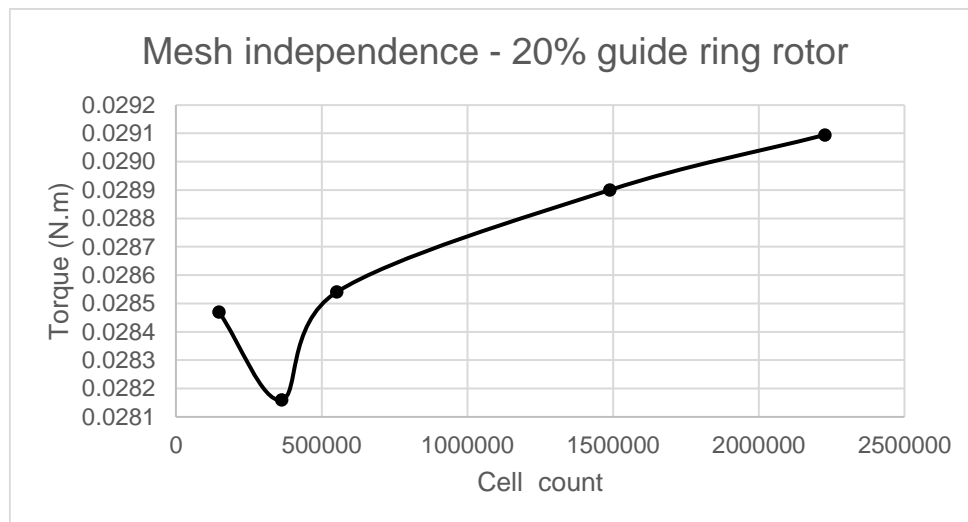
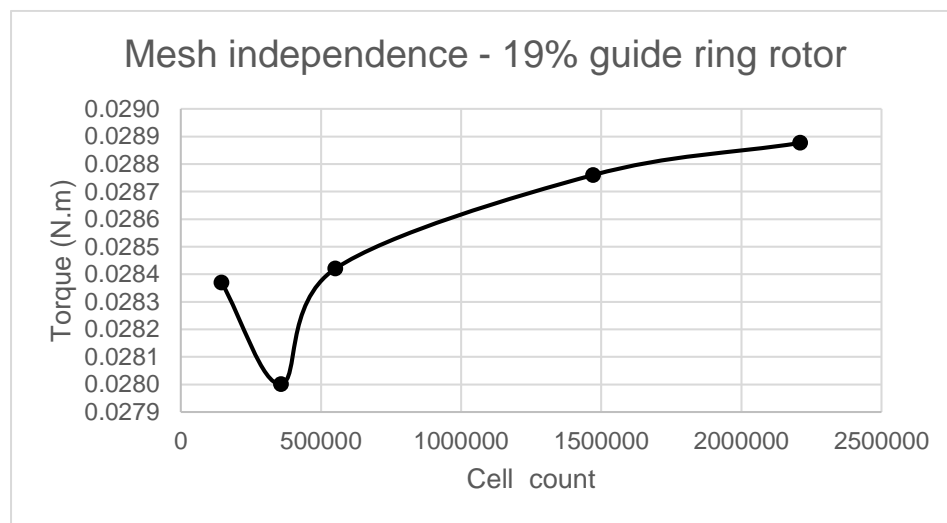
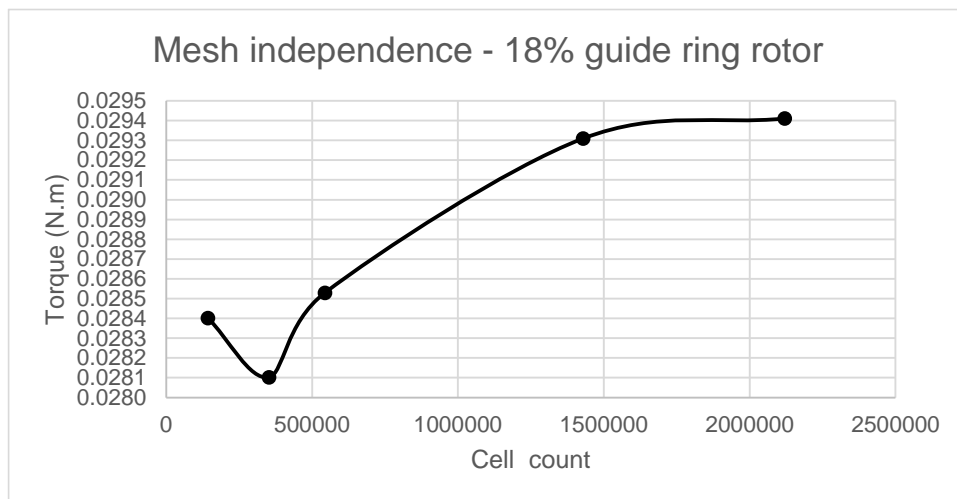


Mesh independence - 16% guide ring rotor



Mesh independence - 17% guide ring rotor





15% ring vane rotor at 180 rpm

Cell count	Torque hub	Torque blade	Torque total	Percentage change
153694	0.00E+00	0.027805	0.027805	-
337701	3.80E-06	0.028145	0.028149	1.24%
520829	3.80E-06	0.028455	0.028459	1.10%
1402699	3.80E-06	0.028757	0.028761	1.06%
2058634	3.90E-06	0.028624	0.028628	-0.46%

16% ring vane rotor at 180 rpm

Cell count	Torque hub	Torque blade	Torque total	Percentage change
183771	3.90E-06	0.028281	0.028285	-
463523	3.80E-06	0.027720	0.027724	-1.98%
732324	3.80E-06	0.028257	0.028261	1.94%
2124246	3.90E-06	0.028790	0.028794	1.89%
3156602	3.10E-06	0.028905	0.028908	0.40%

17% ring vane rotor at 180 rpm

Cell count	Torque hub	Torque blade	Torque total	Percentage change
183771	3.80E-06	0.028281	0.028285	-
463523	3.80E-06	0.027900	0.027904	-1.35%
732324	3.80E-06	0.028196	0.028200	1.06%
2124246	3.90E-06	0.028627	0.028631	1.53%
3156602	3.90E-06	0.028645	0.028649	0.06%

18% ring vane rotor at 180 rpm

Cell count	Torque hub	Torque blade	Torque total	Percentage change
142738	3.80E-06	0.028402	0.028406	-
352457	3.90E-06	0.028102	0.028106	-1.06%
544733	3.90E-06	0.028530	0.028534	1.52%
1428777	3.90E-06	0.029310	0.029314	2.73%
2120265	3.80E-06	0.029411	0.029415	0.35%

19% ring vane rotor at 180 rpm

Cell count	Torque hub	Torque blade	Torque total	Percentage change
144921	3.80E-06	0.028370	0.028374	-
357021	3.80E-06	0.028001	0.028005	-1.30%
550817	3.80E-06	0.028420	0.028424	1.50%
1470353	3.80E-06	0.028760	0.028764	1.20%
2208979	3.80E-06	0.028877	0.028880	0.41%

20% ring vane rotor at 180 rpm

Cell count	Torque hub	Torque blade	Torque total	Percentage change
147060	3.90E-06	0.028470	0.028474	-
361627	3.80E-06	0.028160	0.028164	-1.09%
550616	3.80E-06	0.028540	0.028544	1.35%
1488141	3.90E-06	0.028900	0.028904	1.26%
2225662	3.80E-06	0.029094	0.029098	0.67%

Appendix E: Handheld measuring device specifications



MT950 Tachometer

The MT950 provides fast and accurate non-contact revolutionary measurements for rotating objects. Using reflective tape on an object to be measured, simply point the laser at the object, the tachometer RPM will then measure up to a maximum of 100,000 revolutions with an accuracy of $\pm 0.05\%$ and a fast sampling time of 0.5 seconds. The MT950 has a built-in memory that recalls the Min/Max and last value stored. The meter can also be used as a Total TOT counter where the meter can be set up to count passing objects. The MT950 is lightweight and easy to operate.



Features

- Fast and accurate non-contact RPM and TOT measurements of rotating objects
- RPM Non-contact range 2 - 100 000RPM
- TOT count mode range from 1 - 100 000RPM
- Detecting distance 50 - 500mm
- 5 Digit backlit LCD
- Auto Range
- Data Hold
- 40 Reading memories
- Min / Max
- Resolution 0.1RPM
- Built-in laser spot

Function	Range	Accuracy
Non contact test range	3 to 99 999RPM	$\pm(0.05\% + 1)$
Non contact resolution	0.1RPM	
Count range	1 to 99 999 REV	
Sampling time	0.5 seconds (over 120RPM)	
Detection distance	50mm to 500mm	
Time base	Quartz crystal	
Size	160 x 58 x 39mm	
Weight	151g	



Measuring speed
of a rotating object



Large 5 digit Backlit
LCD Display

MT950 | Contact & Non-contact Tachometer

Contact Us South Africa

🌐 www.major-tech.com ✉ sales@major-tech.com

Australia

🌐 www.major-tech.com.au ✉ info@major-tech.com.au

Brymen TBM811

Electrical Specifications

Accuracy is \pm (% reading digits + number of digits) or otherwise specified, at $23^{\circ}\text{C} \pm 5^{\circ}\text{C}$ & less than 75% relative humidity.

True RMS voltage & current accuracies are specified from 10 % to 100 % of range or otherwise specified. Maximum Crest Factor < 2:1 at full scale & < 4:1 at half scale, and with frequency components within the specified frequency bandwidth for non-sinusoidal waveforms.

DC Voltage

Function	RANGE	Accuracy
mV	60.00mV	0.12%+2d
	600.0mV	0.06%+2d
V	9.999V, 99.99V, 999.9V	0.08%+2d

Input Impedance: $10\text{M}\Omega$, 50pF nominal
(80pF nominal for 600mV range)

AC Voltage

Function	RANGE	Accuracy
50Hz ~ 60Hz		
mV	60.00mV, 600.0mV	0.5% + 3d
V	9.999V, 99.99V, 999.9V	
40Hz ~ 500Hz		
mV	60.00mV, 600.0mV	0.8% + 4d
V	9.999V, 99.99V	1.0%+4d
	999.9V	2.0%+4d
500Hz ~ 1kHz		
mV	60.00mV, 600.0mV	2.0% + 3d

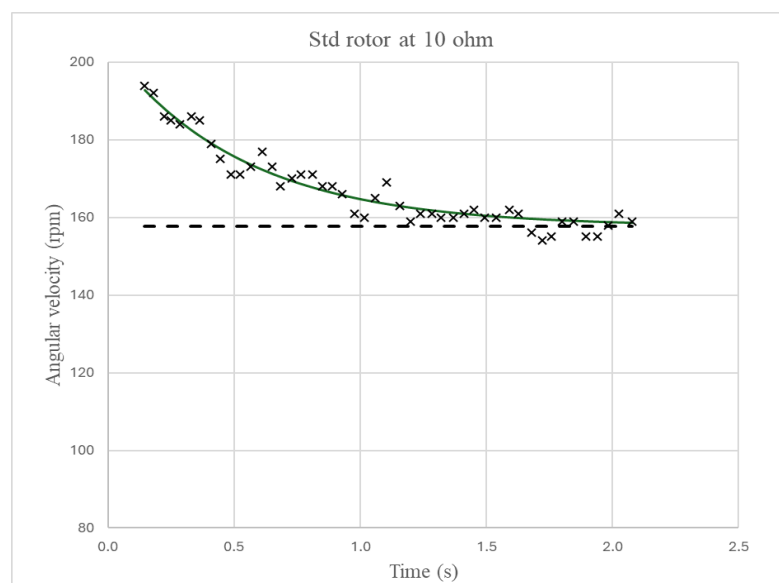
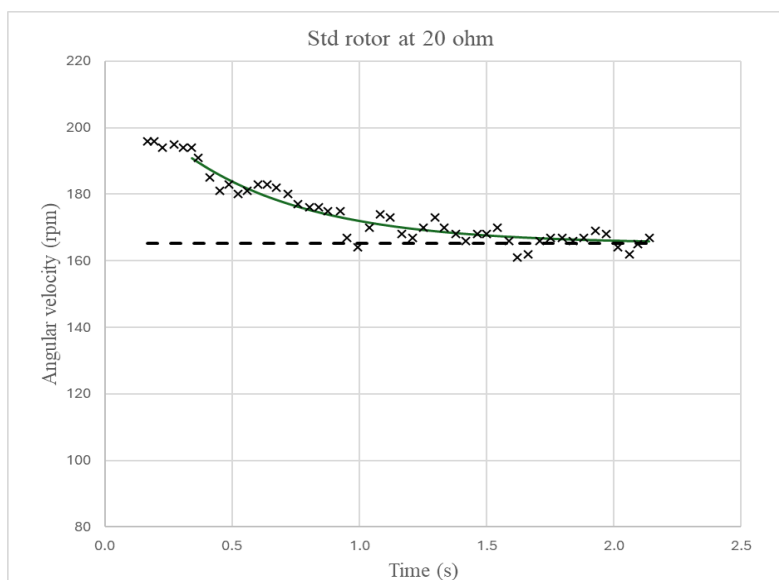
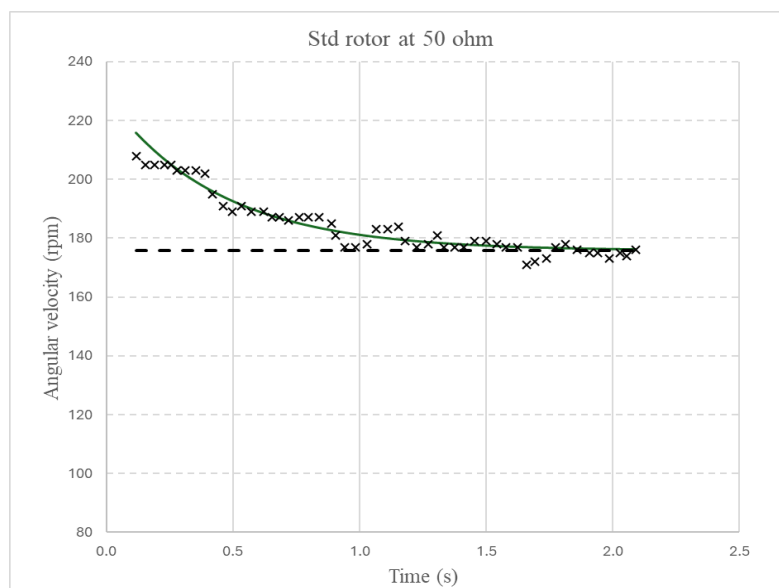
V	9.999V, 99.99V	1.0%+4d
	999.9V	2.0%+4d
1kHz ~ 3kHz		
mV	60.00mV, 600.0mV	2.0%+3d
V	9.999V, 99.99V, 999.9V	3.0%+4d
3kHz ~ 20kHz		
mV	60.00mV ¹⁾ , 600.0mV ¹⁾	2%+3d
V	9.999V ²⁾ , 99.99V	3dB
	999.9V	Unspec'd

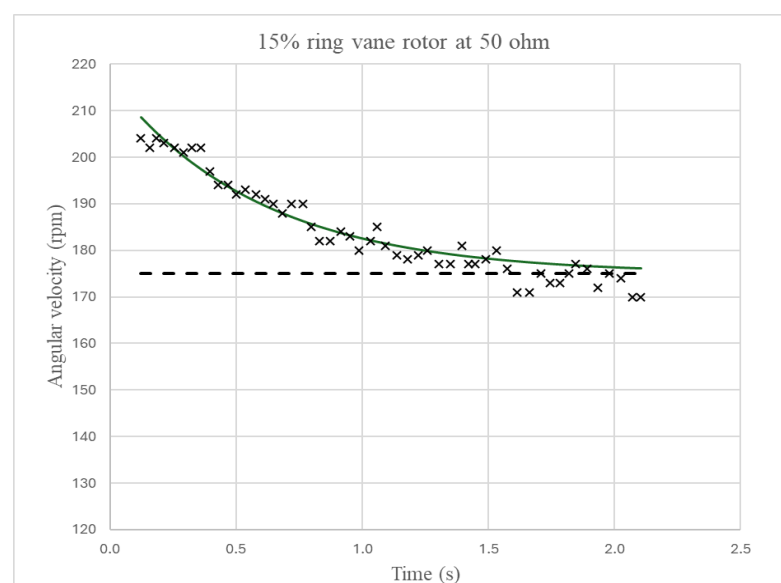
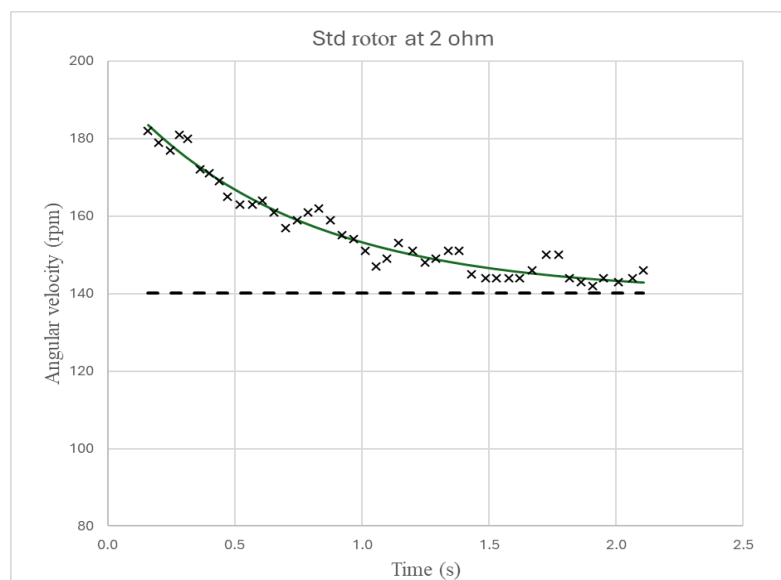
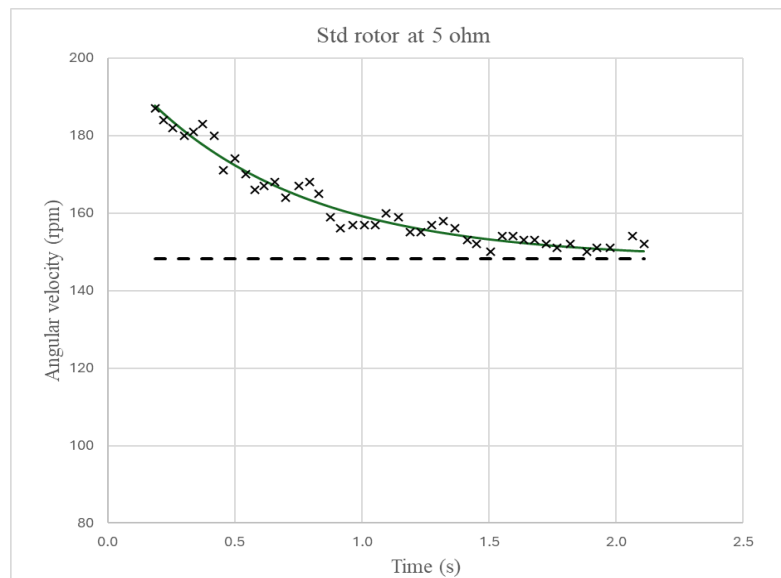
¹⁾Specified from 30% to 100% of range.

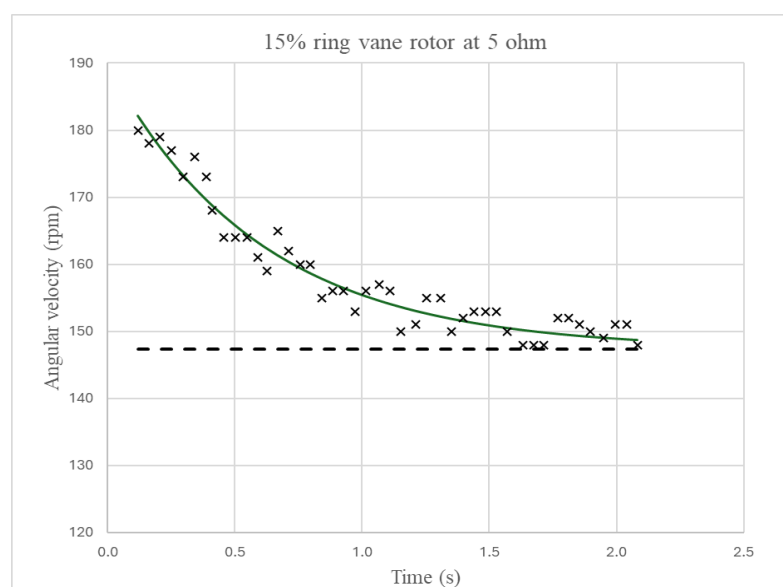
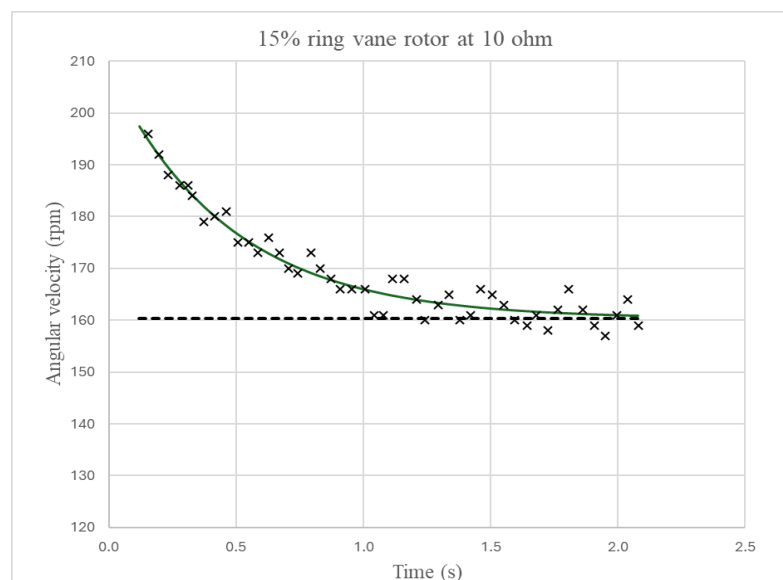
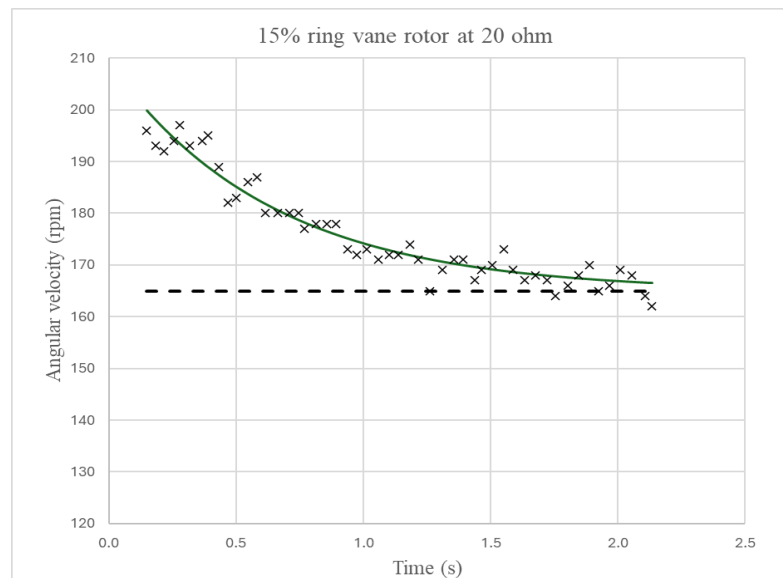
²⁾for 3kHz ~ 15kHz only

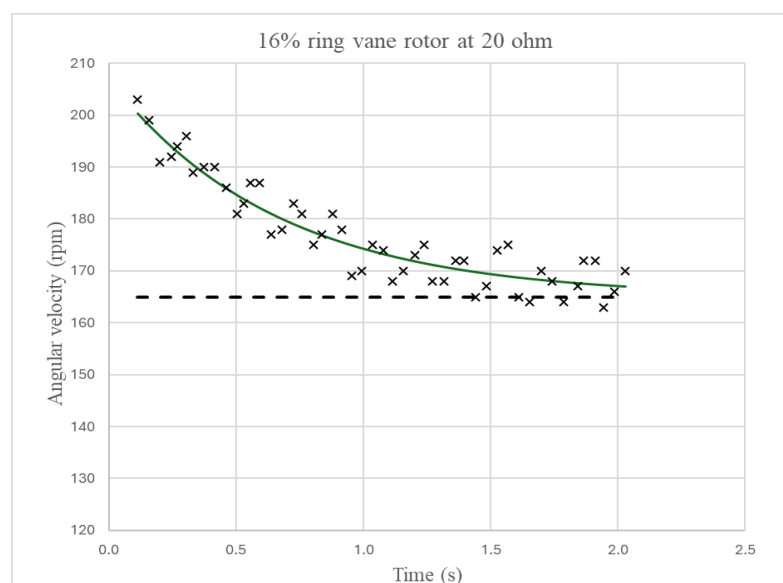
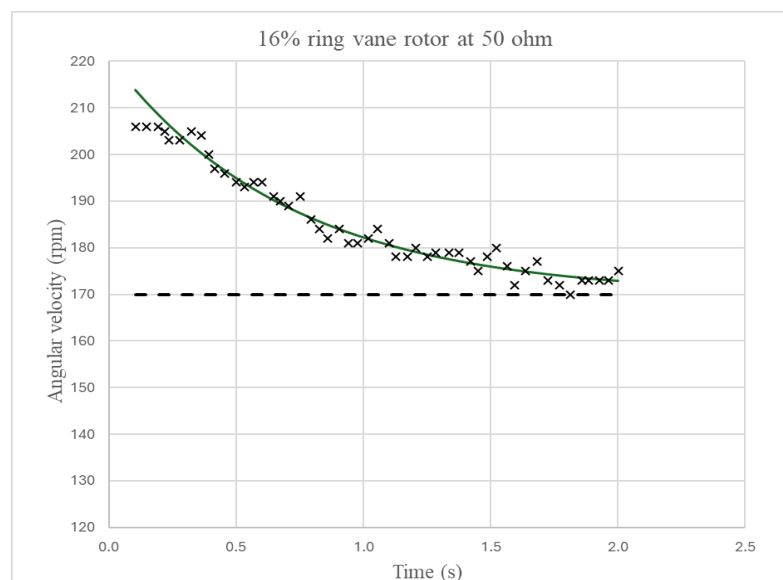
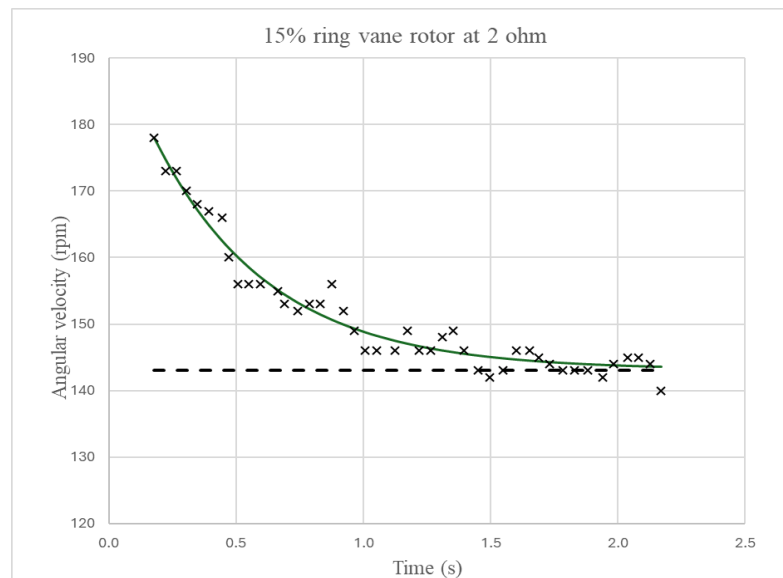
Input Impedance: $10\text{M}\Omega$, 50pF nominal
(80pF nominal for mV ranges)

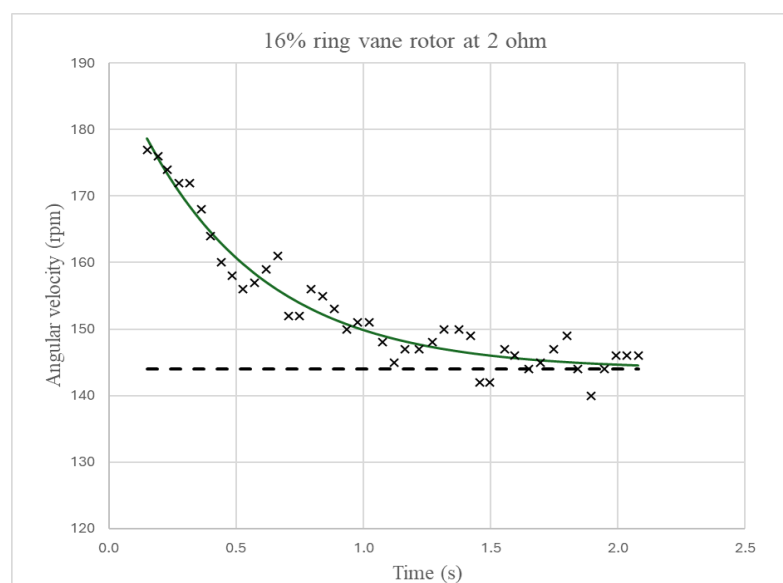
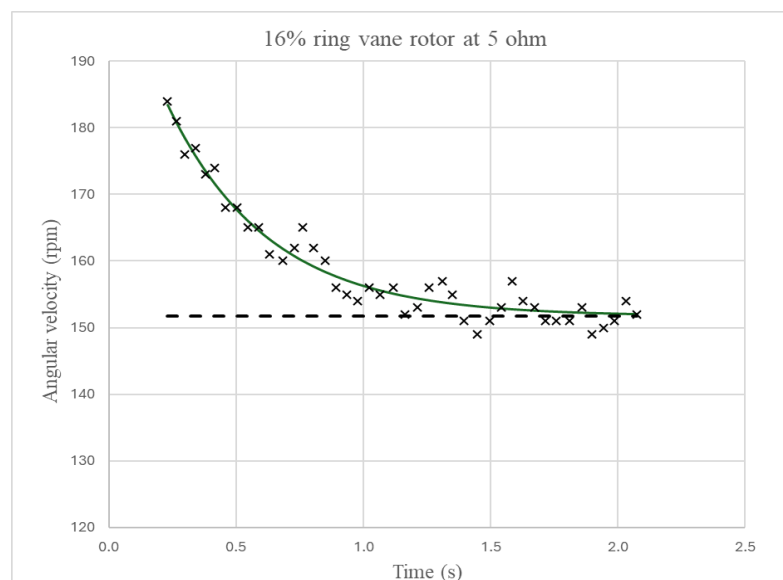
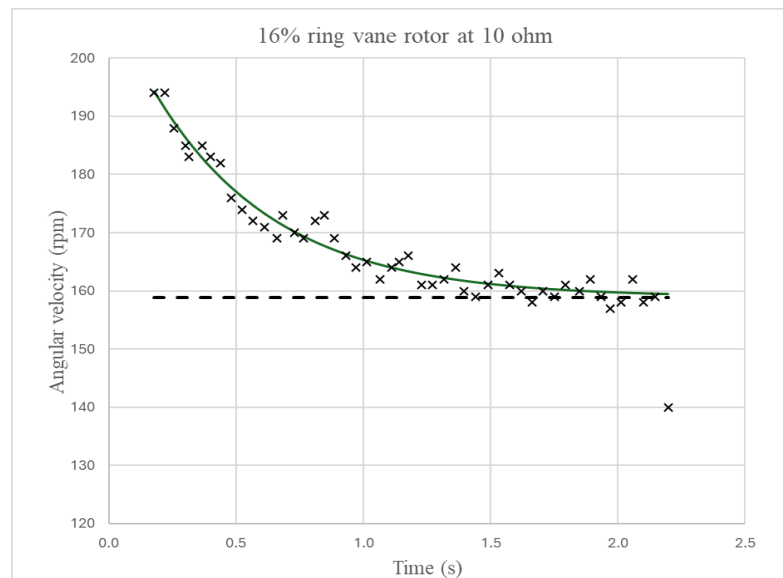
Appendix F: Experimental decay curves and standard deviation

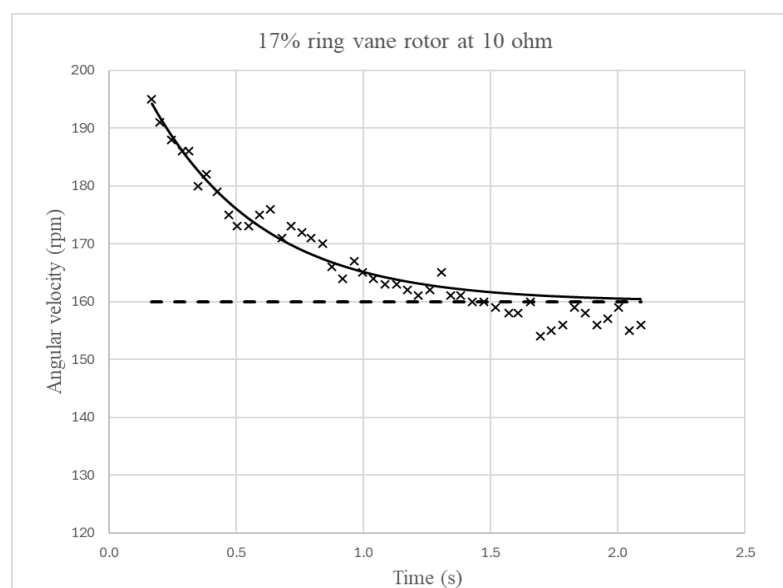
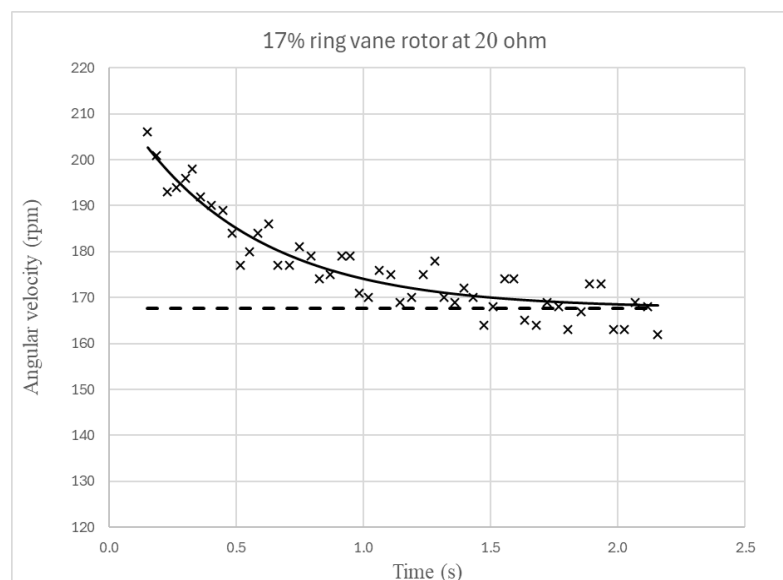
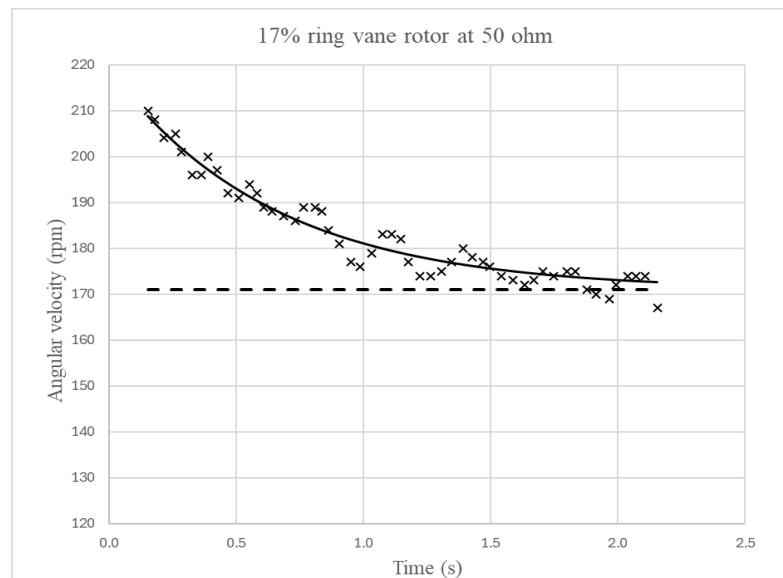


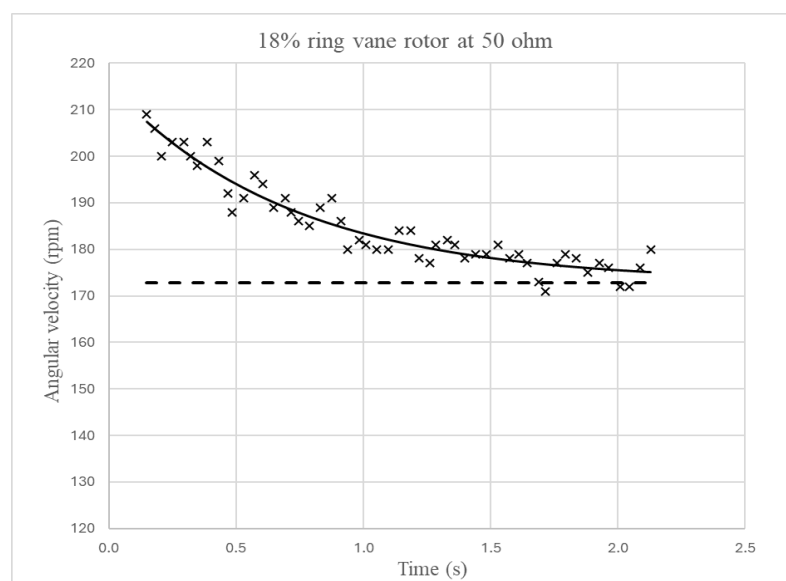
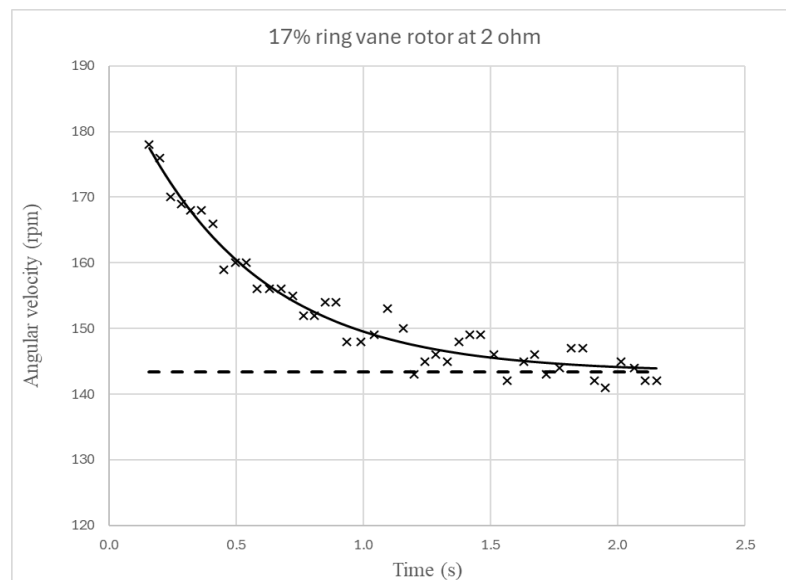
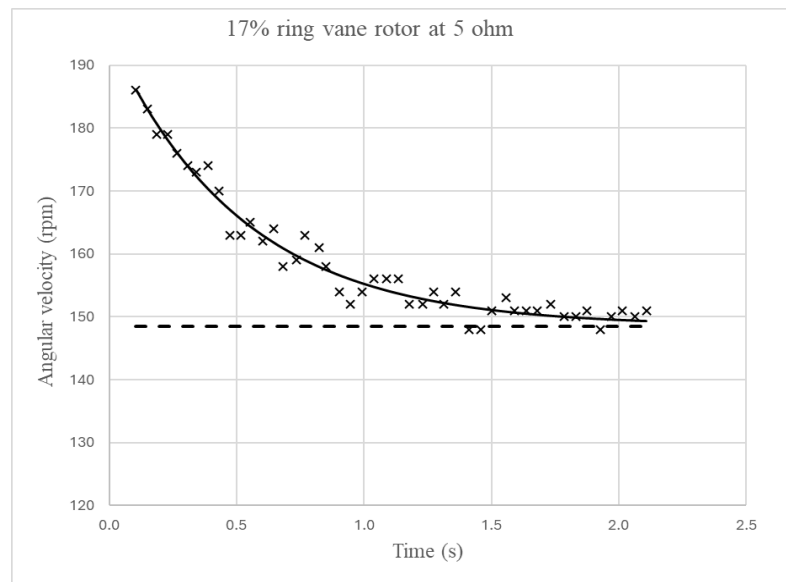


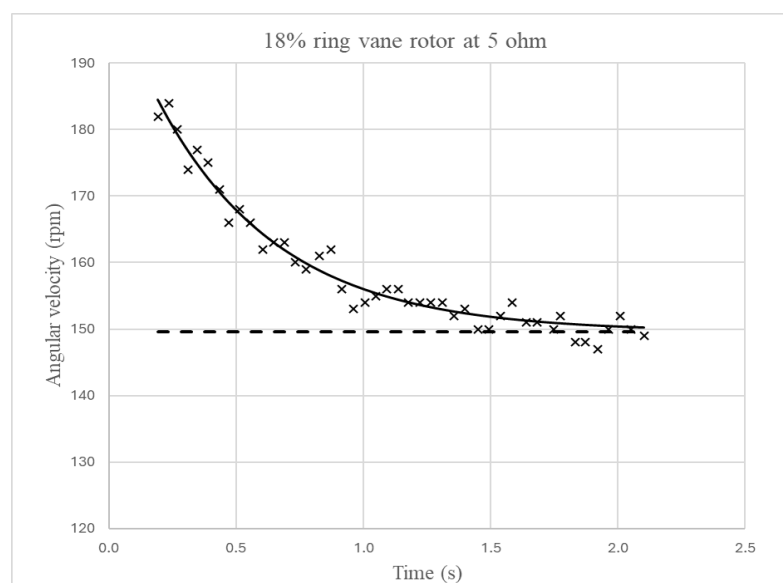
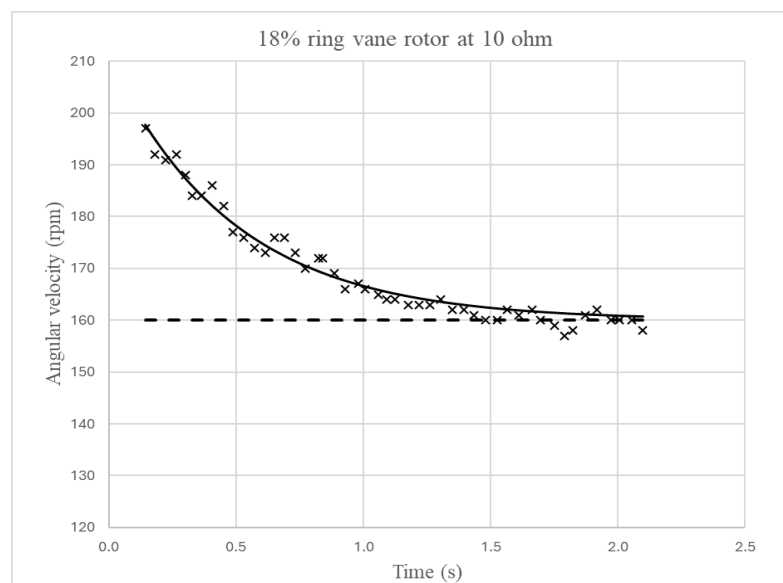
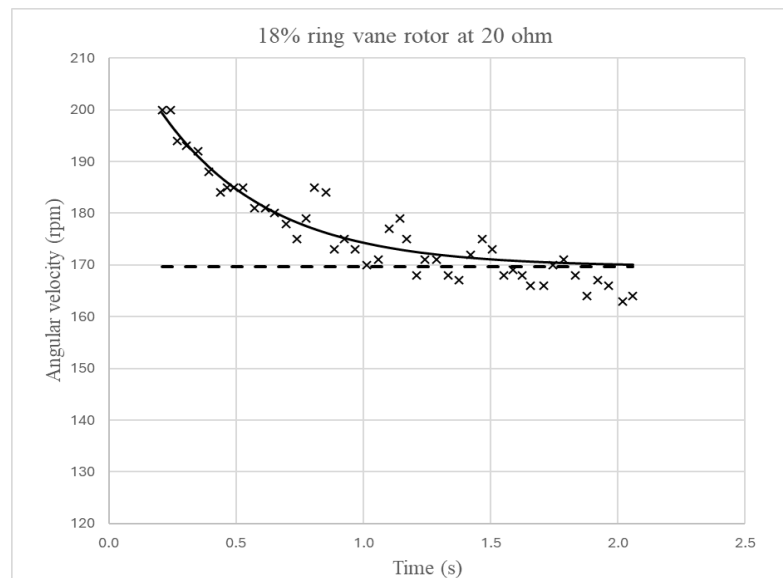


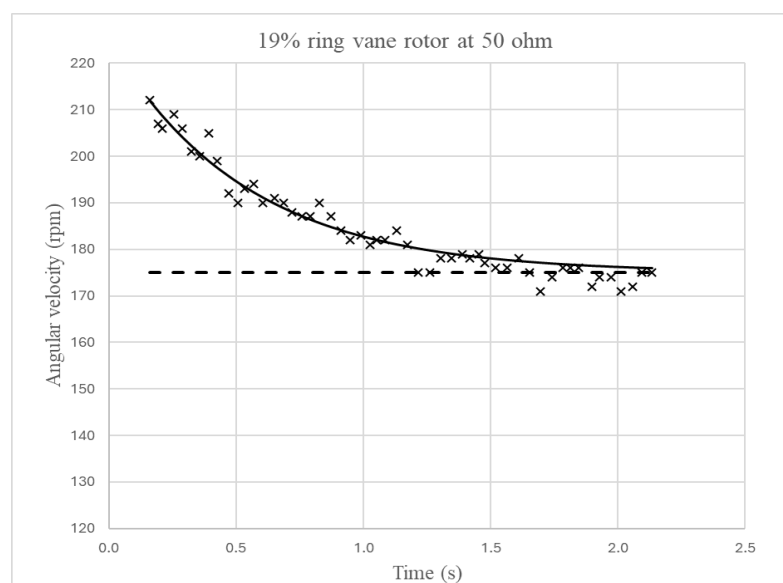
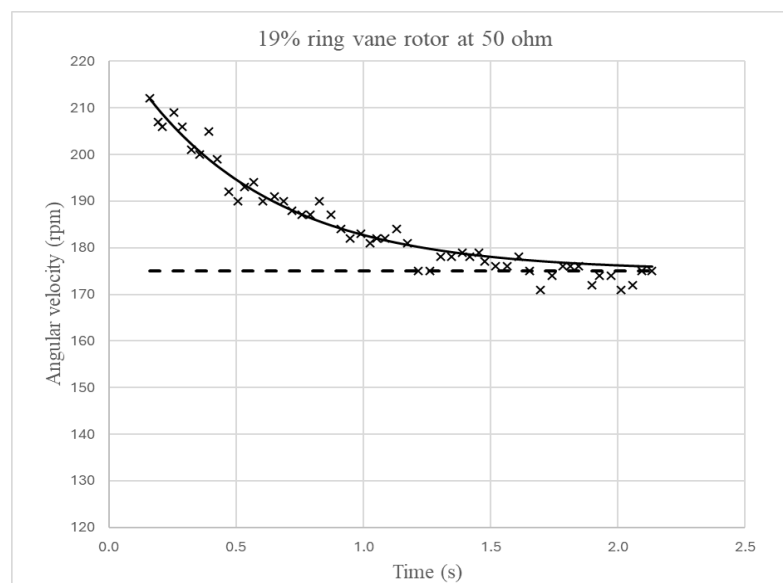
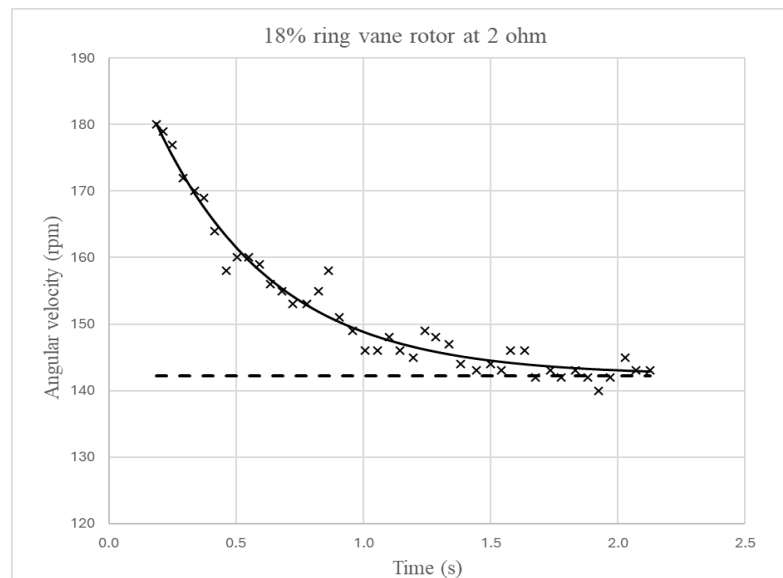


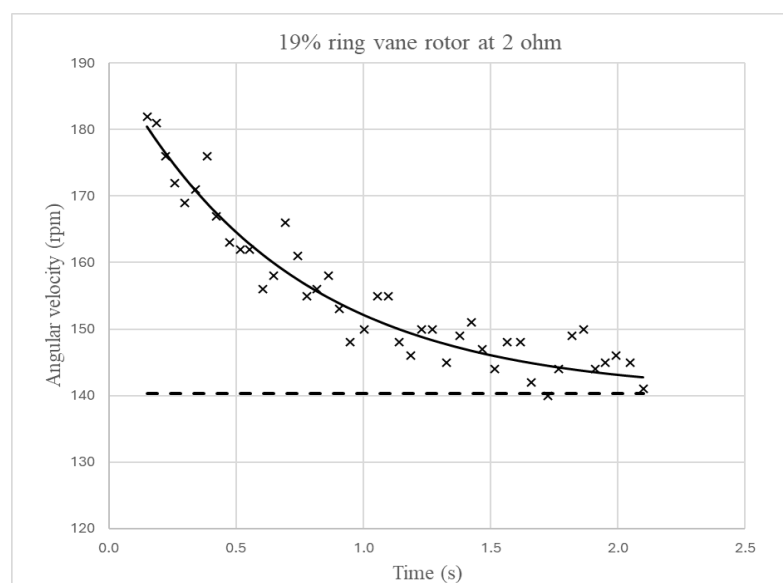
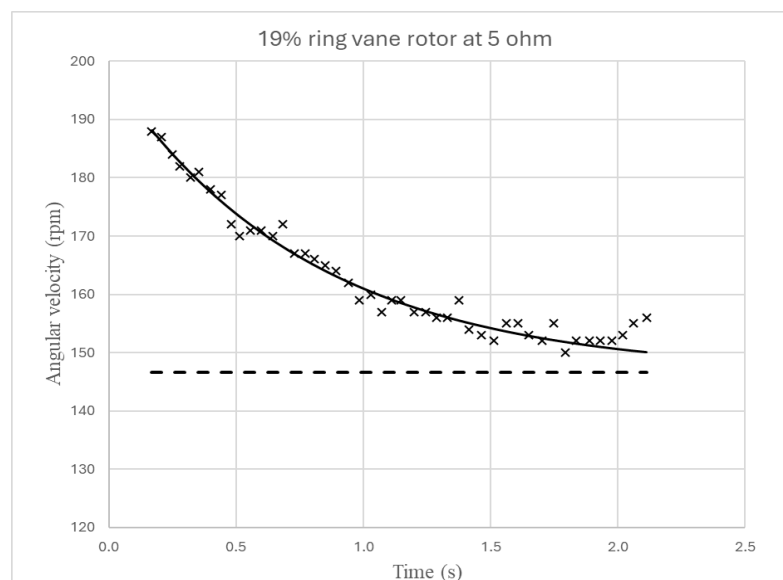
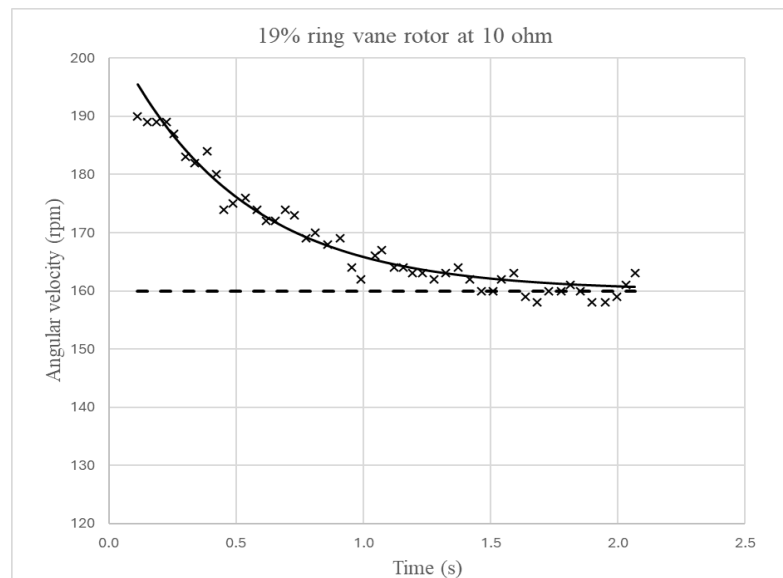


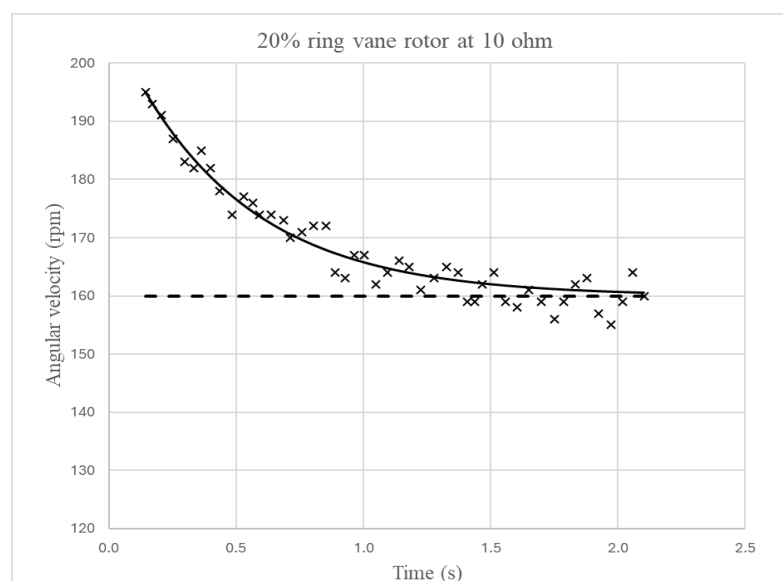
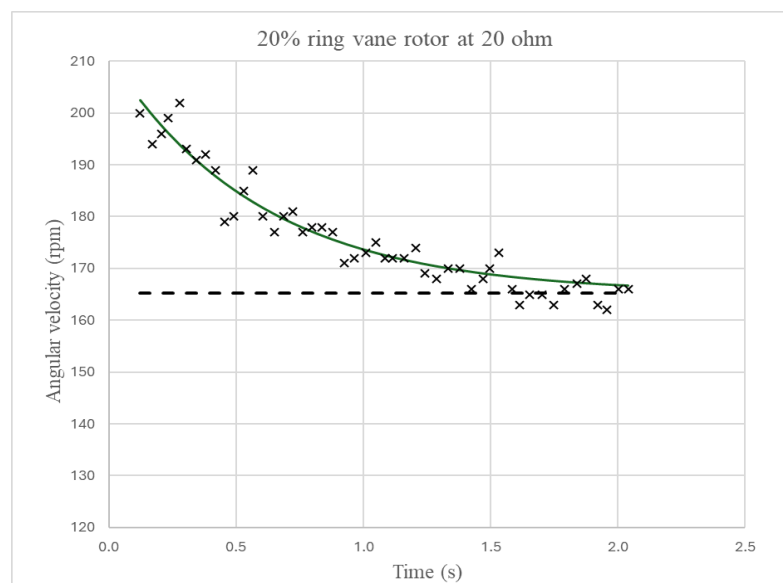
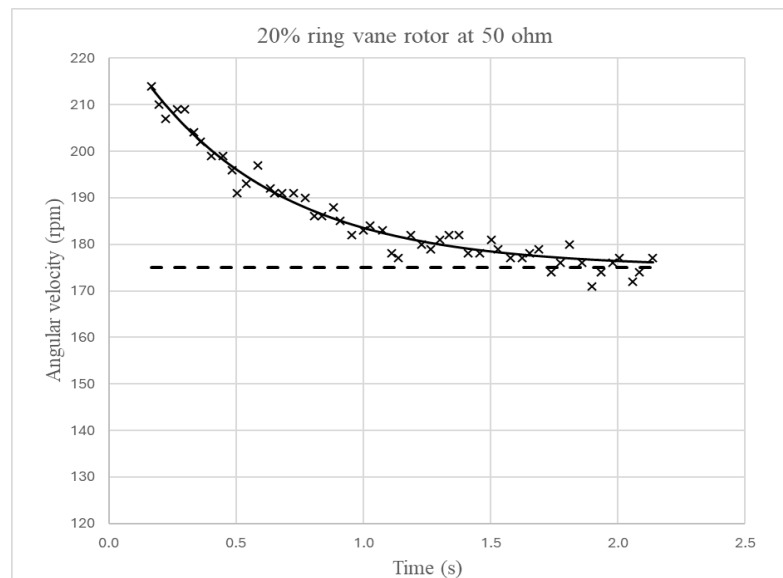


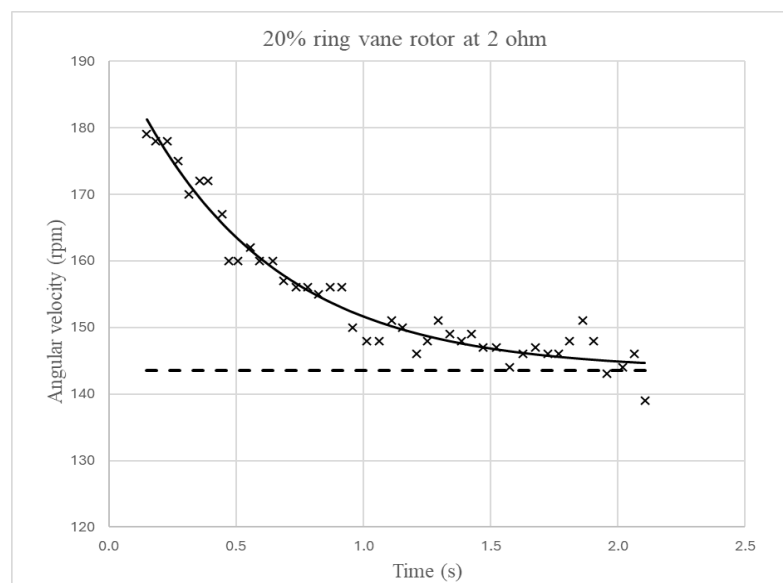
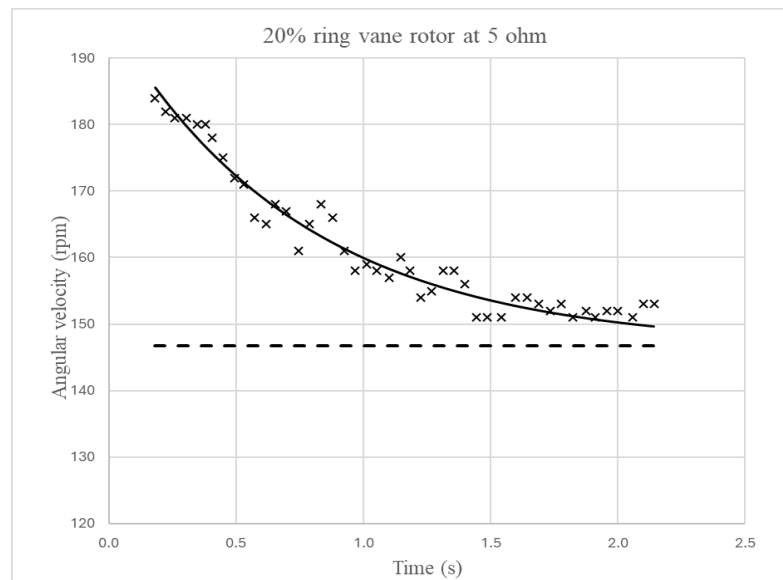












Appendix G: Statistical summary of the decay curves for all experimental data on all rotors

Std rotor

Resistive load	Total deviation = $\Sigma(\delta^2)$	Standard Deviation (s)
R50	451.81	2.92
R20	419.65	2.90
R10	333.98	2.67
R5	230.16	2.29
R2	249.60	2.38

15% ring vane rotor

Resistive load	Total deviation = $\Sigma(\delta^2)$	Standard Deviation (s)
R50	416.72	2.80
R20	345.85	2.60
R10	304.26	2.52
R5	206.65	2.14
R2	165.99	1.94

16% ring vane rotor

Resistive load	Total deviation = $\Sigma(\delta^2)$	Standard Deviation (s)
R50	272.29	2.31
R20	523.02	3.27
R10	181.24	1.92
R5	177.26	2.03
R2	250.76	2.41

17% ring vane rotor

Resistive load	Total deviation = $\Sigma(\delta^2)$	Standard Deviation (s)
R50	341.17	2.54
R20	615.70	3.47
R10	351.47	2.73
R5	168.16	1.91
R2	184.97	2.05

18% ring vane rotor

Resistive load	Total deviation = $\Sigma(\mathcal{J})$	Standard Deviation (s)
R50	307.08	2.48
R20	320.98	2.73
R10	164.85	1.87
R5	142.11	1.80
R2	165.85	1.96

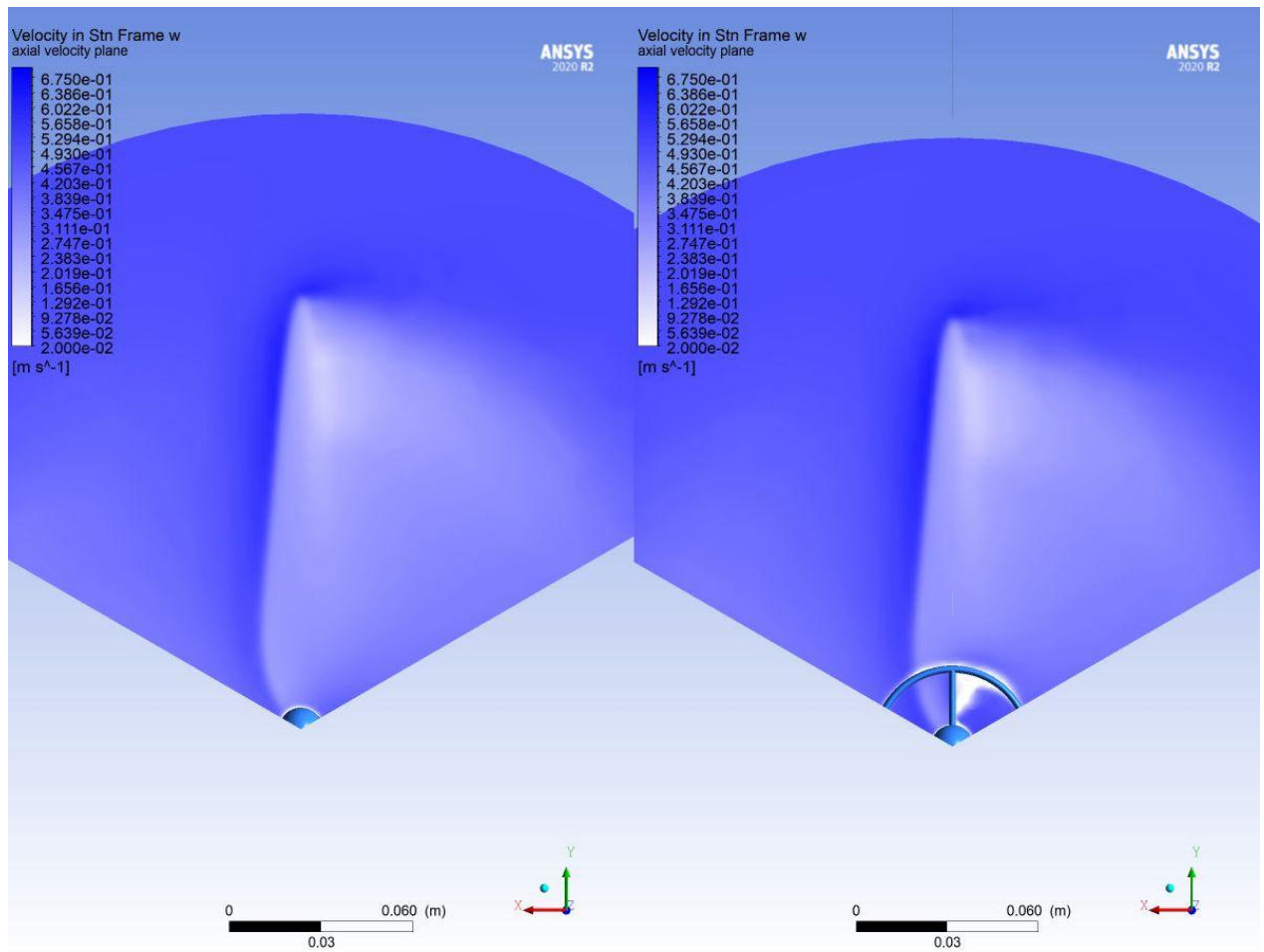
19% ring vane rotor

Resistive load	Total deviation = $\Sigma(\mathcal{J})$	Standard Deviation (s)
R50	333.66	2.51
R20	316.46	2.52
R10	151.51	1.81
R5	161.72	1.87
R2	329.83	2.87

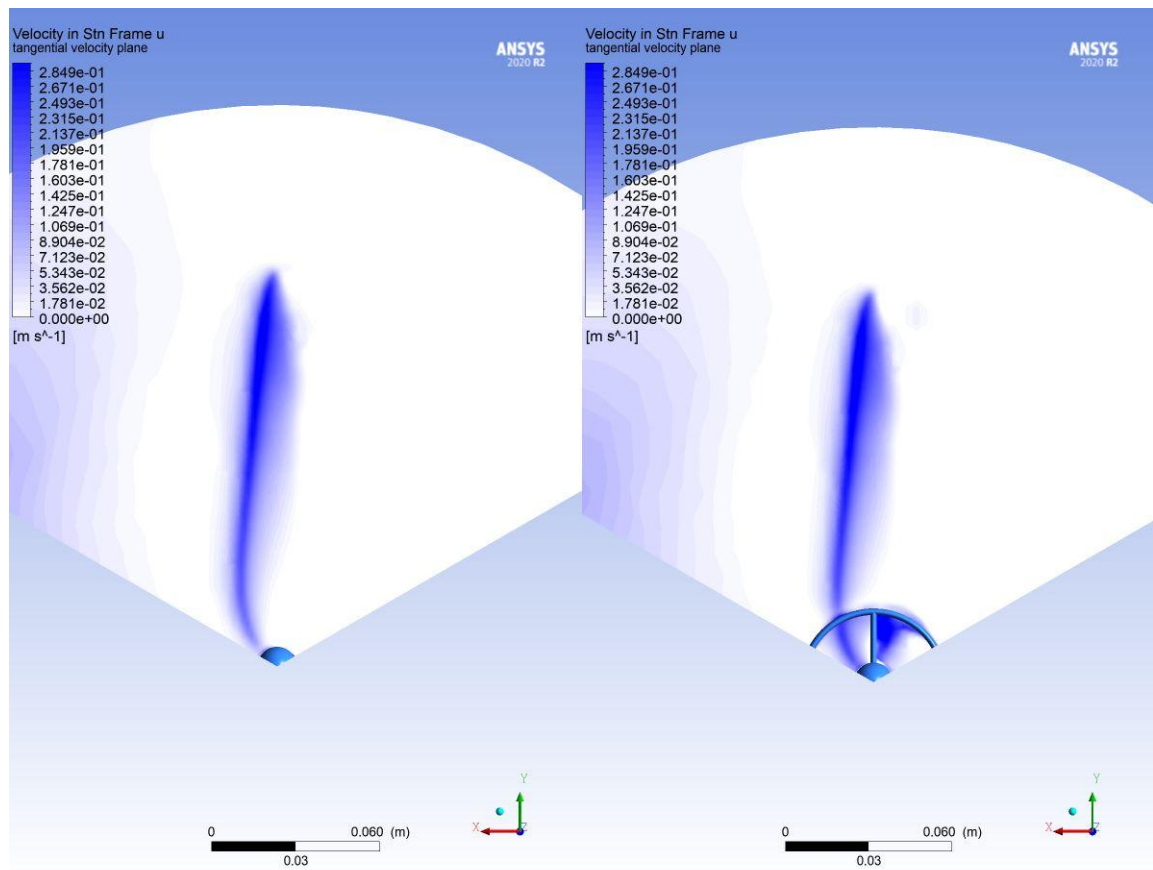
20% ring vane rotor

Resistive load	Total deviation = $\Sigma(\mathcal{J})$	Standard Deviation (s)
R50	247.46	2.16
R20	450.26	3.06
R10	278.31	2.43
R5	213.02	2.15
R2	228.19	2.28

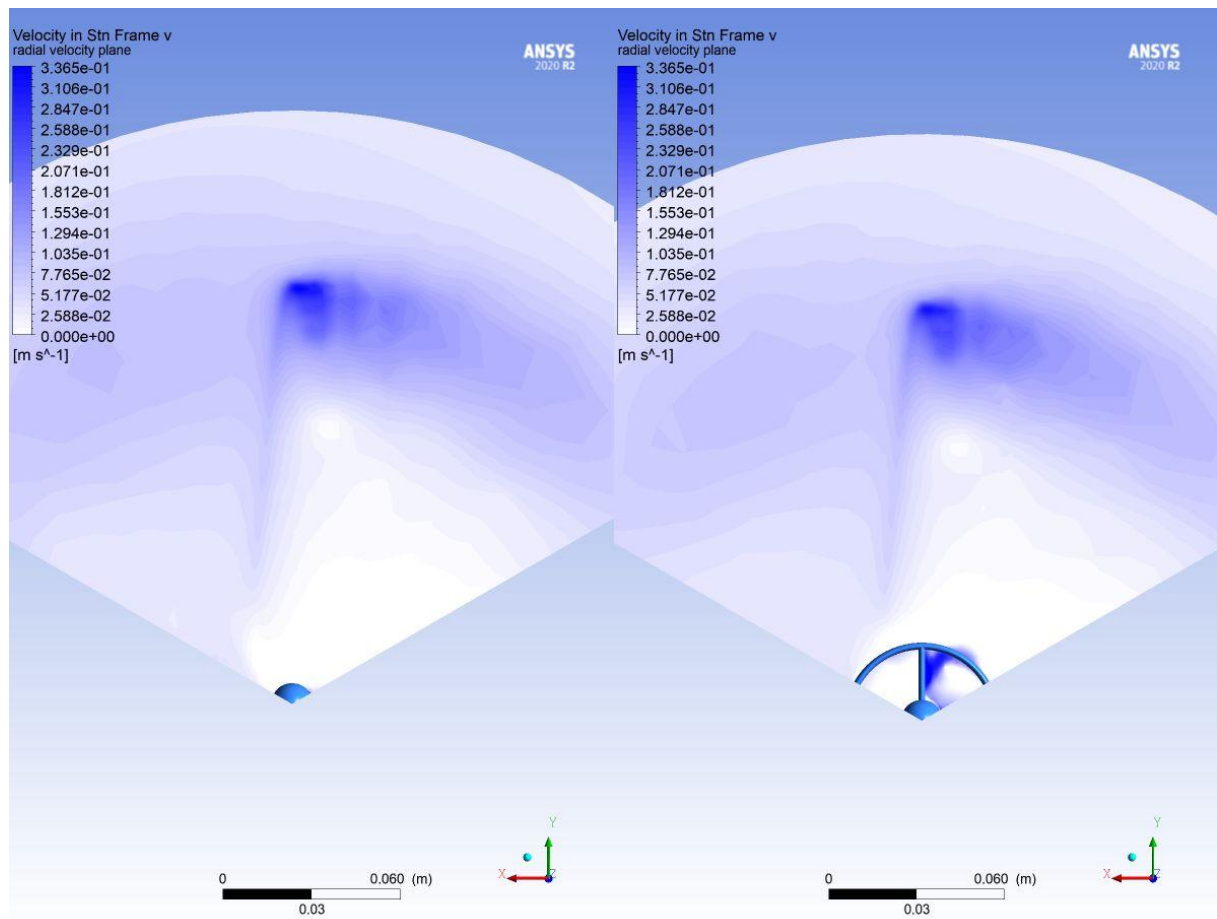
Appendix H: Axial, radial and tangential flow visualisation for the standard and 18% ring vane rotors for 0.5 m/s free stream velocity



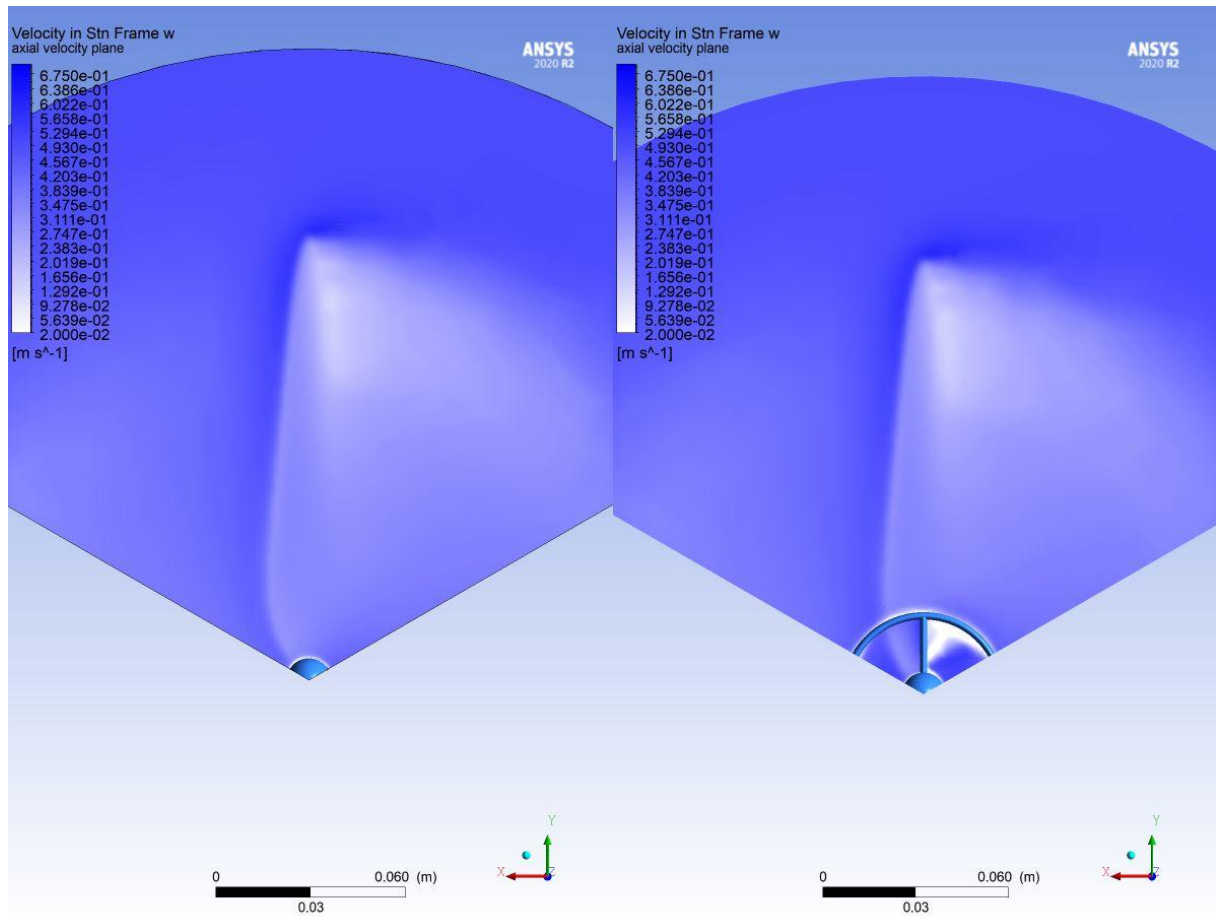
Axial velocity contours on standard rotor (left) and 18% ring vane rotor (right) at 4.7 TSR for 0.5 m/s free stream velocity at plane 2mm in front of rotor



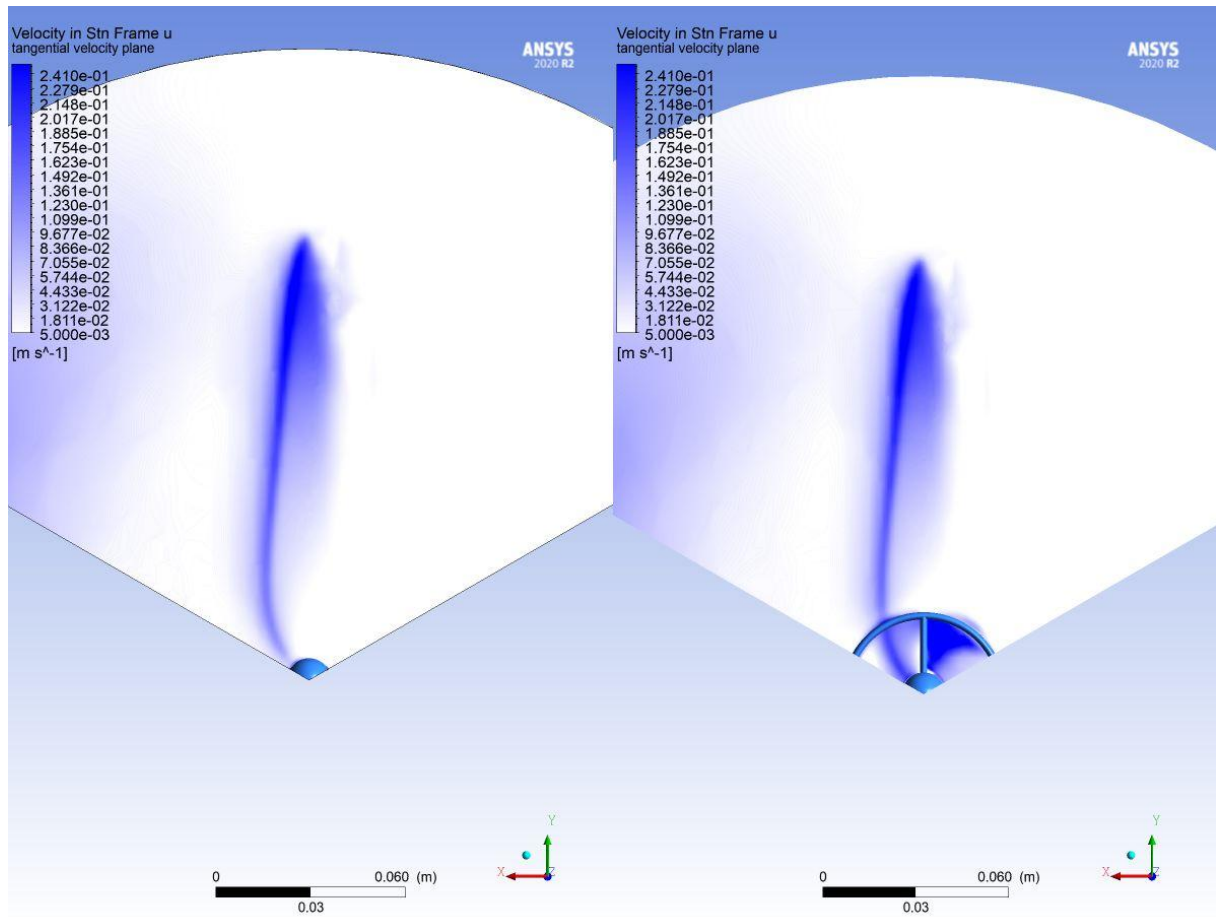
Tangential velocity contours on standard rotor (left) and 18% ring vane rotor (right) at 4.7 TSR for 0.5 m/s free stream velocity at plane 2mm in front of rotor



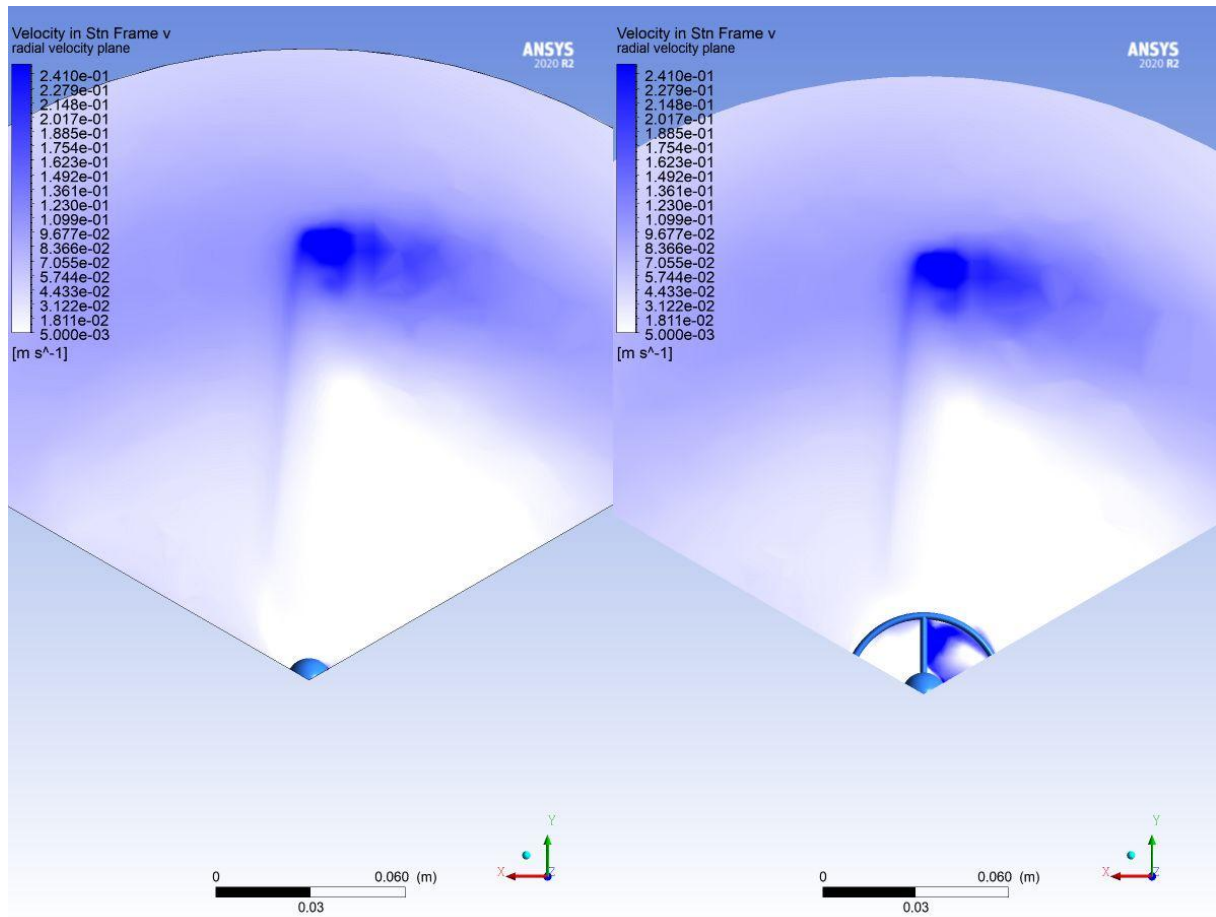
Radial velocity contours on standard rotor (left) and 18% ring vane rotor (right) at 4.7 TSR for 0.5 m/s free stream velocity at plane 2mm in front of rotor



Axial velocity contours on standard rotor (left) and 18% ring vane rotor (right) at 5.9 TSR for 0.5 m/s free stream velocity at plane 2mm in front of rotor

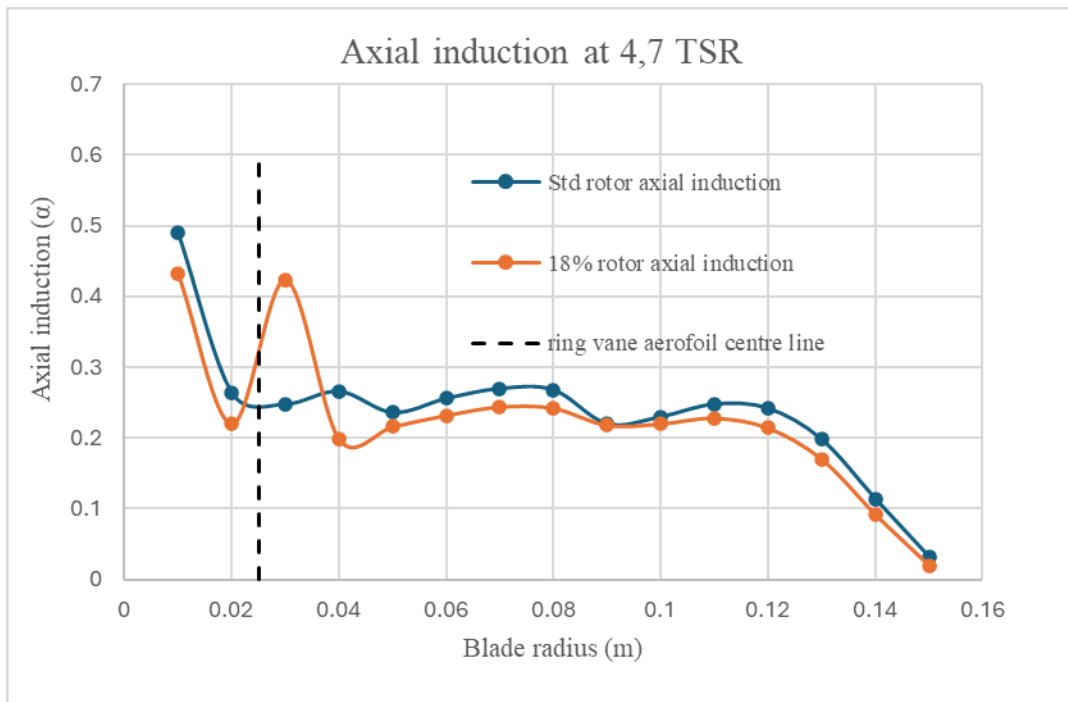


Tangential velocity contours on standard rotor (left) and 18% ring vane rotor (right) at 5.9 TSR for 0.5 m/s free stream velocity at plane 2mm in front of rotor

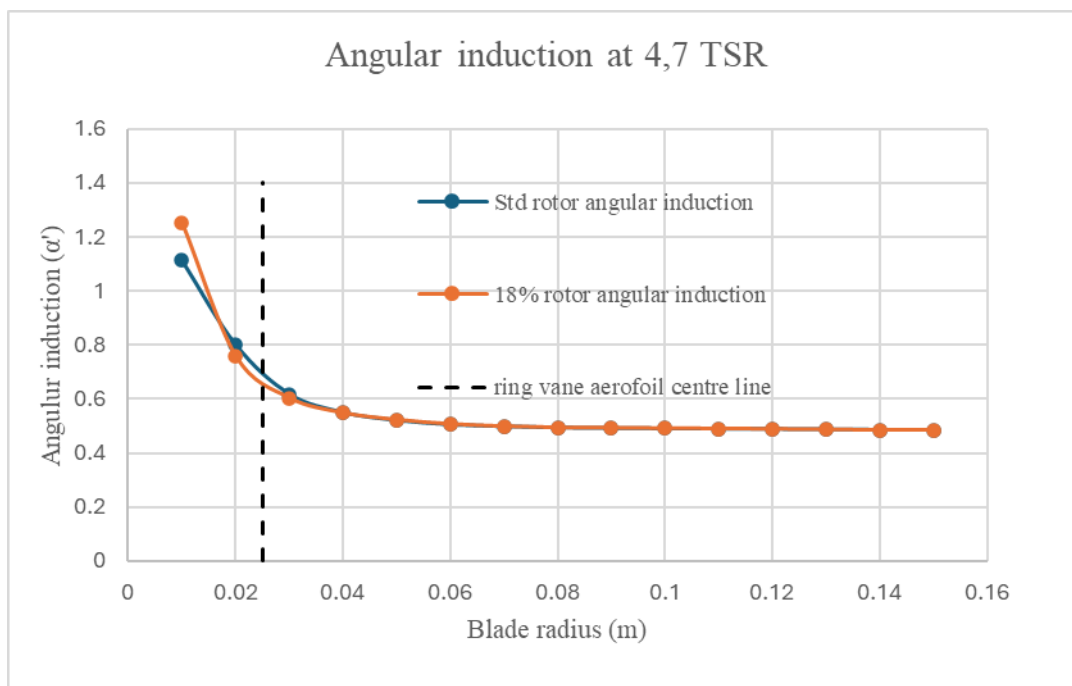


Radial velocity contours on standard rotor (left) and 18% ring vane rotor (right) at 5.9 TSR for 0.5 m/s free stream velocity at plane 2mm in front of rotor

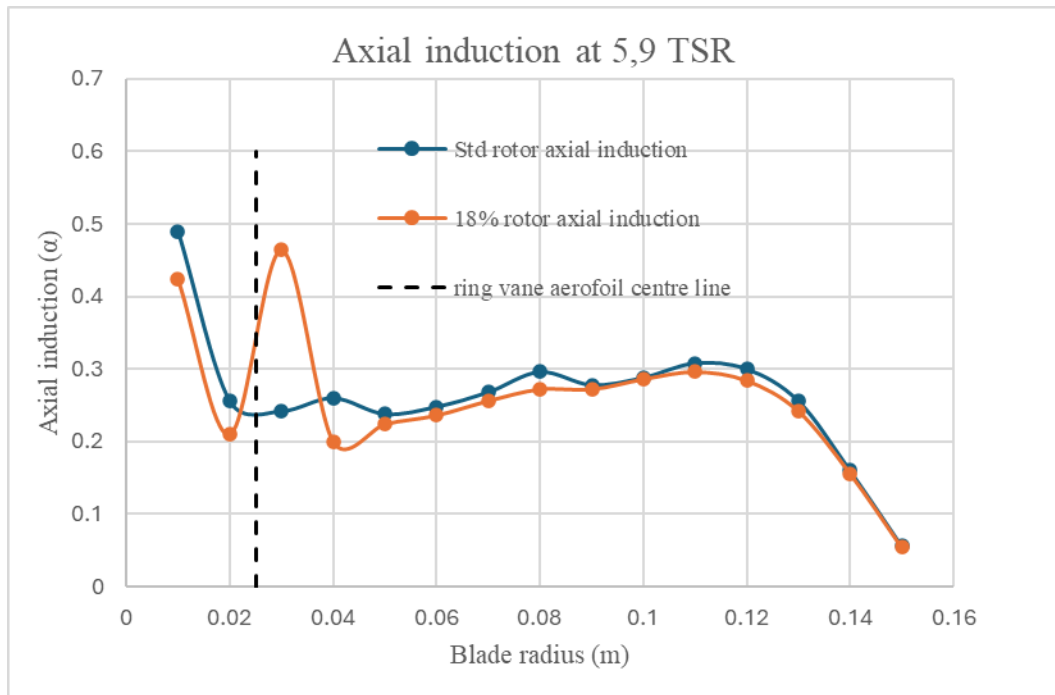
Appendix I: Axial and angular induction factor for standard and 18% ring vane rotor at off-peak performance at 4.7 and 5.9 tip speed ratios



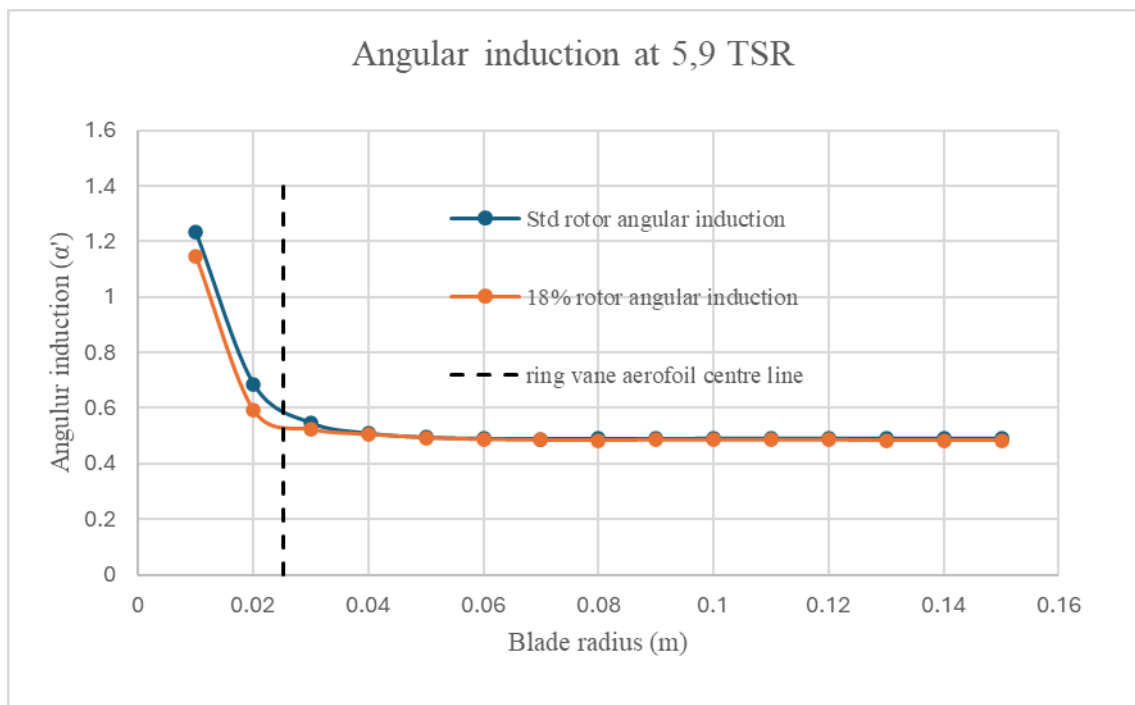
Axial induction factor for standard and 18 % ring vane rotor at 4.7 TSR



Angular induction factor for standard and 18 % ring vane rotor at 4.7 TSR

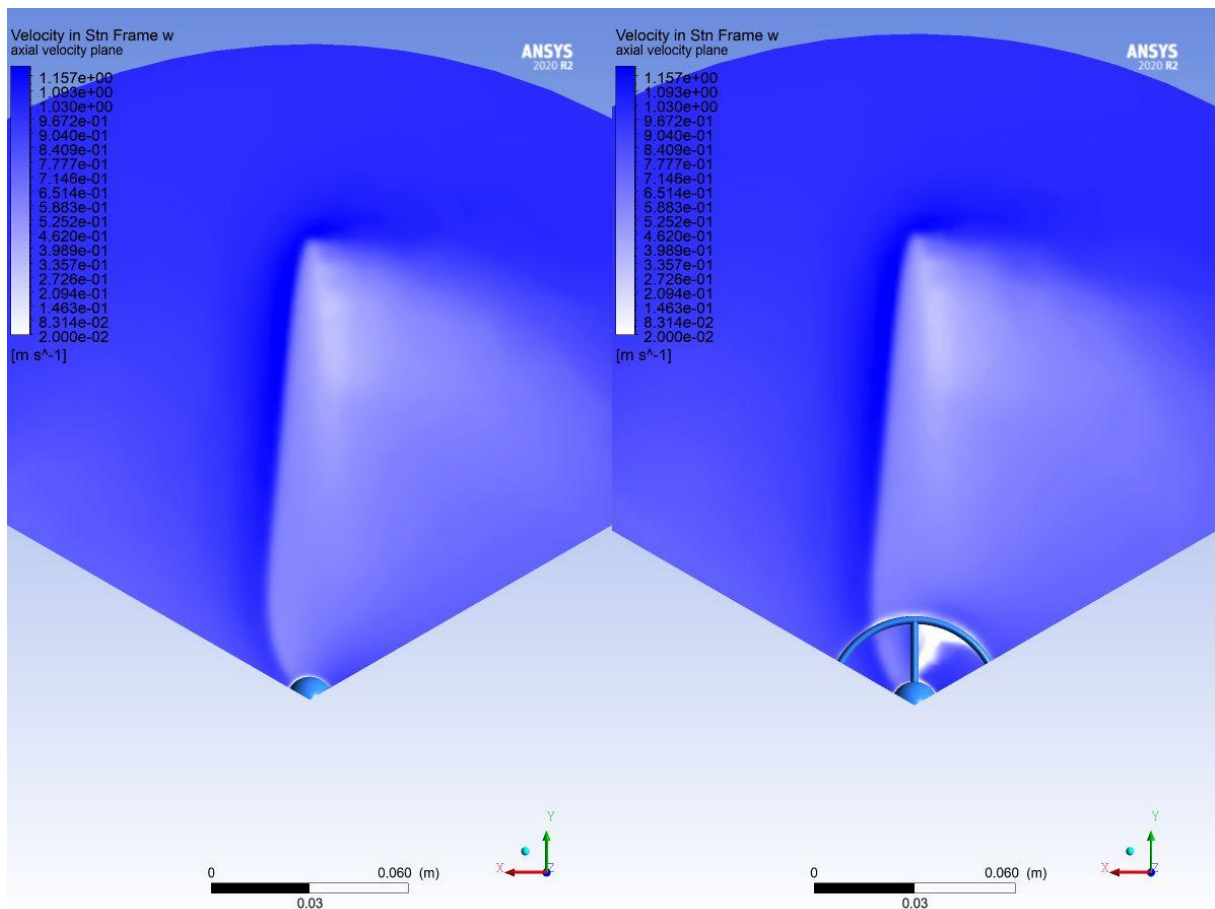


Axial induction factor for standard and 18 % ring vane rotor at 5.9 TSR

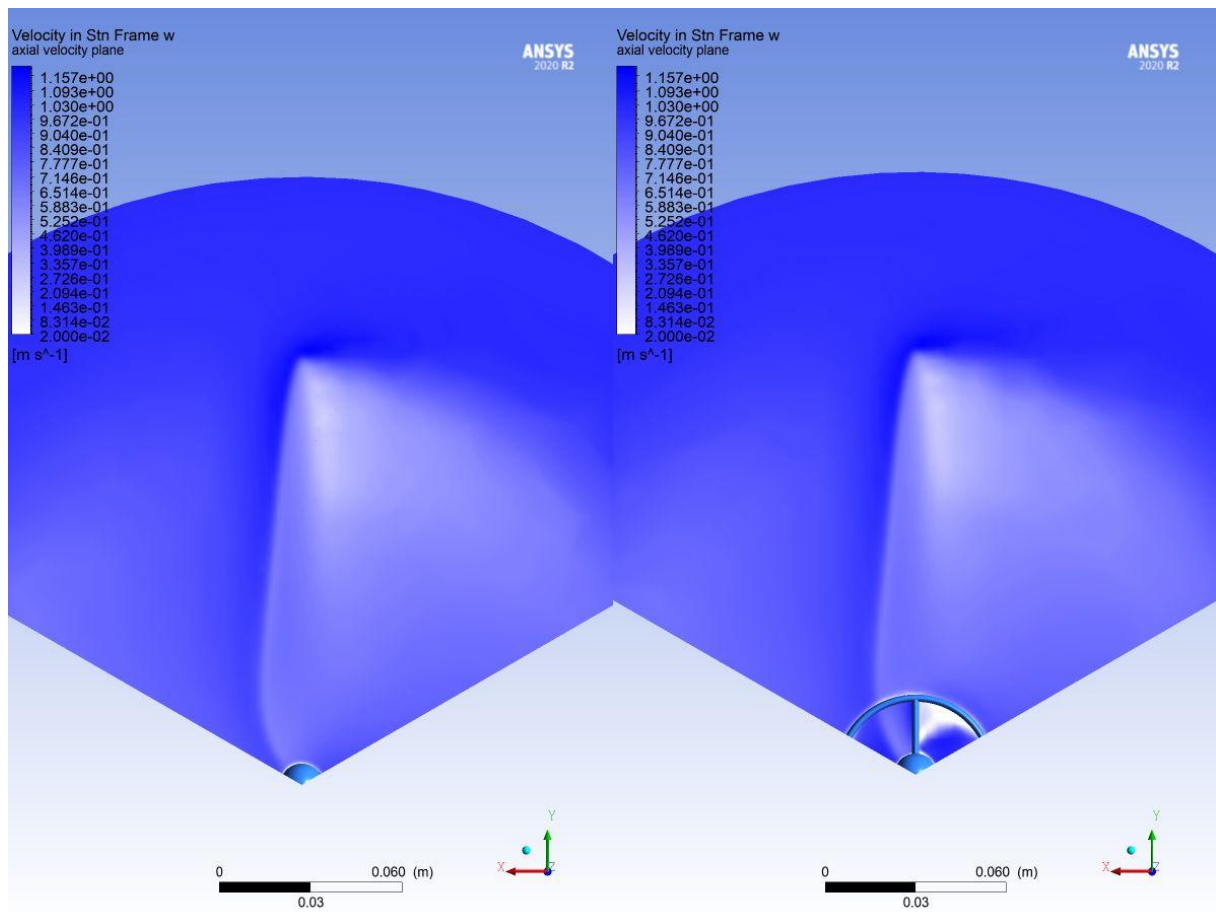


Angular induction factor for standard and 18 % ring vane rotor at 5.9 TSR

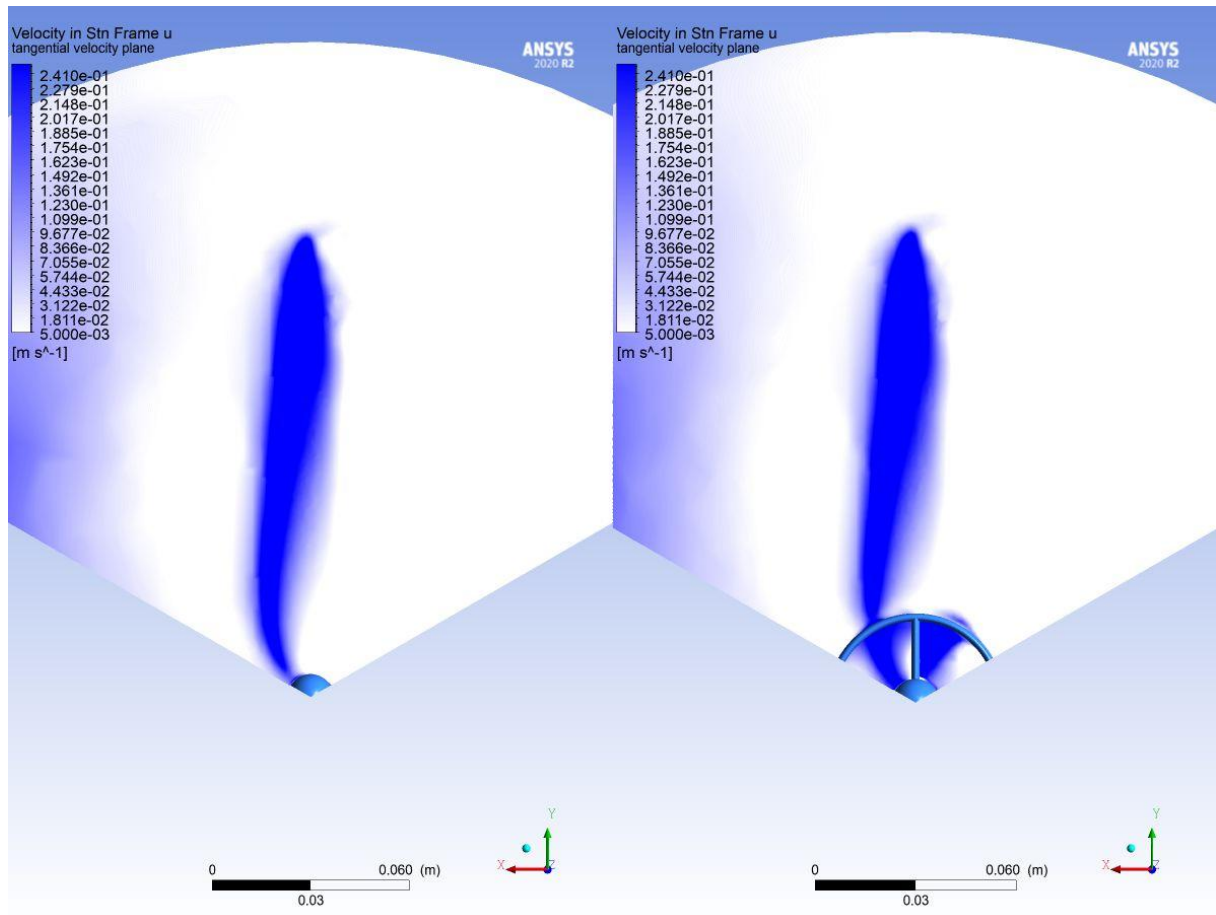
Appendix J: Axial, radial and tangential flow visualisation for the standard and 18% ring vane rotors for 1 m/s free stream velocity



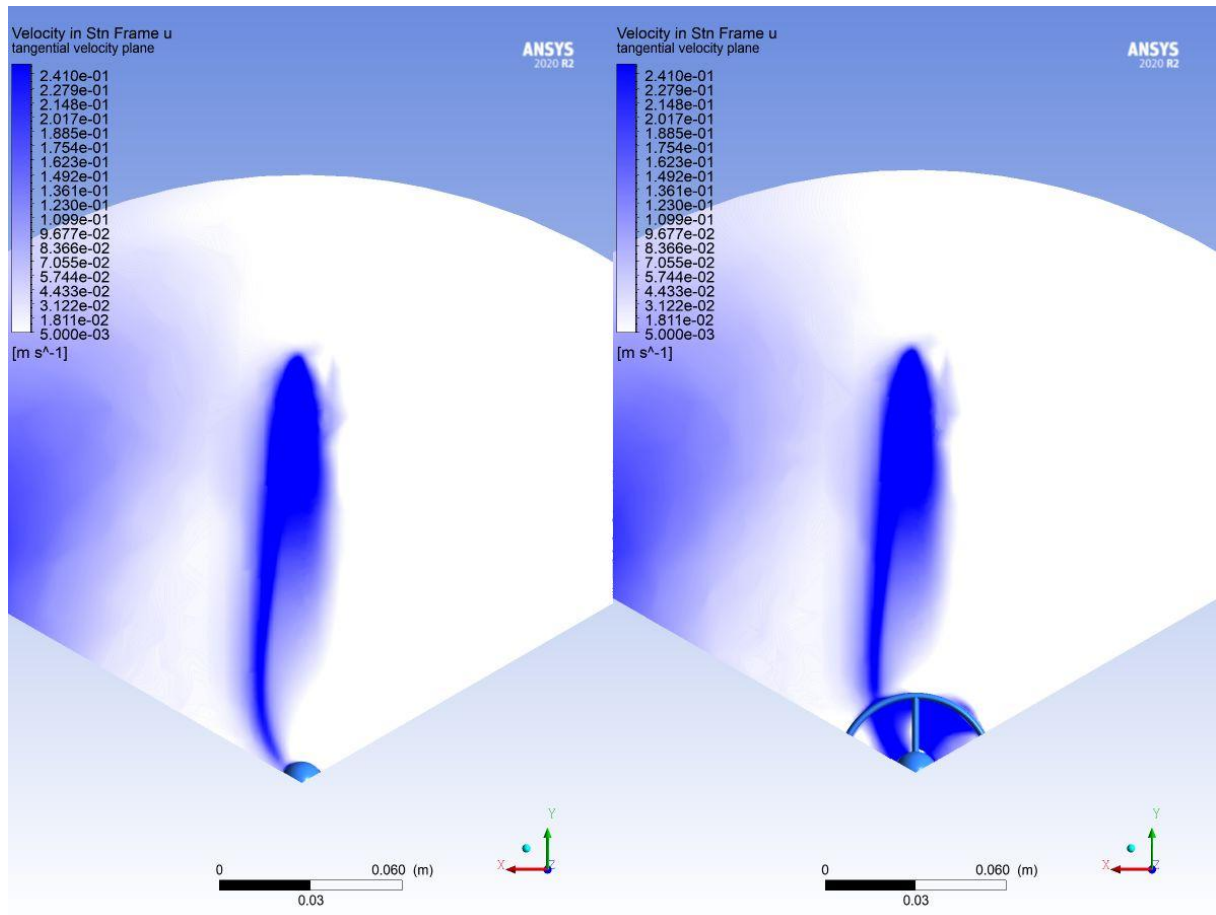
Axial velocity contours on standard rotor (left) and 18% ring vane rotor (right) at 4.4 TSR for 1 m/s free stream velocity at plane 2mm in front of rotor



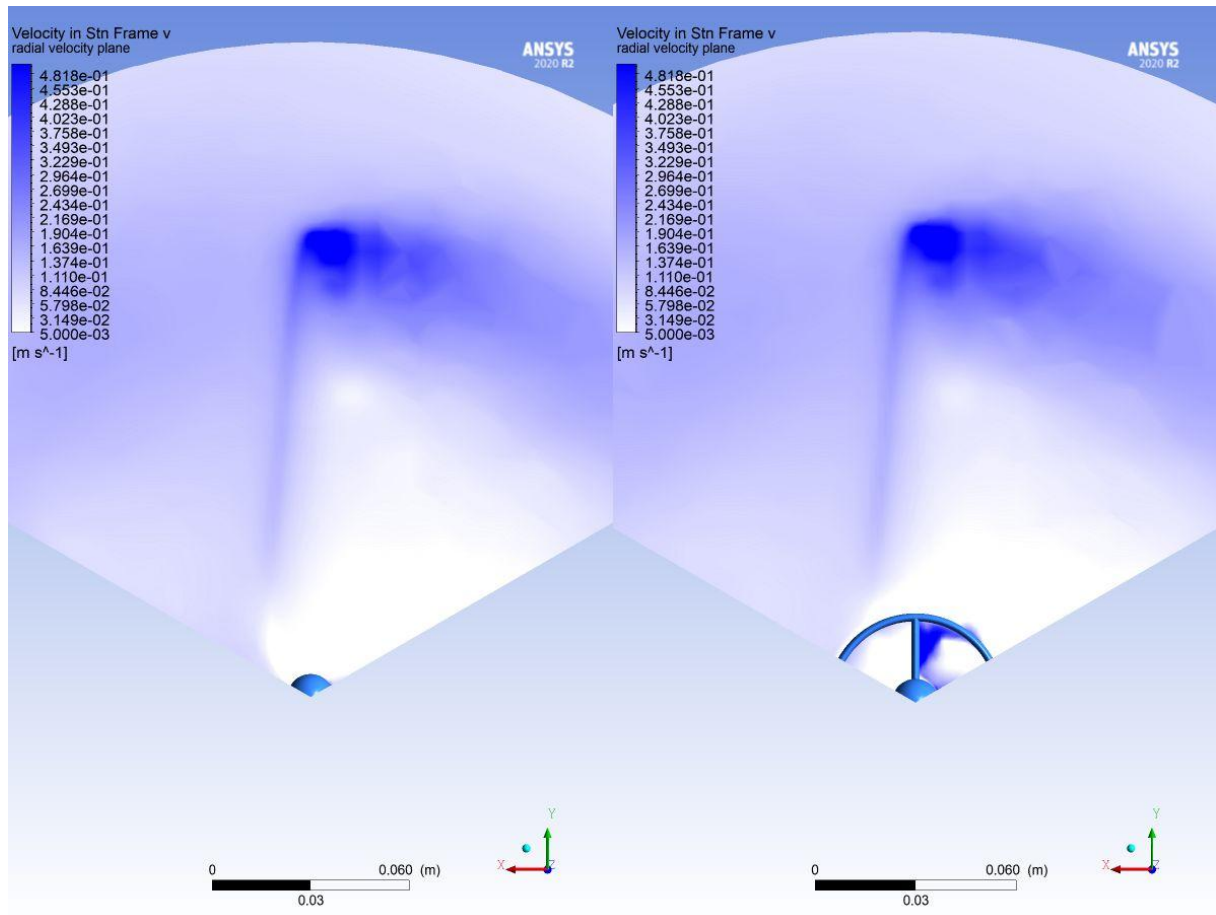
Axial velocity contours on standard rotor (left) and 18% ring vane rotor (right) at 6 TSR for 1 m/s free stream velocity at plane 2mm in front of rotor



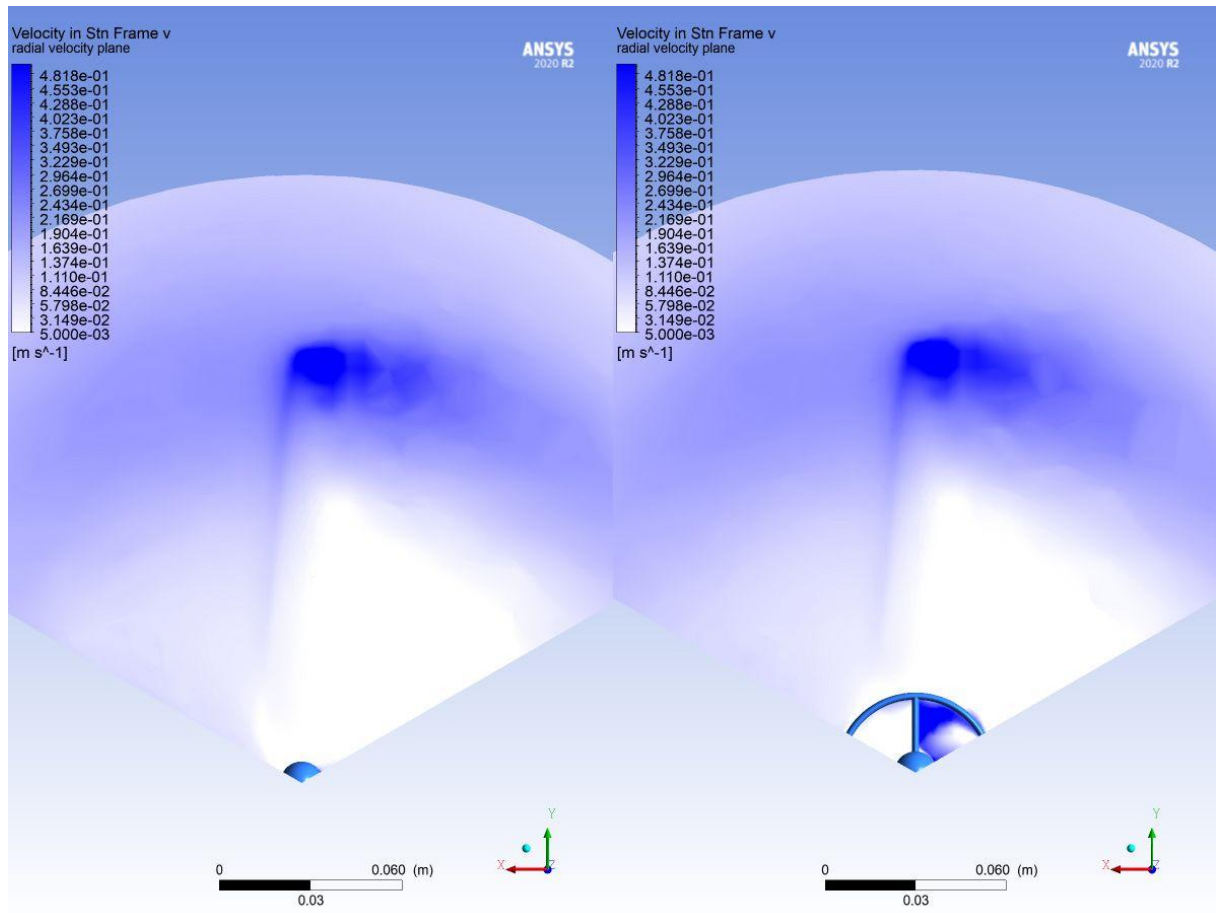
Tangential velocity contours on standard rotor (left) and 18% ring vane rotor (right) at 4.4 TSR for 1 m/s free stream velocity at plane 2mm in front of rotor



Tangential velocity contours on standard rotor (left) and 18% ring vane rotor (right) at 6 TSR for 1 m/s free stream velocity at plane 2mm in front of rotor

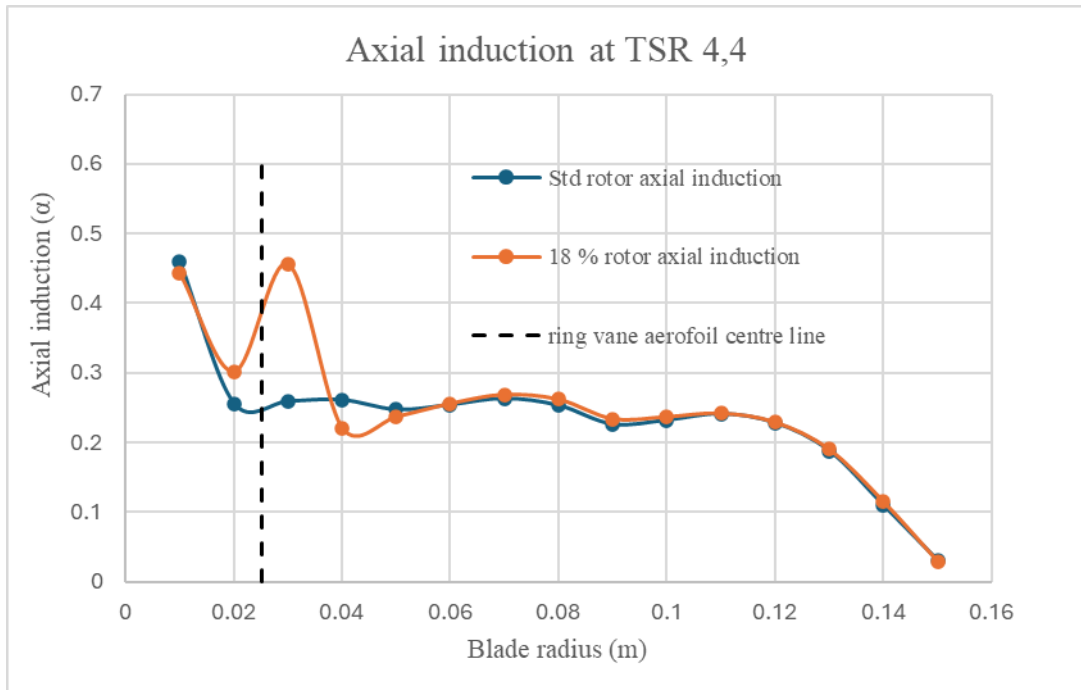


Radial velocity contours on standard rotor (left) and 18% ring vane rotor (right) at 4.4 TSR for 1 m/s free stream velocity at plane 2mm in front of rotor

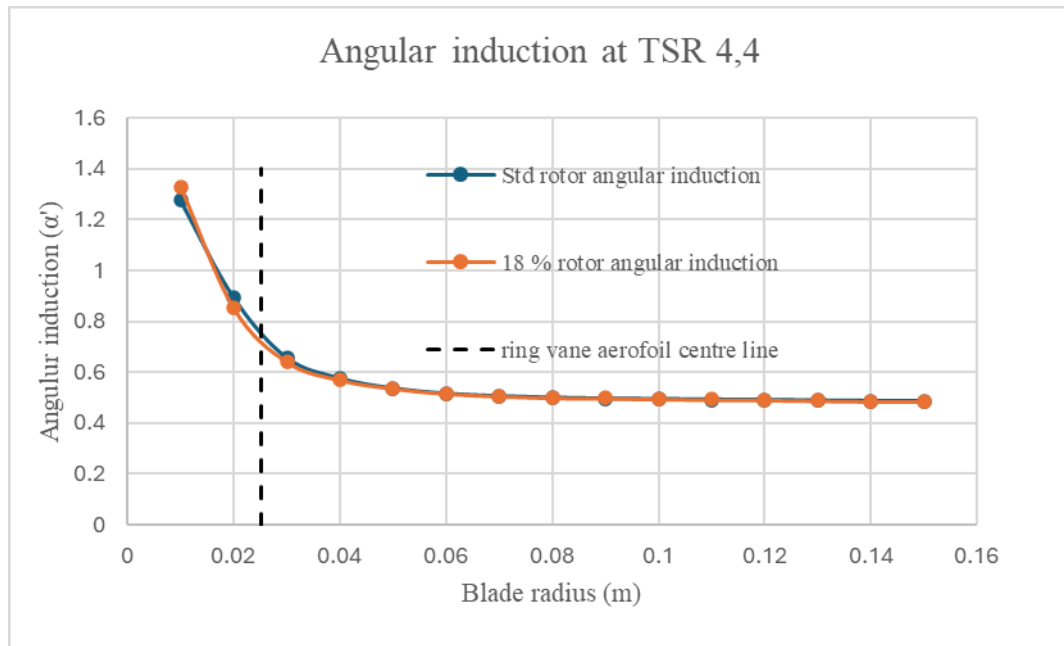


Radial velocity contours on standard rotor (left) and 18% ring vane rotor (right) at 6 TSR for 1 m/s free stream velocity at plane 2mm in front of

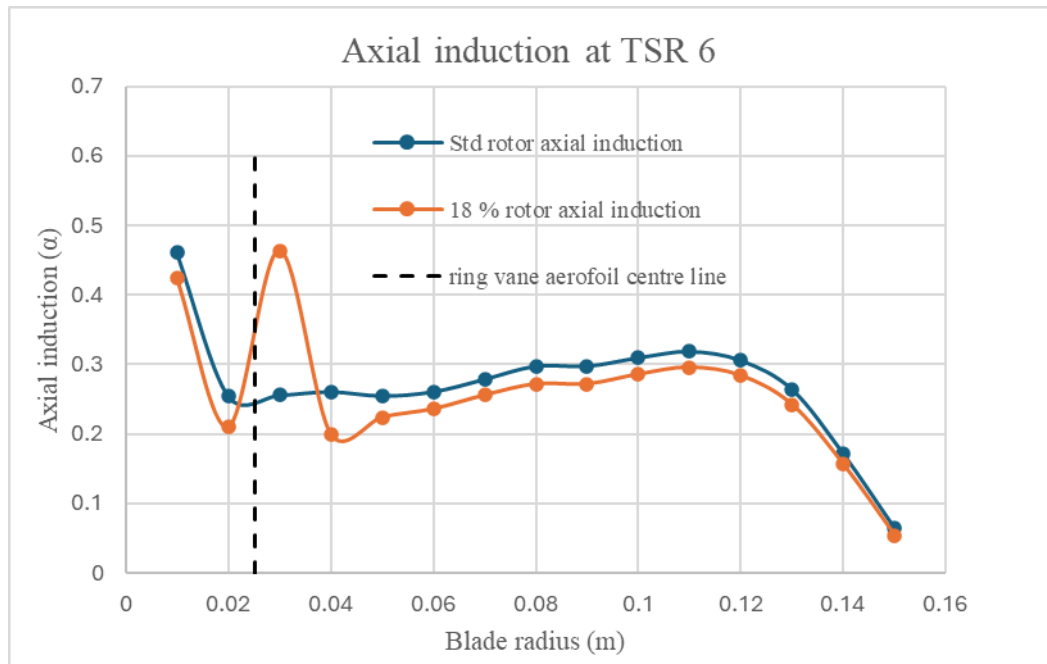
Appendix K: Axial and angular induction factor for standard and 18% ring vane rotor at off-peak performance at 4.4 and 6 TSR for 1 m/s free stream velocity



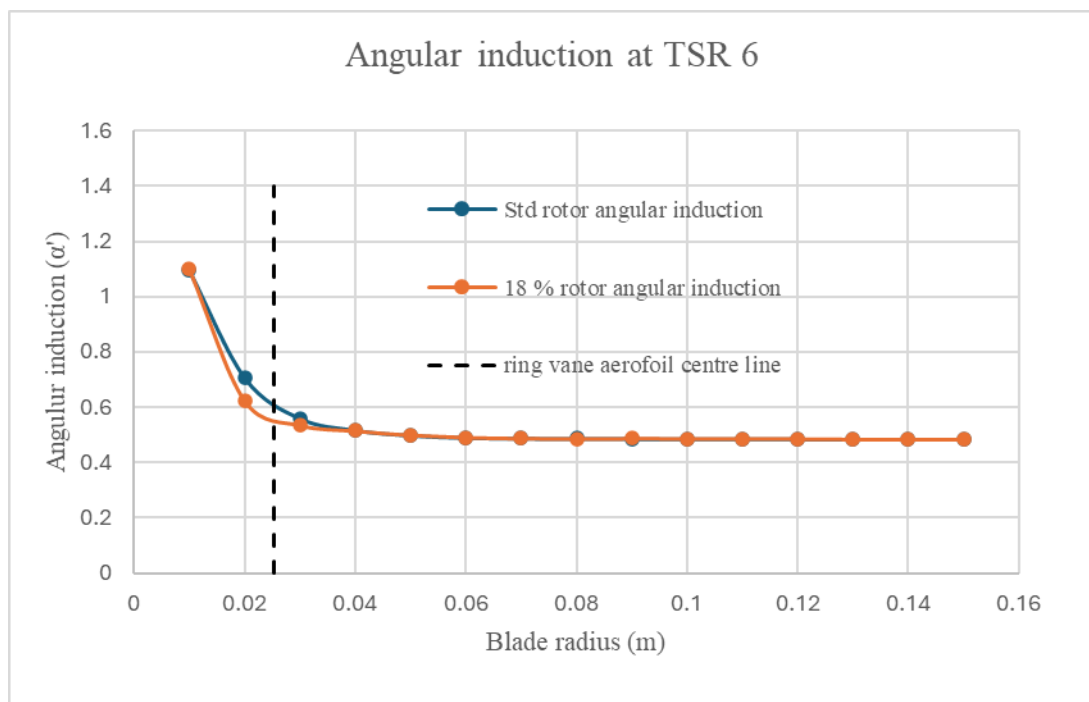
Axial induction factor for standard and 18% ring vane rotor at 4.4 TSR for 1 m/s free stream velocity



Angular induction factor for standard and 18% ring vane rotor at 4.4 TSR for 1 m/s free stream velocity



Axial induction factor for standard and 18% ring vane rotor at 6 TSR for 1 m/s free stream velocity



Angular induction factor for standard and 18% ring vane rotor at 6 TSR for 1 m/s free stream velocity

REFERENCES

Airfoil profiles. n.d. <https://texample.net/tikz/examples/airfoil-profiles> [September 28, 2023]

Álvarez-Álvarez, E., Rico-Secades, M., Fernández-Jiménez, A., Espina-Valdés, R., Corominas, E.L. & Calleja-Rodríguez, A.J. 2020. Hydrodynamic water tunnel for characterization of hydrokinetic microturbines designs. *Clean Technologies and Environmental Policy*, 22(9):1843–1854. doi.org/10.1007/s10098-020-01924-w.

Aranake, A.C. and Duraisamy, K. (2017) “Assessment of Shrouded Wind Turbine Concepts Using a Three-Dimensional RANS Solver,” *Wind Energy*, 20(2), pp. 289–303. Available at: <https://doi.org/10.1002/we.2008>.

Ansys. n.d. <https://www.ansys.com/resource-center/technical-paper/best-practice-geko-turbulence-modeling-in-ansys-cfd> [May 10, 2024]

Arumugam, S., Subramania, N. & Chidambaram, S. et al. 2016. Effect of Boundary Layer Fence Location on HAWT Power Performance. *Circuits and Systems*, 7(8):1177–1189. doi.org/10.4236/CS.2016.78101.

Barlas, T.K. and van Kuik, G.A.M. 2010. Review of state of the art in smart rotor control research for wind turbines. *Progress in Aerospace Sciences*, 46(1):1–27. doi.org/10.1016/j.paerosci.2009.08.002.

Barnard, D.R. and Ismail, D.F. (2022) “CFD Simulation of Horizontal Axis Wind Turbine Rotor with fitted guide ring.” Available at: <https://doi.org/10.5281/ZENODO.7366044>.

Berg, J.C., Barone, M.F. and van Dam, C.P. (2009) “Aerodynamic Performance Testing of Small Wind Turbines on a Moving Platform,” *Journal of Solar Energy Engineering*, 131, p. 31009.

Bastankhah, M. and Porté-Agel, F. 2017. A new miniature wind turbine for wind tunnel experiments. Part I: Design and performance. *Energies*, 10(7) doi.org/10.3390/en10070908.

Burton, T., Sharpe, D., Jenkins, N. & Bossanyi, E. 2001. *Wind Energy Handbook*. Wind Energy Handbook. John Wiley & Sons. doi.org/10.1002/9781119992714.

Carmicheal, B.H. 1981. Low Reynolds number airfoil survey. NASA CR 165803

Celik, I., Ghia, U. and Roache, P. (2008) “Procedure for Estimation and Reporting of Uncertainty due to Discretization in CFD Applications,” *Journal of Fluids Engineering*, 130(7), p. 78001.

Chamorro, L.P. and Porté-Agel, F. (2010) “Effects of Turbulent Intensity on Wind Turbine Performance,” *Journal of Wind Engineering and Industrial Aerodynamics*, 108, pp. 30–36.

Chen, T.Y. and Liou, L.R. (2011) “Blockage corrections in wind tunnel tests of small horizontal-axis wind turbines,” *Experimental Thermal and Fluid Science*, 35(3), pp. 565–569. Available at: <https://doi.org/10.1016/j.expthermflusci.2010.12.005>.

Civelek, Z., Lüy, M. and Çam, E. 2015. Control of Pitch Angle of Wind Turbine by Fuzzy Pid Controller. *Intelligent Automation & Soft Computing*, 22:1–9. doi.org/10.1080/10798587.2015.1095417.

Dawoud, B., Amer, E. and Gross, D. 2007. Performance analysis of CCHP and CHP systems operating following the thermal and electric load. *International journal of energy research*, 31(August

2007):135–147.
doi.org/10.1002/er.

Derksen, R.W., Agelinchaab, M. and Tachie, M. 2008. Characteristics of the flow over a NACA 0012 airfoil at low Reynolds numbers. *Advances in Fluid Mechanics*, 7:142–153.
doi.org/10.2495/AFM080141.

Det Norske Veritas. n.d. <http://www.dnvgl.com> [2019]

Dong, J., Viré, A. and Li, Z. 2022. Analysis the vortex ring state and propeller state of floating offshore wind turbines and verification of their prediction criteria by comparing with a CFD model. *Renewable Energy*, 184:15–25.
doi.org/10.1016/j.renene.2021.11.053

Elkodama, A., Ismaiel, A., Abdellatif, A., Shaaban, S., Yoshida, S., & Rushdi, M. A. 2023.

Control Methods for Horizontal Axis Wind Turbines (HAWT): State-of-the-Art Review. *Energies*, 16(17).
doi.org/10.3390/en16176394.

Fawkes, H.T. 2023. Hub ratio of horizontal axis wind turbine rotors for optimal performance. Cape Peninsula University of Technology, Bellville.
doi.org/https://etd.cput.ac.za/handle/20.500.11838/3960.

Gorban', A.N., Gorlov, A.M. and Silantyev, V.M. (2001) "Limits of the turbine efficiency for free fluid flow," *Journal of Energy Resources Technology, Transactions of the ASME*, 123(4), pp. 311–317. Available at: <https://doi.org/10.1115/1.1414137>.

Guoqiang, L., Weiguo, Z., Yubiao, J. & Pengyu, Y. 2019. Experimental investigation of dynamic stall flow control for wind turbine airfoils using a plasma actuator. *Energy*, 185:90–101.
doi.org/https://doi.org/10.1016/j.energy.2019.07.017.

Hansen, M.O.L. 2008. AERODYNAMICS OF WIND TURBINES Hearth Scan. London Sterling [Preprint].

Hartwanger, D. & Horvat, A. 2008. 3d modelling of a wind turbine using cfd.NAFEMS:1–14.

Herráez, I., Stoevesandt, B. and Peinke, J. 2014. Insight into rotational effects on a wind turbine blade using navier-stokes computations. *Energies*, 7(10):6798–6822.

Howland, M., Lele, S. and Dabiri, J. 2019. Wind farm power optimization through wake steering. *Proceedings of the National Academy of Sciences*, 116:201903680

Huang, R.F. and Lin, C.L. 1995. Vortex shedding and shear-layer instability of wing at low-Reynolds numbers. *AIAA Journal*, 33(8):1398–1403.

Jiang, Y., Finnegan, W., Flanagan, T. & Goggins, J. 2022. Optimisation of Highly Efficient Composite Blades for Retrofitting Existing Wind Turbines. *Energies*, 16:102.

Johnson, G. 2006. *Wind Energy Systems*. Manhattan,KS.

Jonkman, J.M. 2015. *AeroDyn v15 User's Guide and Theory Manual*, National Renewable Energy Laboratory 15013 Denver West Parkway Golden.

Katooli, M.H. and Noorollahi, Y. 2022. Shrouded wind turbines: a critical review on research and development. *International Journal of Ambient Energy*, 43(1):8775–8791.

Kaya, M.N., Kose, F., Ingham, D., Ma, L. & Pourkashanian, M. 2018. Aerodynamic performance of a horizontal axis wind turbine with forward and backward swept blades. *Journal of Wind Engineering and Industrial Aerodynamics*, 176(March):166–173.

Koç, E., Günel, O. and Yavuz, T. 2016. Comparison of Qblade and CFD results for small-scaled horizontal axis wind turbine analysis. 2016 IEEE International Conference on Renewable Energy Research and Applications, ICRERA 2016, (November 2016):204–209. Available at: <https://doi.org/10.1109/ICRERA.2016.7884538>

Manwell, J.F., McGowan, J.G. and Rogers, A.L. 2010. *Wind Energy Explained: Theory, Design and Application*, Wind Energy Explained: Theory, Design and Application. John Wiley & Sons Ltd., Available at: <https://doi.org/10.1002/9781119994367>

Marten, D. 2012. QBlade Guidelines. Berlin. <https://doi.org/10.13140/RG.2.1.3819.8882> [2023].

NACA 0024 (naca0024-il). n.d. <http://airfoiltools.com/airfoil/details?airfoil=naca0024-il#polars> [April 17, 2024].

National Aeronautics and Space Administration. n.d. Open return wind tunnel. <https://www.grc.nasa.gov/www/k-12/airplane/tunoret.html> [May 3, 2019].

Nava, S., Bot, P., Cater, J. & Norris, S.E. 2016. Modelling the lift crisis of a cambered plate at 0° angle of attack. *Proceedings of the 20th Australasian Fluid Mechanics Conference, AFMC 2016*, (March 2017):0–4

Ning, S. and Lu, X. 2019. Numerical simulation of boundary layer suction on the aerodynamic performance of wind turbine blade. *Journal of Renewable Energy*, 132:681–693.

Park, J.H. and Kim, J.J. 2016. Advanced wind turbine blade inspection and evaluation techniques, *Renewable and Sustainable Energy Reviews*.
[doi.org/https://research.tue.nl/en/studentTheses/improvement-of-aerodynamic-performance-of-vertical-axis-wind-turb](https://research.tue.nl/en/studentTheses/improvement-of-aerodynamic-performance-of-vertical-axis-wind-turb)

Parthasarathi Bera R. V. Lakshmi, S.M.P.V.B.L.M.J. and Barshilia, H.C. 2024. Recent Progress in the Development and Evaluation of Rain and Solid Particle Erosion Resistant Coatings for Leading Edge Protection of Wind Turbine Blades. *Polymer Reviews*, 64(2): 639–689.
doi.org/10.1080/15583724.2023.2270050.

Rajan, A. and Ponta, F.L. 2019. A novel correlation model for horizontal axis wind turbines operating at high-interference flow regimes. *Energies*, 12(6).
doi.org/10.3390/en12061148.

Refan, M. and Hangan, H. (2012) “Aerodynamic performance of a small horizontal axis wind turbine,” *Journal of Solar Energy Engineering, Transactions of the ASME*, 134(2), pp. 1–7. Available at: <https://doi.org/10.1115/1.4005751>.

Ram, K.R., Lal, S.P. and Ahmed, M.R. 2019. Design and optimization of airfoils and a 20 kW wind turbine using multi-objective genetic algorithm and HARP_Opt code. *Renewable Energy*, 144: 56–67.
[doi.org/https://doi.org/10.1016/j.renene.2018.08.040](https://doi.org/10.1016/j.renene.2018.08.040).

Resolved Analytics. n.d. <https://www.resolvedanalytics.com/theflux/comparing-cfd-software> [May 3, 2024]

Rodríguez-López, M., Del Rio, P. and Cerdá, E. 2020. Modeling Wind-Turbine Power Curves: Effects of Environmental Temperature on Wind Energy Generation. *Energies*, 13.
doi.org/10.3390/en13184941.

Sareen, A., Sapre, C.A. and Selig, M.S. (2014) “Effects of Leading Edge Erosion on Wind Turbine Blade Performance,” *Renewable Energy*, 66, pp. 428–436. Available at: <https://doi.org/10.1016/j.renene.2013.12.036>.

Semantic Scholar. n.d. <https://www.semanticscholar.org/paper/Best-Practice-%3A-Generalized-k-Two-Equation-Model-in-Menter-Lechner/3fb36ad80d8a5059c5a3b9034b9dab8cefa30156> [May 10, 2024]

SimScale. n.d. <https://www.simscale.com/docs/simulation-setup/global-settings/k-omega-sst/> [May 10, 2024].

SMART BLADE - Blade Aerodynamics & Design .n.d. <https://www.smart-blade.com/blade-design-1> [May 3, 2019].

Song, Q. 2012. Design, fabrication, and testing of a new small wind turbine blade. Unpublished Master Thesis, University of Guelph, Canada.

Spalart, P.R. (2009) “Detached-Eddy Simulation,” *Annual Review of Fluid Mechanics*, 41, pp. 181–202. Available at: <https://doi.org/10.1146/annurev.fluid.010908.165130>.

Vermeer, L.J., Sørensen, J.N. and Crespo, A. (2003) “Wind turbine wake aerodynamics,” *Progress in Aerospace Sciences*, 39(6–7), pp. 467–510.

Vos, E.M. 2018. Improvement of aerodynamic performance of vertical axis wind turbines using boundary layer suction. Eindhoven University of technology, Netherlands.
[doi.org/https://pure.tue.nl/ws/portalfiles/portal/131845511/Vos_0794831.pdf](https://pure.tue.nl/ws/portalfiles/portal/131845511/Vos_0794831.pdf).

Wilson, R.E. (1980) *Wind Energy Systems*. Prentice Hall.

Wind Turbine Components - Windmills Tech. n.d. <https://windmillstech.com/wind-turbine-blade-forces/> [February 5, 2024].

Zhao, D., Han, M., Goh, E., Cater, J. & Reinecke, A. 2019. Offshore wind turbine aerodynamics modelling and measurements. *Wind Turbines and Aerodynamics Energy Harvesters*, pp. 373–400. doi.org/10.1016/B978-0-12-817135-6.00005-3.

Zhao, Z., Jiang, R., Feng, J., Liu, H., Wang, T., Shen, W., Chen, M., Wang, D. & Liu, Y. 2022. Researches on vortex generators applied to wind turbines: A review. *Ocean Engineering*, 253:111266. [doi.org/https://doi.org/10.1016/j.oceaneng.2022.111266](https://doi.org/10.1016/j.oceaneng.2022.111266).

Zhou, F. and Liu, J. 2018. Pitch Controller Design of Wind Turbine Based on Nonlinear PI/PD Control. *Shock and Vibration*, 2018. doi.org/10.1155/2018/7859510